

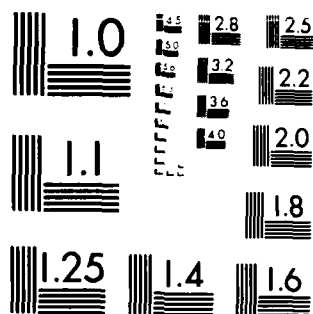
AD-A189 158

PREDICTIONS AND STUDIES WITH A ONE-DIMENSIONAL
ICE/OCEAN MODEL (U) NAVAL OCEAN RESEARCH AND DEVELOPMENT
ACTIVITY NSIL STATION MS S H RIEDLINGER ET AL APR 87
NORDA-195 F/G 8/3

1/2

UNCLASSIFIED

ML



MICROCOPY RESOLUTION TEST CHART
NATIONAL BUREAU OF STANDARDS-1963-A



DTIC FILE COPY

Predictions and Studies with a One-Dimensional Ice/Ocean Model

AD-A189 158

DTIC
ELECTE
DEC 04 1987
S H D

Shelley H. Riedlinger
Alex Warn-Varnas
Ocean Sensing and Prediction Division
Ocean Science Directorate

Foreword

The Fleet's interest in the Arctic environment is constantly increasing, and the need to be able to understand and forecast the arctic environmental phenomena has become an important issue of ocean research. This report deals with a one-dimensional coupled ice/ocean model that embodies the relevant Arctic thermodynamic and dynamic phenomena. This work is a first step toward a three-dimensional ice/ocean model.



A. C. Esau, Captain, USN
Commanding Officer, NORDA

Executive summary

A coupled one-dimensional ice/ocean model is developed in differential form. The ice/snow system is represented by the simplified thermodynamic model of Semtner and a dynamic approximation that neglects the internal stresses. The ocean is represented by the Mellor-Yamada Level-2 turbulence mixed-layer model.

The thermodynamic coupling considers a moving ice/ocean interface and a salinity flux generated by the freezing or melting of ice. The dynamic coupling occurs via the turbulent stress that exists in the mixed layer beneath the ice.

Two test cases are used for model validation and scientific studies. One is the standard climatological test used by Semtner and others. The other test case is with the AIDJEX data.

The ice/ocean model is compared to Semtner's ice model to determine the effect of a variable-depth mixed layer as opposed to an isothermal, fixed-depth mixed layer. The sensitivity of the ice/ocean model to changes in certain parameters and forcing is also examined. Finally, the ability of the model to simulate Arctic conditions is shown by comparison of model results to data obtained during AIDJEX.



Accession For	
NTIS GRA&I	<input checked="checked" type="checkbox"/>
DTIC TAB	<input type="checkbox"/>
Unannounced	<input type="checkbox"/>
Justification	
By _____	
Distribution/	
Availability Codes	
Dist	Avail and/or Special
A-1	

Acknowledgments

This work was supported by the Office of Naval Research, program element, 61153N, Herbert C. Eppert, Jr., program manager. The authors would like to acknowledge valuable assistance provided by Dr. Albert J. Semtner, Dr. William B. Hibler, and Dr. Ruth Preller.

Contents

1. Introduction	1
2. Description of the model	2
a. Introduction	2
b. Grid	2
c. Initial conditions and forcing	2
d. Ocean currents	2
e. Ice thermodynamics model	2
f. Ice dynamics model	4
g. Ocean model	4
h. Boundary conditions	4
i. Solar radiation in the ocean	5
j. Computing oceanic heat flux	5
3. Case 1—climatology model runs	6
a. Setup of models	6
b. Comparing model results	6
c. Oceanic heat flux	9
d. Sound speed	10
4. Effect of changing σ and q_b	10
5. Deep ocean heat flux (H_{deep})	11
6. Case 2—solar radiation stored in brine pockets	11
a. Setup of model	11
b. Results	12
7. Case 3—run with AIDJEX data	16
a. Setup of model	16
b. Diurnal cycle	16
c. No diurnal cycle	17
d. Diurnal cycle versus no diurnal cycle	17
e. Model results versus AIDJEX data	18
f. Open water and AIDJEX	19
8. Summary and conclusions	20
9. References	21
Appendix A: Ocean Model Equations	111
Appendix B: List of Symbols	115
Appendix C: Corresponding Calendar Date and Model Time Steps	117

Predictions and Studies with a One-Dimensional Ice/Ocean Model

1. Introduction

Our work was motivated by the need to further develop the coupling of Arctic ice and ocean. The present status of the coupling ranges from an ocean described by prescribed heat fluxes and currents to a coarse coupling of ice and ocean. We will introduce a detailed polar mixed-layer representation and couple the Arctic ice and ocean through it. This will enable the ice to influence the ocean and the ocean to influence the ice. We will develop and validate the representation of the associated physical processes and coupling mechanics.

Most of the previous ice models treated the ocean in a passive or a semipassive sense. The passive approach consisted of a prescription of climatological ocean currents and heat fluxes. The semipassive approach included a heat budget calculation with a constant depth mixed-layer prescription (Hibler, 1980). The climatologies ranged from mean annual to seasonal time scales. Examples are the work of Coachman and Aagaard (1974) for annual ocean currents, or the diagnostic use of the Hibler-Bryan (1984) results for providing seasonally varying ocean currents and heat fluxes. In ice forecasting, the use of the seasonally varying ocean currents and heat fluxes has been shown to yield a more realistic ice edge (R.H. Preller, personal communication, 1986).

The coupling of ice and ocean has so far been approached at various levels of sophistication. The thermodynamic part usually contains Semtner's (1976) snow and ice model. The simplest thermodynamic coupling to the ocean involves the prescription of a constant depth mixed layer and a heat budget calculation (Parkinson and Washington, 1979; Hibler and Bryan, 1984).

More sophisticated thermodynamic models of the snow, ice, and water system involved representations of the polar mixed-layer region at various levels of sophistication. Pollard et al. (1983) have experimented with a slab model superposed on a prescribed thermocline. The model was used to simulate the thermodynamic cycle of a snow, ice, and water system.

The simplest dynamic coupling of a snow, ice, and water system was accomplished through the use of a drag law between ice and ocean (Parkinson and Washington, 1979; Hibler and Bryan, 1984). A more

sophisticated approach incorporates boundary layer formalism and uses an iteration technique to calculate the Reynolds stress between the ice and water (Overland et al., 1984).

Recently, Mellor et al. (1986) developed a time-dependent, second-moment, turbulence closure representation of the coupled ice and water system. The model has a detailed boundary layer representation and considers freezing and melting phase transitions, and represents the associated unstable and stable states.

Our approach considers a time-dependent, horizontally homogeneous snow, ice, and water system. The coupling of the snow, ice, and water system is developed on a stretched vertical grid. Second-order closure is used for the representation of the polar mixed layer.

The thermodynamics of the ice and snow system is represented by the Semtner 0-layer model. The ice dynamics is represented by momentum equations that neglect the internal ice stresses. The coupling of the ice and polar mixed layer is developed through the interfacial stresses, heat fluxes, and freezing/melting processes representation.

Studies of the climatological, seasonal, and diurnal cycles are performed with the coupled ice/ocean model. The previous climatological simulations of Semtner (1976) are repeated. Feedback due to ice/ocean coupling plays a role in these simulations. The effects of feedback can be seen in the multiyear equilibrium cycle of ice thickness, heat budget, surface temperature, and other variables.

The cycle of open-water appearance changes from Semtner's (1976) previous results. Sensitivity studies of the appearance and disappearance of open water are conducted with the coupled ice/ocean model by varying various parameters. During the open-water period, the water is heated by the incoming solar radiation. As the water refreezes a hot spot moves downward into the ocean and gradually diffuses.

Another set of studies is performed with the AIDJEX data. The data spans a period of a year and contains daily measurements. Model simulations of the seasonal cycle are performed with a time step that resolves the diurnal variations. The simulated

conditions are compared with the AIDJEX data. The diurnal, seasonal, and climatological responses are studied.

2. Description of the model

a. Introduction

This paper is concerned with the design and testing of a one-dimensional numerical ice/ocean model. In this model, Semtner's (1976) 0-layer ice model, together with simplified ice dynamics, is coupled with an ocean mixed-layer model that uses a turbulence parameterization scheme based on Mellor-Yamada Level-2 turbulence closure theory (Mellor and Yamada, 1974).

Semtner's ice model assumes a state of conductive equilibrium for heat and has three prognostic variables: snow thickness, h_s ; ice thickness, h_i , and surface temperature, T_s . His model uses the imbalance in atmospheric fluxes at the snow/ice surface, and the conductive heat flux within the snow/ice system to compute the surface temperature of the system. If this temperature rises above the freezing point, the surface temperature is set at the freezing point, and the amount of surface melt is computed from the heat surplus. At the bottom of the ice, the imbalance between a prescribed, constant oceanic heat flux and the conductive flux within the snow/ice system is used to determine the accretion or ablation of ice. Semtner assumes a 30-m-deep, vertically isothermal mixed layer and calculates the associated heat budget during open-water periods in order to simulate seasonal transition between an ice-covered ocean and an ice-free ocean. When the mixed-layer temperature drops to or below the freezing point, ice reforms.

A simplified, one-dimensional ice dynamics model is constructed. The model assumes a horizontally homogeneous layer of ice and neglects the internal ice stresses. This is the free-drift approximation that is valid for ice drifting in the ocean and not experiencing internal stresses and pressure.

The vertically isothermal mixed layer in Semtner's model is replaced by a dynamic, thermodynamic mixed layer. This polar mixed layer is represented by a level-2 turbulent closure model (Mellor and Durbin, 1975; Clancy and Martin, 1981). This model has prognostic equations for temperature, salinity, and velocity. The model is in differential form and resolves the Reynolds and thermal stresses.

b. Grid

The vertical grid used in the coupled ice/ocean model has two points in the snow/ice system and 17 levels between the ocean surface and 500 m depth (Fig. 1). Temperature, salinity, density, and velocity for the water column are defined at depth of 2.5, 7.5, 12.5,

17.5, 25, 32.5, 40, 50, 62.5, 75, 100, 125, 150, 200, 300, 400, and 500 m. The vertical eddy fluxes are defined midway between these depths.

c. Initial conditions and forcing

Two different test cases are used for model validation and scientific studies. One is the standard central Arctic climatological test case used by Semtner (1976) and others. The other case is the AIDJEX experiment. The AIDJEX experiment resolves the diurnal time scale.

For both test cases, the mixed layer was initialized with temperature and salinity profiles taken from AIDJEX data. In particular, profiles from station Blue Fox, January 1, 1976, were chosen. These profiles represent typical winter profiles for the Beaufort Sea, where the AIDJEX data was taken (Figs. 2 and 3). For the climatological test case, the model was forced with radiative fluxes from Fletcher's monthly mean climatology (Table 1, Semtner, 1976). Semtner's snowfall rate and average monthly winds from 1983 Fleet Numerical Oceanography Center (FNOC) analysis were also used. Figures 4-10 show these fluxes interpolated to each time step. (The AIDJEX test case will be described later.)

d. Ocean currents

Ice and ocean velocities are calculated and used in estimates of mechanical stirring within the mixed layer. A constant geostrophic current of $u_g = -1.2$ cm/sec and $v_g = -0.65$ cm/sec is assumed. Horizontal advection however, is not included.

e. Ice thermodynamics model

A complete description of Semtner's 0-layer ice model is contained in his paper. The following is an outline of the relevant equations.

The conductive heat flux through the snow/ice system (assuming heat flux and z are positive downward) for snow-covered ice is

$$F_S = \frac{-k_i(T_B - T_S)}{h_i + (h_s k_i / k_s)}, \quad (1)$$

and for snow-free ice is

$$F_S = \frac{-k_i(T_B - T_S)}{h_i}, \quad (2)$$

where $k_i = 4.86\text{E-}3$ cal/cm/sec/°C and $k_s = 7.4\text{E-}4$ cal/cm/sec/°C are the conductivities of ice and snow, respectively. The quantity T_B is the temperature at the bottom of the ice, T_S the temperature at the surface of the snow/ice system, h_i the ice thickness, and h_s the snow thickness.

Table 1. Listing of parameters and assigned values used in Case 1 for both the CML case and the VML case.

	Constant Mixed Layer	Variable Mixed Layer
H_i :	50 cm	50 cm
H_b :	30 cm	30 cm
F_b :	-1.929E-4 cal/cm ² /sec	-1.929E-4 cal/cm ² /sec
T_s :	-2.0°C	-2.0°C
T_b :	-2.0°C	Varies with salinity
σ :	1.385E-12 cal/cm ² /K ⁴ /sec	1.385E-12 cal/cm ² /K ⁴ /sec
α_i :	0.66448	0.66448
α_w :	0.07	0.07
q_s :	72 cal/cm ³	72 cal/cm ³
q_b :	64 cal/cm ³	64 cal/cm ³
γ :	1.065	1.065
MLD:	30 m	Variable
SFF:	None	3.341E-5 cm/sec
Time step:	8 hours	8 hr/30 min
Forcing:		
Heat fluxes:	Climatology	Climatology
Winds:	None	FNOC average monthly
T&S profile:	None	AIDJEX data (Beaufort Sea)

The change in the surface temperature T_s is computed from a heat balance between the atmospheric fluxes and the conductive flux F_s at the surface of the snow/ice system. The surface temperature at a previous time step is denoted by T_p and $T_s = T_p + \Delta T_s$ is the temperature at the present time step. Thus ΔT_s can be solved from the heat balance by making the above substitution for T_s . The result is

$$\Delta T_s = \left[F_l + F_t + F_L + (1-\alpha_s)F_R - \sigma T_p^4 + k_i(T_b - T_p)/\{h_i + (h_s k_i/k_s)\} \right] / \left[4\sigma T_p^3 + k_i/\{h_i + (h_s k_i/k_s)\} \right], \quad (3)$$

when snow-covered, and by

$$\Delta T_s = \left[F_l + F_t + F_L + (1-\alpha_i)F_R - \sigma T_p^4 + k_i(T_b - T_p)/h_i \right] / \left[4\sigma T_p^3 + k_i/h_i \right], \quad (4)$$

when snow-free. The quantity F_l represents latent heat flux, F_t sensible heat flux, F_L incoming longwave radiation, α_i and α_s the albedos of ice and snow, respectively, F_R incoming solar radiation, and σ the Stefan-Boltzmann constant. Second-order or greater terms in ΔT_s are ignored in the previous equations.

The accumulation of snow is determined by a set snowfall rate. The amount of snow melt is computed from

$$\Delta h_s = \Delta t (F_s - F_A)/q_s, \quad (5)$$

when T_s is above freezing.

The growth or decay of ice at the bottom is determined from

$$\Delta h_b = \Delta t (F_b - F_s)/q_b, \quad (6)$$

and the melting of ice at the surface when snow-free and T_s is above freezing, is computed from

$$\Delta h_i = \Delta t (F_s - F_A)/q_i. \quad (7)$$

The quantity F_A represents the sum of the atmospheric fluxes, i.e., the first five terms on the right side of Eq. (3) and Eq. (4), F_b the oceanic heat flux, q_i the volumetric heat of fusion for the snow, q_b and q the volumetric heats of fusion at the bottom and the top of the ice, and Δt the time step.

f. Ice dynamics model

The equations defining the ice drift are

$$\frac{\partial u}{\partial t} i = f(v_i - v_g) + \frac{\tau_{ax}}{m} + \frac{\tau_{wx}}{m}, \quad (8)$$

$$\frac{\partial v}{\partial t} i = -f(u_i - u_g) + \frac{\tau_{ay}}{m} + \frac{\tau_{wy}}{m}, \quad (9)$$

where u_i and v_i are the x- and y-components of the ice velocity, τ_{ax} and τ_{ay} are the x- and y-components of the wind stress, τ_{wx} and τ_{wy} are the x- and y-components of the water stress, and m is the mass of the ice.

g. Ocean model

The ocean model consists of a mixed layer and the upper ocean down to 500 m. Physical processes included are vertical mixing, radiation, and planetary rotation. The conservation equations for temperature, salinity, and momentum are

$$\begin{aligned} \frac{\partial \bar{T}}{\partial t} = & \frac{\partial}{\partial z} (-\bar{w}T) + \frac{\partial}{\partial z} (-\bar{w}'T' + v \frac{\partial \bar{T}}{\partial z}) \\ & - \frac{1}{\rho_o c} \frac{\partial F_{SR}}{\partial z}, \end{aligned} \quad (10)$$

$$\frac{\partial \bar{S}}{\partial t} = \frac{\partial}{\partial z} (-\bar{w}S) + \frac{\partial}{\partial z} (-\bar{w}'S' + v \frac{\partial \bar{S}}{\partial z}), \quad (11)$$

$$\frac{\partial \bar{u}}{\partial t} = f\bar{v}_w - f\bar{v}_g + \frac{\partial}{\partial z} (-\bar{w}'u'_w + v \frac{\partial \bar{u}}{\partial z}), \quad (12)$$

$$\frac{\partial \bar{v}}{\partial t} = -f\bar{u}_w + f\bar{u}_g + \frac{\partial}{\partial z} (-\bar{w}'v'_w + v \frac{\partial \bar{v}}{\partial z}), \quad (13)$$

where T is the temperature, S the salinity, F_{SR} the downward flux of solar radiation, u_w and v_w the x- and y-components of the current velocity, w the z-component of the current velocity, u_g and v_g the x- and y-component of the geostrophic current velocity, v a diffusion coefficient, f the Coriolis parameter, ρ_o a reference density for the ocean (1.025 g/cm³), c the specific heat for the ocean (0.954 cal/g/°C), t the time, and z the vertical coordinate. Ensemble means are denoted by $(\bar{\quad})$, and primes indicate departure from these means. Thus, for example, the quantity $\bar{w}'S'$ represents the vertical eddy (i.e., turbulent) flux of salinity.

The terms involving v in Eqs. (10)–(13) represent very weak "background" eddy diffusion that exists even below the mixed layer. The value of v is set to 0.3 cm²/sec.

The vertical eddy fluxes of temperature, salinity, and momentum are given by

$$\bar{w}'T' = -K_H \frac{\partial \bar{T}}{\partial z}, \quad (14)$$

$$\bar{w}'S' = -K_H \frac{\partial \bar{S}}{\partial z}, \quad (15)$$

$$\bar{w}'u'_w = -K_M \frac{\partial \bar{u}}{\partial z}, \quad (16)$$

$$\bar{w}'v'_w = -K_M \frac{\partial \bar{v}}{\partial z}, \quad (17)$$

where K_H and K_M are eddy diffusion coefficients.

For a more detailed description of the ocean model equations see Appendix A.

h. Boundary conditions

The boundary conditions for the upper snow/ice boundary are provided by the surface fluxes, F_i , F_L , and F_R . These fluxes are used in the heat balance at the surface. The lower boundary condition is that the bottom of the ice remains at the freezing point.

The upper boundary conditions for the ocean depend on whether it is ice-covered or ice-free. When ice-covered, the boundary condition for the temperature is the freezing point of the surface waters. The salinity boundary condition is dependent upon whether the ice is melting or freezing. It is assumed that when the ocean freezes all the salt is excluded from the ice, thus increasing the salinity of the surface layers. When the ice melts, fresh water is added to the surface layer. The salinity flux is then given by

$$(\bar{w}'S')_o = \frac{\rho_i}{\rho_o} \frac{\Delta S}{1000} \frac{\Delta h_i}{\Delta t}, \quad (18)$$

where ρ_i is the density of ice (0.92 g/cm³), $\Delta S/1000$ is the salinity difference per mill, assumed to be 30, and $\Delta h_i/\Delta t$ is the change in the ice thickness with time. Thus, an increase in ice thickness means the salinity flux is increased at the surface, and a decrease in ice thickness means a decrease in the salinity flux at the surface. A constant fresh-water influx of 72 g/cm²/year is also assumed (Pollard et al., 1983).

When there is no ice the upper boundary conditions for the temperature, salinity, and momentum equations are provided by the surface fluxes. Thus,

$$[-\bar{w}'T' + v \frac{\partial \bar{T}}{\partial z}]_{z=0} = \frac{(F_{SR} + F_t + F_l)}{\rho_o c}, \quad (19)$$

$$[-\bar{w}'S' + v \frac{\partial \bar{S}}{\partial z}]_{z=0} = \frac{-F_l \bar{S}_o}{\rho_o}, \quad (20)$$

$$\left[-\overline{w'u'_w} + v \frac{\partial \bar{u}}{\partial z} \right]_{z=0} = \frac{\tau_{ax}}{\rho_o}, \quad (21)$$

$$\left[-\overline{w'v'_w} + v \frac{\partial \bar{v}}{\partial z} \right]_{z=0} = \frac{\tau_{ay}}{\rho_o}. \quad (22)$$

The lower boundary conditions for the ocean are provided by holding the initial temperature, salinity, and momentum at the bottom of the water column constant.

The upper boundary condition for the ice velocity is provided by the wind stress. The lower boundary condition is provided by the stress of the water velocity relative to the ice velocity. The stress in both instances are computed using the drag law as follows:

$$\frac{\tau_{ax}}{m} = 2.7E-3 \rho_a / (\rho_i h_i) \sqrt{[u_a^2 + v_a^2]} \left[\begin{matrix} u_a \\ v_a \end{matrix} \right], \quad (23)$$

$$\frac{\tau_{ay}}{m} = 2.7E-3 \rho_a / (\rho_i h_i) \sqrt{[u_a^2 + v_a^2]} \left[\begin{matrix} v_a \\ u_a \end{matrix} \right], \quad (24)$$

$$\begin{aligned} \frac{\tau_{wx}}{m} = & 5.5E-3 \rho_o / (\rho_i h_i) \sqrt{[(u_g - u_i)^2 + (v_g - v_i)^2]} \left[\begin{matrix} (u_g - u_i) \cos 25^\circ \\ -(v_g - v_i) \sin 25^\circ \end{matrix} \right], \end{aligned} \quad (25)$$

$$\begin{aligned} \frac{\tau_{wy}}{m} = & 5.5E-3 \rho_o / (\rho_i h_i) \sqrt{[(u_g - u_i)^2 + (v_g - v_i)^2]} \left[\begin{matrix} (v_g - v_i) \cos 25^\circ \\ (u_g - u_i) \sin 25^\circ \end{matrix} \right], \end{aligned} \quad (26)$$

where ρ_o is the density of air, u_a and v_a are the x- and y-components of the wind, and the angle 25° is the value assumed for the turning angle between the ice and the water.

i. Solar radiation in the ocean

When the ocean is ice-free, solar radiation can penetrate into the water column and warm the surface layers. The solar radiation absorbed at each depth level is determined from the following equation:

$$\Delta F_{SR}(z) = (1 - \alpha_w) F_R (e^{-0.00067z_k} - e^{-0.00067z_{k+1}}), \quad (27)$$

where α_w is the albedo of open water, and z_k and z_{k+1} are depth levels within the ocean.

j. Computing oceanic heat flux

The oceanic heat flux F_B is computed by keeping track of the change in the heat content of the water column and the heat input by solar radiation, diffusion, and from the deep ocean. The equation used to do this is derived by first integrating Eq. (10) over the water column to get

$$\begin{aligned} \int_{z=0}^{z=z_1} \frac{\partial \bar{T}}{\partial t} dz = & - \int_{z=0}^{z=z_1} \frac{\partial (\overline{wT})}{\partial z} dz \\ & - \int_{z=0}^{z=z_1} \frac{\partial (\overline{w'T'})}{\partial z} dz \\ & - \int_{z=0}^{z=z_1} \frac{\partial F_{SR}}{\partial z} dz, \end{aligned} \quad (28)$$

where the term involving v is combined with the $\overline{w'T'}$ term, and $z_1 = 500$ m. Evaluating the integral yields

$$\begin{aligned} \int_{z=0}^{z=z_1} \frac{\partial \bar{T}}{\partial t} dz = & -\overline{wT}|_{z_1} + \overline{wT}|_0 - \overline{w'T'}|_{z_1} \\ & + \overline{w'T'}|_0 - F_{SR}|_{z_1} \\ & + F_{SR}|_0. \end{aligned} \quad (29)$$

Assuming that w at the surface is zero and solving for $\overline{w'T'}|_0$, the heat flux at the surface, Eq. (29) becomes

$$\begin{aligned} \overline{w'T'}|_0 = & \int_{z=0}^{z=z_1} \frac{\partial \bar{T}}{\partial t} dz + \overline{wT}|_{z_1} \\ & + \overline{w'T'}|_{z_1} + F_{SR}|_{z_1} \\ & - F_{SR}|_0. \end{aligned} \quad (30)$$

Then, the oceanic heat flux is

$$F_B = \rho_o c [\overline{w'T'}|_0]. \quad (31)$$

The quantity $\overline{wT}|_{z_1}$ represents heat brought into the water column from the deep ocean, $\overline{w'T'}|_{z_1}$ represents the exchange of heat across the bottom boundary by diffusion, and $[F_{SR}|_{z_1} - F_{SR}|_0]$ represent heating by solar radiation.

3. Case 1— climatology model runs

a. Setup of models

The first case to be considered is a repeat of one of the test cases from Semtner (1976). In particular, the multiyear ice cycles, shown in his Figure 8 (Fig. 11, this paper). In this example all the ice melted, which yielded an open-water period during the summer. In the fall the ice reappeared and grew rapidly through the winter. The ice persisted for 6 years before another open-water period occurred. This case was chosen so that our simulation of Semtner's model could be verified and so that we could compare the effects of the different treatments of the mixed layer on the growth and decay of ice. Henceforth, Semtner's model will be referred to as the constant mixed-layer model (CML) and ours as the variable mixed-layer model (VML).

To more readily compare the models, many of the same parameters used in the CML model are used in the VML model. These parameters and a few used only in the VML model are listed in Table 1. The values for H_i and H_s are the initial ice thickness and snow thickness, respectively. The oceanic heat flux, F_b , is a constant in the CML model. In this simulation, its value is $-6 \text{ kcal/cm}^2/\text{year}$ ($-1.929\text{E-}4 \text{ cal/cm}^2/\text{sec}$ or -8.07 W/m^2). In the VML model, F_b is determined from Eq. (31) in Section 2j. The heat flux from the deep ocean, wT_d , however, is a constant and is given the value of $-6 \text{ kcal/cm}^2/\text{year}$. The surface temperature T_s is initialized to -2°C in both models. The temperature at the bottom of the ice T_b is assumed to always be at the freezing point of the surface water. In the CML model, this value was always -2°C . In the VML model, the freezing point varies with the salinity of the mixed layer. The Stefan-Boltzmann constant σ is about 2% higher than the standard value. Semtner used this value to compare his results with those of Maykut and Untersteiner (1969). In Section 4 the effect of changing this value to the accepted one will be discussed. The value given for α_i is used in the 0-layer ice model to account for some of the solar radiation which penetrates into snow-free ice (appendix, Semtner, 1976). The quantities q_t and q_b are the volumetric heats of fusion at the top and the bottom of the ice. Semtner questioned the validity of using two different values for this quantity, but again used it for the sake of comparison with Maykut and Untersteiner. γ is a correction factor Semtner used, since the 0-layer ice model does not keep track of solar radiation stored in the ice in brine pockets. Without the brine pockets the ice is thinner than it should be. To compensate for this error, Semtner increased the snow and ice conductivities by the amount

1.065. The mixed-layer depth (MLD), as mentioned earlier, was 30 m in the CML model. In the VML model, this quantity is determined by the dynamics of the mixed-layer. The parameter SFF represents freshwater input. The time step for the 0-layer ice model is 8 hours. The time step for the mixed-layer model is 30 minutes.

b. Comparing model results

Each model was integrated for 20 years. The ice thickness and ice plus snow thickness values for both cases are shown in Figure 12. The top graph in this figure is the CML case. The bottom graph is the VML case.

A 6-year, no-ice cycle, such as the one obtained by Semtner, quickly develops in the CML simulation. In the VML simulation, a short open water period occurs during year 2 and again in year 4. Then beginning in year 6, open-water occurs every year, with the length of the open-water period increasing each successive year. The no-ice cycles for these cases are obviously quite different. These differences must be due to the differences in the treatment of the mixed layer.

In the CML case, the only time the mixed layer is used is when open water occurs, and only the temperature of the mixed layer is computed. A typical plot of mixed-layer temperature for a year in which open water occurs is shown in Figure 13. The water temperature increases to a maximum of -1.002°C during the open-water period, and then decreases back to a -2.0°C value before ice is reformed. When the ocean is ice covered the water temperature remains near the freezing point, which is assumed to be -2.0°C . This pattern changes little throughout the simulation. From Table 2, one can see that the maximum mixed-layer temperature varies by less than 0.3°C between the open-water periods.

The length of each open-water period is also fairly constant. In the case shown in Figure 13, the open-water period lasted for 59.7 days. The average open-water period during the simulation is 54.7 days. Each year in which open water occurs, the ice cover disappears in late August (around Aug. 20) and re-forms in mid-October (around October 15). The heaviest snowfall in the simulation occurs during the months of September and October (Fig. 10). Thus, open water exists during the time when the snowfall is the greatest. Snow cover acts as an insulator that slows down the growth of ice. With a very thin snow cover, which develops in the latter part of the year, this insulating effect is greatly reduced, and ice growth is quite rapid. From Table 2, it is seen that the ice thickness is the greatest in the year following an open-water event. The ice thins each successive year until open water occurs again. The snow cover during these years is thicker than in the year following the open-water event. The thicker snow cover insulates the ice from the surface fluxes

Table 2. Listing of ice thicknesses, number of open-water days, and mixed-layer temperatures for a 20-year simulation of the CML model. (Case 1)

Year	# Open Water Days	Mean Annual Ice Thickness	Maximum Ice Thickness	T(1) Max °C
1	0.0	52.09	94.13	-2.000
2	59.7	52.06	89.31	-1.002
3	0.0	105.79	159.85	-2.015
4	0.0	84.12	124.65	-2.015
5	0.0	70.18	110.61	-2.015
6	0.0	60.90	101.35	-2.015
7	0.0	54.67	95.26	-2.015
8	51.0	53.59	91.12	-1.267
9	0.0	101.07	153.75	-2.002
10	0.0	80.94	121.44	-2.002
11	0.0	68.06	108.49	-2.002
12	0.0	59.49	99.96	-2.002
13	0.0	53.71	94.33	-2.002
14	54.7	53.02	90.48	-1.154
15	0.0	102.88	156.33	-2.004
16	0.0	82.04	122.55	-2.004
17	0.0	68.79	109.22	-2.004
18	0.0	59.97	100.44	-2.004
19	0.0	54.04	94.65	-2.004
20	53.3	53.22	90.70	-1.197

T(1) Max—maximum temperature of mixed layer

and slows down the freezing rate; however, the oceanic heat flux is unaffected, since it is a prescribed constant. The oceanic heat flux then gradually reduces the ice thickness by melting at the bottom.

In the VML simulation, the mixed layer interacts with the ice or the atmosphere every time step. The heat, salt, and momentum fluxes at the water surface affect heating and mixing within the water column. Heating and mixing within the water column then affects the growth and decay of the ice. The mixed-layer temperature for year 2 from the VML simulation is shown in Figure 14. The temperature varies from -1.705°C to -1.546°C during this year. The maximum value occurs during the open-water period. The mixed-layer temperature shown here is actually the temperature at the 2.5-m depth level (which is the first level in the vertical grid), since the depth of the mixed-layer deepens and shallows in response to forcing. The mixed-layer depth throughout year 2 is shown in Figure 15. The mixed-layer depth is defined as the maximum depth at which the salinity has changed by no more than 0.1 ppt from its surface value. Salinity is used, since the density is strongly influenced by the salinity in the Arctic regions. As expected, the mixed layer, as seen in the figure, deepens in the winter and shallows in the summer. During the open-water period, the mixed layer is only 2.5 m deep. Also, open water occurs rather late in the year. A little heating occurs

in the mixed layer, but because it is thin, it quickly cools to the freezing point and ice re-forms. The open-water period is short in this case, since a thin layer of water is being heated and cooled. The open-water period is only 4.7 days. As with the CML case, the open water occurs late in August, but unlike the CML case, ice re-forms quickly; so ice exists during the heavy snowfall months. The resulting snow cover insulates the ice and slows down the freezing rate. The ice thickness in year 3 in the VML case is quite thinner than in year 3 in the CML case (maximum of 94.04 cm, as compared with a maximum of 159.89 cm). The decrease in ice growth eventually results in more frequent open-water periods later in the simulation. Snow cover is not, however, the only factor in the thinner ice. The oceanic heat flux is also important.

The oceanic heat flux is not constant in the VML simulation, but is computed from the change in the heat content of the water column as described in Section 2j. Table 3 is a listing of several values computed by the model and includes the amount of heat input into the water column from the deep ocean, from diffusion, and from solar heating. The heat input from the deep ocean and from diffusion vary little from year to year. A large variability occurs in the solar heating term. This results in variability in the oceanic heat flux and the net heating of the water column. Solar radiation penetrates into the water column as described in

Table 3. Listing of ice thicknesses, number of open-water days, mixer-layer temperatures, and oceanic heating for a 20-year simulation of the VML model. (Case 1)

Year	# Open Water Days	Mean Annual Ice Thickness	T(1) Max °C	T Max °C	cal/cm ² /year				
					H _{deep}	Diff	Solar	F _B	Net
1	0.0	51.68	-1.611	-1.460	5999.0	259.0	0.0	-6193.4	65.6
2	4.7	50.08	-1.546	-1.381	5998.4	314.8	982.2	-7005.5	289.6
3	0.0	53.31	-1.625	-1.449	5997.8	358.5	0.0	-6292.3	64.0
4	4.3	50.37	-1.555	-1.408	5997.4	392.9	901.5	-7026.4	265.0
5	0.0	53.10	-1.632	-1.397	5997.1	419.8	0.0	-6338.3	78.6
6	9.3	48.63	-1.572	-1.105	5996.8	440.7	2040.5	-7884.2	593.0
7	24.0	46.35	-1.391	-0.546	5996.6	456.9	4988.6	-10454.0	988.0
8	40.0	43.66	-0.976	-0.123	5996.5	469.3	7950.7	-13369.0	1047.6
9	35.7	45.26	-1.090	-0.224	5996.4	478.5	7176.5	-13103.0	548.1
10	38.3	44.68	-1.020	-0.156	5996.3	480.5	7648.9	-13526.0	604.3
11	41.3	43.84	-0.924	-0.065	5996.3	489.3	8218.7	-14082.0	622.2
12	43.0	43.11	-0.850	0.005	5996.2	491.5	8591.3	-14482.0	597.3
13	46.7	42.11	-0.724	0.123	5996.2	492.0	9294.7	-15145.0	638.3
14	49.0	41.36	-0.619	0.221	5996.2	491.0	9807.7	-15659.0	636.3
15	52.3	39.99	-0.463	0.363	5996.3	488.9	10573.0	-16419.0	639.3
16	54.3	39.00	-0.353	0.464	5996.3	485.8	11073.0	-16934.0	621.5
17	53.0	37.72	-0.298	0.517	5996.3	481.8	11173.0	-16838.0	813.5
18	62.0	33.15	0.161	0.946	5996.4	477.2	13347.0	-18552.0	1269.0
19	67.3	30.56	0.458	1.227	5996.5	472.0	14732.0	-19978.0	1222.9
20	80.7	30.04	0.672	1.431	5996.5	466.3	16077.0	-22374.0	165.8

T(1) Max—maximum temperature at depth level 1 (2.5 m)

T Max—maximum temperature in the water column

H_{deep}—total heat input into the water column by advection from the deep ocean

Diff—total heat input into the water column by diffusion across the bottom

Solar—total heat input into the water column by solar radiation

F_B—total heat transfer across the ice/ocean or ice/water interface

Net—H_{deep} + Diff + Solar + F_B

Section 2i. Each depth level absorbs different amounts of heat from solar radiation. The surface level (2.5-m level) absorbs the most solar heat. It also reacts the fastest with the atmospheric forcing; thus, the heating or cooling of the surface layer can be quite rapid. Figure 16 shows some temperature profiles for steps before (step 695), during (steps 700–720), and after (steps 725 and 730) the open-water period. One sees that the water column is being warmed during the open-water period. The subsurface waters are warmed the most, since they are slower to respond to surface forcing. The subsurface layers are insulated from the surface forcing at this time because the water column is highly stratified and because no mixing occurs until ice starts to grow again (Fig 17). The maximum temperature that occurs in the water column in this case is -1.381°C and occurs at the 12.5-m depth level at time step 720.

Ice begins to grow again at step 721, since the temperature in the surface waters has dropped below the freezing point. The temperature in the subsurface waters, however, remains slightly above the freezing

point after ice has re-formed (steps 725 and 730). This heat in the subsurface waters is released as the mixed layer deepens as the ice grows. This can be seen in Figure 18, which shows some temperature profiles for the last part of year 2. During this time ice grows from 1 cm to approximately 40 cm thick and the mixed layer deepens from 2.5 m to 32.0 m. The release of this heat in the subsurface waters during the growth of ice slows down the freezing rate of ice. This effect yields thinner ice, and in combination with the snow cover, explains why years 2 and 3 are so different between the CML and the VML simulation.

Year 4 in the VML simulation is quite similar to year 2. In year 6, however, open water occurs slightly earlier in the year than in year 2 or 4, and it lasts a few days longer. The warming of the water column is thus greater, and the ice thickness for this year is thinner than in the previous years. Following this year open water occurs every year. The length of the open-water period tends to increase each successive year, and so does the heating in the water column.

Using year 10, as an example, the heating of the water column will be examined in more detail. The open-water period this year lasted 38.3 days. It opened up on August 10 and began to refreeze on September 20. This period is not 38.3 consecutive days of open water, but 36 days of open water followed by a brief period of ice growth between September 16 and September 18. During this time 2 cm of ice formed. The mixed layer deepened as a result of the ice growth releasing some heat from below the mixed layer. The heat was sufficient to melt the thin ice cover and to keep the ocean ice-free until September 20 when continuous ice growth began.

Temperature profile plots for this year are shown in Figures 19 and 20. At step 655 in Figure 19, no warm spot is observed in the water column down to 100 m. At step 680, the warm spot begins to form and grows until step 780 (open water is from step 659 to step 780). After this step, the warm spot is seen to decrease at the same time that the mixed layer deepens. However, not all the heat in the warm spot is exhausted by the end of the year (step 1080 in Fig. 20). In fact, it is not until early spring of the following year that the warm spot disappears (Fig. 21: step 375 occurs on May 6). Thus, the heat input into the water column during this open-water period affects the growth of ice for several months after ice re-forms. The net result is thinner ice and warmer water below the ice. In general, as seen in Table 3, the heat input into the water column in a year's time is not all released in that year. The previous year greatly affects the following year.

Examining Table 3, one sees that the solar heat input tends to increase with each successive year, beginning with year 9, and that the oceanic heat flux, F_B , also tends to increase, except between years 16 and 17. The net heating, however, fluctuates from year to year. This implies that the release of heat from the water column is not in a steady manner, but is highly variable.

c. Oceanic heat flux

The variability of the oceanic heat flux throughout a year is shown in Figure 22. The dashed line in the plot is the value $-6.0 \text{ kcal/cm}^2/\text{year}$, the constant heat input from the deep ocean. The oceanic heat flux throughout much of this year is considerably larger than this constant value. The only time F_B remains near this constant value is in the early summer when ice is melting and the mixed-layer is shallowing. The largest values of oceanic heat flux occur in the winter following the open-water period. Comparing this plot to the plot of the salinity mixed layer depth (Fig. 23), one sees that these large oceanic heat flux values correspond to times when the mixed layer is deepening. So, just as was seen in the temperature profiles, the heat stored in the water column is released as the mixed layer deepens. From Figure 22, it is clear that this heat is released in bursts and that some of these bursts are quite large.

The features shown in year 10 are repeated in other years. Figure 24 is a plot of the last 5 years of the simulation showing the oceanic heat flux, the salinity mixed-layer depth, and the ice thickness. The main differences between these years is in the length of the open-water periods, the deepening of the mixed layer, and the magnitude of the oceanic heat flux bursts. One interesting feature is the spikes in the mixed layer depth plot. These spikes correspond to times in which the mixing process brings up sufficient heat to melt a few centimeters of ice. A thin layer of low-salinity water thus forms in the surface waters. The mixed-layer depth then shallows briefly. The continued growth of ice soon results in mixing of the surface waters, which brings the mixed-layer depth back to its previous depth.

In the VML model, the deepening of the mixed layer is controlled by density instabilities and velocity shears in the water column. The density instabilities are controlled primarily by the salinity flux, since in the Arctic the temperature usually changes less than the salinity. In this simulation, when ice is growing the salinity and thus density of the surface layers increase. Eventually the density structure becomes unstable and mixing occurs. If warmer water exists below the mixed layer, this water is mixed into the mixed layer, and the heat in the water tries to increase the temperature of the mixed layer. The temperature of the mixed layer is constrained when ice cover exists, since the temperature at the bottom of the ice must remain at the freezing point. So this heat either slows down the freezing rate or melts a few centimeters of ice. The mixed layer then stabilizes until density instabilities arise again from the salinity flux.

Velocity shears, which arise from the relative motion of the ice and water, also generate mixing in the water column. In this simulation, the velocity shears are not strong enough to overcome the density structure, but can greatly affect the rate of mixing and the rate at which the heat is released from the water column. This is evident from Figure 25, which is a plot of the oceanic heat flux for year 10 for a simulation in which the winds were shut off; no winds, thus no velocity shears occur in the water column. This plot is similar to Figure 22, except for the spikes observed in the latter. The oceanic heat flux values in Figure 25 appear to vary more gradually and to have fewer jumps.

Table 4 is a listing of some important quantities from the no-winds simulation. Things change when the velocity shears are removed from the simulation. The most noticeable changes are that the net heating values are generally larger, the open-water periods tend to be longer, and the water temperature tends to be warmer in the no-winds case. Starting at year 12 in the no-winds case, a 3-year cycle is observed in the net heating, the number of open-water days, and the temperature of the water column. The net heating decreases from a large positive value to a negative value over the 3-year cycle. The number of open-water days increases and

Table 4. Listing of ice thicknesses, number of open-water days, mixed-layer temperatures, and oceanic heating for a 20-year simulation of the VML model when no shears are developed in the water column (Case 1D).

Year	# Open Water Days	Mean Annual Ice Thickness	T(1) Max °C	T Max °C	cal/cm ² /year				
					H _{deep}	Diff	Solar	F _g	Net
1	0.0	52.80	-1.612	-1.460	5999.0	259.8	0.0	-6097.5	161.3
2	3.7	51.06	-1.563	-1.437	5998.4	314.8	754.3	-6776.1	291.3
3	0.0	55.32	-1.628	-1.446	5997.8	358.5	0.0	-6292.5	63.7
4	0.0	50.57	-1.628	-1.419	5997.4	392.8	0.0	-6213.4	176.8
5	17.7	47.77	-1.383	-0.759	5997.1	419.7	3719.3	-8999.1	1137.0
6	30.0	46.27	-1.142	-0.351	5996.8	440.6	6185.1	-11394.0	1228.2
7	40.3	43.44	-0.843	0.012	5996.6	456.6	8355.4	-13444.0	1365.0
8	49.0	40.54	-0.474	0.360	5996.5	468.7	10242.0	-15264.0	1443.0
9	55.3	38.07	-0.165	0.652	5996.4	477.4	11715.0	-16744.0	1445.0
10	61.0	35.77	0.127	0.930	5996.3	482.9	13079.0	-18082.0	1476.3
11	65.7	33.84	0.366	1.161	5996.3	485.7	14201.0	-19241.0	1442.1
12	69.0	32.37	0.553	1.340	5996.3	486.0	15046.0	-20161.0	1368.0
13	81.3	32.61	0.710	1.492	5996.3	484.1	16092.0	-22139.0	433.3
14	54.3	40.55	-0.211	0.626	5996.4	480.1	11456.0	-18097.0	-164.8
15	66.3	33.72	0.402	1.200	5996.4	474.2	14347.0	-19311.0	1506.7
16	81.3	32.79	0.709	1.493	5996.5	467.2	16092.0	-22080.0	475.3
17	55.7	40.19	-0.154	0.680	5996.6	459.1	11739.0	-18365.0	-170.3
18	67.3	33.26	0.464	1.260	5996.7	450.4	14622.0	-19607.0	1462.4
19	83.0	32.15	0.773	1.556	5996.8	441.3	16379.0	-22515.0	302.0
20	55.0	40.46	-0.181	0.656	5996.9	432.1	11598.0	-18365.0	-338.8

T(1) Max—maximum temperature at depth level 1 (2.5 m)

T Max—maximum temperature in the water column

H_{deep}—total heat input into the water column by advection from the deep ocean

Diff—total heat input into the water column by diffusion across the bottom

Solar—total heat input into the water column by solar radiation

F_g—total heat transfer across the ice/ocean or ice/water interface

Net—H_{deep} + Diff + Solar + F_g

then decreases during this time. It varies from about 55 to 81 days. The water temperature also increases and then decreases. This value varies from about -0.2°C to about 0.7°C.

d. Sound speed

The discussion of the results for Case 1 will be concluded with a brief examination of sound speed profile plots for year 20 of the simulation. These plots are shown in Figure 26. The corresponding temperature and salinity profiles are shown in Figures 27 and 28. These profiles were chosen to depict the differing physical conditions throughout the year. The profiles at steps 1 thru 300 and steps 900 and 1050 were taken during ice growth. The profile at step 450 was taken during ice melt, and those at steps 600 and 750 were taken during open water (open water lasts from step 598 to 840).

The sound speed in these profiles is clearly dominated by the temperature. Some salinity influence, however, is observed at the surface in the profile at step 600. Here the decrease in salinity due to melting is

greater than the change in temperature in the water column. In general, these profiles show that sound energy is trapped in a duct near the surface. A sound channel, however, forms around 50 m depth when the water column has been warmed during an open-water event. (Wilson's (1960) equation was used to compute sound speed.)

4. Effect of changing σ and q_b

It was mentioned earlier that the values of σ and q_b were not the generally accepted values. They were used by Semtner for the sake of comparison with Maykut and Untersteiner. The value used for σ is 2% higher than the standard value. This increased value causes more heat in the form of longwave radiation to be released from the snow/ice system, resulting in thicker ice than if the standard value had been used. The value used for q_b was questioned by Semtner. He stated that the reduced value of q_b at the bottom of the ice "implied an additional loss of heat over what is prescribed in surface fluxes must occur before the

ice reaches the upper surface." In later work, he used the value of 72 cal/cm³ for both the upper and lower boundaries of the ice, and the standard value of σ (personal communication). In this section, the effects on the VML model of changing these parameters will be examined. Table 5 is a listing of the mean annual ice thicknesses and the number of open-water days for four cases: CASE 1, the standard case as described earlier; CASE 1A, where q_b is the same as q_s ; CASE 1B, where σ is changed to the standard value of 1.3545E-12 cal/cm²/sec/°K⁴ and CASE 1C, where both σ and q_b are changed.

Both reducing σ by 2% and changing q_b to 72 causes more heat to remain in the snow/ice system, which results in thinner ice. In this example, it results in an average decrease in the mean annual ice thickness of 17.3% for Case 1A, 23.7% for Case 1B, and 26.6% for Case 1C. The no-ice cycle also changes significantly. Each subsequent case has more frequent and longer open water periods. (In the rest of the report, any model runs discussed will have the corrected values for σ and q_b .)

5. Deep ocean heat flux (H_{deep})

Open water that occurs every year is reasonable for the marginal ice zones, since the deep ocean heat flux, H_{deep} , can be quite large. The exact value of this heat flux depends on what Arctic area is being considered. It can vary from near zero in the central Arctic (Aagaard, 1981; McPhee and Untersteiner, 1982) to several hundred W/m² in the Greenland Sea (Hibler and Bryan, 1984). At this point in the study, we do not wish to simulate a specific region, but to examine how changes in the prescribed deep ocean heat flux can affect the ice/ocean interaction.

In Figure 29 is an ice and ice plus snow thickness plot, and an oceanic heat flux plot for a 20-year simulation of the VML model using 1.5 kcal/cm²/year (2.02 W/m²) as the deep ocean heat input value. One can see that heat in the water column is not sufficient in this case to cause open water. In fact, the mean annual ice thickness increases until it reaches a value of 115.8 cm in year 20. Spikes occur in the oceanic heat flux-plot even though there are no open-water periods. This is because the mixed layer always deepens in the winter, and in this simulation the temperature, in general, increases with depth. So warmer water is always below the mixed layer. Figures 30 through 32 are similar plots for simulations using 3.0 kcal/cm²/year (4.04 W/m²), 4.0 kcal/cm²/year (5.38 W/m²), and 6.0 kcal/cm²/year (8.07 W/m²). It is obvious that as the value of H_{deep} increases, the frequency of the open-water periods also increases. Though not as obvious the mean annual ice thickness decreases as H_{deep} increase, and the length of the open-water period increases. In all the runs, the oceanic heat flux

F_B hovers near the deep ocean heat flux value, H_{deep} , except for the burst of heat that occurs when the mixed layer deepens and vents heat stored in the water column. These bursts become more frequent and larger as the value of H_{deep} increases, and open water becomes more frequent.

6. Case 2—solar radiation stored in brine pockets

a. Setup of model

The variable mixed-layer model is extended by simulating the heat stored in the ice in brine pockets when solar radiation penetrates into snow-free ice. To do this, a heat reservoir was created. Heat is added to this reservoir whenever the ice is snow-free, and the surface temperature of the ice is above freezing. The following equation is used to determine the amount of heat stored in the reservoir each time step when the ice is snow-free:

$$F_{BR} = (1 - \alpha_i) I_o F_R (1 - e^{-0.15 h_i}) \Delta t, \quad (32)$$

where I_o is the percentage (17%) of solar radiation that penetrates into the ice. It is also assumed that some of the penetrating solar radiation goes through the ice and enters the water column. The amount of heat entering the water column is determined from

$$F_{RW} = (1 - \alpha_i) I_o F_R e^{-0.15 h_i} \Delta t. \quad (33)$$

Thus for thick ice most of the penetrating solar radiation is stored in the brine pockets, but very little radiation, if any, enters the water column. For thin ice, however, solar radiation warms the water column and is stored in brine pockets. This heat reservoir results in less heat being available for melting at the surface during the summer. It can also delay the growth of ice in the fall until all the heat in the reservoir is released.

Some limitations were put on the heat reservoir. First, heat is not allowed to accumulate in the reservoir when the ice thickness is less than 25 cm. Second, a maximum value is set for the amount of heat that can be stored in the brine pockets. This maximum depends on the thickness of the ice and is determined as follows:

$$H_{max} = 0.5 (h_i - h_{i min}) q_b, \quad (34)$$

where $h_{i min}$ is the minimum ice thickness (25 cm) for which solar radiation accumulates in the reservoir.

Table 5. Listing of ice thicknesses and number of open water days for a 10-year simulation of the VML model when the values of σ and q_b are changed.

Mean Annual Ice Thickness (cm)				
Year	Case 1	Case 1A	Case 1B	Case 1C
1	51.68	49.63	43.67	42.04
2	50.08	44.08	36.92	34.01
3	53.31	41.80	40.32	33.90
4	50.37	39.26	40.77	39.14
5	53.10	40.20	31.59	29.51
6	48.63	39.57	39.44	36.78
7	46.35	38.61	35.72	34.61
8	43.66	37.61	33.06	38.31
9	45.26	36.76	37.28	34.16
10	44.68	35.43	32.87	34.96
Average	48.71	40.29	37.16	35.74

Number of Open-Water Days				
Year	Case 1	Case 1A	Case 1B	Case 1C
1	0.0	0.0	58.3	57.7
2	4.7	19.0	76.3	78.0
3	0.0	32.7	70.7	89.0
4	4.3	46.3	67.3	68.0
5	0.0	45.3	95.3	96.7
6	9.3	47.0	73.3	76.0
7	24.0	49.3	80.0	88.3
8	40.0	52.3	93.0	73.7
9	35.7	54.3	77.7	88.0
10	38.3	53.7	93.7	86.0

Case 1 — $\sigma = 1.3850\text{E-}12$ and $q_b = 64.0$

Case 1A — $\sigma = 1.3850\text{E-}12$ and $q_b = 72.0$

Case 1B — $\sigma = 1.3545\text{E-}12$ and $q_b = 64.0$

Case 1C — $\sigma = 1.3545\text{E-}12$ and $q_b = 72.0$

The heat in the reservoir is released whenever the surface temperature of the ice falls below freezing. Just enough heat is released to raise the surface temperature to the freezing point. Thus the surface temperature of the ice is maintained at the freezing point until all the heat in the reservoir is released. For thin ice the maximum allowed heat storage is usually reached before the surface temperature falls below freezing. When this occurs, no more heat is diverted to the heat reservoir ($I_o = 0.0$), and heat in the reservoir is gradually released. This heat is treated as additional ice melt. This simulation is similar to that used by Semtner in his model.

Two of the parameters listed in Table 1 had to be changed for the simulation of the storage of solar radiation in brine pockets. These parameters are α_i and γ . The value of α_i is changed to 0.64 and γ is changed to 1.0. Both of these parameters had larger values in Case 1 to loosely simulate solar radiation being stored in brine pockets. (See Table 6 for a list of all the parameters used in this run.)

Table 6. Listing of parameters and assigned values used in Case 2 for the VML model. Brine pockets and penetrating solar radiation are included in this simulation.

Variable Mixed Layer	
H_i :	50 cm
H_b :	30 cm
F_b :	$-9.6451\text{E-}5 \pm$ heat change (cal/cm ² /sec)
T_s :	-2.0°C
T_b :	Varies with salinity
σ :	$1.3545\text{E-}12$ cal/cm ² /°K ⁴ /sec
α_i :	0.64
α_w :	0.07
q_s :	72 cal/cm ³
q_b :	72 cal/cm ³
γ :	1.0
MLD:	Variable
SFF:	$3.341\text{E-}5$ cm/sec
Time Step:	8 hours/30 minutes
Forcing:	
Heat Fluxes:	Climatology
Winds:	FNOG average monthly
T&S Profiles:	AIDJEX data (Beaufort Sea)

b. Results

This version of the VML model (Case 2) was integrated for 20 years. The results of this simulation will be compared with those for the case shown in Figure 30 (Case 1F). The ice and ice plus snow thickness plot for Case 2 is shown in Figure 33. Comparing Figures 30 and 33, it is apparent that thinner ice and more frequent open-water periods occur when penetrating solar radiation is simulated than when it is not. Tables 7 and 8 list several important values obtained from the simulations. In Case 2 open-water occurs beginning at year 1. By year 11, the length of the open-water period each year alternates between approximately 88 and 67 days. In case 1F, open water does not occur until year 20, and then for only two days. The mean annual ice thicknesses are on the order of 10 to 20 cm thinner in Case 2 than in Case 1F, and the water temperatures are a few degrees warmer in Case 2 than in Case 1F. The reason for these differences is seen in the heat flux values listed in the tables. The controlling difference is the solar values. In Case 1F, no solar heating of the water column occurs until year 20. In Case 2, however, solar heating is quite pronounced and begins at year 1. Several thousands of cal/cm² of heat are input into the water column in a year's time by solar heating. This is particularly countered by an increase in the oceanic heat flux, F_b . The net heating

Table 7. Listing of ice thicknesses, number of open-water days, mixed-layer temperatures, and oceanic heating for a 20-year simulation of the VML model when no brine pockets or penetrating solar radiation is allowed (Case 1F).

Year	# Open Water Days	Mean Annual Ice Thickness	T(1) Max °C	T Max °C	cal/cm ² /year				
					H _{deep}	Diff	Solar	F _g	Net
1	0.0	55.16	-1.611	-1.460	2999.5	260.1	0.0	-3226.1	33.5
2	0.0	57.15	-1.619	-1.487	2999.2	315.7	0.0	-3195.7	119.2
3	0.0	58.32	-1.623	-1.458	2998.9	360.0	0.0	-3225.0	133.9
4	0.0	58.80	-1.626	-1.432	2998.7	395.0	0.0	-3254.7	139.0
5	0.0	58.78	-1.628	-1.410	2998.5	422.4	0.0	-3284.0	136.9
6	0.0	58.41	-1.629	-1.391	2998.4	443.8	0.0	-3311.7	130.5
7	0.0	57.84	-1.630	-1.376	2998.3	460.5	0.0	-3336.2	122.5
8	0.0	57.17	-1.631	-1.363	2998.2	473.4	0.0	-3357.2	114.4
9	0.0	56.47	-1.631	-1.352	2998.2	483.3	0.0	-3375.0	106.4
10	0.0	55.78	-1.632	-1.343	2998.1	490.8	0.0	-3389.9	99.0
11	0.0	55.12	-1.632	-1.336	2998.1	496.5	0.0	-3402.4	92.1
12	0.0	54.52	-1.632	-1.329	2998.1	500.6	0.0	-3412.9	85.8
13	0.0	53.98	-1.632	-1.324	2998.0	503.6	0.0	-3421.6	80.1
14	0.0	53.49	-1.632	-1.319	2998.0	505.7	0.0	-3428.9	74.9
15	0.0	53.06	-1.632	-1.315	2998.0	507.1	0.0	-3435.0	70.1
16	0.0	52.69	-1.632	-1.312	2998.0	507.9	0.0	-3440.1	65.8
17	0.0	52.36	-1.631	-1.309	2998.0	508.3	0.0	-3444.5	61.9
18	0.0	52.07	-1.631	-1.306	2998.0	508.4	0.0	-3448.1	58.3
19	0.0	51.83	-1.631	-1.304	2998.0	508.2	0.0	-3451.3	55.0
20	2.0	52.85	-1.630	-1.300	2998.0	507.9	390.7	-3851.5	45.1

T(1) Max—maximum temperature at depth level 1 (2.5 m)

T Max—maximum temperature in the water column

H_{deep}—total heat input into the water column by advection from the deep ocean

Diff—total heat input into the water column by diffusion across the bottom

Solar—total heat input into the water column by solar radiation

F_g—total heat transfer across the ice/ocean or ice/water interface

Net—H_{deep} + Diff + Solar + F_g

of the water column and the temperature of the water column are thus greater in Case 2 than in Case 1F.

Year 1 of the above simulation will be examined in greater detail to get a better understanding of how the penetrating solar radiation simulation affects the ice and the ocean. The simulations of Case 1F and Case 2 are nearly identical for the first part of year 1. A slight difference in ice thicknesses results due to the difference in the value of γ . This parameter affects the conduction of heat in the ice.

The snow is totally melted by step 502 in both cases. At this point the penetrating solar radiation simulation begins to act. Table 9 lists the amount of ice melt and the ice thickness at several time steps during the melting process. The amount of ice melted at the surface is decreased, and that melted at the bottom is increased in Case 2 as was expected. The total melt, however, is less in Case 2 than in Case 1F because some heat is stored in the heat reservoir, and some goes to warming of the water column. The warming of the

water column is apparent from Figure 34, which plots temperature profiles for Case 1F (the dashed line) and Case 2 (the solid line) at several time steps during the ice-melting phase. At step 502 the profiles are identical. At later time steps, the temperature of the surface waters for Case 2 is seen to increase due to solar heating. The increase is not great, but it does have an effect on the growth of ice.

The heat stored in the heat reservoir gradually increases until a maximum value is reached. A maximum value tied to the thickness of the ice is set for the heat reservoir, so that the heat in the reservoir cannot exceed the amount needed to melt all the ice. In this case a maximum value of 644.6 cal/cm² for the heat reservoir is reached at step 595. After this step, the heat in the reservoir decreases and the total ice melt increases. The ice melt listed in Table 9 from step 602 on shows some increase in the melting at the bottom and at the surface of the ice for Case 2. The values listed in the table are only the melt due to the heat

Table 8. Listing of ice thicknesses, number of open-water days, mixed-layer temperatures, and oceanic heating for a 20-year simulation of the VML model when brine pockets and penetrating solar radiation are allowed (Case 2).

Year	# Open Water Days	Mean Annual Ice Thickness	T(1) Max °C	T Max °C	cal/cm ² /year				
					H _{deep}	Diff	Solar	F _B	Net
1	33.7	50.02	-1.030	-0.302	2999.5	260.1	6745.8	-8384.9	1620.5
2	50.3	45.19	-0.329	0.336	2999.2	315.7	10131.0	-11687.0	1758.7
3	61.7	39.95	0.251	0.862	2998.9	359.8	12674.0	-14247.0	1785.8
4	69.7	35.94	0.711	1.287	2998.7	394.1	14648.0	-16254.0	1786.7
5	77.3	33.64	1.027	1.584	2998.5	420.0	16062.0	-18403.0	1077.4
6	68.7	37.30	0.641	1.221	2998.4	439.3	14398.0	-17006.0	829.4
7	86.3	33.71	1.122	1.676	2998.4	452.2	16590.0	-19625.0	416.2
8	57.3	43.91	0.005	0.646	2998.3	460.0	11671.0	-15016.0	114.1
9	74.7	35.24	0.866	1.438	2998.3	463.7	15382.0	-17640.0	1204.2
10	71.0	36.12	0.760	1.331	2998.3	464.3	14937.0	-17488.0	911.7
11	88.3	32.50	1.215	1.768	2998.3	462.4	17051.0	-20072.0	439.4
12	66.0	39.22	0.482	1.078	2998.3	458.8	13739.0	-16780.0	416.1
13	86.7	32.90	1.151	1.707	2998.3	453.7	16769.0	-19634.0	587.9
14	67.7	38.24	0.574	1.162	2998.4	447.6	14135.0	-17103.0	478.2
15	87.7	32.53	1.184	1.739	2998.4	440.8	16915.0	-19928.0	426.1
16	67.7	38.47	0.574	1.163	2998.5	433.5	14137.0	-17136.0	433.5
17	88.3	32.37	1.216	1.770	2998.5	425.9	17048.0	-20087.0	385.9
18	67.7	38.44	0.574	1.163	2998.6	418.2	14137.0	-17187.0	367.3
19	89.0	32.24	1.248	1.802	2998.6	410.5	17188.0	-20241.0	356.6
20	67.7	38.45	0.574	1.164	2998.6	402.9	14137.0	-17229.0	309.4

T(1) Max—maximum temperature at depth level 1 (2.5 m)

T Max—maximum temperature in the water column

H_{deep}—total heat input into the water column by advection from the deep ocean

Diff—total heat input into the water column by diffusion across the bottom

Solar—total heat input into the water column by solar radiation

F_B—total heat transfer across the ice/ocean or ice/water interface

Net—H_{deep} + Diff + Solar + F_B

fluxes at the interfaces. The melt at the surface increases, since solar radiation no longer penetrates the ice; thus, more heat is available for melting at the surface. The melt at the bottom increases, since some of the heat stored in the water column is released and melts ice. On top of this is added the melt due to the heat stored in the heat reservoir. This may be as much as that melted by the interface heat fluxes alone. Thus the melting of ice greatly accelerates until the heat in the reservoir is exhausted. This can be observed from the values listed in Table 10. This process is repeated in other simulations whenever the ice thickness becomes so thin that no more heat can be stored in the heat reservoir.

When the ice is thicker, the heat reservoir will increase until the surface temperature of the ice falls below freezing. To examine this case, the initial ice thickness was increased to 340 cm and the previous cases were repeated. For the case with penetrating solar radiation (Case 2D) the mean annual ice thickness for year 1 was 331.42 cm, and the minimum ice thickness that year was 293.35 cm. For the case without

penetrating solar radiation (Case 1G), the mean annual ice thickness was 320.47 cm and the minimum ice thickness was 269.22 cm. Case 2D had thicker ice, since some of the heat from solar radiation was stored in the heat reservoir, and then was released when the surface temperature falls below freezing. For this case, the maximum amount of heat stored in the reservoir during the first year was 1740.3 cal/cm³. This heat delayed the drop in the surface temperature to freezing for only 3 days, but greatly affected the melt of ice at the surface during the ice-melt phase. The total amount of ice melted at the surface was 66.14 cm. The total growth of ice at the bottom was 42.49 cm. The net ice melt for the year, then, was 23.64 cm. For Case 1G, the total melt at the surface was 90.83 cm. The total growth of ice at the bottom was 44.03 cm, and the net ice melt for the year was 46.81 cm. The amount of ice grown at the bottom was not affected much by the brine pocket simulation in this case, since no solar radiation penetrated through the ice to warm the water column. The main difference between the cases was due to the melt at the surface.

Table 9. Listing of bottom melt, surface melt, total melt, and ice thickness for year 1 of Case 1F and Case 2 from the onset of ice melt until open water occurs in Case 2.

Step #	Melt at Bottom		Melt at Surface		Total Melt		H _i	
	C1F	C2	C1F	C2	C1F	C2	C1F	C2
502	0.0703	0.0696	0.0000	0.0000	0.0703	0.0696	94.720	91.723
512	0.0633	0.0771	0.5712	0.4681	0.6346	0.5452	88.363	86.330
522	0.0649	0.0823	0.5692	0.4695	0.6341	0.5518	82.016	80.836
532	0.0678	0.0874	0.5607	0.4649	0.6285	0.5523	75.701	75.310
542	0.0715	0.0927	0.5463	0.4547	0.6178	0.5474	69.471	69.809
552	0.0759	0.0984	0.5263	0.4394	0.6022	0.5378	63.375	64.384
562	0.0812	0.1044	0.5011	0.4191	0.5823	0.5235	57.458	59.081
572	0.0876	0.1109	0.4712	0.3944	0.5588	0.5053	51.761	53.942
582	0.0950	0.1181	0.4367	0.3656	0.5318	0.4837	46.319	49.005
592	0.1042	0.1251	0.4028	0.3370	0.5071	0.4621	41.143	44.289
602	0.1151	0.1158	0.3664	0.4207	0.4816	0.5365	36.210	36.226
612	0.1285	0.1395	0.3250	0.3607	0.4535	0.5002	31.547	25.913
622	0.1450	0.1783	0.2777	0.2941	0.4228	0.4724	27.178	20.128
632	0.1574	0.2189	0.2318	0.2175	0.3892	0.4364	23.133	15.599
642	0.1812	0.2828	0.1712	0.1144	0.3524	0.3972	19.440	11.448
652	0.2113	0.3619	0.1012	0.0000	0.3125	0.3619	16.133	7.694
662	0.2501	0.3449	0.0198	0.0000	0.2699	0.3449	13.240	4.164
672	0.2396	0.3211	0.0000	0.0000	0.2396	0.3211	10.721	0.0000
TOTAL MELT:							83.999	91.723

Table 10. Listing of ice melt, heat stored in the heat reservoir, oceanic heat flux, and ice thickness for year 1 of Case 2. The values shown occur after the heat in the reservoir has reached its maximum and is being released.

Step #	Melt at Bottom	Melt at Surface	Solar	Total Melt	F _g	H
594	0.1267	0.3312	640.35	0.4579	-1.4807E-4	43.37
595	0.1274	0.3282	644.60	0.4556	-1.4827E-4	42.91
596	0.1282	0.3252	625.39	0.7786	-1.4847E-4	42.14
597	0.1284	0.4441	593.41	1.0166	-1.4590E-4	41.12
598	0.1241	0.4396	561.76	1.0034	-1.3117E-4	40.12
599	0.1189	0.4351	530.43	0.9891	-1.1379E-4	39.13
600	0.1164	0.4304	499.44	0.9771	-1.0307E-4	38.15
601	0.1155	0.4256	468.80	0.9668	-9.6371E-5	37.18
602	0.1158	0.4207	438.51	0.9573	-9.2112E-5	36.23
603	0.1167	0.4158	400.17	1.0646	-8.9333E-5	35.16
604	0.1179	0.4104	362.13	1.0566	-8.6677E-5	34.10
605	0.1194	0.4049	324.39	1.0486	-8.4113E-5	33.06
606	0.1213	0.3992	286.91	1.0410	-8.2411E-5	32.01
607	0.1236	0.3933	249.69	1.0339	-8.1229E-5	30.98
608	0.1263	0.3872	212.72	1.0270	-8.0422E-5	29.95
609	0.1291	0.3810	175.99	1.0203	-7.9840E-5	28.93
610	0.1323	0.3745	139.50	1.0136	-7.9451E-5	27.92
611	0.1358	0.3677	103.25	1.0069	-7.9176E-5	26.91
612	0.1395	0.3607	67.23	1.0004	-7.8975E-5	25.91
613	0.1435	0.3534	31.46	0.9937	-7.8842E-5	24.92
614	0.1478	0.3457	0.0	0.9305	-7.8781E-5	23.99
615	0.1532	0.3379	0.0	0.4911	-8.1077E-5	23.50
616	0.1574	0.3320	0.0	0.4895	-8.5072E-5	23.01
617	0.1612	0.3260	0.0	0.4872	-8.7933E-5	22.52

This simulation of brine pockets is rather crude, but it shows that any diversion of solar heat to brine pockets can significantly affect the growth and decay of ice.

7. Case 3— run with AIDJEX data

a. Setup of model

In this last section, the ice/ocean model is run with forcing data obtained from the AIDJEX experiment. The results of this run will be discussed and compared to selected fields from the AIDJEX data. The ice/ocean model requires the following as input: incoming solar radiation, incoming longwave radiation, latent heat flux, sensible heat flux, albedo, winds, snowfall rates, and the heat flux from the deep ocean. The model also needs the initial values for the ice thickness, snow thickness, and the temperature and salinity profiles in the ocean. Most of the meteorological forcing data was obtained from two AIDJEX reports. The first is *Report on the AIDJEX Meteorological Experiment* by Leavitt et al. (1978). From this report, the latent and sensible heat fluxes, the average air temperature, and the wind speed and direction were obtained. The second report is *Radiation Program during AIDJEX: A Data Report* by Pautzke and Hornof (1978). This report gives the daily total of the incoming solar radiation, and the daily average for the albedo. The incoming longwave radiation is not given directly in the AIDJEX data, but can be computed from the average air temperature with the method used in Parkinson and Washington (1979). The initial ice thickness and the initial temperature and salinity profiles can be obtained from AIDJEX technical reports. Ice thickness measurements were made at the beginning of the experiment. These values ranged from 250 cm to 470 cm at the four camps; the average thickness was 340 cm. This value is used to initialize the model. The snowfall rates, initial snow thickness, and the deep ocean heat flux are not given in any of the AIDJEX reports. Therefore, the climatology values used in the previous model runs are used in the runs in this section.

The forcing fields from the AIDJEX reports are plotted in Figures 35 through 41. The data runs from May 1, 1975, to April 29, 1976. All fluxes except for the albedo and solar radiation are given at 6-hour intervals. Thus, the time step used for the model is 6 hours. The solar radiation in the report is a daily total, so the question arises as to how to partition the solar radiation data into 6-hour intervals like the other data. Two methods of partitioning the solar radiation will be examined. The first method is to assume a diurnal cycle for the solar radiation. There is no readily available data on the diurnal cycle in the Beaufort Sea,

but one can be deduced from Figure 10 in the report by Pautzke and Hornof (Fig. 42). The second method is to evenly distribute the daily total solar radiation between the four periods within a day, i.e., to assume that the solar flux is constant throughout the day.

The heat flux from the deep ocean H_{deep} will initially be set to $3.25 \text{ kcal/cm}^2/\text{year}$; however, other values will be tried. A listing of other parameters for this simulation is shown in Table 11.

b. Diurnal cycle

Most of the input data is given at 0, 6, 12, and 18 hours GMT. Local time is about 10 hours earlier, thus the first period in the model is from 2 p.m. to 8 p.m., the second period is from 8 p.m. to 2 a.m., the third period is from 2 a.m. to 8 a.m., and the fourth period is from 8 a.m. to 2 p.m. The first and fourth periods are daytime hours, and the second and third periods are nighttime hours. It is further assumed that the maximum solar radiation influx occurs during the fourth period, i.e., the 8 a.m. to 2 p.m. interval. Next, the year is divided into four groups. The first group is summer, i.e., the months of May, June, and July. During these months some solar radiation exists at each period. In particular, 30% of the daily total of solar radiation is assumed to arrive during the first period, 10% during each of the next two periods (the nighttime hours), and 50% during the last period. The second

Table 11. Listing of parameters and assigned values used in Case 3 for the VML model. AIDJEX data is used to force the model.

Variable Mixed Layer	
H_i	340 cm
H_o	30 cm
F_a	$-1.0306E-4 \pm \text{heat change (cal/cm}^2/\text{sec)}$
T_o	-2.0°C
T_a	Varies with salinity
α	$1.3545E-12 \text{ cal/cm}^2/\text{K}^4/\text{sec}$
ν	0.64
ν_m	0.07
q_i	72 cal/cm^2
q_o	72 cal/cm^2
r	1.0
MLD	Variable
SFF	$3.341E-5 \text{ cm/sec}$
Time Step	6 hours/30 minutes
Forcing	
Heat Fluxes	AIDJEX Data
Winds	AIDJEX Data
T&S Profiles	AIDJEX Data

group is the fall and spring months of August, September, March, and April. During these months no solar radiation arrives during the nighttime hours. The total solar radiation for the day is divided between the daytime hours: 30% for one, 70% for the other. The third group is the months of October and February. For these months, solar radiation exists during only one of the daytime periods. The rest of the time the solar radiation is zero. The last group is the winter months of November, December, and January, where the solar radiation is zero throughout the day. This partitioning of the solar radiation is shown graphically in Figure 43.

The time series for the solar radiation field, which results when the above partitioning is applied to the solar radiation data in Figure 35 is shown in Figure 44. The resulting solar radiation values are quite variable, with most of the energy being concentrated during the daytime hours and little or none existing during the nighttime hours.

c. No diurnal cycle

The second method of partitioning the solar radiation is to assume that the solar flux during the day is constant. The solar flux is then determined by dividing the daily total solar radiation by the seconds in a day. The resulting time series for this partitioning of the solar radiation is shown in Figure 45. The extremes in the values are much less in this case, and the energy is more evenly distributed between time steps than in the diurnal case.

d. Diurnal cycle versus nondiurnal cycle

To examine how the partitioning of the solar radiation may affect the model results, the ice/ocean model was run for 1 year with the diurnal cycle and for 1 year without the diurnal cycle. The model results for these cases will be discussed in this section.

Table 12 is a listing of some results from the model simulations. The case with the diurnal cycle has somewhat thinner ice than the case without. This difference in the ice thickness is due to increased melting at the surface. Growth of ice at the bottom is somewhat larger in the diurnal case, but not enough to offset the ice melt at the surface. The net result is increased melting and thinner ice.

The surface temperatures throughout the year for both simulations are shown in Figures 46 and 47. In these figures, it is obvious that the temperature extremes are greater in the diurnal case. There can be as much as 30°C difference in the daytime and the nighttime temperatures in this case (this value occurred in April). The maximum difference in the nondiurnal case was about 8°C. For the diurnal case, Figure 46, T_s first reaches zero degrees on May 5, and frequently gets this warm throughout May and the rest of the summer (in the model if T_s is above the

Table 12. Listing of results from a 1-year simulation of the VML model forced with data from AIDJEX.

	No Diurnal Cycle	Diurnal Cycle
Mean annual ice thickness (cm)	325.99	310.01
Mean annual oceanic heat flux (cal/cm ² /sec)	- 1.1146E-4	- 1.1065E-4
Deep ocean heat input (cal/cm ² /year)	3291.90	3291.90
Diffusive heat input (cal/cm ² /year)	264.12	264.12
Solar heat input (cal/cm ² /year)	27.05	40.78
Total oceanic heat flux (cal/cm ² /year)	3514.90	3489.40
Net heating (cal/cm ² /year)	68.13	107.37
Number of snow-free days	63.25	76.00
Net change in ice thickness for the year (cm)	2.32	- 17.07
Ice melt at surface for the year (cm)	16.77	42.33
Ice growth at bottom for the year (cm)	19.09	25.25

freezing point, it is set to the freezing temperature, and the additional heat is applied to ice melt). However, the surface temperature for the nondiurnal case, Figure 47, does not reach 0° until the end of May. Thus, surface melting begins much earlier in the diurnal simulation than in the nondiurnal simulation. In fact, the snow cover is totally melted by step 189 (June 16) in the diurnal case, but not until step 240 (June 29) in the nondiurnal case. Thus, ice melt at the surface begins about 13 days earlier in the diurnal case. From the figures, it is also seen that during June and July the surface temperature for the nondiurnal case remains at 0° most of the time, but that the temperatures for the diurnal case decrease at night. For the nondiurnal case the melting at the surface will be fairly constant, while for the diurnal case, melting will be strong during the day and weak at night. In fact, on some nights ice forms on the bottom in the diurnal case.

Ice melt at the surface of the ice, and ice melt and growth at the bottom for the two simulations are shown in Figures 48 through 51. Ice melt at the surface in both cases lasts from June through August. The magnitude of ice melt at the surface is generally largest during the month of July. The maximum melt per time period in the diurnal case is just over 1 cm, while for the nondiurnal case it is less than 0.5 cm. The figures of growth or melt of ice at the bottom (Figs. 50 and 51) show the expected trend of melt during the summer and

growth during the winter in both cases. For the diurnal case, however, melt may occur during the daytime hours, while growth occurs during the nighttime hours. During the spring and fall the melt during the day can almost be offset by growth at night. But, as mentioned earlier, the surface melt in the diurnal case is sufficient to result in thinner ice in the diurnal case than in the nondiurnal case.

Another factor that affects ice melt at the surface is the brine pockets simulation discussed in the previous section. The storage of heat in the heat reservoir occurs during the summer when the ice is snow-free. In the diurnal case, T_s generally falls below freezing at night during the summer. Thus, no heat is diverted into the heat reservoir during this time, instead most if not all of the heat stored in the reservoir during the day will be released at night. The total amount of heat stored in the reservoir during a day's time, then, is less in the diurnal case than in the nondiurnal case. The maximum amount of heat stored in the reservoir at any one time is about 30 cal/cm² in the diurnal case. While for the nondiurnal case, the heat in the reservoir steadily increases to a maximum of about 500 cal/cm², and then decreases to zero when the surface temperature stays below freezing (Figs. 52 and 53). Thus, the simulation of brine pockets has less effect on the ice thickness when a diurnal cycle is assumed for the solar flux than when the solar flux is constant throughout the day. More information on brine pockets is needed to determine the importance of this effect and how best to simulate it.

e. Model results versus AIDJEX data

The results of a 1 year simulation of the ice/ocean model forced with AIDJEX forcing data, as described in Section 7a, is compared with data obtained during AIDJEX in this section. The diurnal cycle for the solar radiation is chosen for this run (Case 3), and the initial temperature and salinity profiles are from May 10, 1975, Station Blue Fox (Figs. 54 and 55).

Comparison will be made on how well the model simulates the mixed-layer characteristics rather than on the growth and decay of ice. Considerable data exist as to the temperature and salinity structure in the water column below the ice during AIDJEX, but very little on the ice thickness, and ice growth and decay.

The mixed-layer temperature computed by the model for 1-year is shown in Figure 56. For comparison, the mixed-layer temperature at Station Blue Fox and Station Snowbird are shown in Figures 57 and 58. From these figures, one sees that the ice/ocean model simulates the general trends of temperature increase in the summer and decrease in the fall and winter rather well. The magnitude of the mixed-layer temperature is also reasonable. The extremes in the temperature, however, are not well simulated. The data indicates that the mixed-layer temperature is warmer in the

summer than the model indicates and is cooler in the winter. Similar plots for the mixed layer salinity are shown in Figures 59 through 61. The model does a somewhat better job simulating the salinity, except that the salinity is a little too fresh in the winter and early spring. Finally, the mixed-layer depth determined from the salinity (as described earlier in this paper) is plotted in Figures 62 through 64. The model again follows the general trends quite well. It causes shallowing of the mixed-layer in the summer and deepening in the winter. The model, however, shallows too much in the summer and underestimated the mixed-layer deepening in the winter. This discrepancy may be due to several factors. The turbulence parameters prescribed in the model may need to be tuned to cause the mixed layer to deepen more. The shallow mixed layer may also be due to uncertainties in some of the forcing values used in the model, for example, the snowfall rate and the heat flux from the deep ocean. The differences may also be due to advection, which is not accounted for in the model. Some of these possibilities will be examined later in this report.

A comparison of the temperature and salinity profiles for the model results, Station Blue Fox, and Station Snowbird is shown in Figures 65 through 76. The solid line in the plots is the model-determined profile, and the dashed line is from AIDJEX data. Again the general trends and magnitudes compare well, except that the mixed layer is too shallow and the profiles from the data show more variability. In the summer, the upper ocean (30 m to 50 m) is warmer in the temperature profiles from the data than in the model profiles. In the winter, the temperature of the upper ocean is somewhat cooler in the data profiles than in the model profiles. The salinity profiles compare better, but again the mixed layer is too shallow, and the salinity tends to be a little fresher in the model profiles than in the data profiles, particularly when compared to Station Blue Fox. Maximums and minimums for the mixed-layer temperature, salinity, and mixed-layer depth for the four AIDJEX camps and for several model runs are shown in Table 13.

In the depth range of 50 m to 100 m, the temperature profiles from the model are in rough agreement with data, but the model does not indicate the temperature maximum around 60 m depth, which is quite apparent at both Blue Fox and Snowbird in the spring and summer. The model also does not simulate well the variability in the temperature in this depth range.

The temperature maximum that occurs around 60 m depth in the temperature profiles from data is due to Pacific water, which enters the Arctic through the Bering Strait and eventually flows into the Beaufort Sea. This Pacific water shows up in the profiles from 50 m to 130 m depth. The temperature and salinity profiles from AIDJEX data are also perturbed by eddies. Several eddies were observed during the AIDJEX

Table 13. Listing of maximums and minimums in temperature, salinity, and mixed-layer depth for the four camps of AIDJEX and four VML model runs.

	Mixed-Layer Characteristics							
	Bluefox		Snowbird		Big Bear		Caribou	
	Max	Min	Max	Min	Max	Min	Max	Min
Temperature	-1.20	-1.73	-1.44	-1.78	-1.46	-1.71	-1.40	-1.76
Salinity	31.32	29.77	30.98	29.59	31.17	29.76	30.48	29.79
Depth	65.0	10.0	60.0	10.0	60.0	15.0	60.0	15.0
	Model—Case 3		Model—Case 3J		Model—Case 3Q		Model—Case 3O	
	Max	Min	Max	Min	Max	Min	Max	Min
Temperature	-1.616	-1.660	-1.614	-1.665	-1.621	-1.668	-1.013	-1.689
Salinity	30.598	29.794	30.674	29.761	30.741	29.883	31.114	29.460
Depth	50.0	2.5	50.0	2.5	50.0	2.5	50.0	2.5

experiment. These eddies were located from 50 m to 300 m depth. Thus, advection is important in simulating the temperature and salinity structure in the Beaufort Sea, and probably accounts for some of the differences between model results and data.

As mentioned earlier, uncertainties in some of the forcing fluxes may also account for some of the discrepancies in the temperature and salinity fields. Two easily examined fluxes are the snowfall rate and the heat flux from the deep ocean. To test how the snow cover might affect the ocean under the ice, the snowfall rate was divided by two, and the initial snow thickness value was decreased to 20 cm. Snow insulates the ice and the ocean from the atmosphere; thus, less snow means less of an insulating effect. In this test case (Case 3J), the result was an increase in the growth of ice in the winter and less melting in the summer. About 10 cm more ice grew in the winter in this case than in the previous case. This had a small, but noticeable effect on the mixed-layer depth. The mixed layer deepened to 32 m instead of 25 m (Fig. 77). Similar results occurred when the heat flux from the deep ocean is reduced to 1.5 kcal/cm²/year (Case 3Q; Fig. 78). Both changes increased the growth of ice in the winter, which results in increased salinity flux at the surface and increased deepening of the mixed layer.

f. Open water and AIDJEX

The AIDJEX forcing and initial conditions do not yield open water during the simulation. This is not surprising, since the measurements were taken on ice flows. No direct information about open water during AIDJEX is available, except that camp Big Bear broke up and had to be abandoned. It would be interesting, however, to see how an open-water period might affect the temperature and salinity structure in the water column using the same forcing as in the previous AIDJEX cases.

To force open water, the ice thickness was reduced to 65 cm, and the heat flux from the deep ocean H_{deep} was increased to 6.0 kcal/cm²/year (Case 3N). The result was an open-water period of 4.25 days. Another test was run with an initial ice thickness of 63 cm (Case 3O). The result was an open-water period of 43 days. The mixed-layer temperature, mixed-layer salinity, and the ice thickness for both cases are shown in Figures 79 through 81. These cases yield similar results up to the open-water period. During the open-water period, the temperature for Case 3O (the solid line in the plots) warms to -1.013 C, while the temperature for Case 3N (the dashed line in the plots) warms to -1.598°C. The salinity for Case 3O is fresher than for Case 3N, during and following the open-water period. After the open-water period, the temperature and salinity values for both cases gradually approach the same value. The ice thickness for Case 3N increases rapidly after the open-water period, and by the end of the simulation is greater than the ice thickness in Case 3O. This rapid increase in ice thickness is due to thinner snow cover. This effect of snow cover was discussed in Section 3b. The salinity mixed-layer depth for Case 3O is shown in Figure 82. The mixed-layer depth plot for Case 3N is similar, except that the mixed layer starts to deepen sooner, around May 27. The mixed-layer depth in both cases reaches 50 m in the winter. The rapid growth of ice following the open-water period dumps large amounts of salt and causes the mixed layer to deepen.

The temperature and salinity profiles for Case 3O compared with Blue Fox are shown in Figures 83 through 88. In this case, the temperature of the upper 50 cm is closer to the temperature in Blue Fox than was true in Case 3, at least for most of the year. In late August, open water occurs, and by September 1 the surface waters have warmed to about -1.0°C. A warm spot, such as the one observed in the climatology

case, is formed in this case. The warm spot decreases as the mixed layer deepens, and by late December the profiles for Case 30 and Blue Fox look very much alike. The salinity profiles compare well also, mainly after the open-water period.

It is interesting that the open-water period creates a temperature maximum of about the same magnitude and at about the same depth as the temperature maximum from the Pacific water. This is probably a coincidence, but only more research on the relationship between open water and ice growth and movement will tell whether open water accounts for any of the features observed in the AIDJEX profiles.

8. Summary and conclusions

A one-dimensional sea-ice and ocean mixed-layer model has been developed and was used to investigate the interaction between ice and ocean. This model, forced with climatology forcing fields, was compared to Semtner's 0-layer ice model. With the same forcing and initial conditions, Semtner's model yielded a 6-year cycle of open water. Our model yielded open water nearly every year. The primary difference between the models is the treatment of the mixed layer in the ocean. In our ice/ocean model, the depth of the mixed layer varies in response to forcing. The exchange of heat between the ocean and the ice varies with the mixed-layer depth and heat input from below. The heat exchange was the greatest when the mixed layer deepened and entrained warmer water from below the mixed layer. Warmer water existed below the mixed layer because the temperature tended to increase with depth in the simulation. Large temperature differences in the water column developed when several days of open water occurred. Solar radiation penetrating into the ocean would warm the subsurface layers, forming a warm spot in the water column. Some heat remained in this warm spot even after ice was re-formed. This occurred, because the water column was highly stratified during this time, and the exchange of heat between layers was slow. The heat in the warm spot dissipated as the ice grew, dumping salt and deepening the mixed layer. This heat was often released in large bursts, which either slowed the freezing rate or melted a few centimeters of ice. The rate at which the heat was released from the mixed layer was tied to the rate of mechanical stirring generated by shear stresses. This simulation of the ice/ocean model showed that a variable depth mixed layer can significantly alter the results of a sea-ice model. This ice/ocean model should improve sea-ice forecasting by better simulating the mixed layer. The biggest improvement would be in the marginal ice zones where open water frequently occurs.

The sensitivity of the ice/ocean model to forcing and various parameters was also investigated. Changes in the snow cover, assumed flux of heat from the deep

ocean, and incoming longwave radiation were shown to alter the growth of ice, which in turn increased or decreased the deepening of the mixed layer and the exchange of heat between the ice and ocean. Large effects occurred, depending on the treatment of the solar flux. The brine pockets simulation showed that diversion of solar radiation into the brine pockets could significantly decrease the melt at the surface of the snow/ice. This simulation, however, resulted in rapid ice melt if the ice was thin, and the maximum-allowed storage of heat in the brine pockets was reached. Some solar radiation was allowed to penetrate the ice and warm the water column below the ice. This increased the melt of ice at the bottom, but the surface melt dominated. The brine pockets effect was large in the first simulation, since the solar flux was constant throughout the day. The surface temperature did not drop below freezing during most of the summer. Thus, the heat in the reservoir increased each time step and diverted heat from surface melt. If a diurnal cycle was assumed for the incoming solar radiation, the brine pockets simulation had little effect on ice melt. The surface temperature frequently dropped below freezing at night during the summer. Thus, no heat was diverted into the reservoir, and any heat in the reservoir was released at night. The diurnal cycle also concentrated more heat during the day, resulting in increased surface melt and frequent ice growth at night. Surface melt during the summer was sufficient to yield thinner ice than when no diurnal cycle was assumed.

The ice/ocean model was forced with data obtained during the AIDJEX experiment. The results of this simulation showed that the ice/ocean model did a good job of simulating the general trends in the mixed-layer characteristics. The model, however, underpredicted the deepening of the mixed layer and missed the high variability observed in the ocean in the Beaufort Sea. The omission of advection from the model is a primary reason for many of the discrepancies, since the temperature and salinity fields in the Beaufort Sea are perturbed by Pacific water and transit eddies. Other possibilities for the discrepancies were uncertainties in some of the forcing fields, such as the snowfall and the heat input from the deep ocean. These forcing fields affect the growth of ice, which in turn affects the mixed-layer response.

An open-water simulation was examined for the AIDJEX case. The open-water period lasted for 43 days. The surface temperature of the water column warmed to -1.013°C during this time, and a warm spot formed around 10 m depth. This warm spot cooled and migrated down the water column as ice re-formed and grew. By the end of the year a warm spot similar to that attributed to the Pacific water was formed in the model. This result was interesting, but more research is required before we can put much

significance to it, since we have no data about open water in the area during AIDJEX.

This ice/ocean model has shown that a variable depth mixed-layer ocean model can simulate the mixed layer in the Arctic, but the model should be improved by including advection. In the future, we also plan to develop a three-dimensional version of this model and to improve the simulation of the ocean currents and shear stresses.

9. References

- Clancy, R. M. and P. J. Martin (1981). Synoptic Forecasting of the Oceanic Mixed Layer Using the Navy's Operational Environmental Data Base: Present Capabilities and Future Applications. *Bulletin of the American Meteorological Society*, v. 62, n. 6, pp. 770-784.
- Coachman, L. K. and K. Aagaard (1974). Physical Oceanography of Arctic and Subarctic Seas. *Marine Geology and Oceanography of the Arctic Seas*, Y. Herman, Ed., Springer-Verlog, 1-72.
- Fletcher, J. O. (1965). *The Heat Budget of the Arctic Basin and its Relation to Climate*. The Rand Corporation, Santa Monica, Calif., R-444-PR.
- Hibler, W. D. (1980). Modeling a Variable Thickness Sea Ice Cover. *Monthly Weather Review*, v. 108, n. 12, pp. 1944-1973.
- Hibler, W.D. and K. Bryan (1984). Ocean Circulation: Its Effects on Seasonal Sea-Ice Simulations. *Science*, v. 224, n. 4648, pp. 489-491.
- Leavitt E., M. Albright, and F. Carsey (1978). *Report on the AIDJEX Meteorological Experiment*. Department of Oceanography, University of Washington/Seattle, pp. 121-148. (AIDJEX Bulletin 39).
- Maykut, G. A. and N. Untersteiner (1969). *Numerical Prediction of the Thermodynamic Response of Arctic Sea Ice to Environmental Changes*. The Rand Corporation, Santa Monica, Calif., RM-6093-PR.
- Mellor, G. L. and T. Yamada (1974). A Hierarchy of Turbulence Closure Models for Planetary Boundary Layers. *Journal of Atmospheric Sciences*, v. 31, pp. 1791-1806.
- Mellor, G. L. and P. A. Durbin (1975). The Structure and Dynamics of the Ocean Surface Mixed Layer. *Journal of Physical Oceanography*, v. 5, pp. 718-725.
- Mellor, G. L., M. G. McPhee, and M. Steele (1986). *Ice-Seawater Turbulent Boundary Layer Interaction with Melting or Freezing*. Submitted for publication.
- Overland, J. E., H. O. Mofjeld, and C. H. Pease (1984). Wind-Driven Ice Drift in a Shallow Sea. *Journal of Geophysical Research*, v. 89, n. C4, pp. 6525-6531.
- Parkinson, C. L. and W. M. Washington (1979). A Large-Scale Numerical Model of Sea Ice. *Journal of Geophysical Research*, v. 84, n. C1, pp. 311-337.
- Pautzke, C. G. and G. F. Hornof (1978). *Radiation Program During AIDJEX: A Data Report*. Department of Oceanography, University of Washington/Seattle, PP. 165-185. (AIDJEX Bulletin 39).
- Pollard, D., M. L. Batteen, and Y. Han (1983). Development of a Simple Upper-Ocean and Sea-Ice Model. *Journal of Physical Oceanography*, v. 13, pp. 754-768.
- Semtner, A. J. (1976). A Model for the Thermodynamic Growth of Sea Ice in Numerical Investigations of Climate. *Journal of Physical Oceanography*, v. 6, pp. 379-389.
- Wilson, W. D. (1960). Equation for the speed of sound in sea water. *J. Acoust. Soc. Am.* 32(10), 1357.

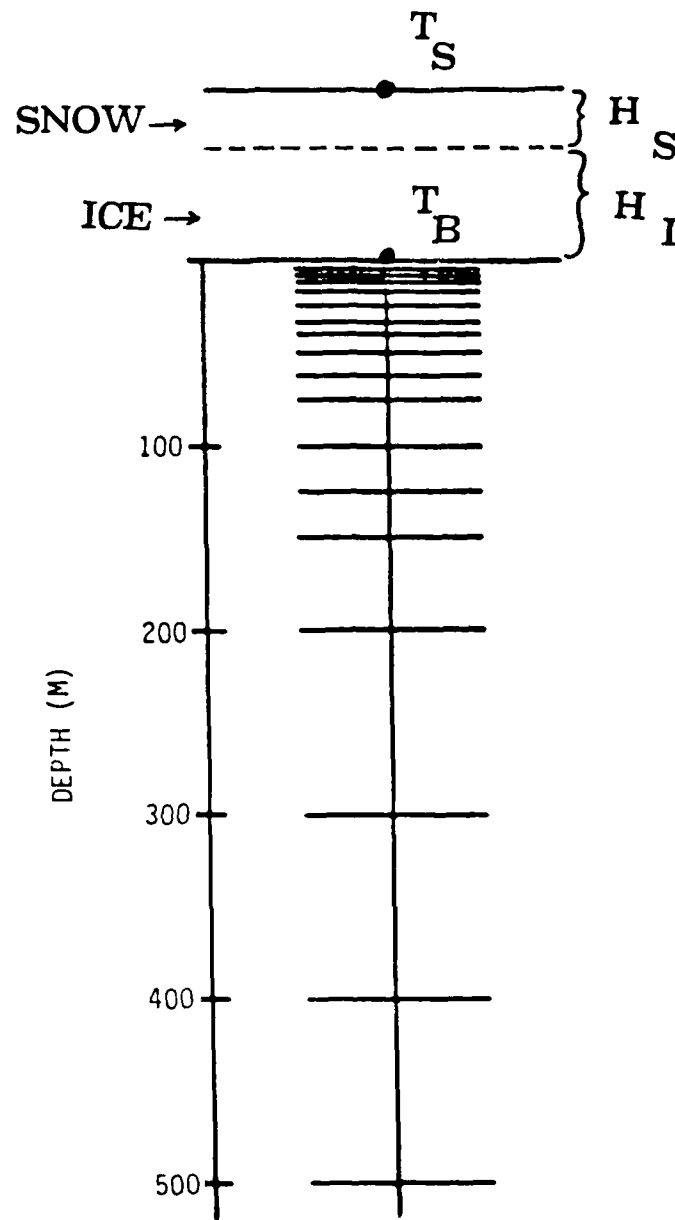
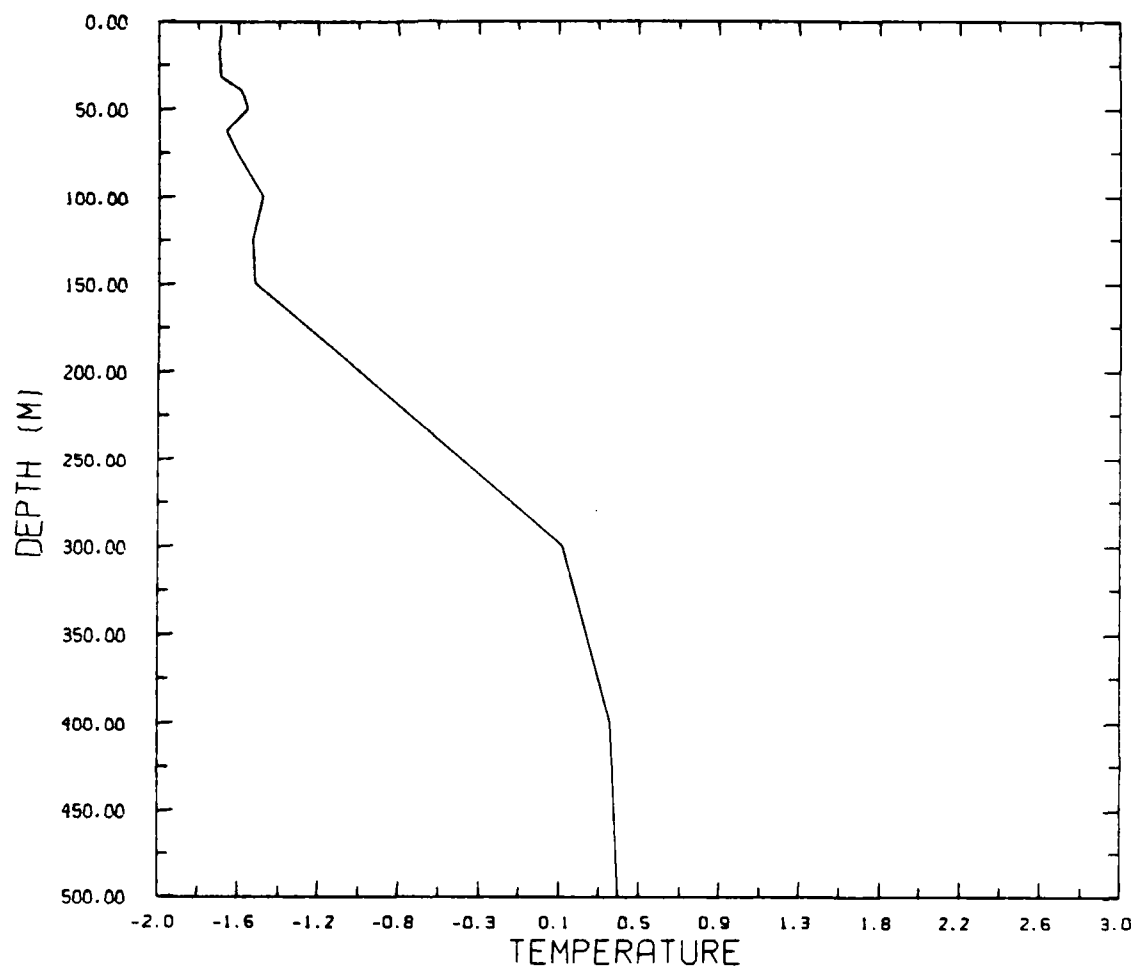


Figure 1. Vertical grid for variable mixed layer ice/ocean model. T_S is the temperature at the surface of the snow/ice system. T_B is the temperature at the bottom of the ice. H_I and H_S are the ice and snow thicknesses, respectively. The quantities T , S , u , and v for the ocean are defined at the depths indicated in the figure. All turbulence quantities are defined midway between these depths.

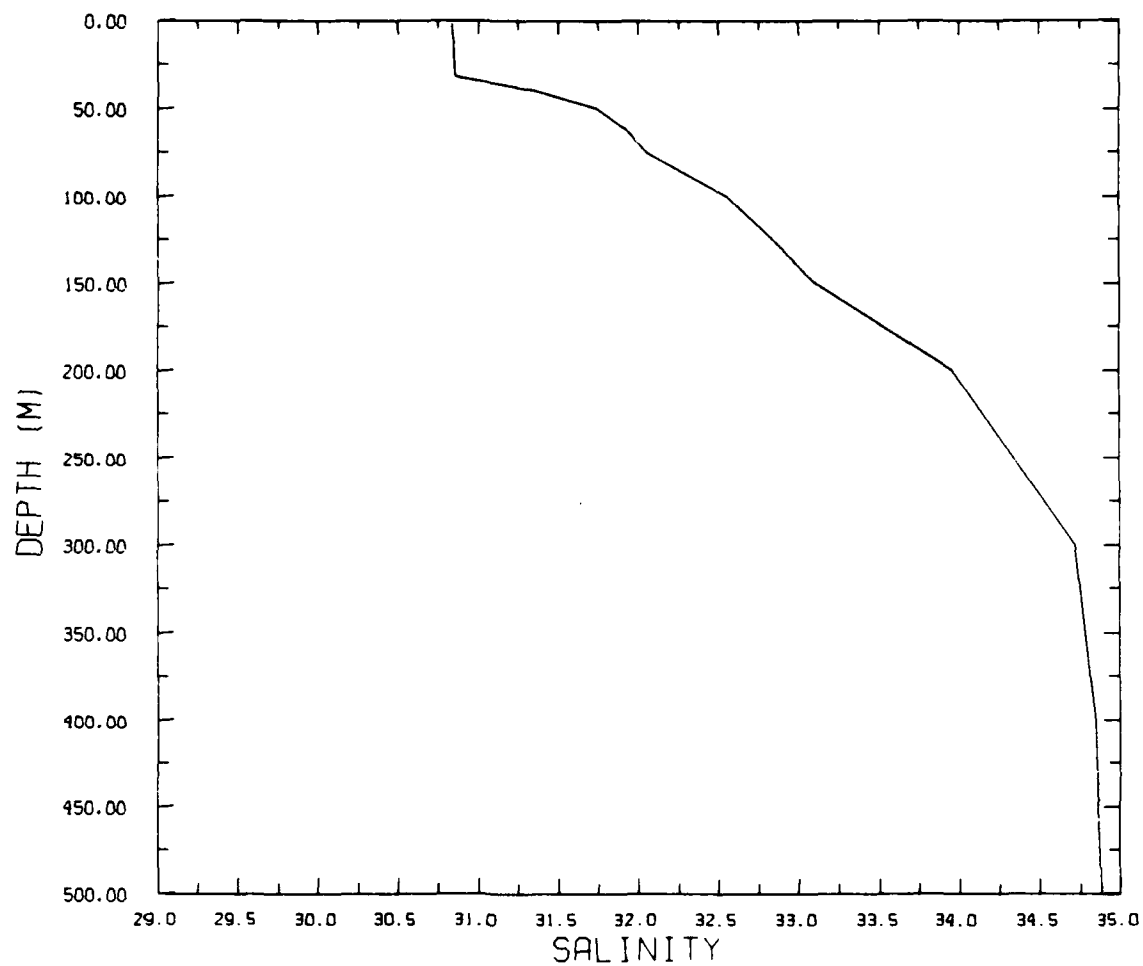
MODEL PROFILES
TEMP. STEP 1



YEAR NO. 1
VARIABLE MIXED LAYER
CASE 1

Figure 2. Temperature profile from Station Blue Fox, January 1, 1976. This profile is used to initialize the ice/ocean model.

MODEL PROFILES SALINITY STEP 1



YEAR NO. 1
VARIABLE MIXED LAYER
CASE 1

Figure 3. Salinity profile from Station Blue Fox, January 1, 1976. This profile is used to initialize the ice/ocean model.

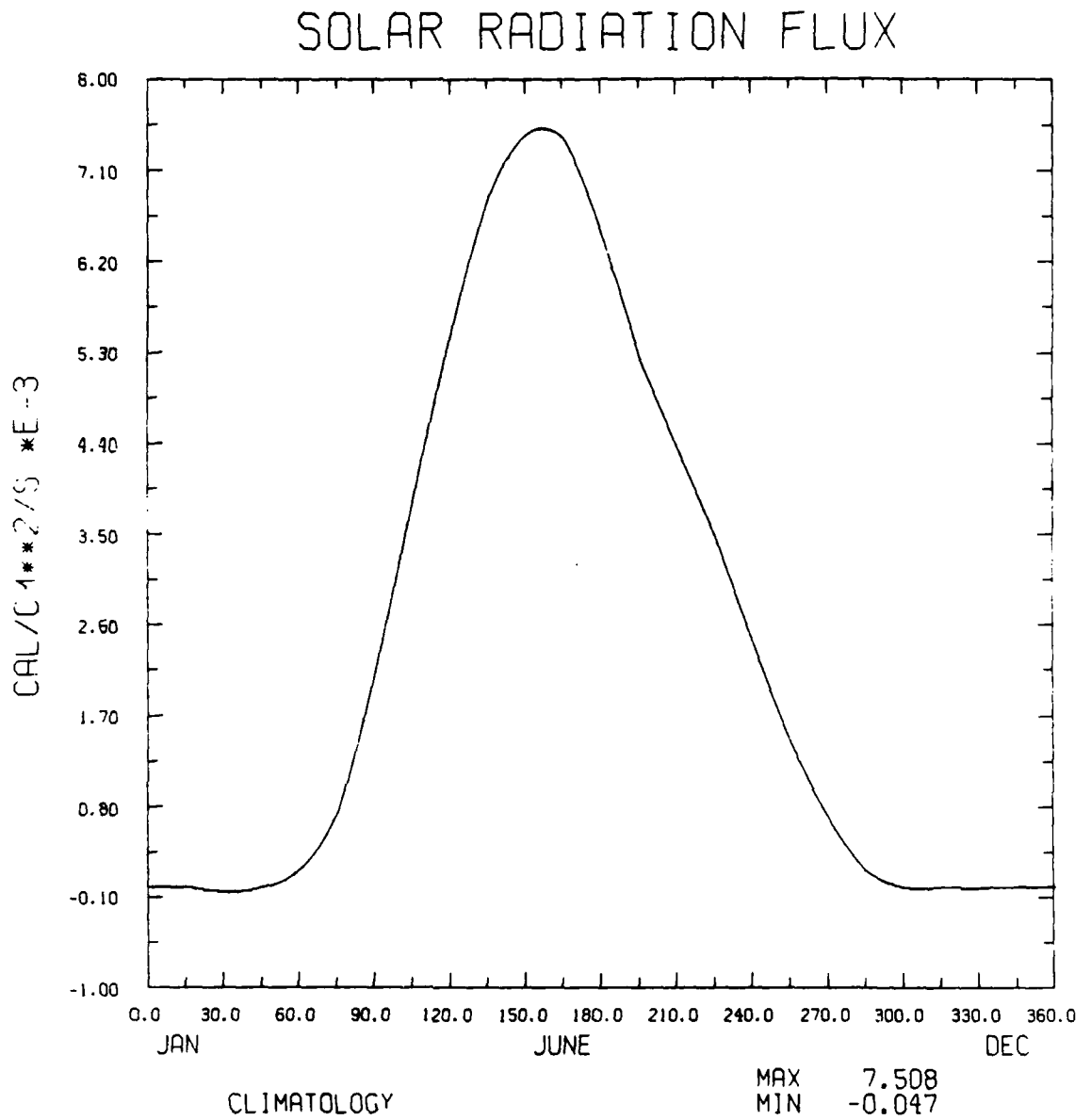


Figure 4. Solar radiation fluxes used to force the climatology test cases. Fluxes are determined from Fletcher's (1965) climatology for the Arctic.

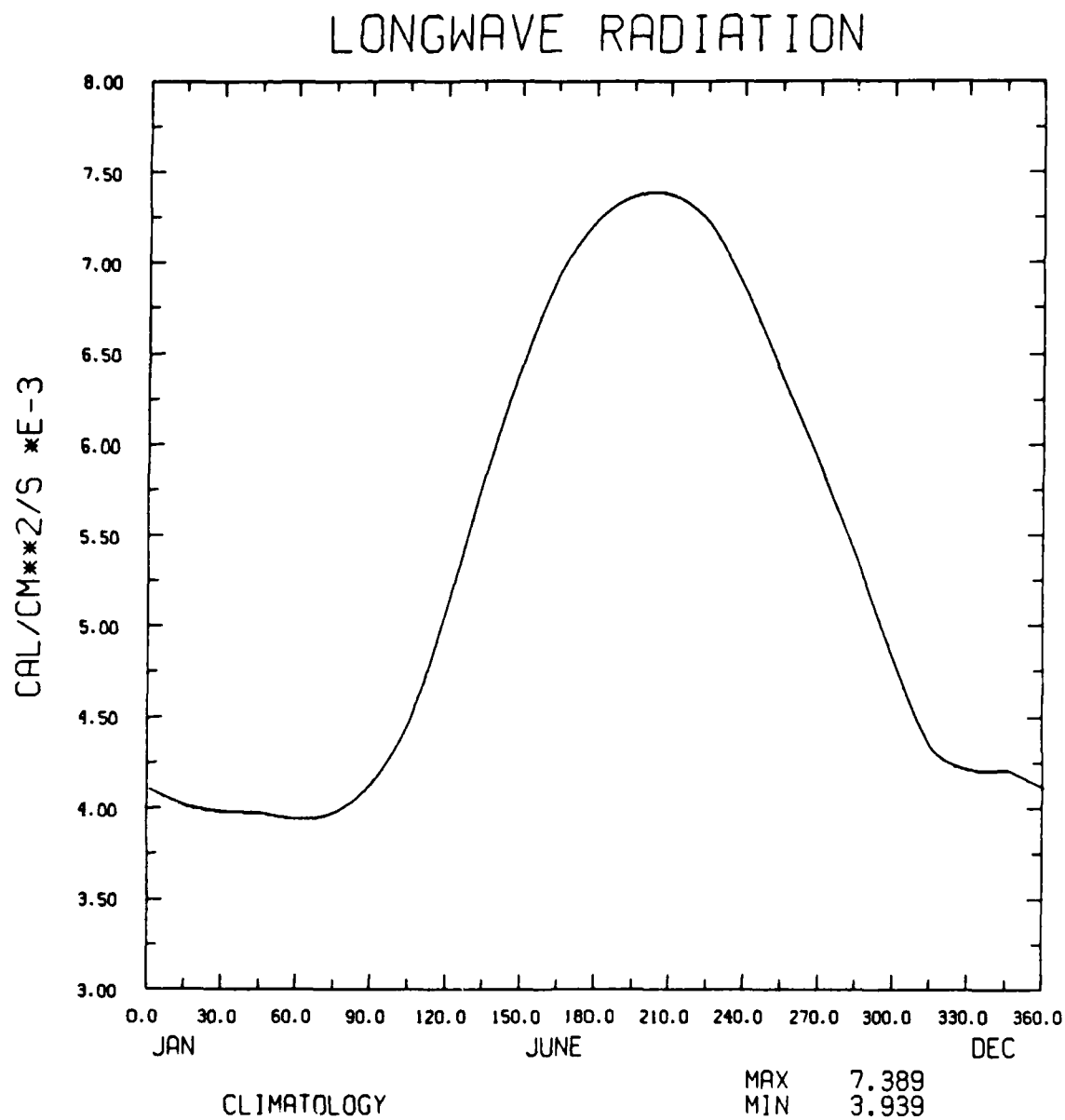


Figure 5. Longwave radiation fluxes used to force the climatology test cases. Fluxes are determined from Fletcher's (1965) climatology for the Arctic.

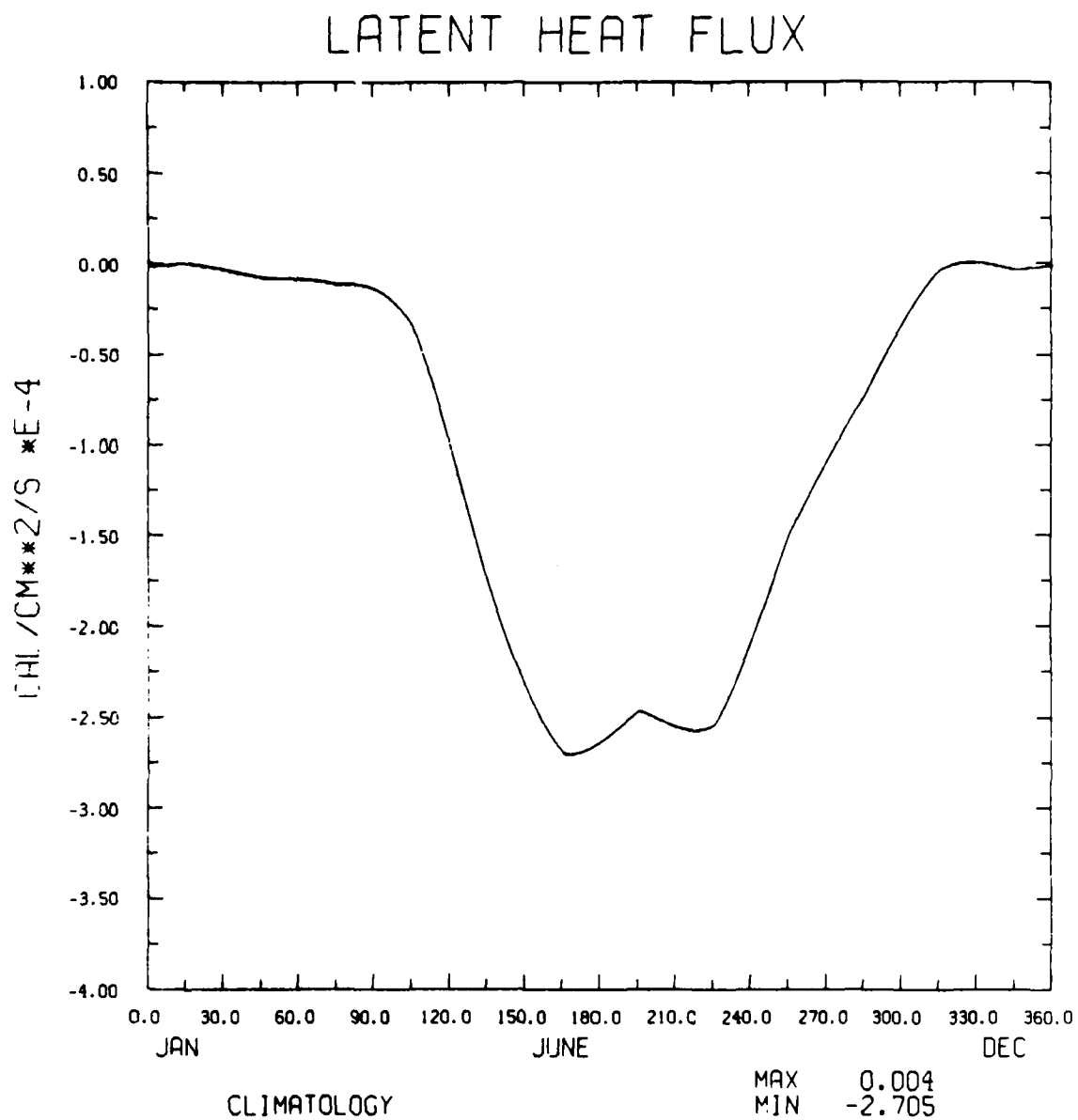


Figure 6. Latent heat fluxes used to force the climatology test cases. Fluxes are determined from Fletcher's (1965) climatology for the Arctic.

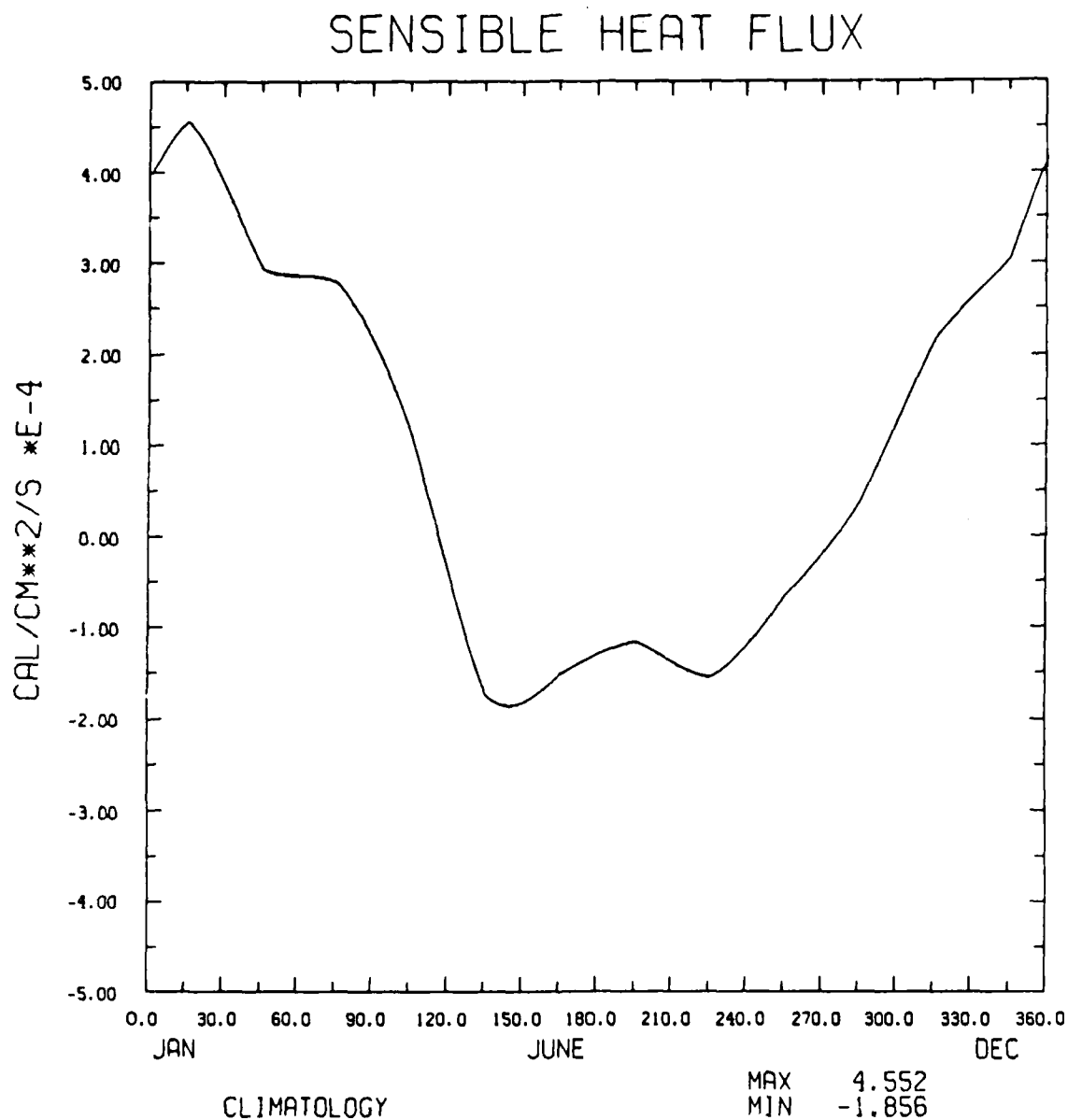


Figure 7. Sensible heat fluxes used to force the climatology test cases. Fluxes are determined from Fletcher's (1965) climatology for the Arctic.

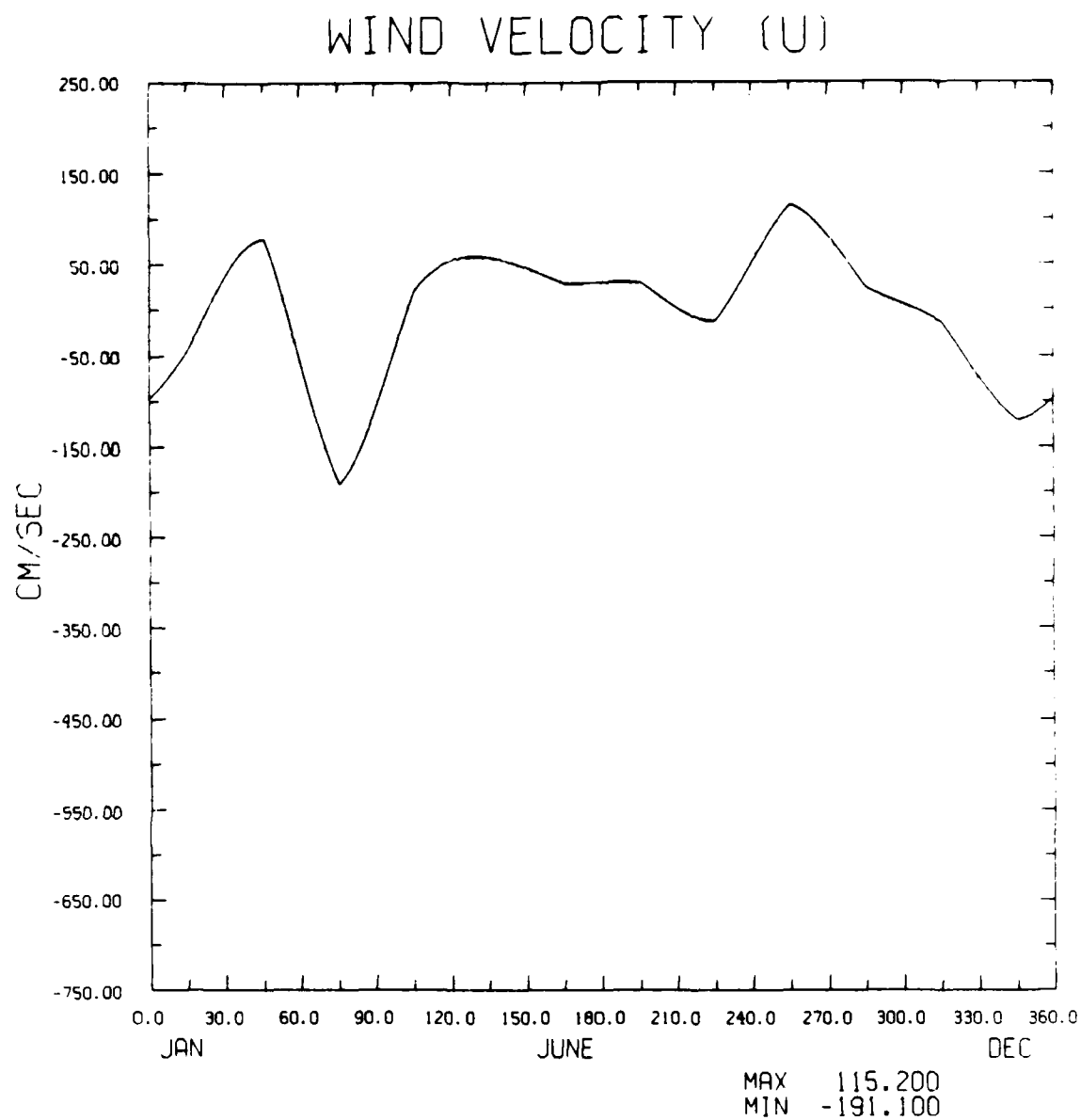


Figure 8. U-component of the wind velocity determined from monthly averaged winds from FNOC's analysis.

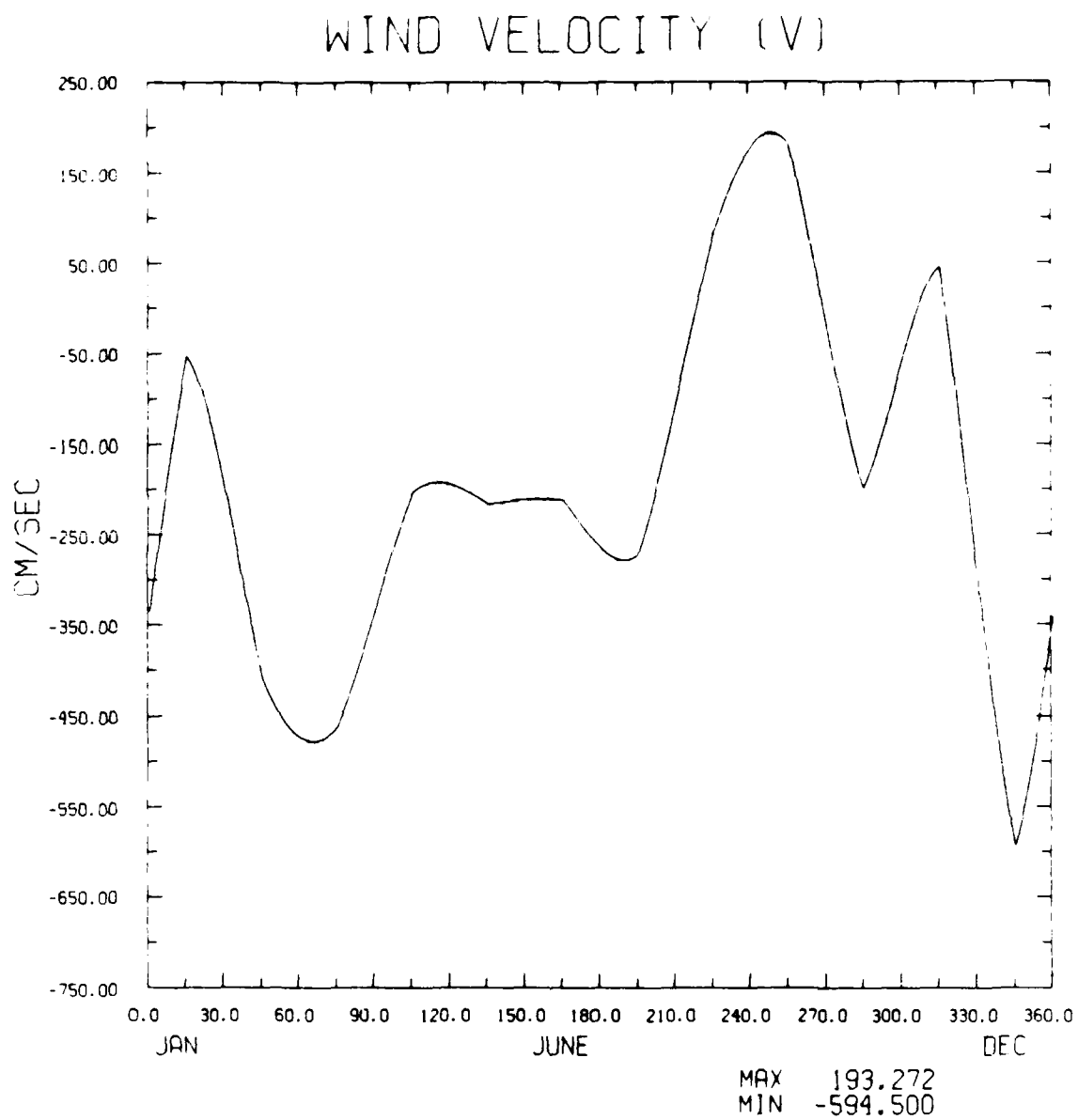


Figure 9. V-component of the wind velocity determined from monthly averaged winds from FNOC's analysis.

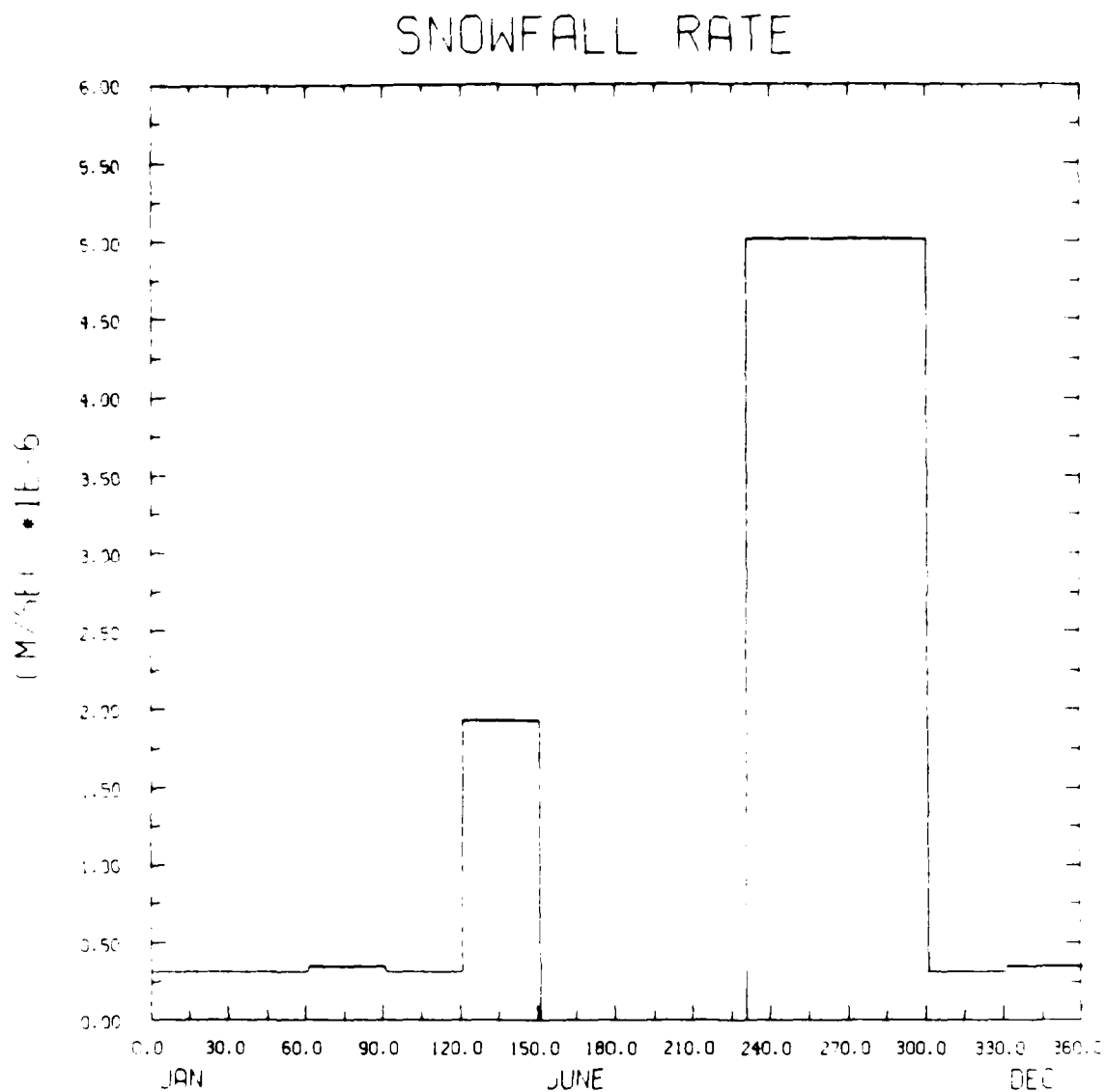


Figure 10. Snowfall rate for Arctic as described in Semtner (1976).

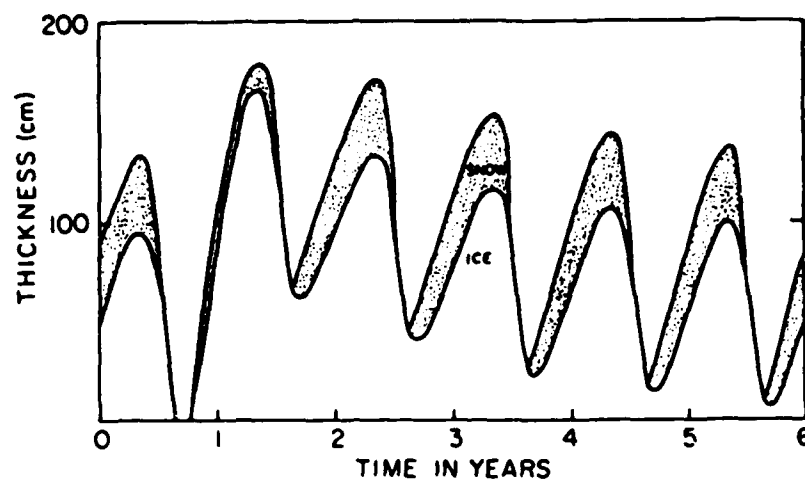


Figure 11. A multiyear equilibrium cycle of ice thickness, as predicted by Semtner's 0-layer ice model, for the case in which the oceanic heat flux is a constant $6 \text{ kcal/cm}^2/\text{year}$, and the mixed-layer depth is a fixed 30 m (from Semtner, 1976).

CASE 1

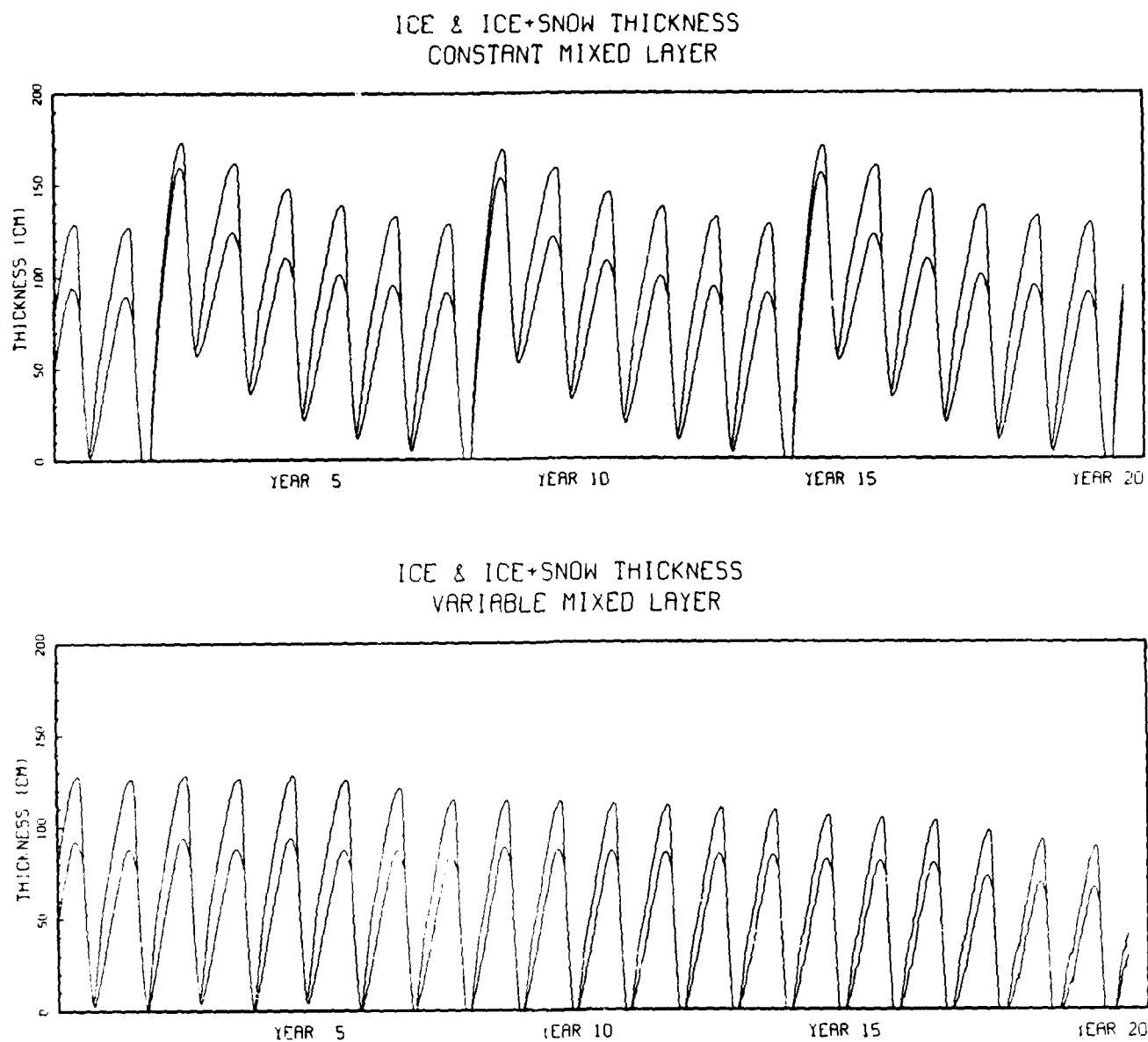


Figure 12. The yearly variability of the ice and ice plus snow thickness for a 20-year simulation of the CML model and the VML model. The upper plot is the results from the CML model. The lower plot is the results from the VML model.

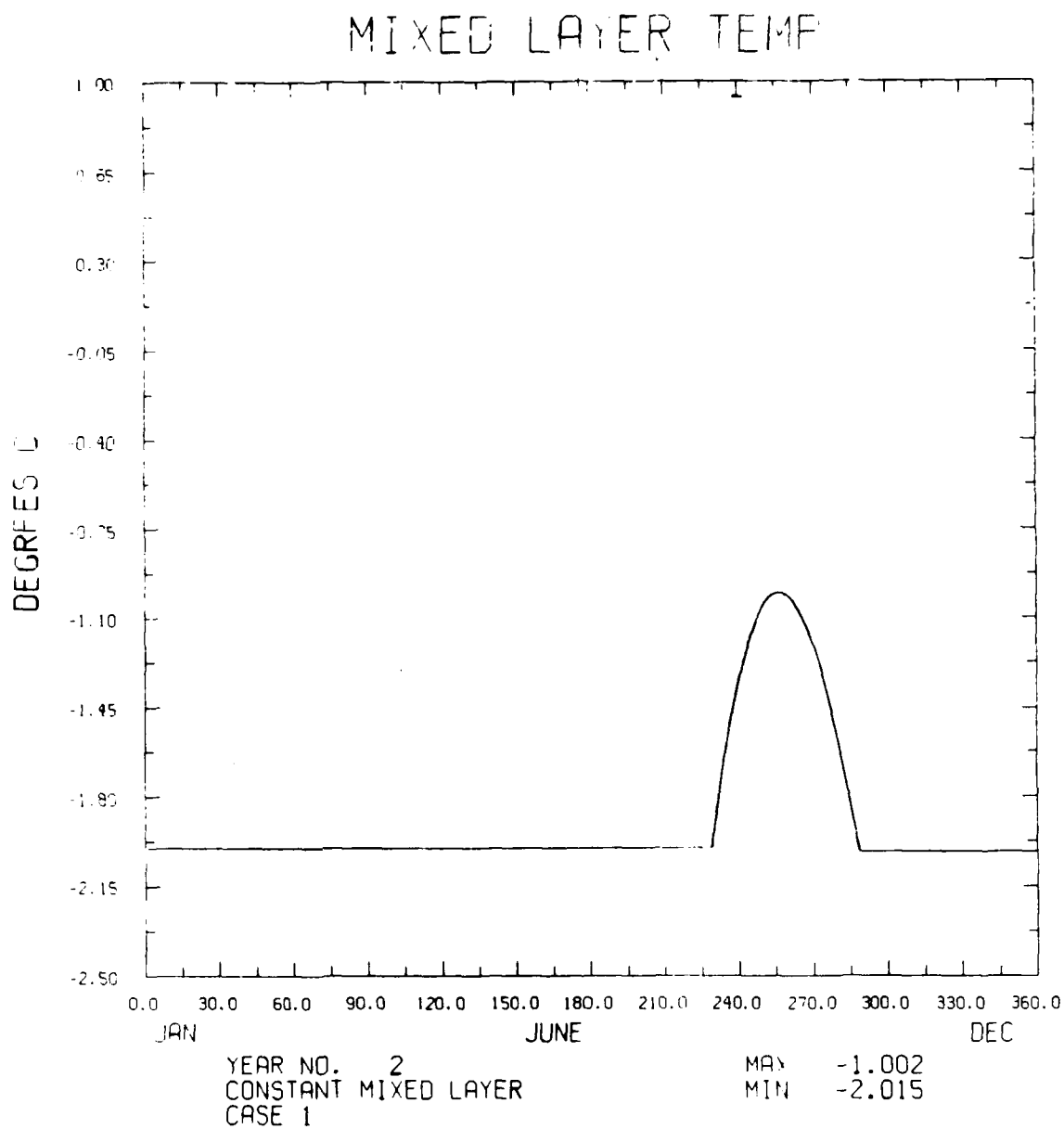


Figure 13. The mixed-layer temperature for year 2 from the CML simulation.

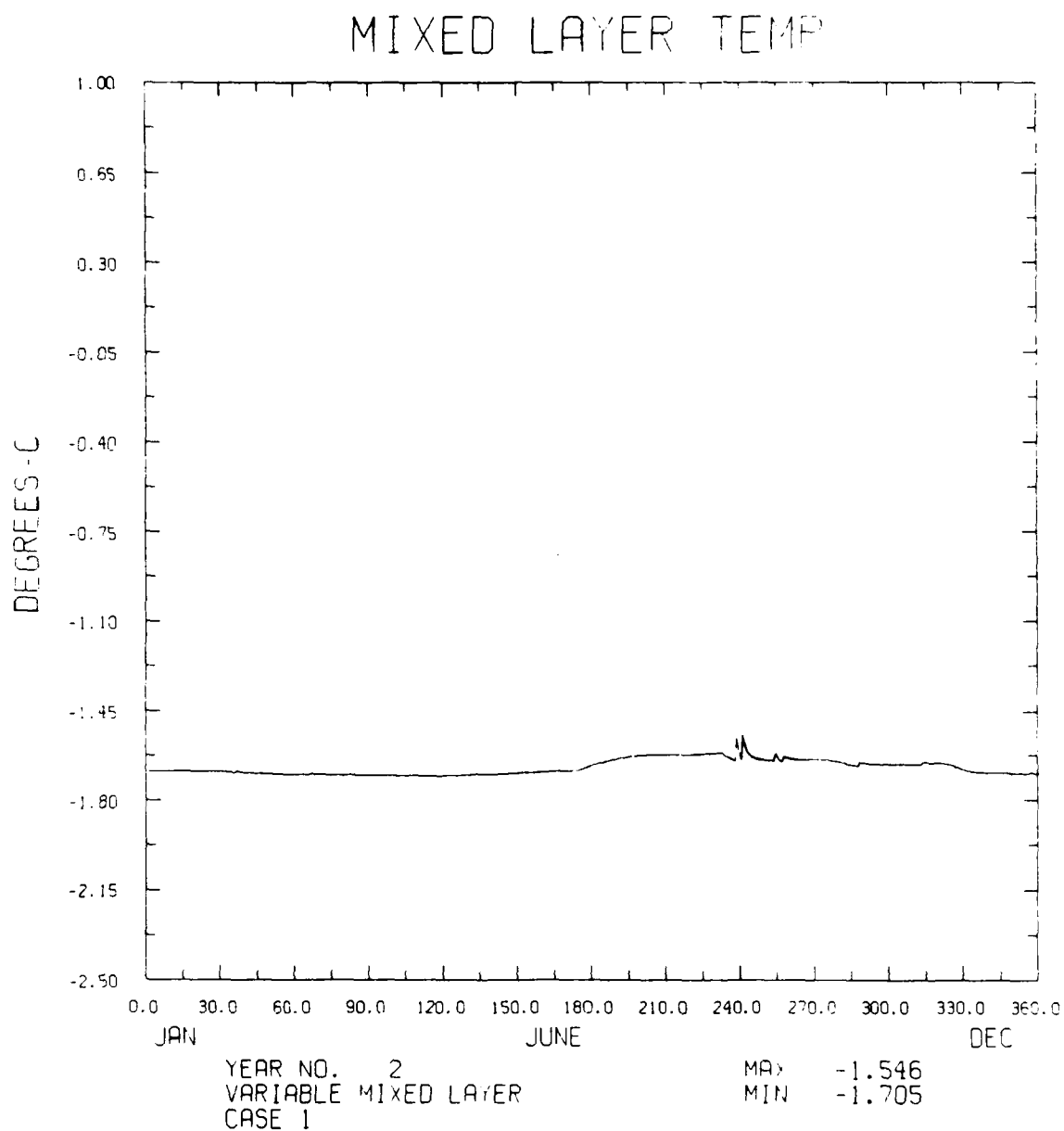


Figure 14. The mixed-layer temperature for year 2 from the VML simulation.

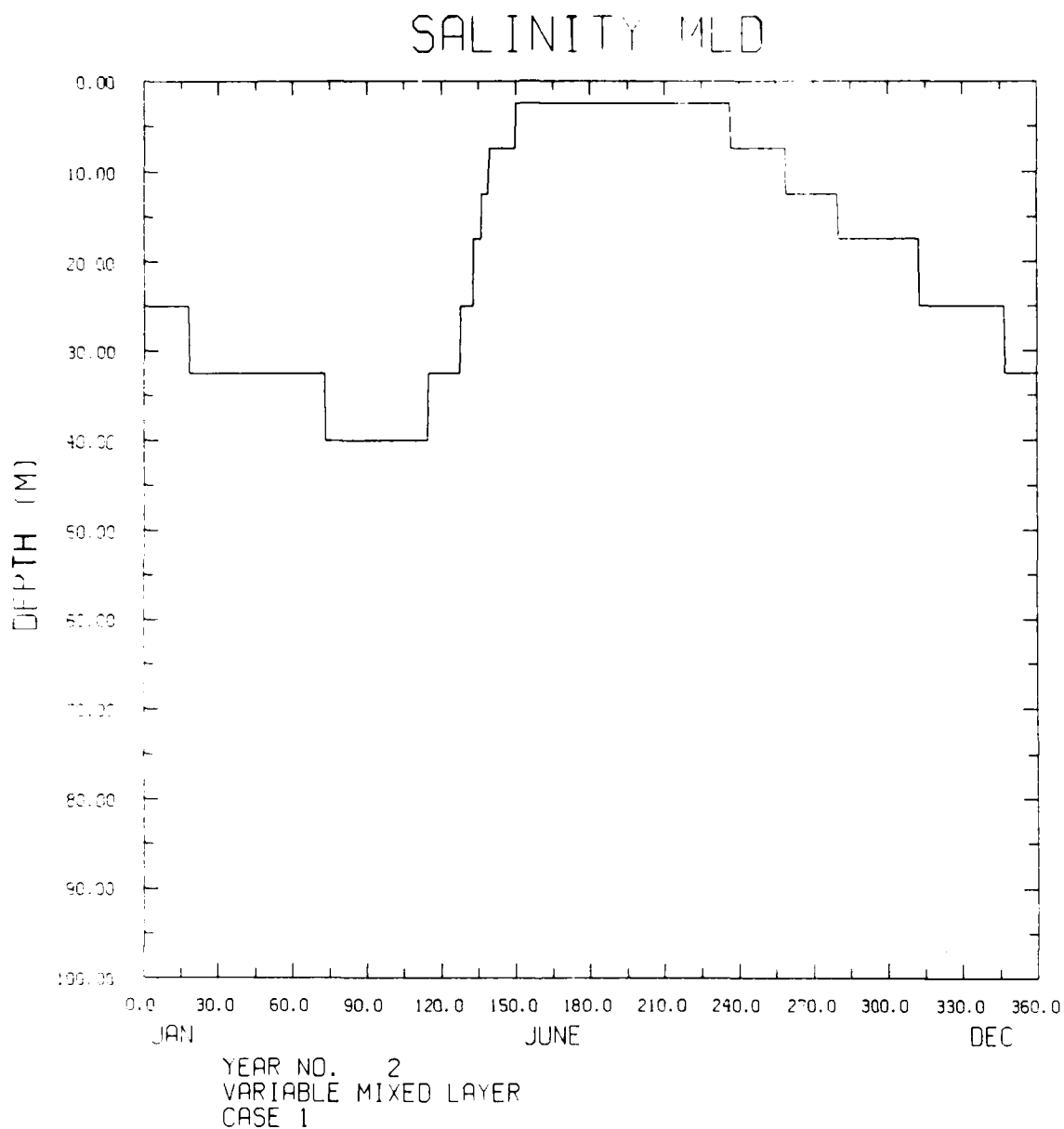


Figure 15. The mixed-layer depth for year 2 from the VML simulation. The mixed-layer depth is the maximum depth at which the salinity has changed by no more than 0.1 ppt. from its surface value.

TEMPERATURE PROFILE PLOTS FROM MIDEU RUN CASE 1
YEAR NO. 2

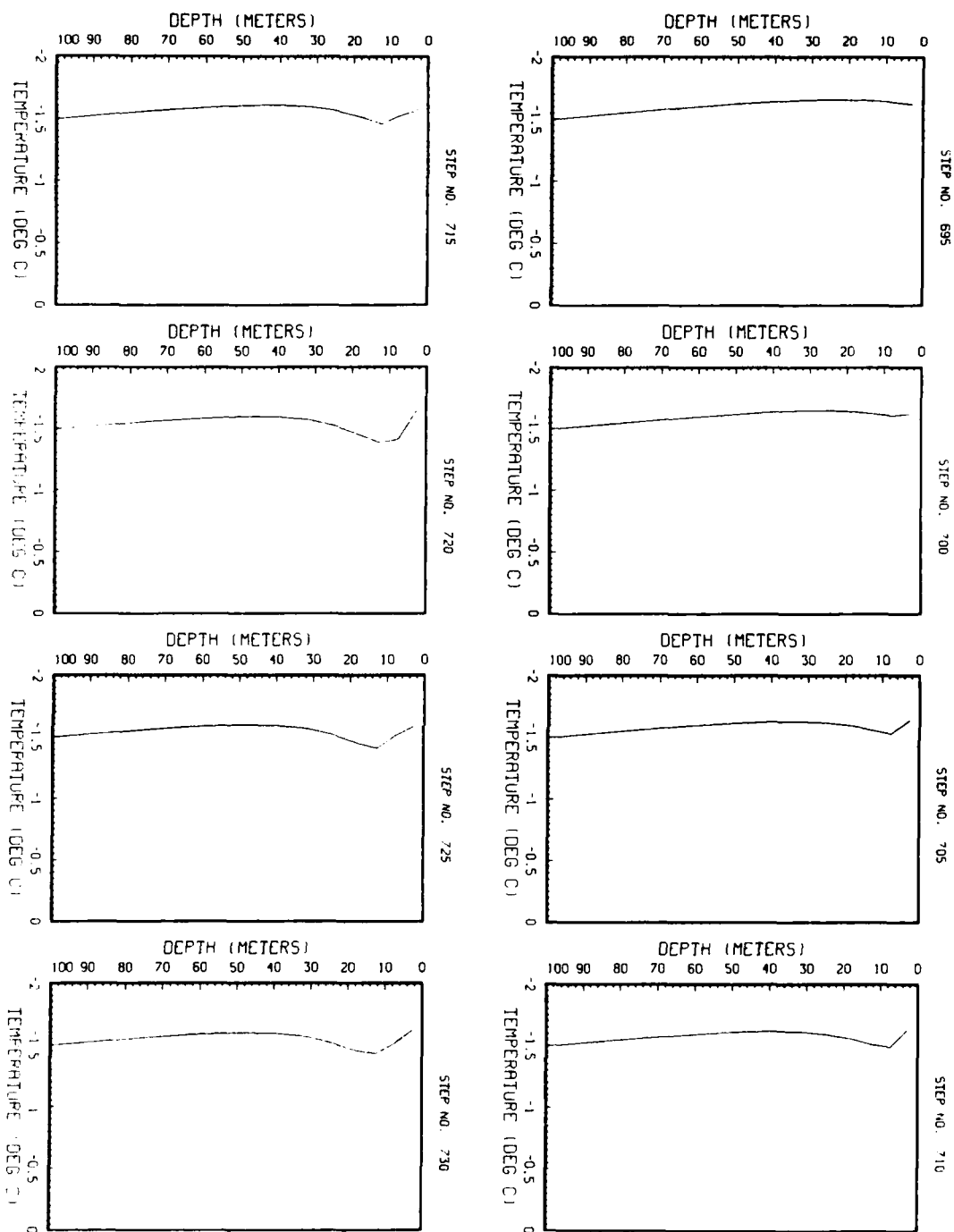


Figure 16. Some temperature profile plots from the VML simulation. These profiles were taken just before, during, and just after the open-water period in year 2 of the simulation.

SALINITY PROFILE PLOTS FOR MODEL RUN CASE 1
YEAR NO. 2

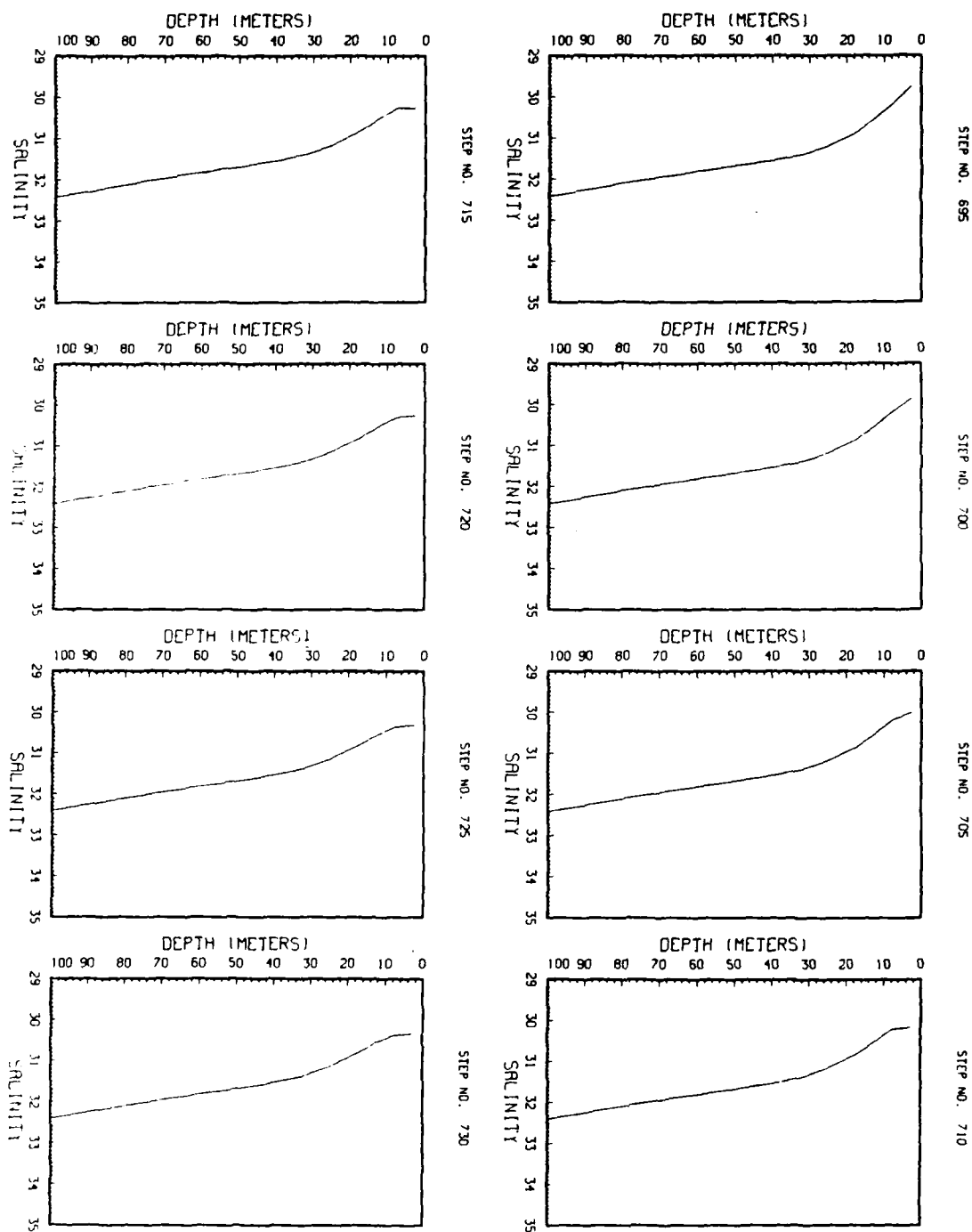


Figure 17. Some salinity profile plots from the VML simulation. These profiles were taken just before, during, and just after the open-water period in year 2 of the simulation.

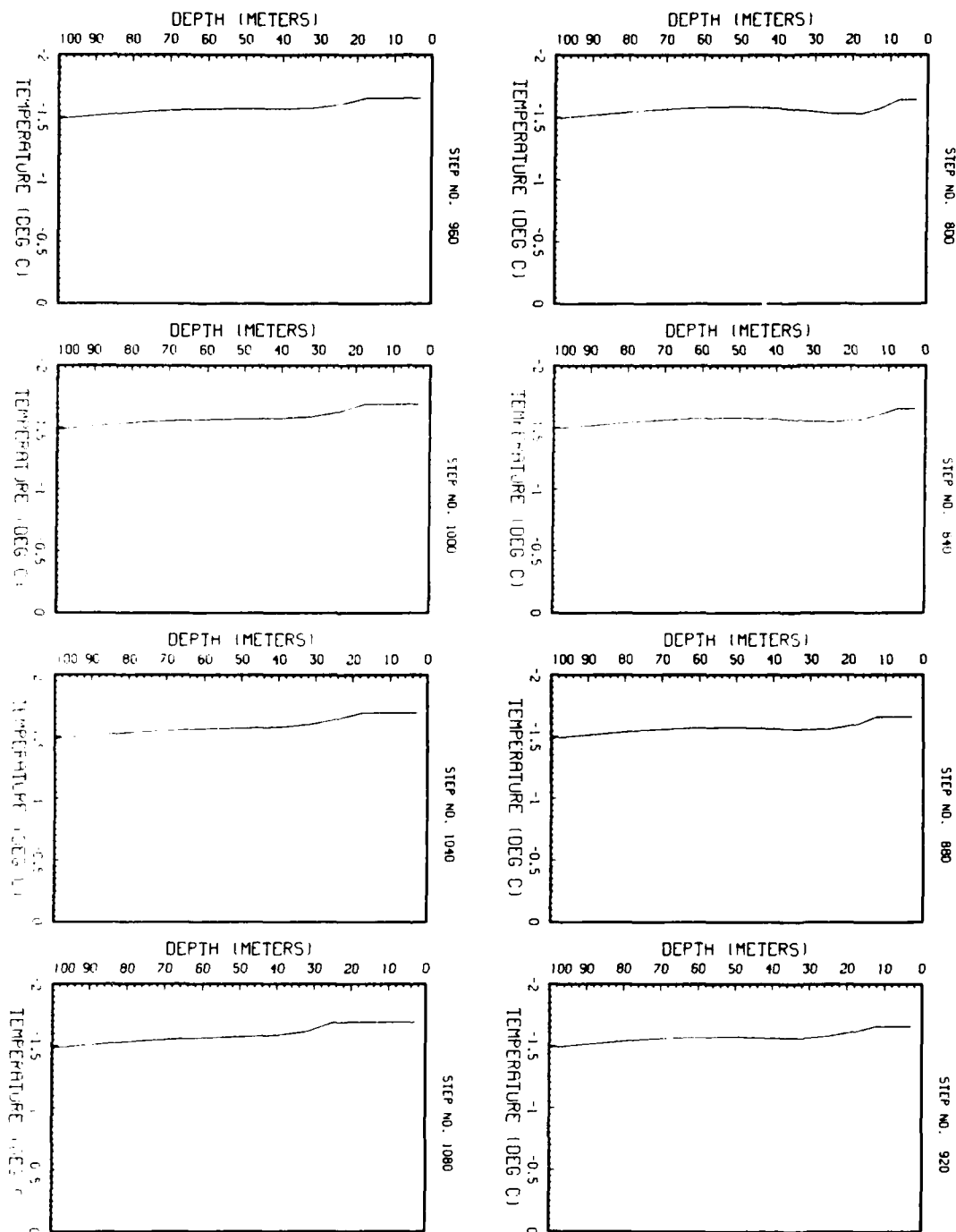


Figure 18. Some temperature profile plots from year 2 of the VML simulation. These profiles were taken following the open-water period as the ice grows from 1 cm to 40 cm.

TEMPERATURE PROFILE PLOTS FOR MODEL RUN CASE 1
YEAR NO. 10

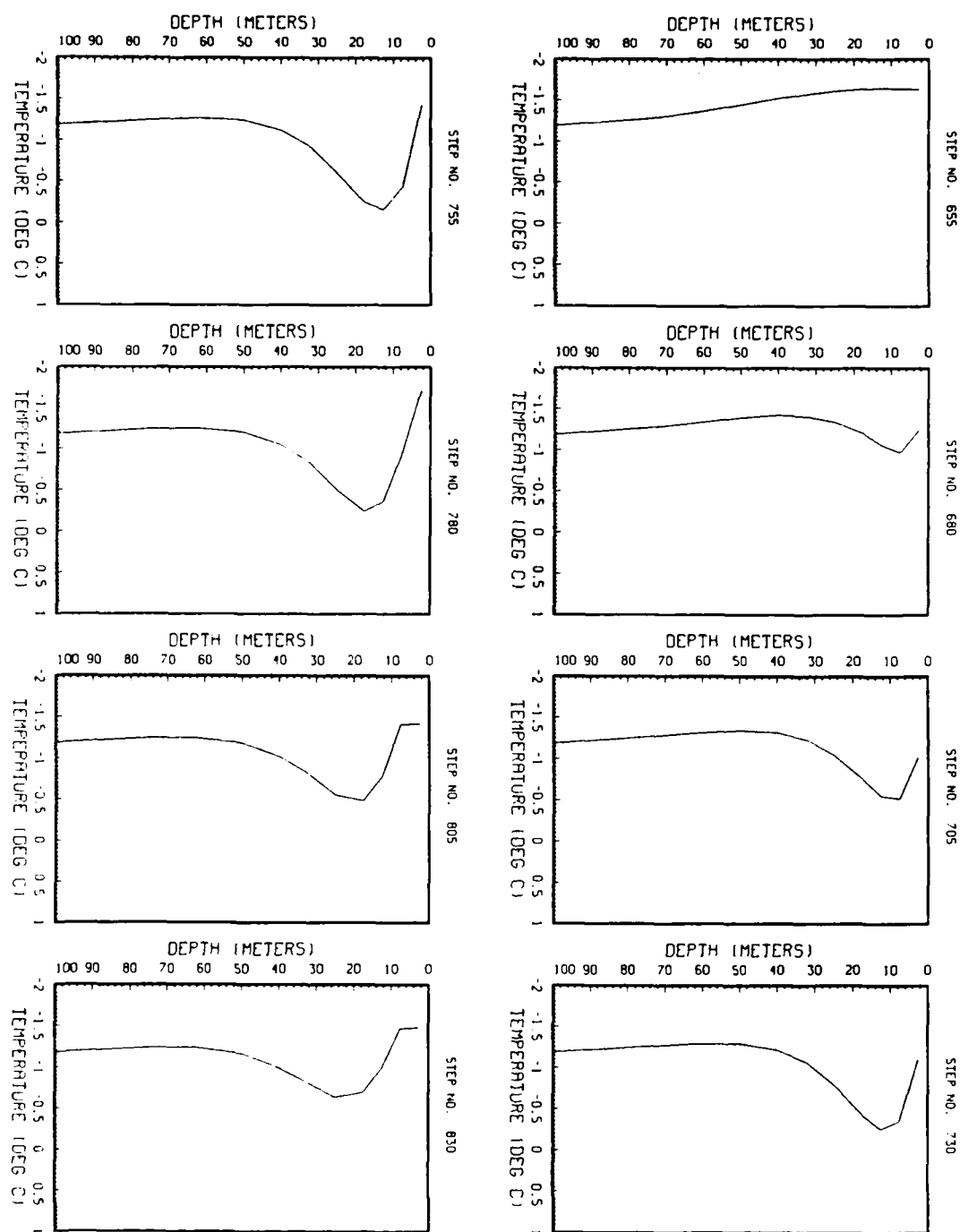


Figure 19. Some temperature profile plots from the VML simulation. These profiles were taken just before, during, and just after the open-water period in year 10 of the simulation. Open water exists from step 659 to step 780.

TEMPERATURE PROFILE PLOTS FOR MODEL RUN CASE 1
YEAR NO. 10

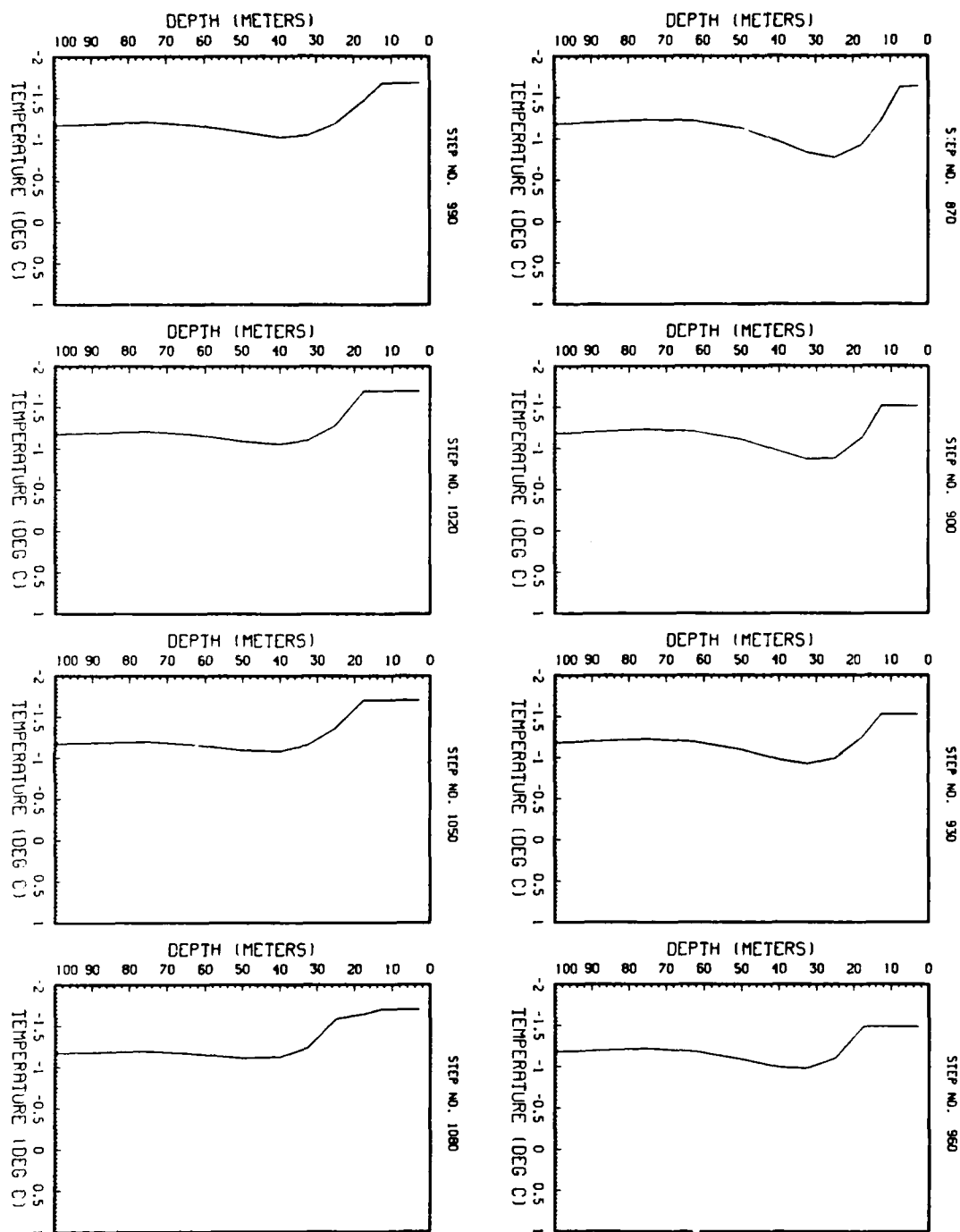


Figure 20. Some temperature profile plots from year 10 of the VML simulation. These profiles were taken following the open water period, during the time ice is growing.

TEMPERATURE PROFILE PLOTS FOR MODEL RUN CASE 1
YEAR NO. 11

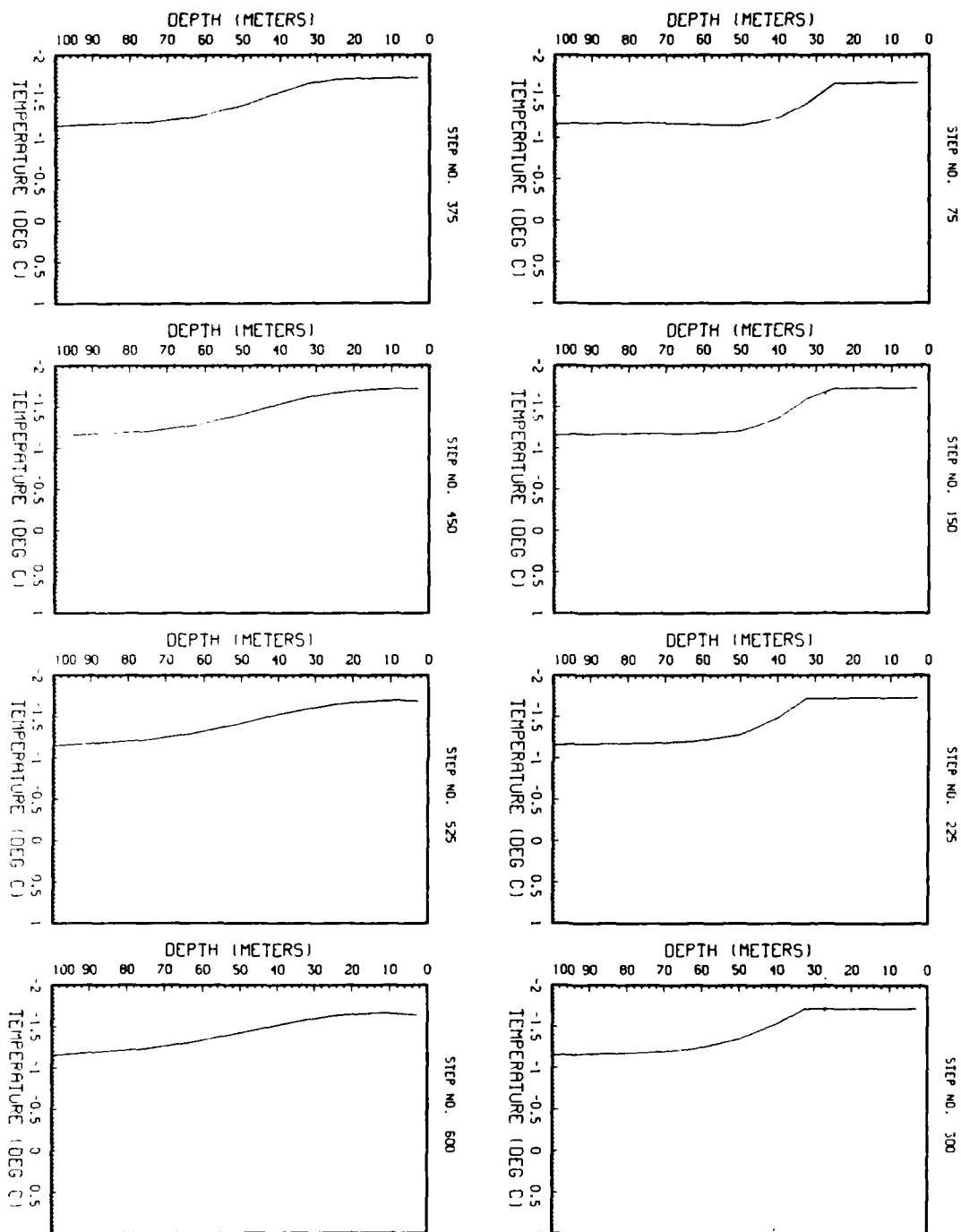


Figure 21. Some temperature profile plots from year 11 of the VML simulation. These profiles were taken from the first half of the year from January 25 to July 20.

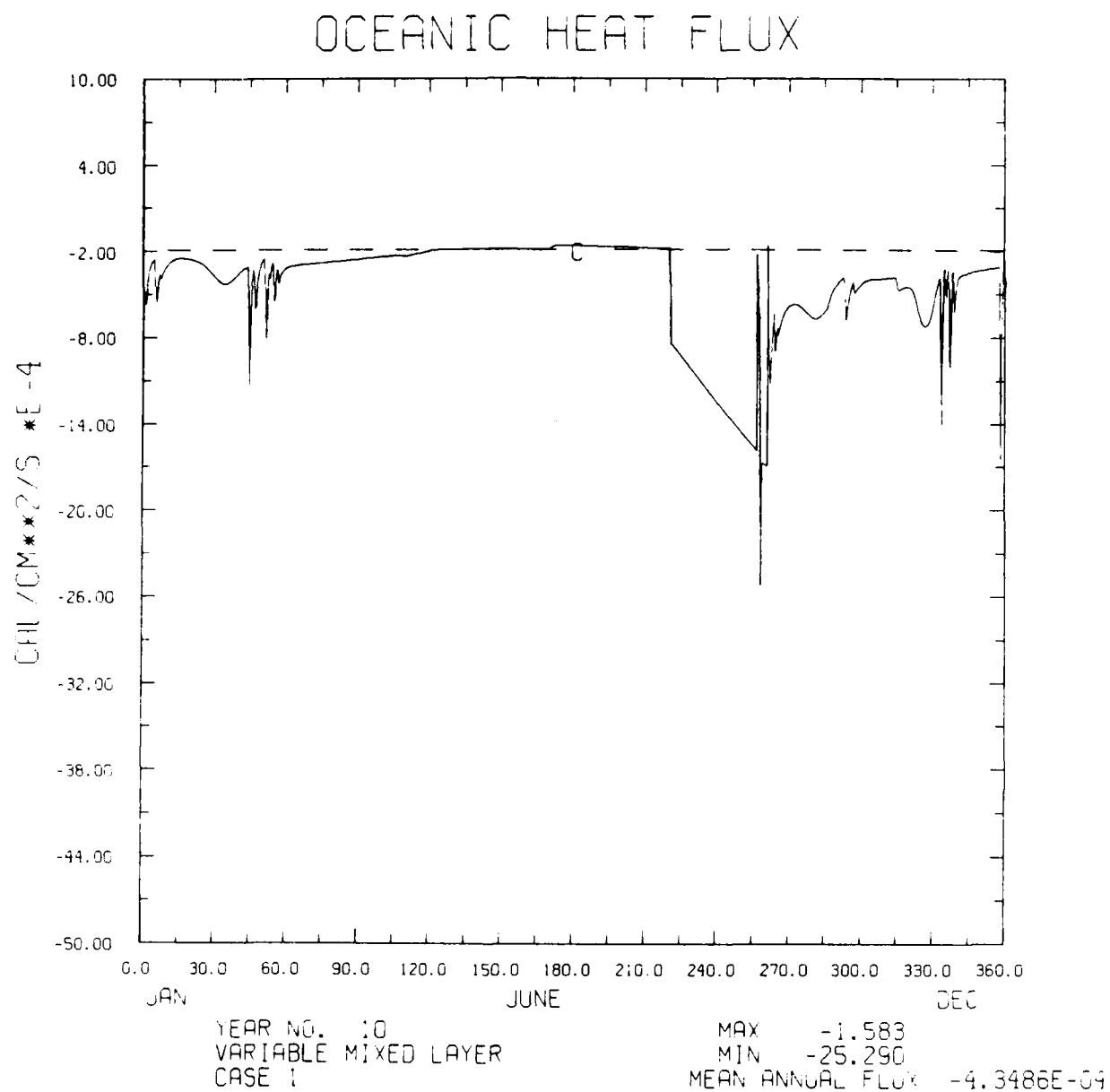


Figure 22. The oceanic heat flux from the VML simulation for year 10.

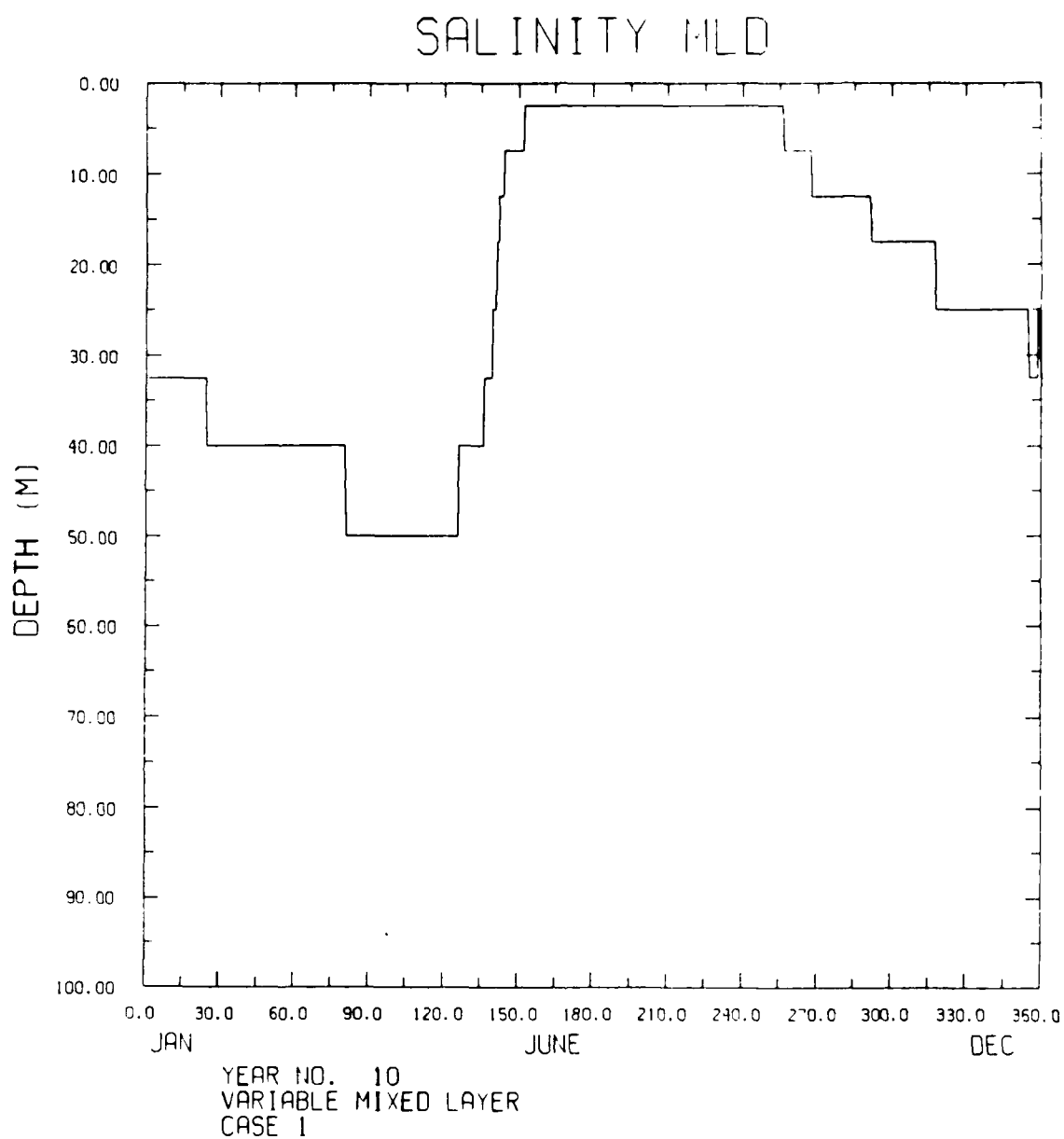


Figure 23. The mixed-layer depth determined from the salinity for year 10 of the VML simulation.

CASE 1 VARIABLE MIXED LAYER FBMAX= -1.65E-4 FBMIN= -50.96E-4

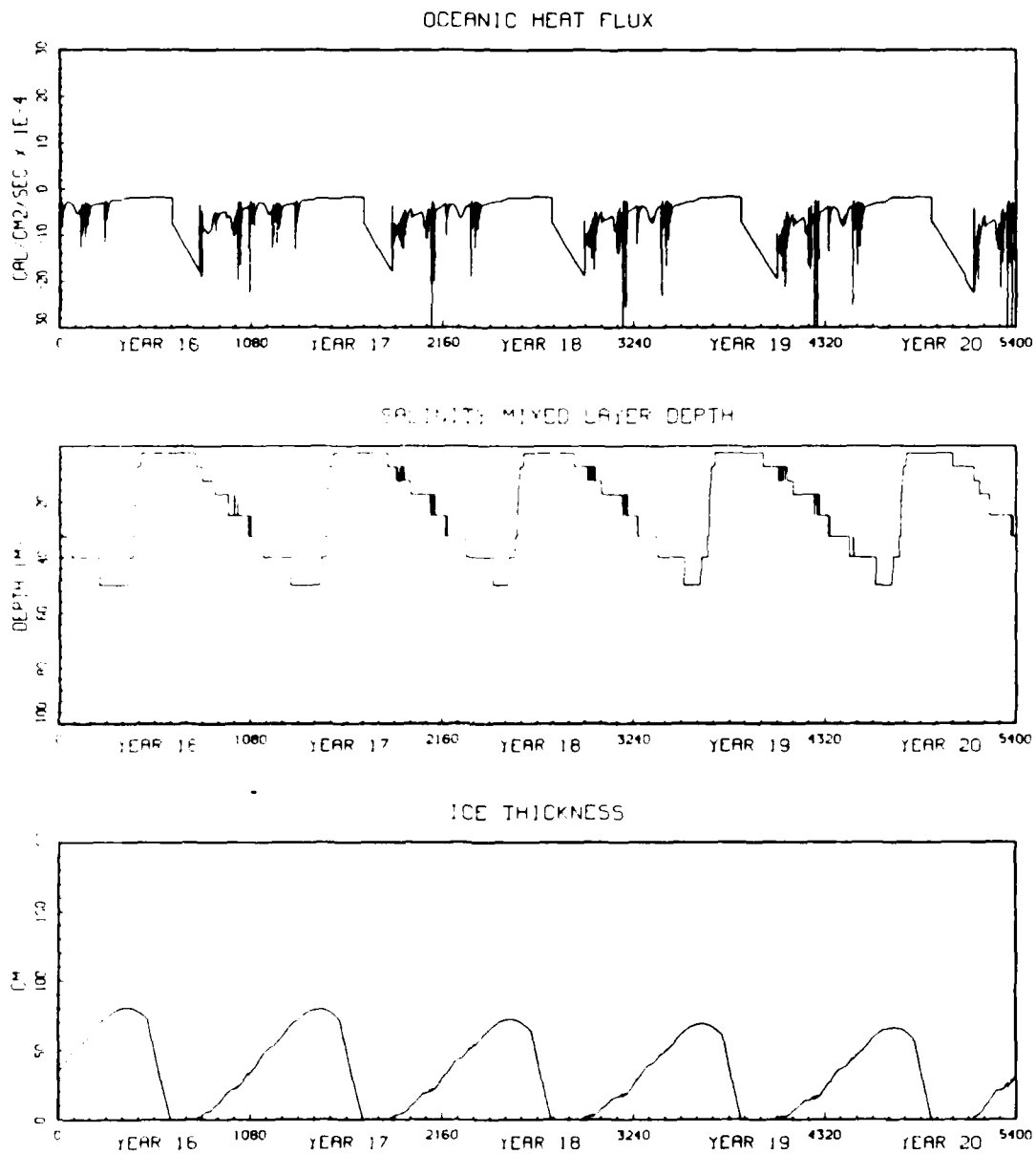


Figure 24. Plots for the oceanic heat flux, the salinity mixed-layer depth, and the ice thickness for the last 5 years of the VML simulation.

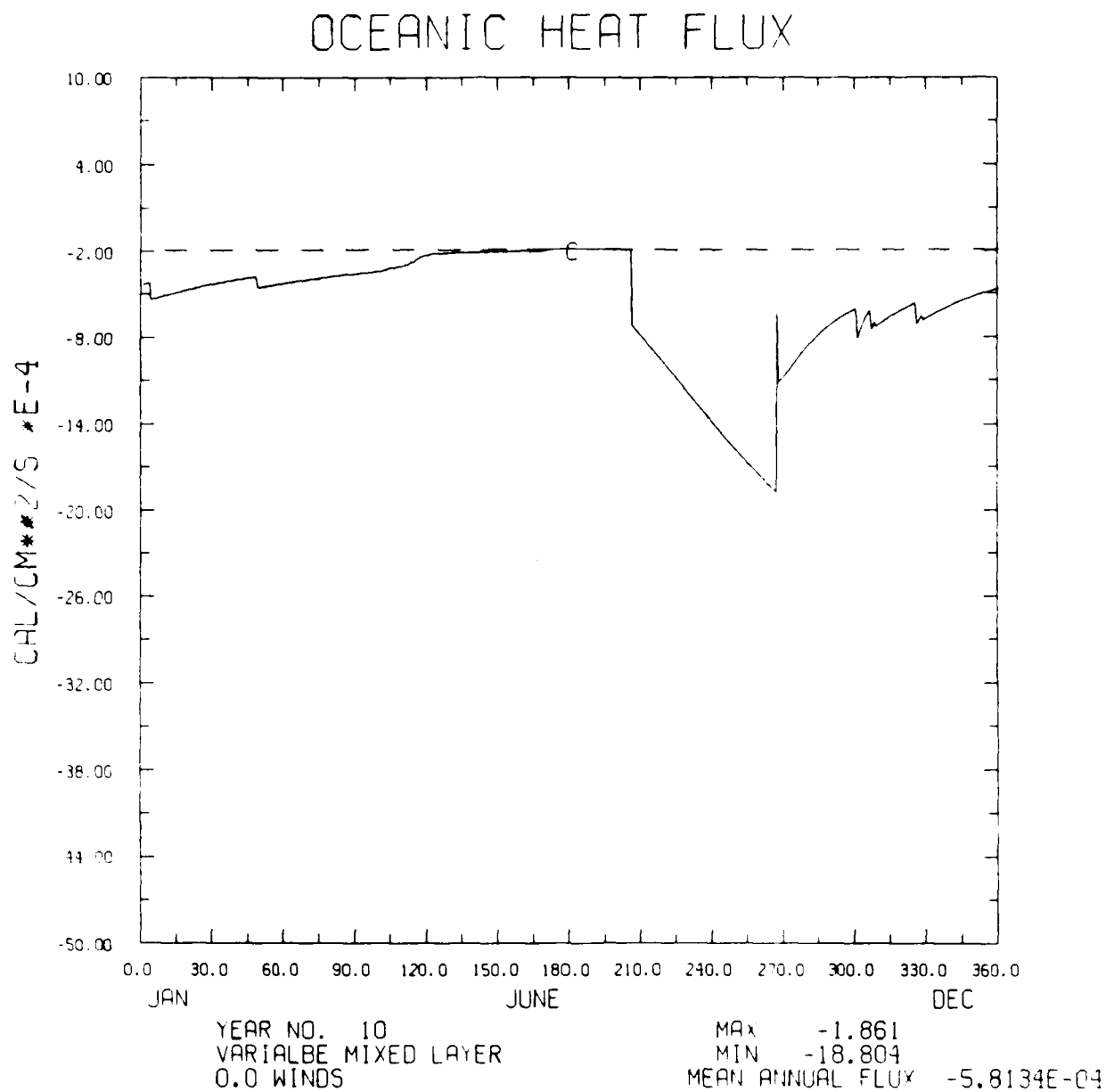


Figure 25. The oceanic heat flux for year 10 of the VML simulation for the case when the winds were set to zero.

SOUND SPEED PROFILE PLOTS FOR MODEL RUN CASE 1
YEAR NO. 20

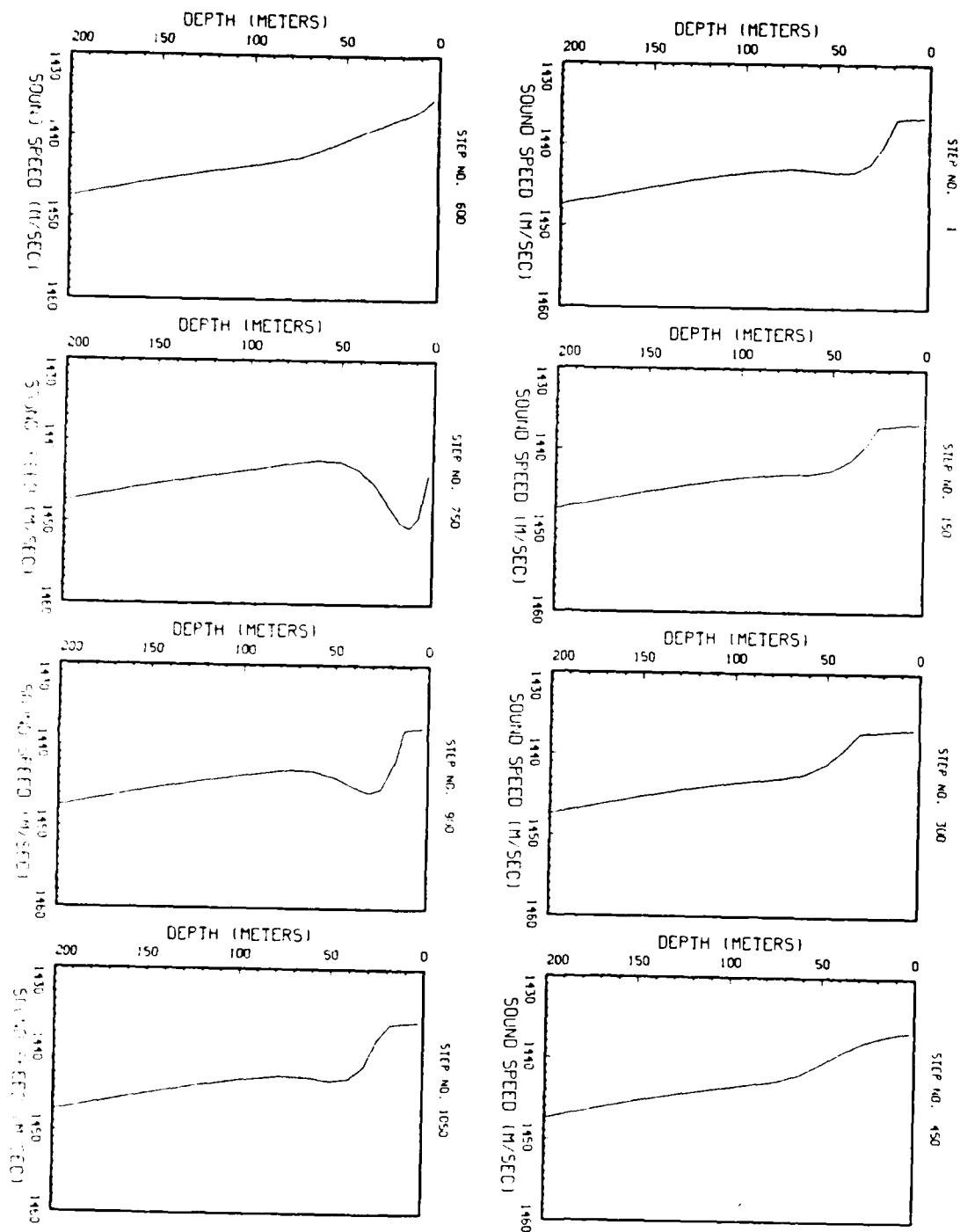


Figure 26. Sound speed profiles calculated from the temperature and salinity values determined by the VML model.

TEMPERATURE PROFILE PLOTS FOR MODEL RUN CASE 1
YEAR 110. 20

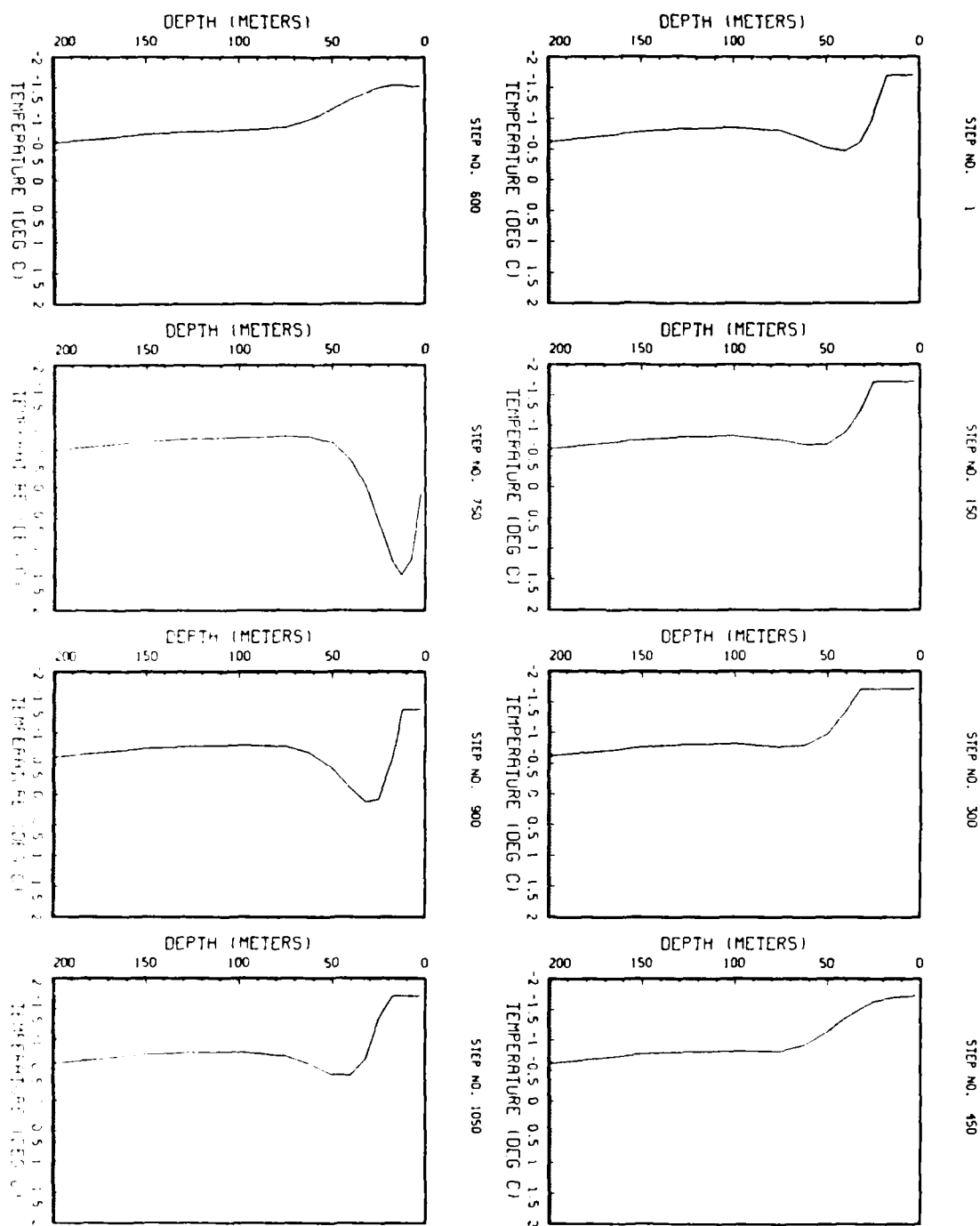


Figure 27. Temperature profiles of the values used in the calculation of sound speed.

SALINITY PROFILE PLOTS FOR CASE 1
YEAR NO. 20

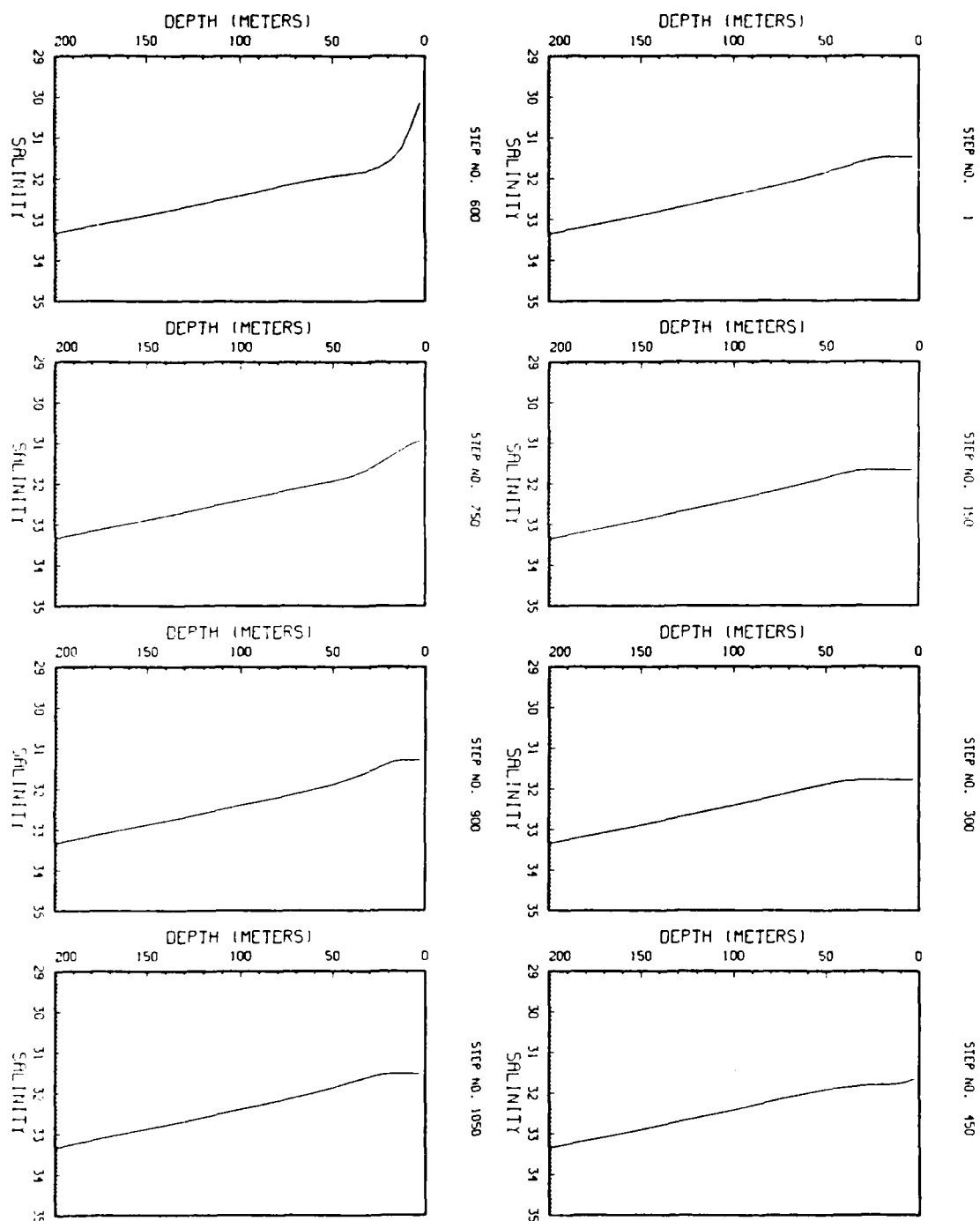
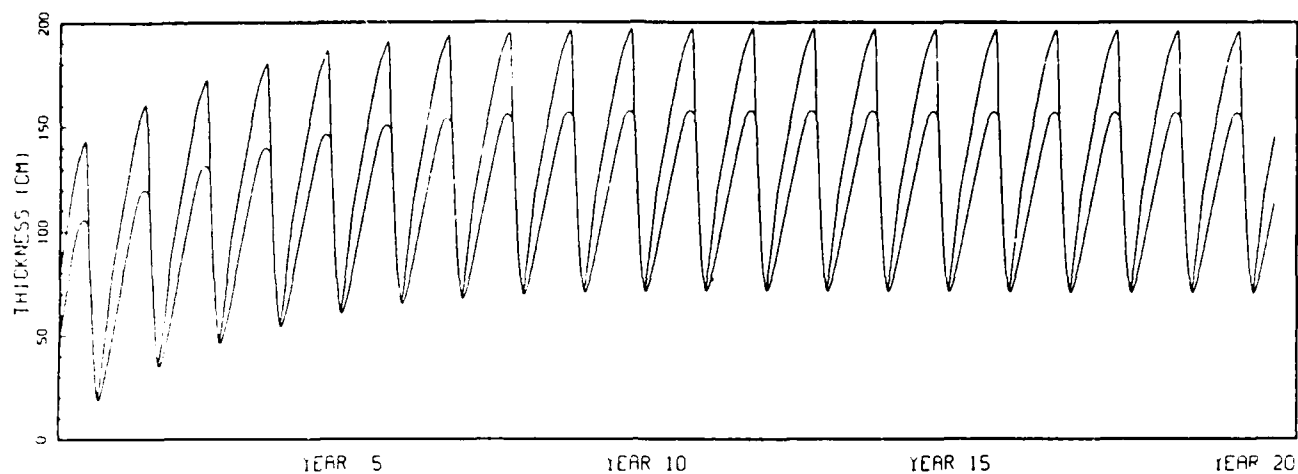


Figure 28. Salinity profiles of the values used in the calculation of sound speed.

1.5 KCAL/CM²/YEAR

ICE & ICE+SNOW THICKNESS
VARIABLE MIXED LAYER



OCEANIC HEAT FLUX
VARIABLE MIXED LAYER

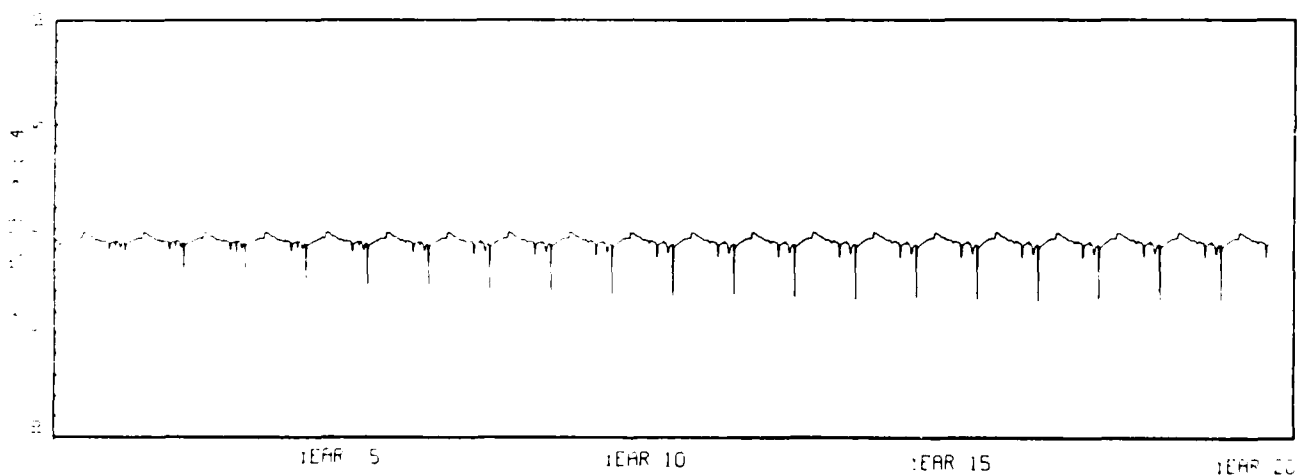
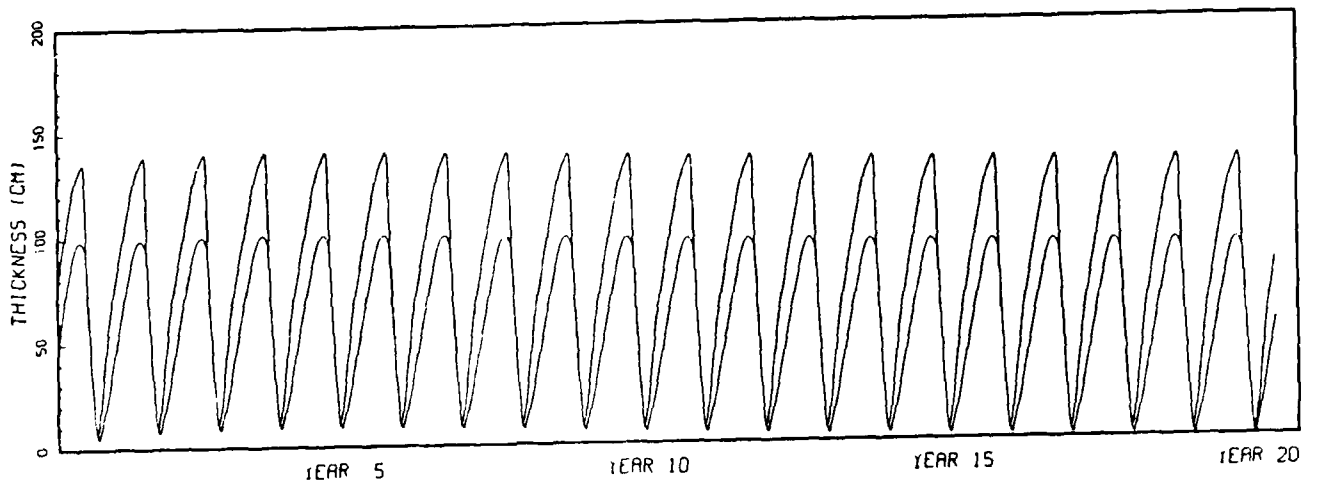


Figure 29. Ice thickness and oceanic heat flux values for a 20-year simulation of the VML model when $H_{\text{net}} = 1.5 \text{ kcal/cm}^2 \text{ year}$.

3.0 Kcal/cm²/YEAR

ICE & ICE+SNOW THICKNESS
VARIABLE MIXED LAYER



OCEANIC HEAT FLUX
VARIABLE MIXED LAYER

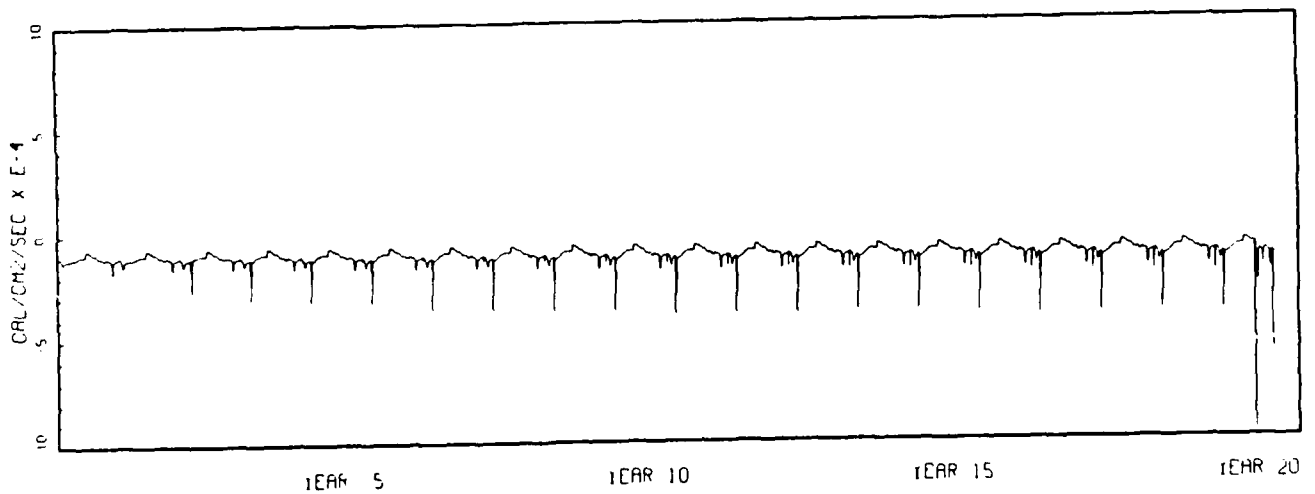
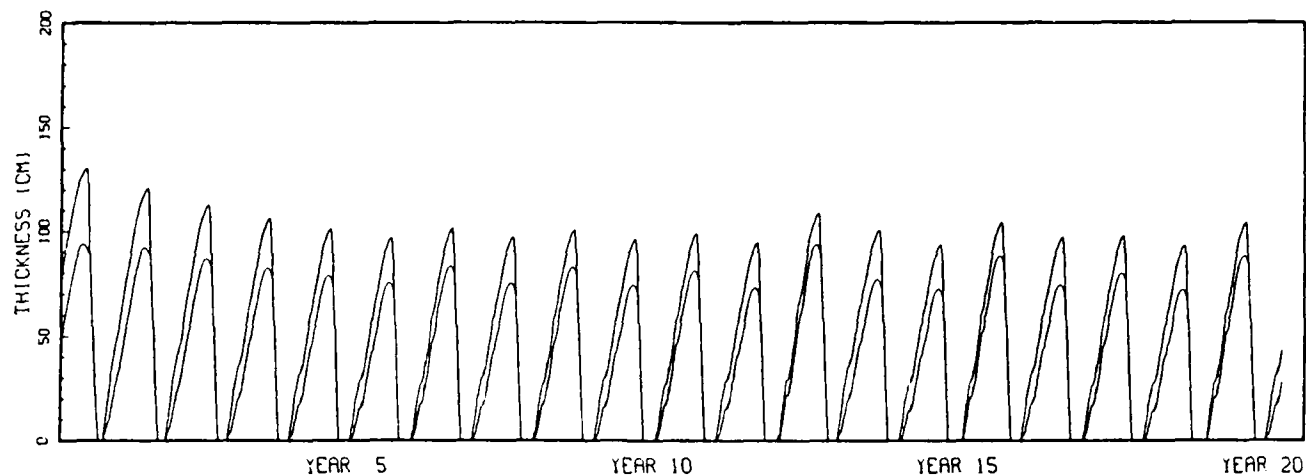


Figure 30. Ice thickness and oceanic heat flux values for a 20-year simulation of the VML model when $H_{\text{deep}} = 3.0 \text{ kcal/cm}^2/\text{year}$.

4.0 KCal/CM²/YEAR

ICE & ICE+SNOW THICKNESS
VARIABLE MIXED LAYER



OCEANIC HEAT FLUX
VARIABLE MIXED LAYER

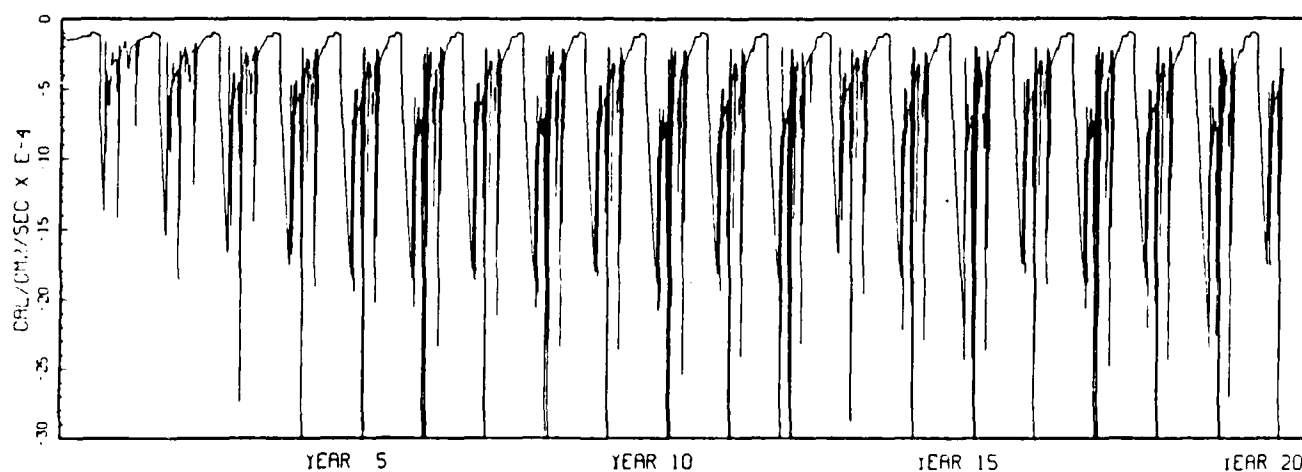
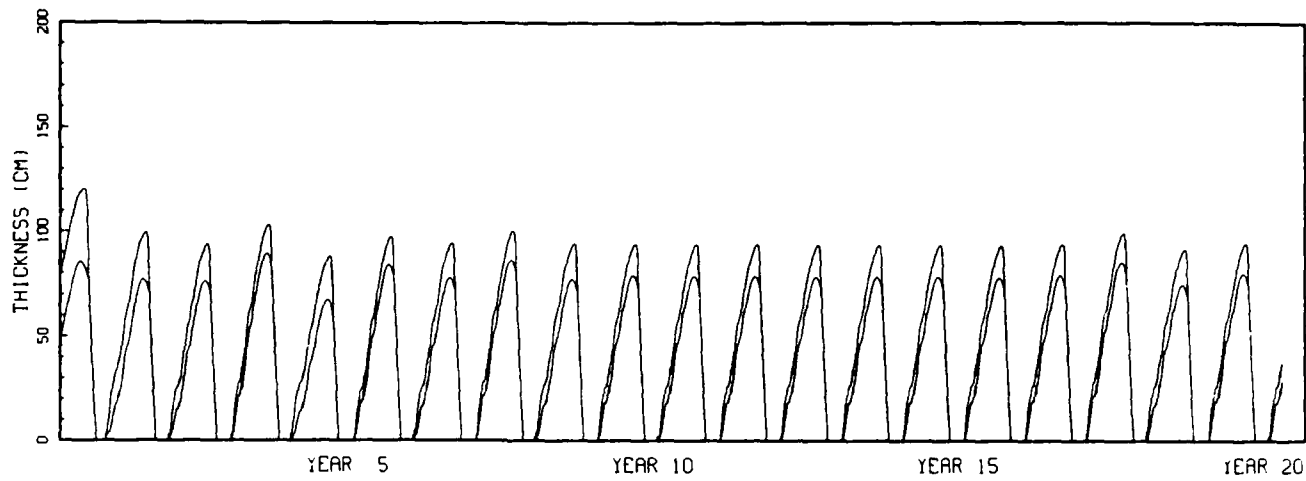


Figure 31. Ice thickness and oceanic heat flux values for a 20-year simulation of the VML model when $H_{\text{deep}} = 4.0 \text{ kcal/cm}^2/\text{year}$.

6.0 KCAL/CM²/YEAR

ICE & ICE+SNOW THICKNESS
VARIABLE MIXED LAYER



OCEANIC HEAT FLUX
VARIABLE MIXED LAYER

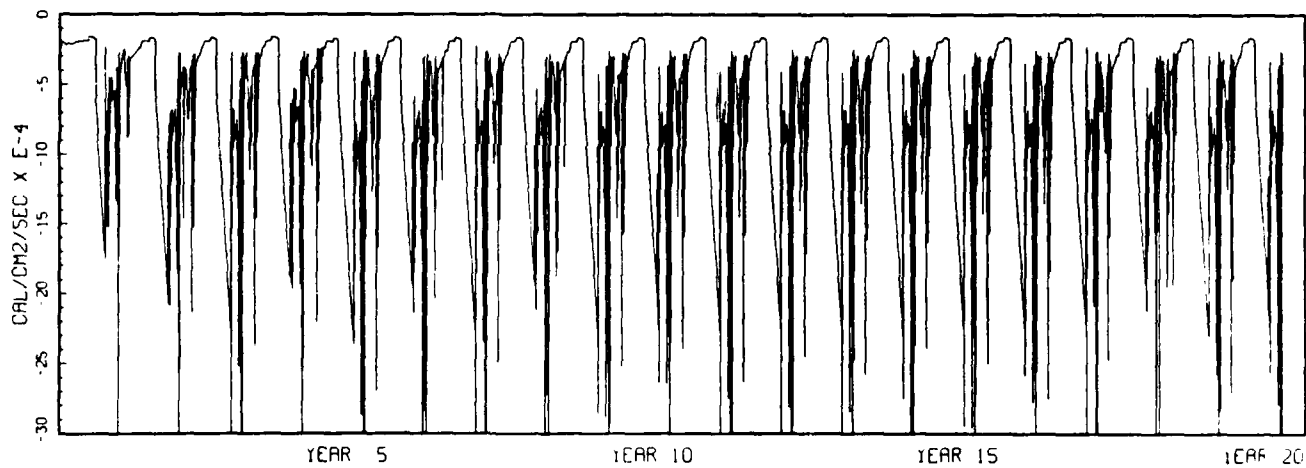
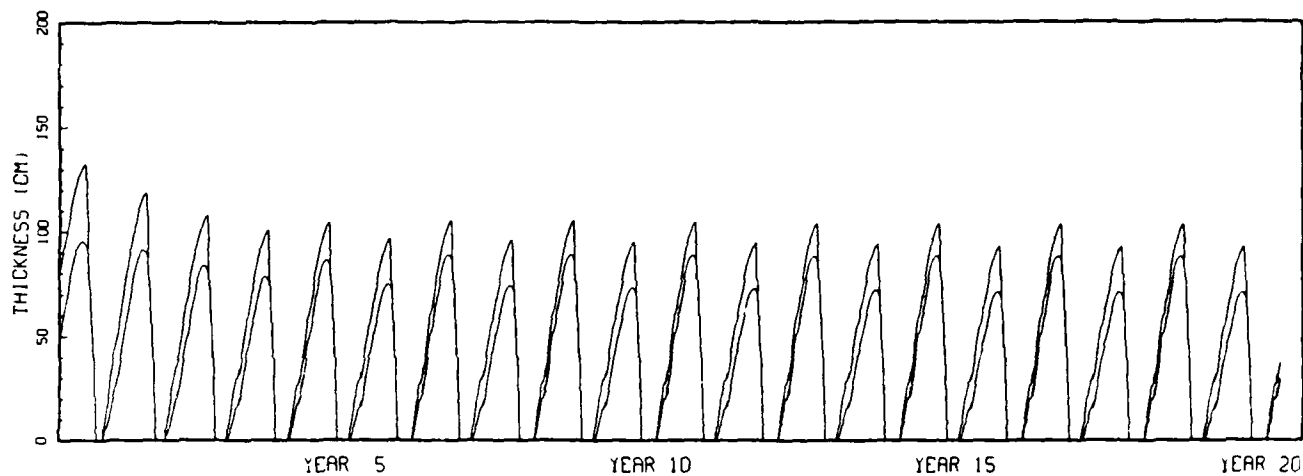


Figure 32. Ice thickness and oceanic heat flux values for a 20-year simulation of the VML model when $H_{\text{deep}} = 6.0 \text{ kcal/cm}^2/\text{year}$.

CASE 2

ICE & ICE+SNOW THICKNESS
VARIABLE MIXED LAYER



OCEANIC HEAT FLUX
VARIABLE MIXED LAYER

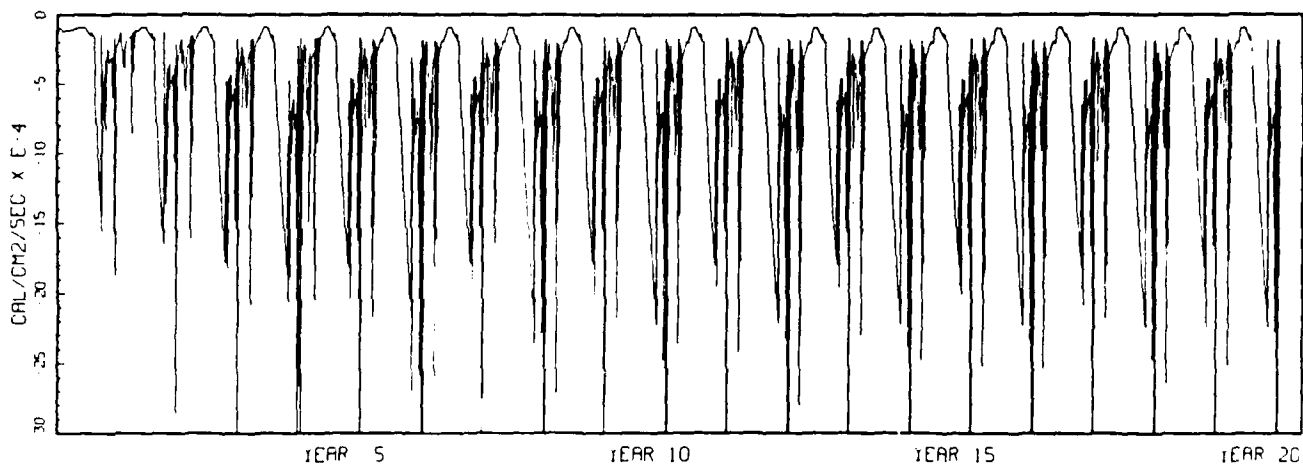


Figure 33. Ice thickness and oceanic heat flux values for a 20-year simulation of the VML model with brine pockets included (Case 2).

TEMPERATURE PROFILE PLOTS FOR MODEL RUN CASES 1F AND 2
YEAR NO. 1

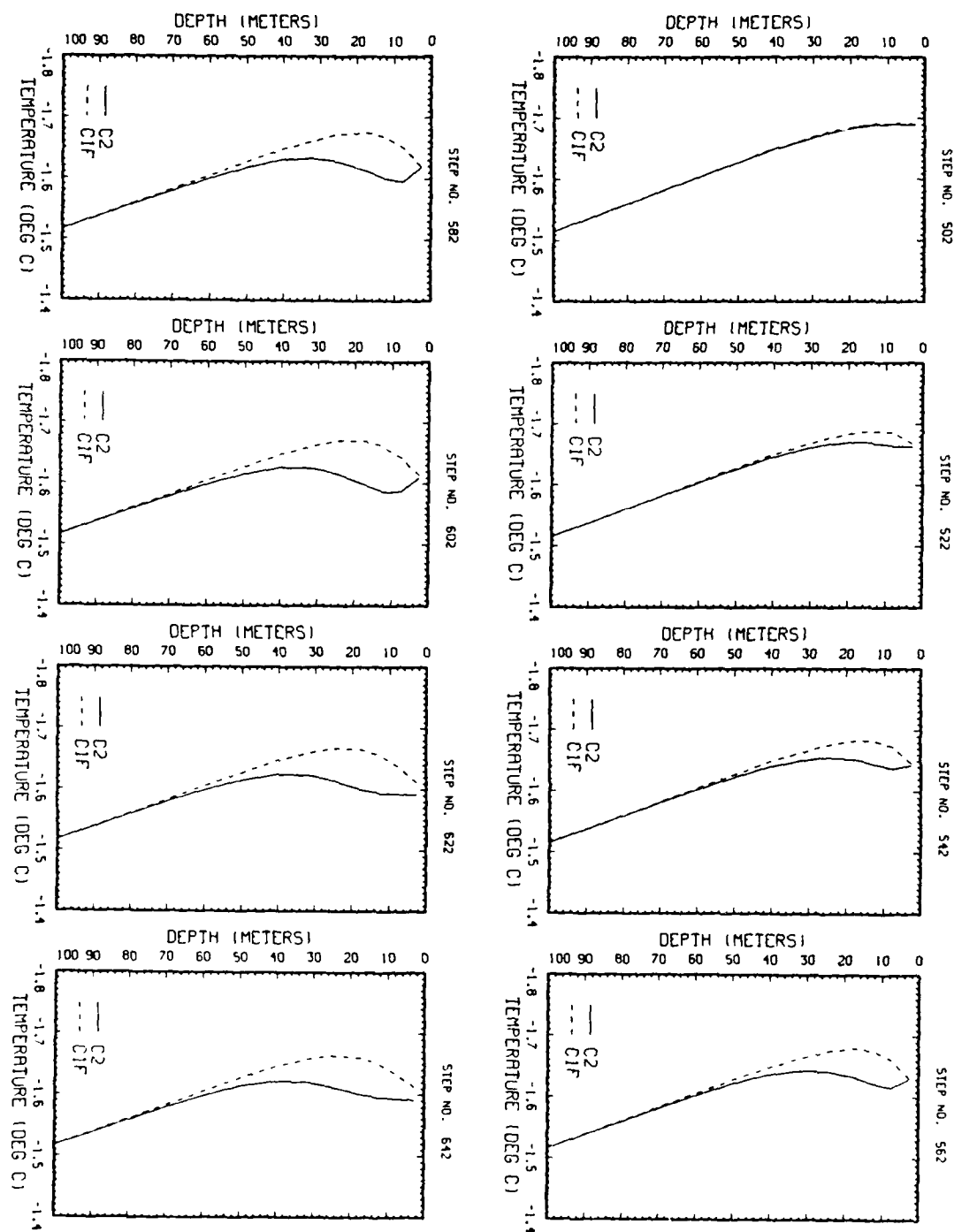


Figure 34. Comparison of temperature profiles for Case 1F and Case 2. Case 1F is without the brine pockets simulation, and Case 2 is with the brine pockets.

SOLAR RADIATION AIDJEX

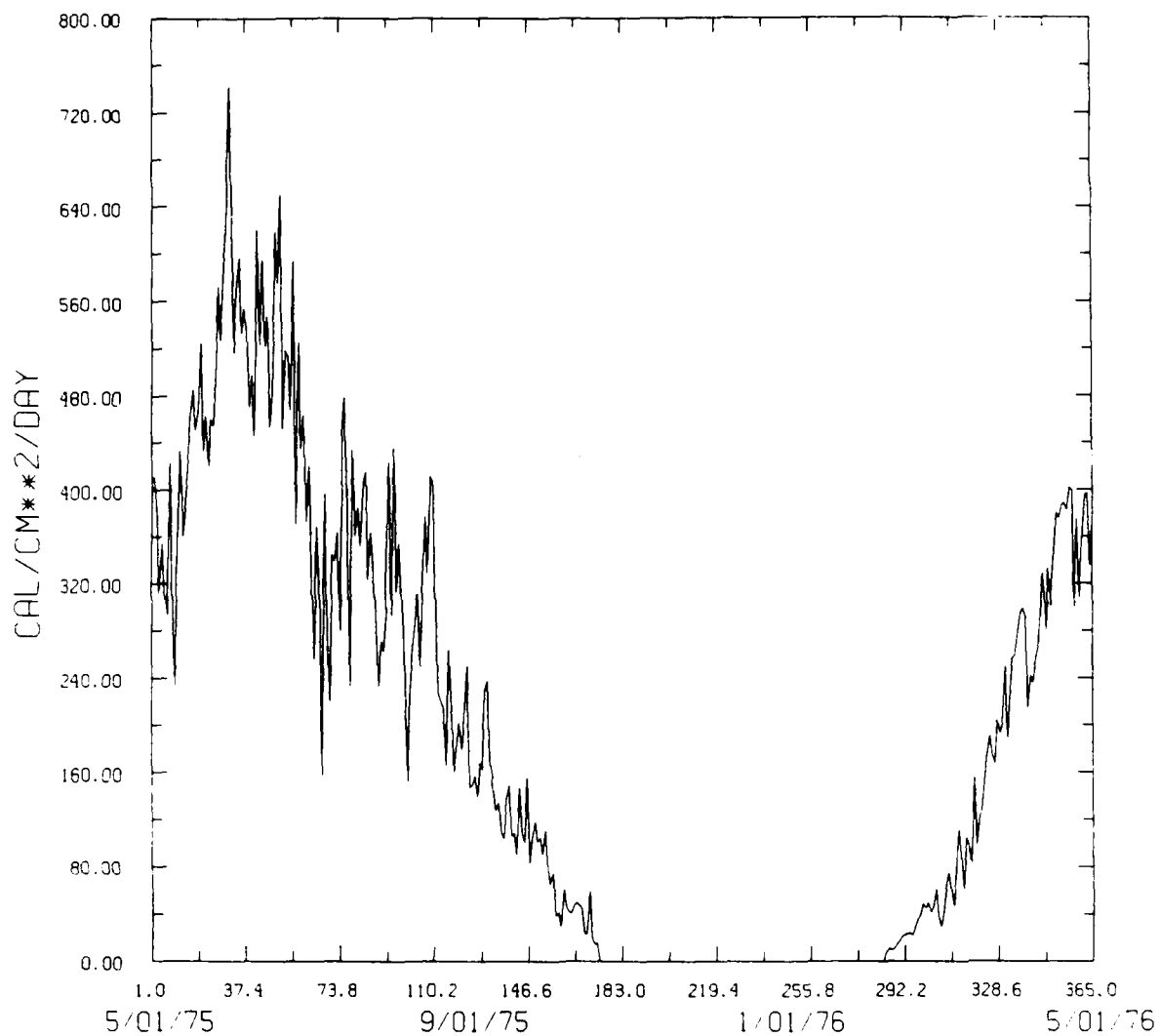


Figure 35. The daily totals of incoming solar radiation obtained during AIDJEX. These values are averages for the four camps from May 1, 1975, to April 29, 1976.

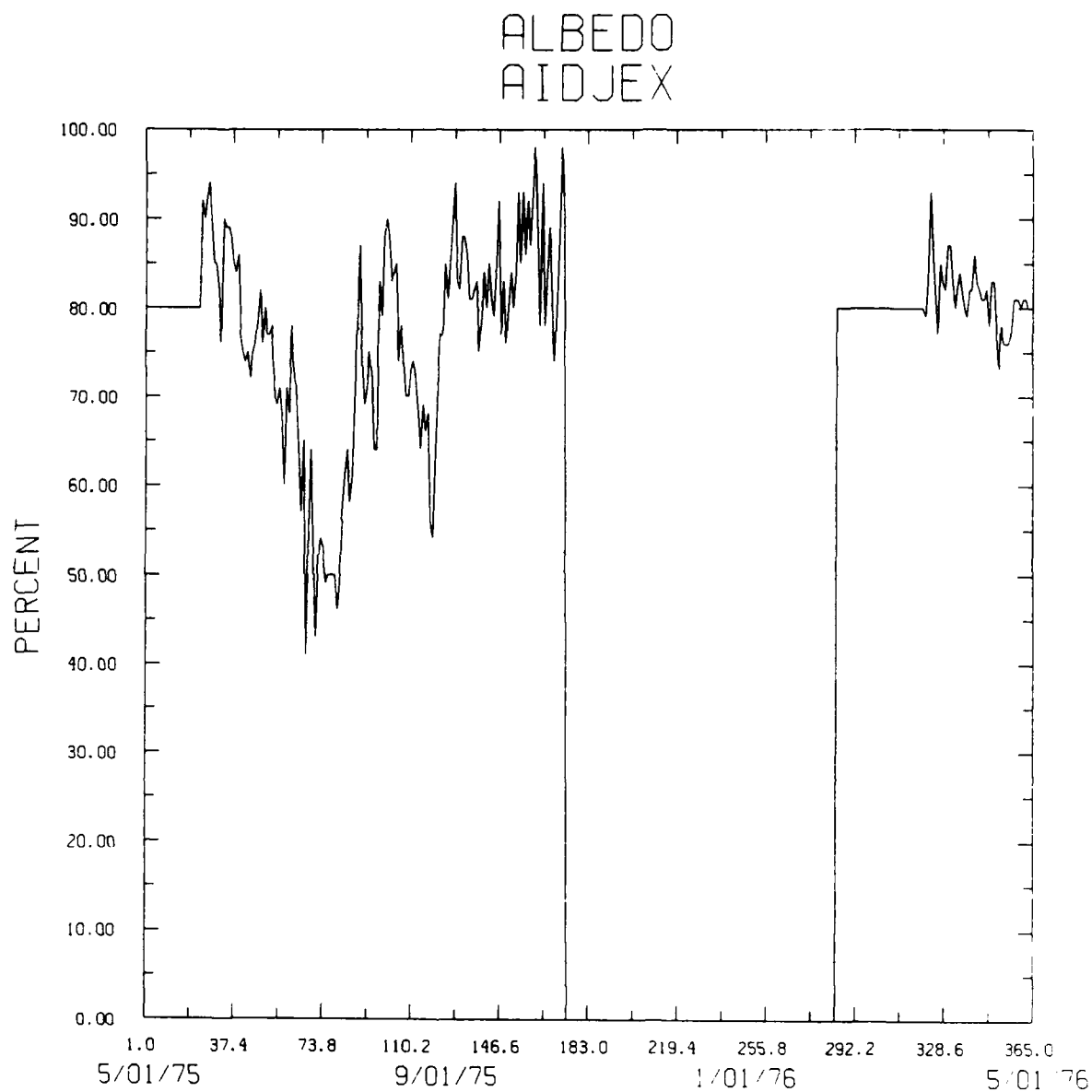


Figure 36. The daily average of the albedo obtained during AIDJEX. These values are averages for the four camps from May 1, 1975, to April 29, 1976.

LONGWAVE RADIATION AIDJEX

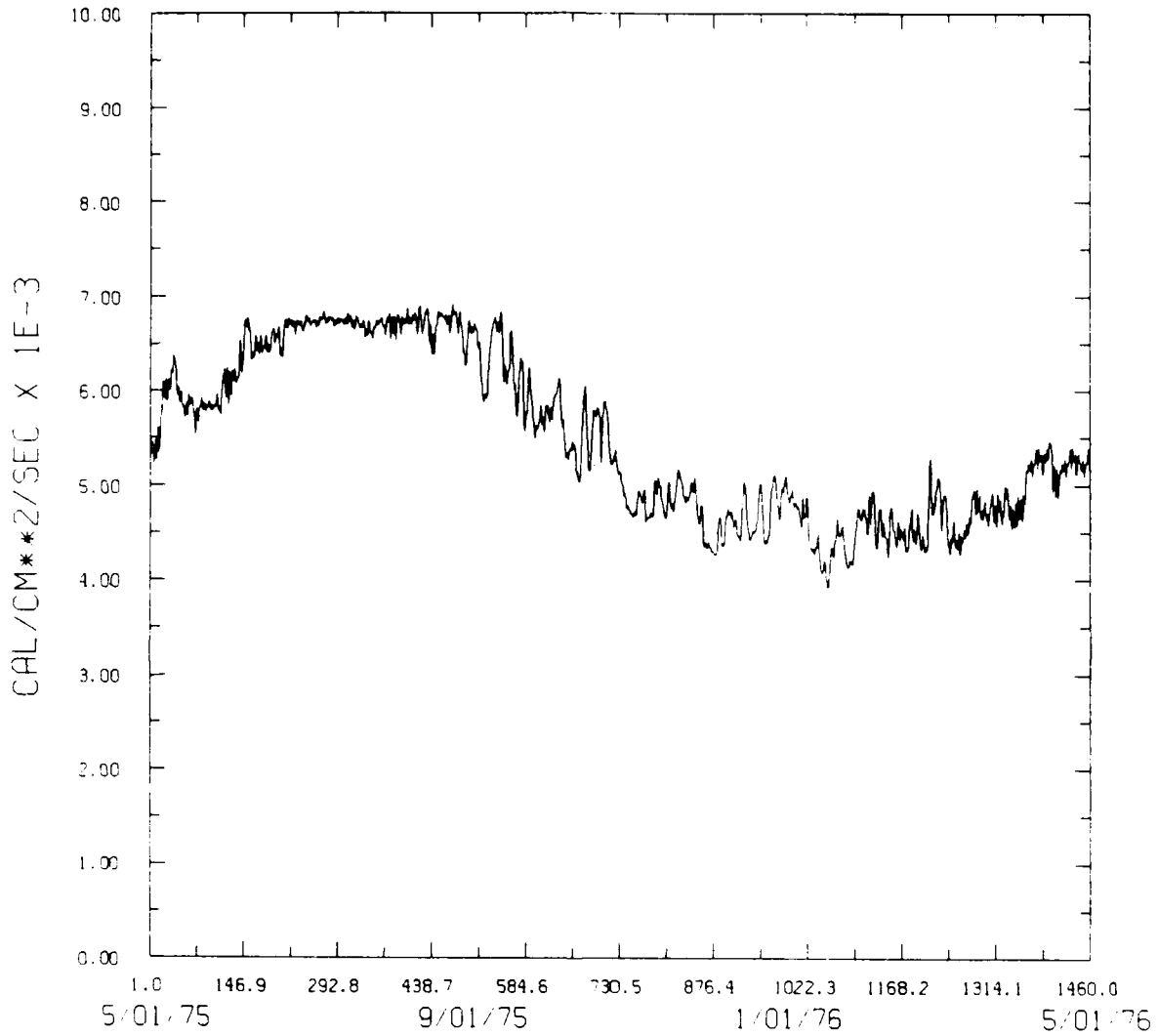


Figure 37. Longwave radiation fluxes from May 1, 1975, to April 29, 1976. These values were computed from the average air temperature obtained during AIDJEX, using the method shown in Parkinson and Washington (1979).

LATENT HEAT FLUX AIDJEX

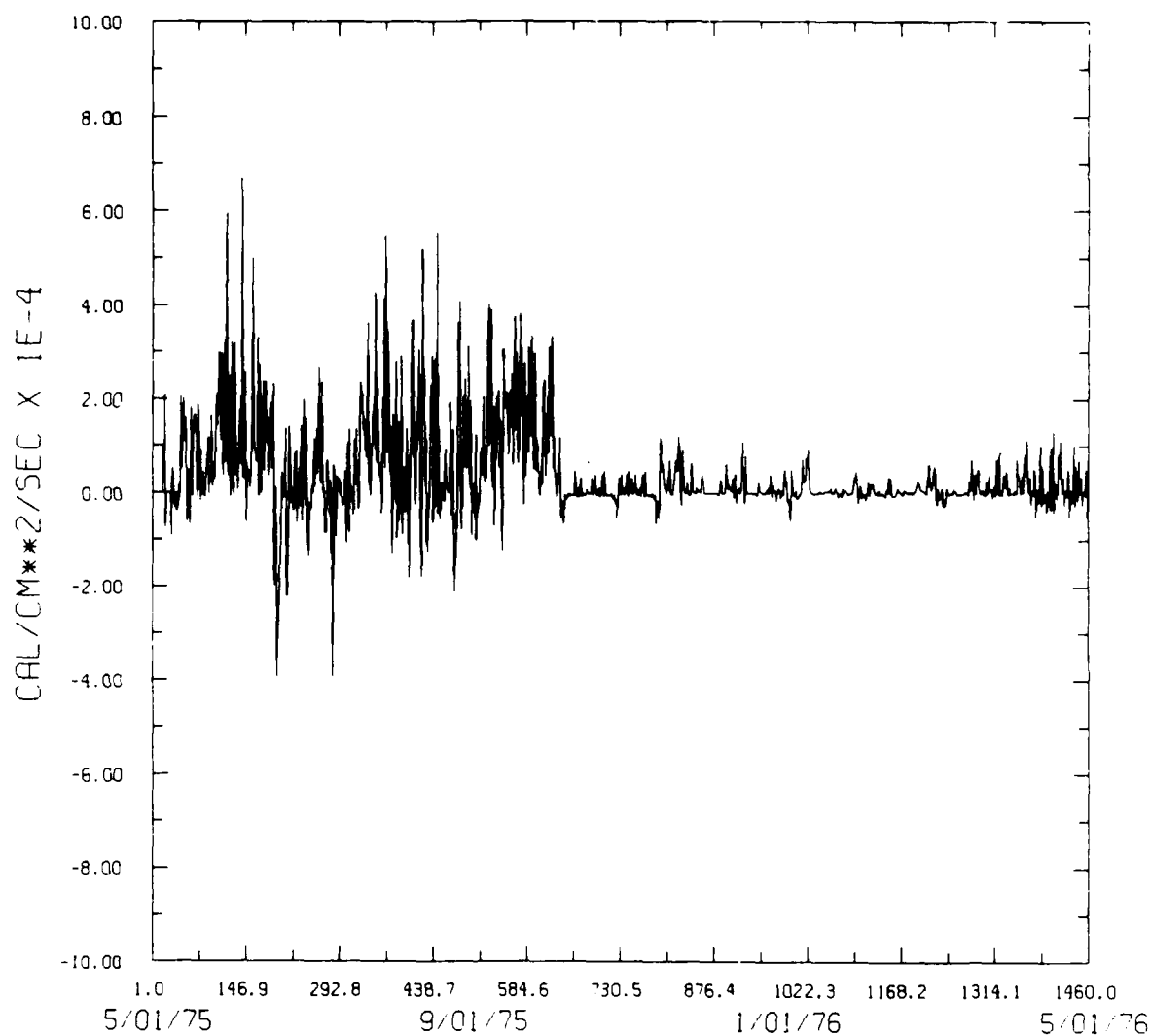


Figure 38. Latent heat fluxes from May 1, 1975, to April 29, 1976. These values are averages between the four camps of the AIDJEX experiment.

SENSIBLE HEAT FLUX AIDJEX

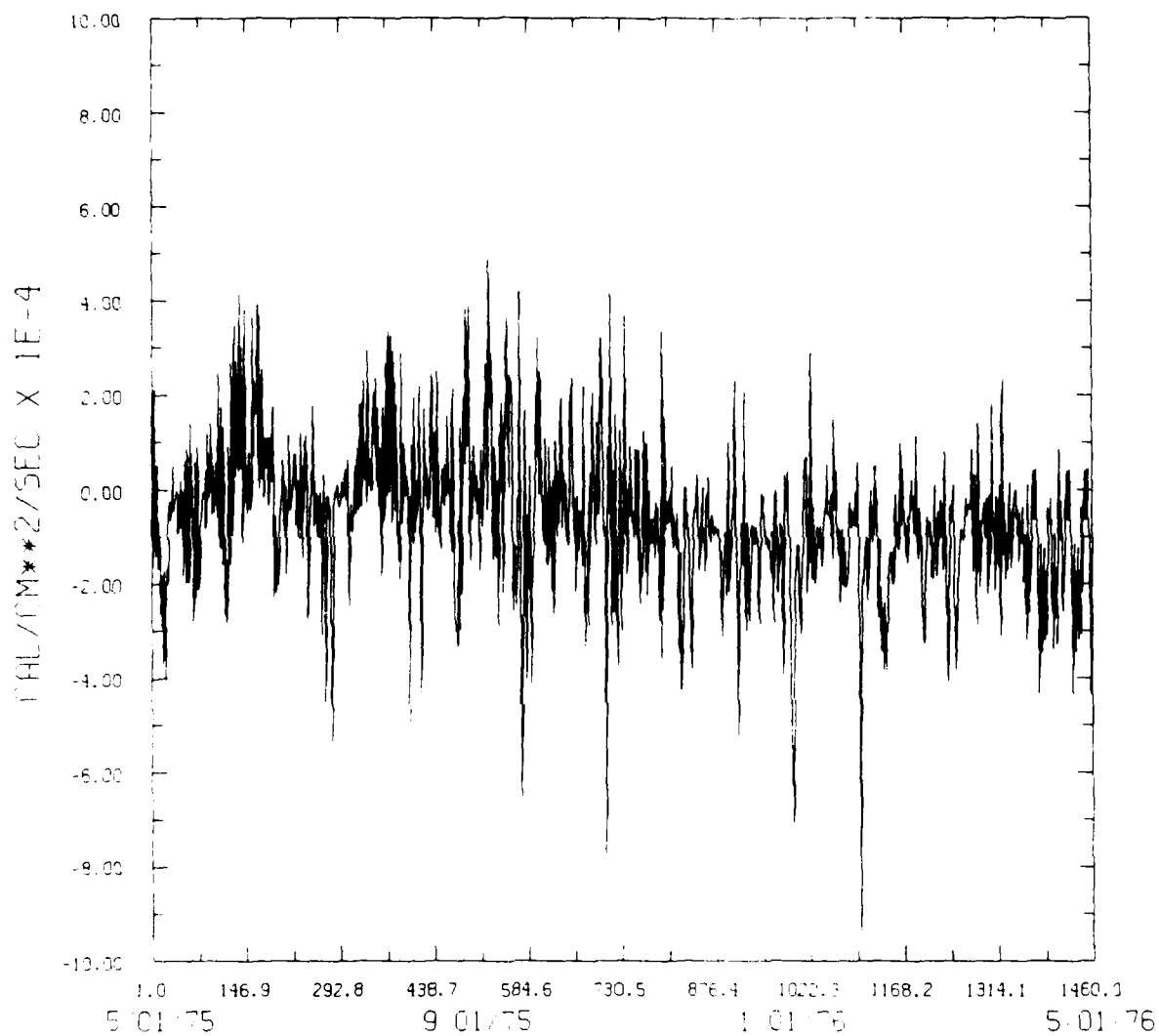


Figure 39. Sensible heat fluxes from May 1, 1975, to April 29, 1976. These values are averages between the four camps of the AIDJEX experiment.

WINDS U-COMPONENT AIDJEX

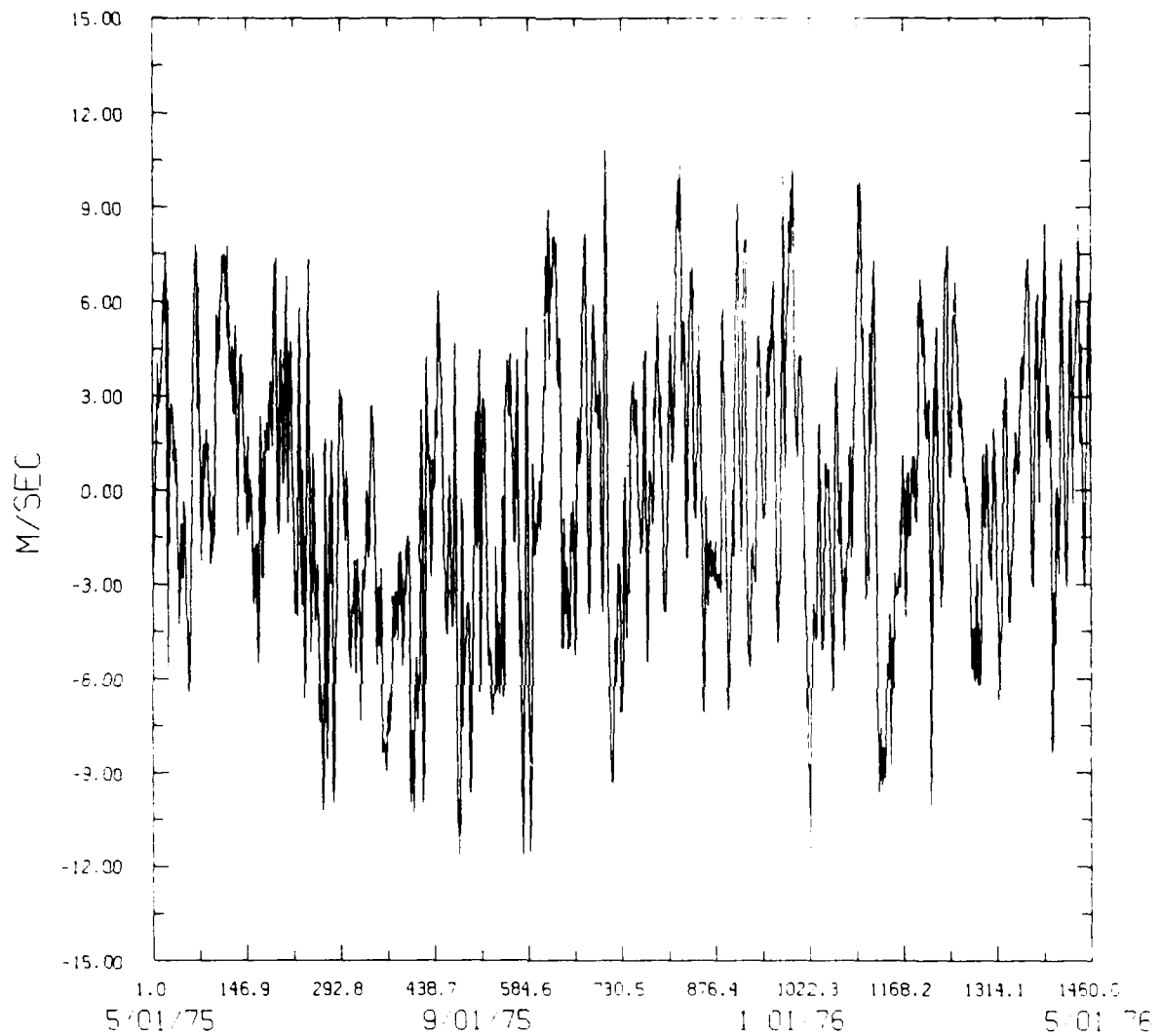


Figure 40. U-component of the winds from May 1, 1975, to April 29, 1976. These values are averages between the four camps of the AIDJEX experiment.

WINDS V-COMPONENT AIDJEX

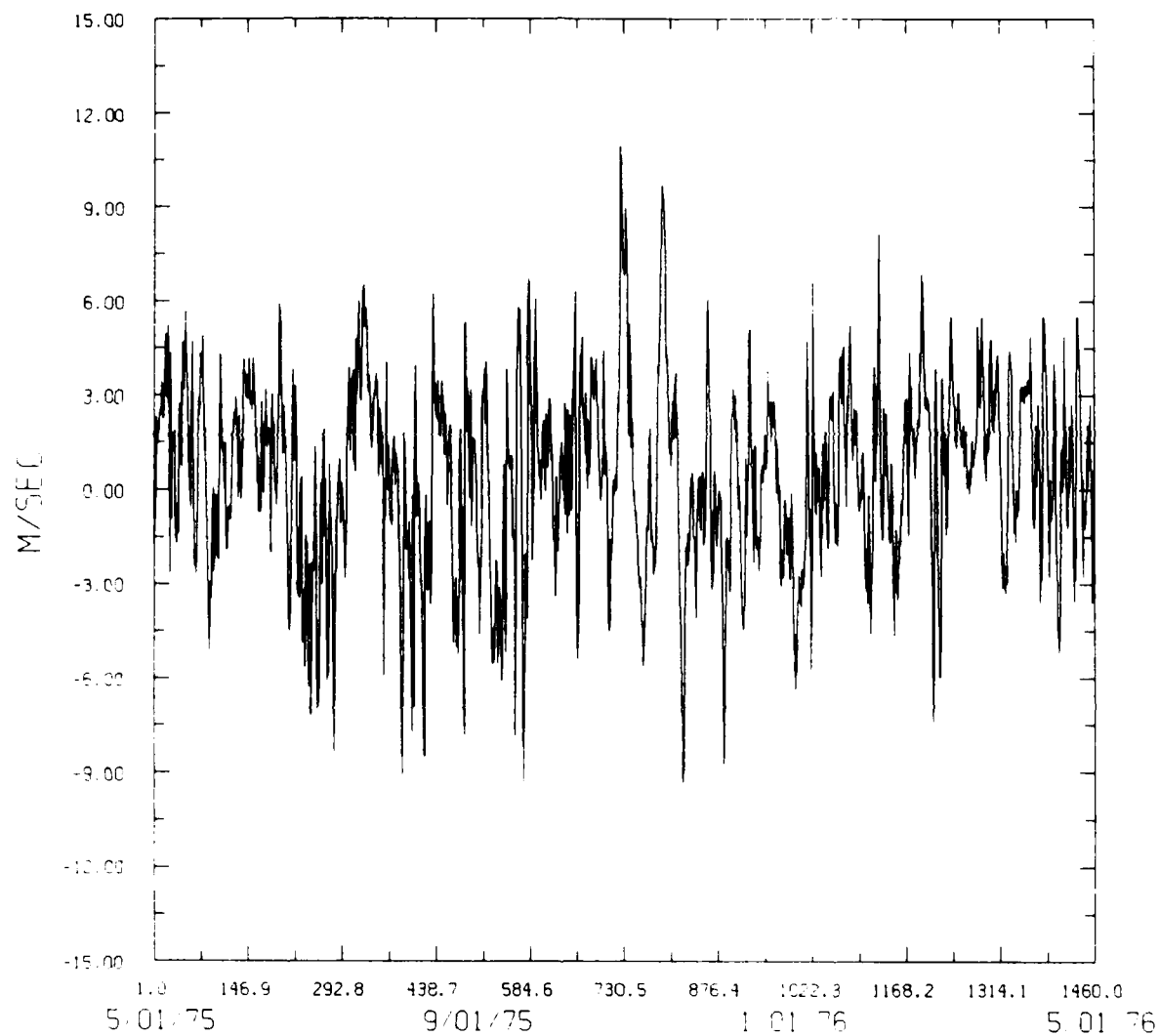


Figure 41. V-component of the winds from May 1, 1975, to April 29, 1976. These values are averages between the four camps of the AIDJEX experiment.

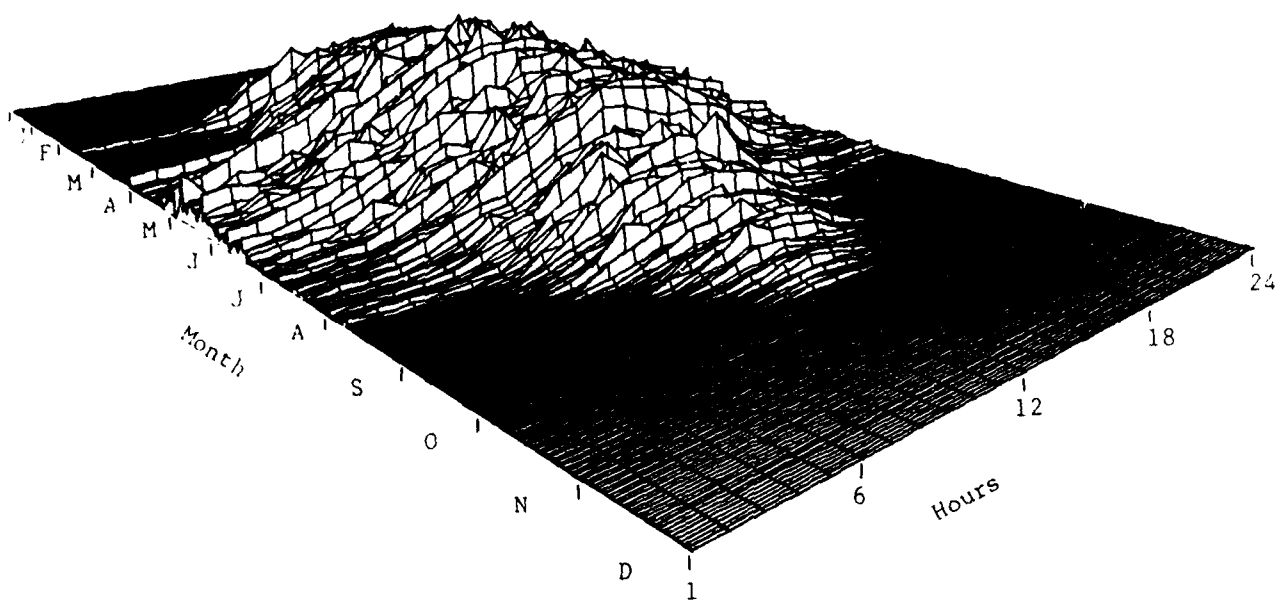


Figure 42. Three-dimensional perspective of the flux of short-wave radiation over one year. (From Pautzke and Hornof, 1978)

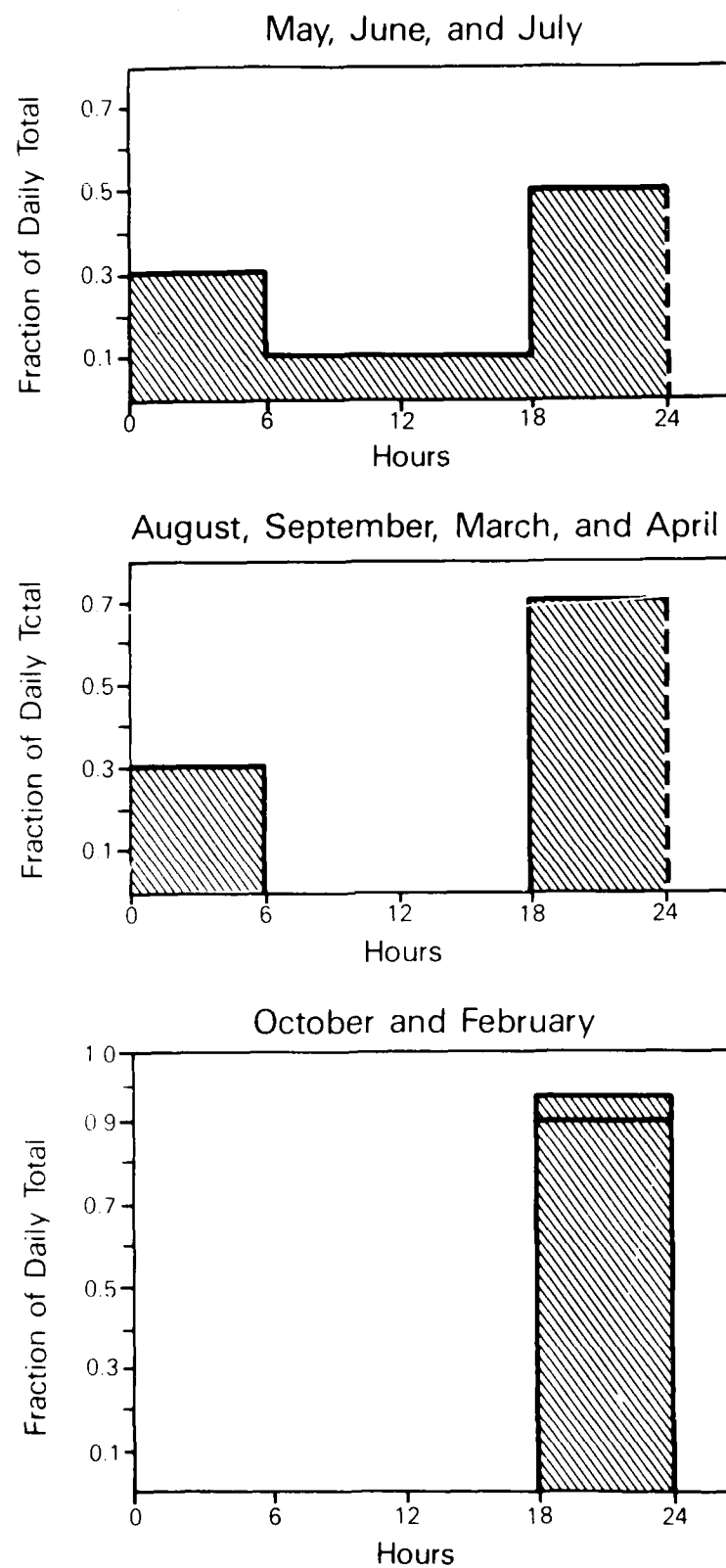


Figure 43. The diurnal cycle assumed for the incoming solar radiation, for use in the VML simulation with AIDJEX data (Case 3).

DIURNAL CYCLE

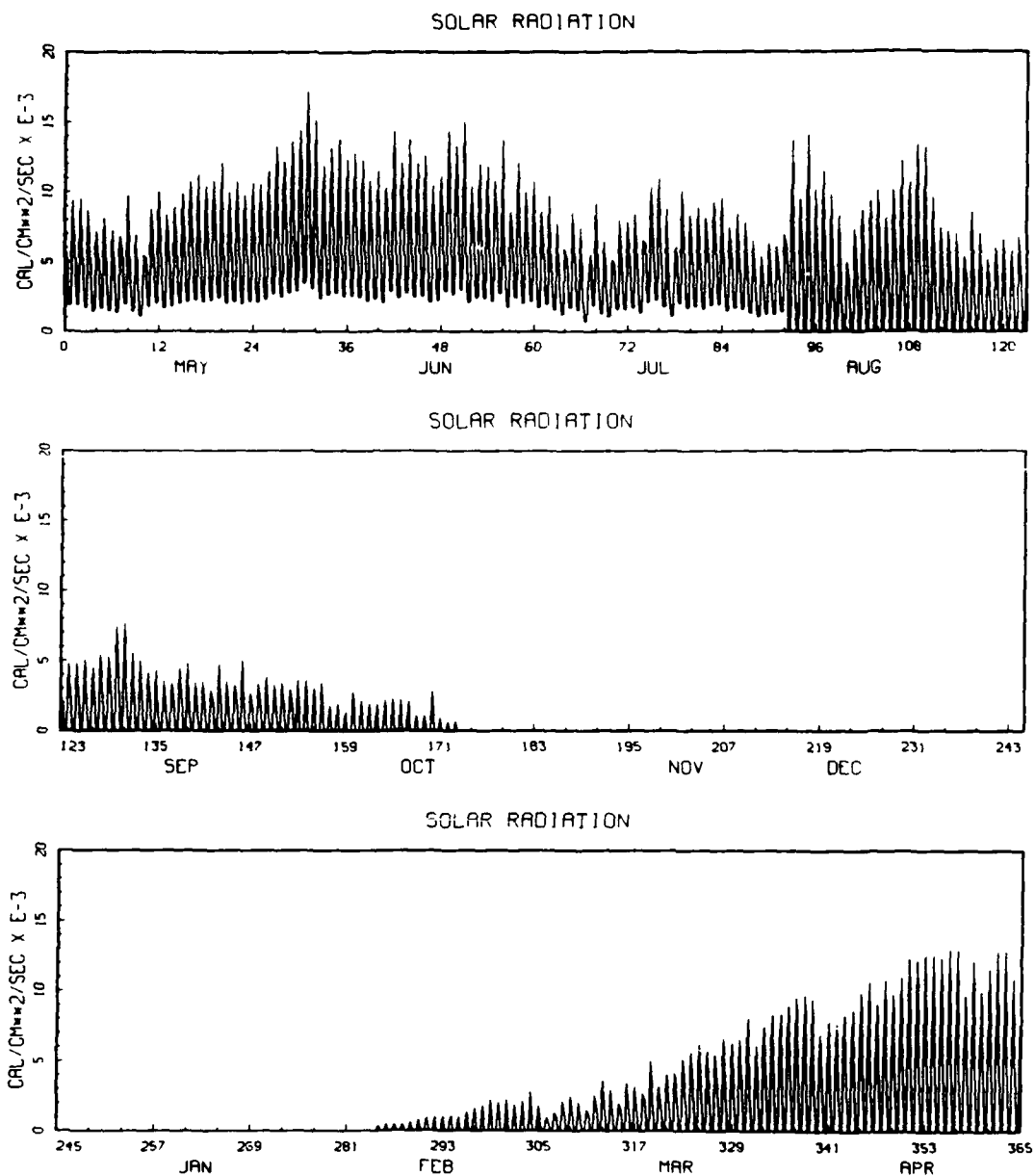


Figure 44. The solar radiation field which results when the diurnal cycle shown in Figure 43 is applied to the daily total solar radiation shown in Figure 35.

NO CYCLE

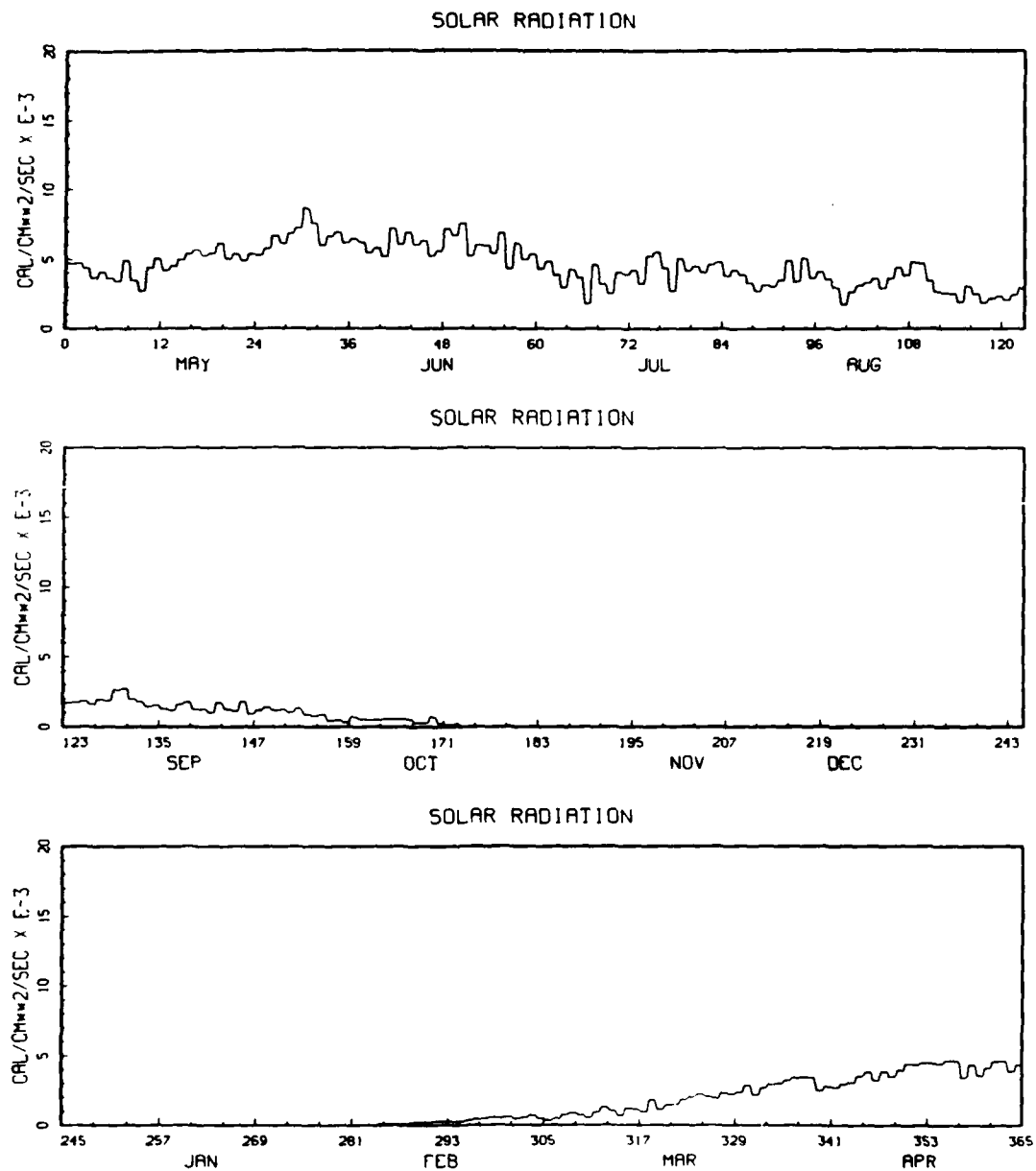


Figure 45. The solar radiation field that results when the solar flux is assumed constant throughout the day and applied to the daily total solar radiation shown in Figure 35.

DIURNAL CYCLE

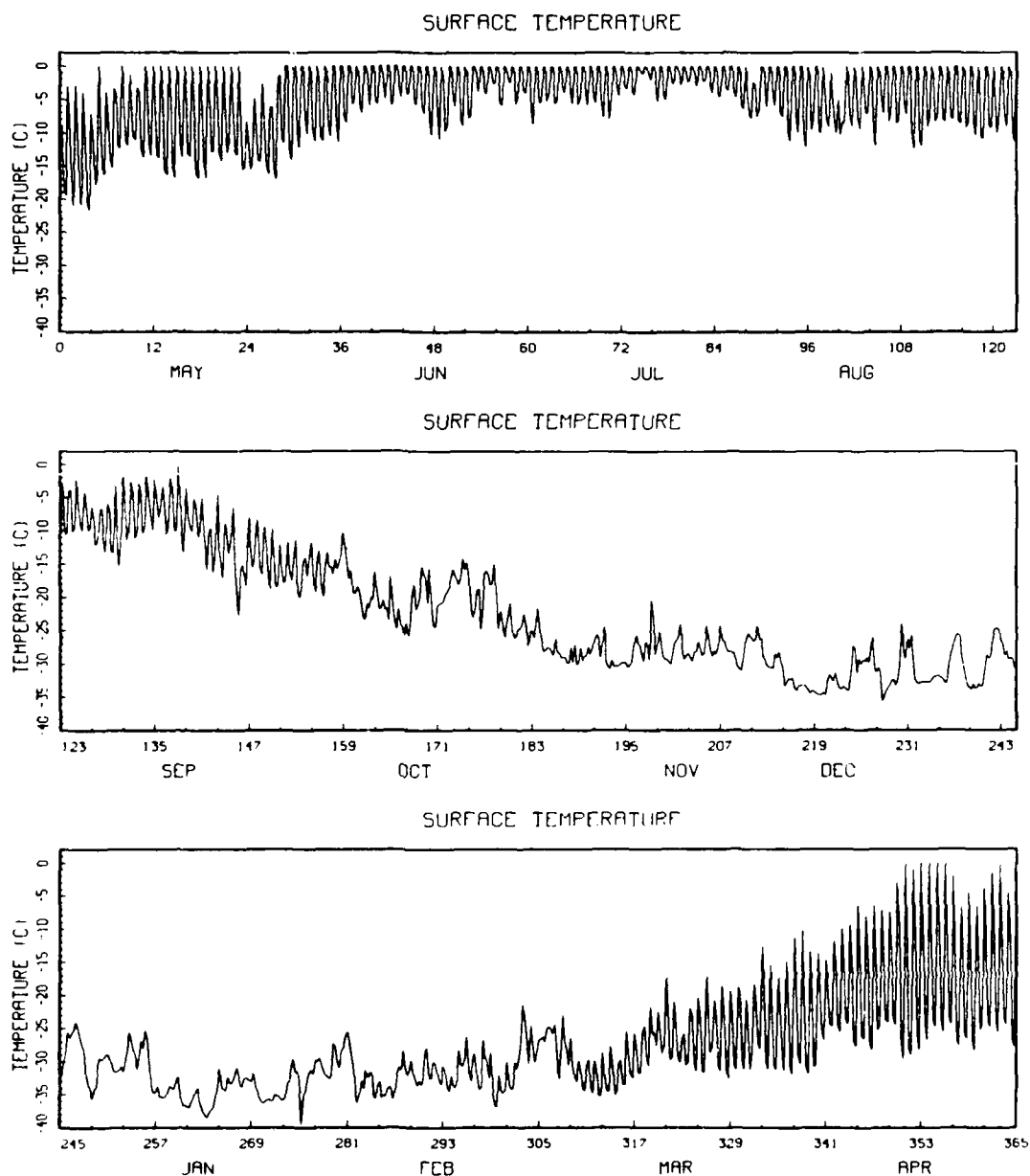


Figure 46. A time series of the surface temperature computed by the VML model, when the diurnal cycle is assumed for the solar flux.

NO DIURNAL CYCLE

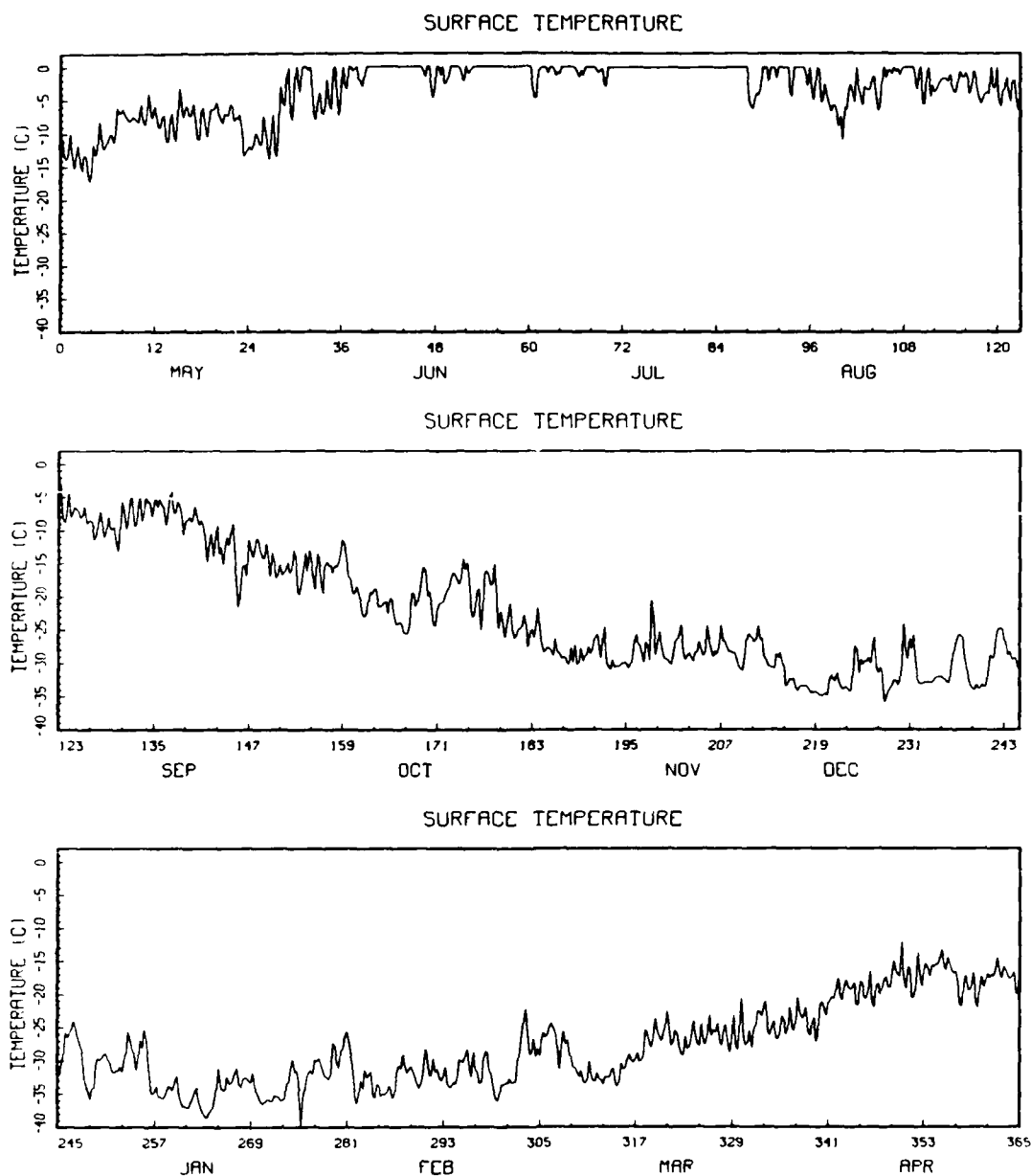


Figure 47. A time series of the surface temperature computed by the VML model when the constant daily flux is assumed for the solar flux.

DIURNAL CYCLE

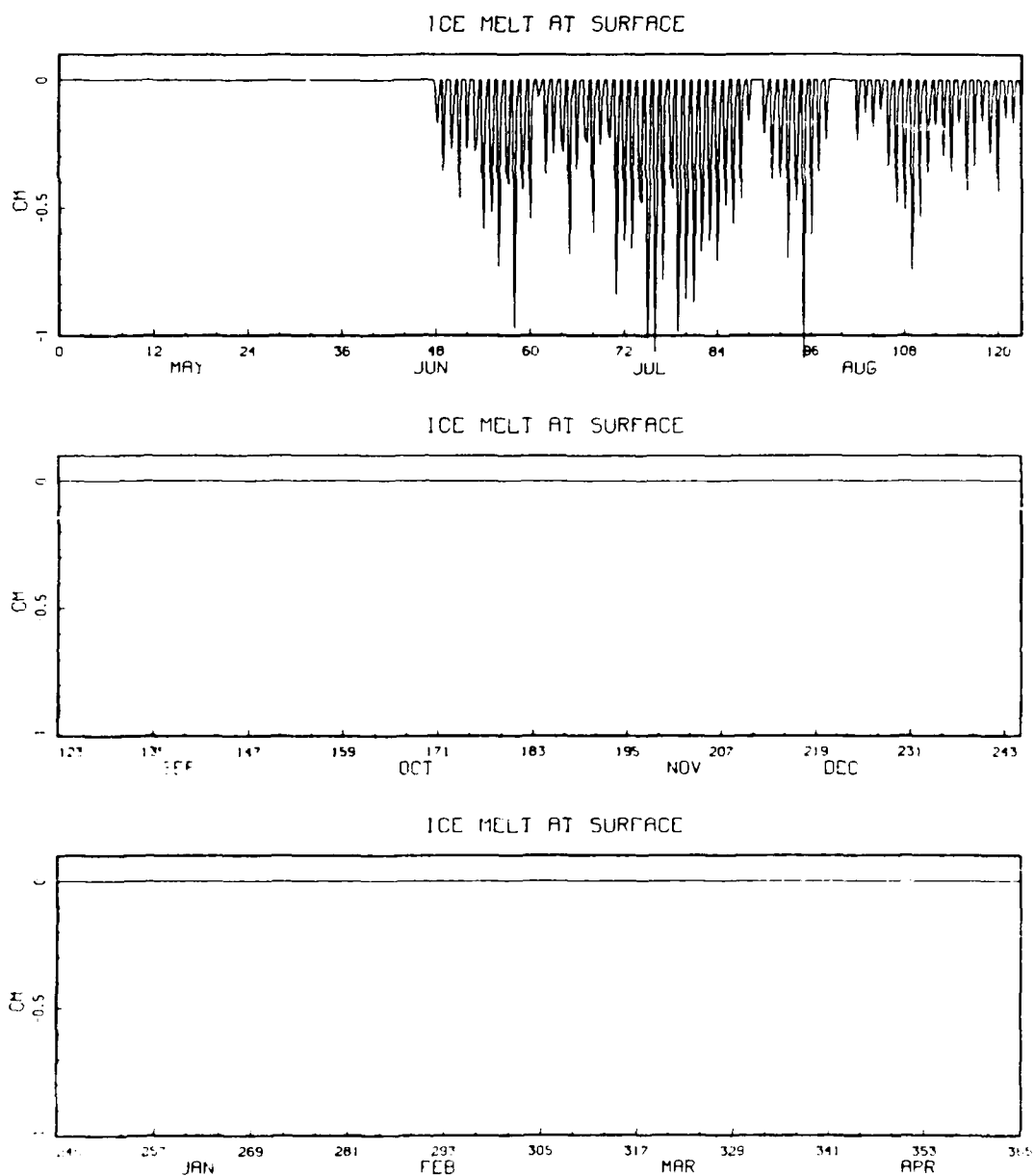


Figure 48. Ice melt at the surface of the ice when the diurnal cycle is assumed.

NO DIURNAL CYCLE

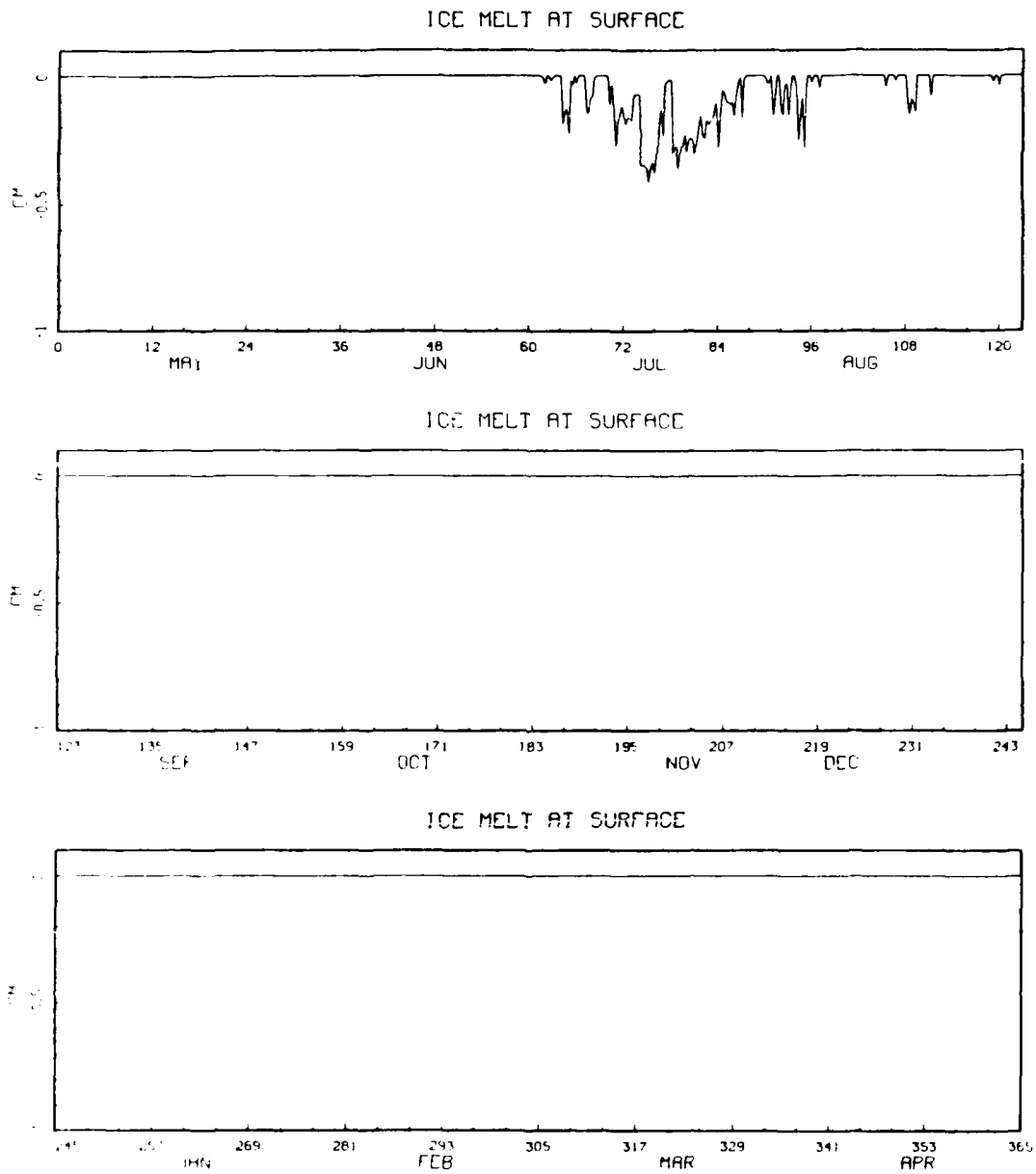


Figure 49. Ice melt at the surface of the ice when no diurnal cycle is assumed.

DIURNAL CYCLE

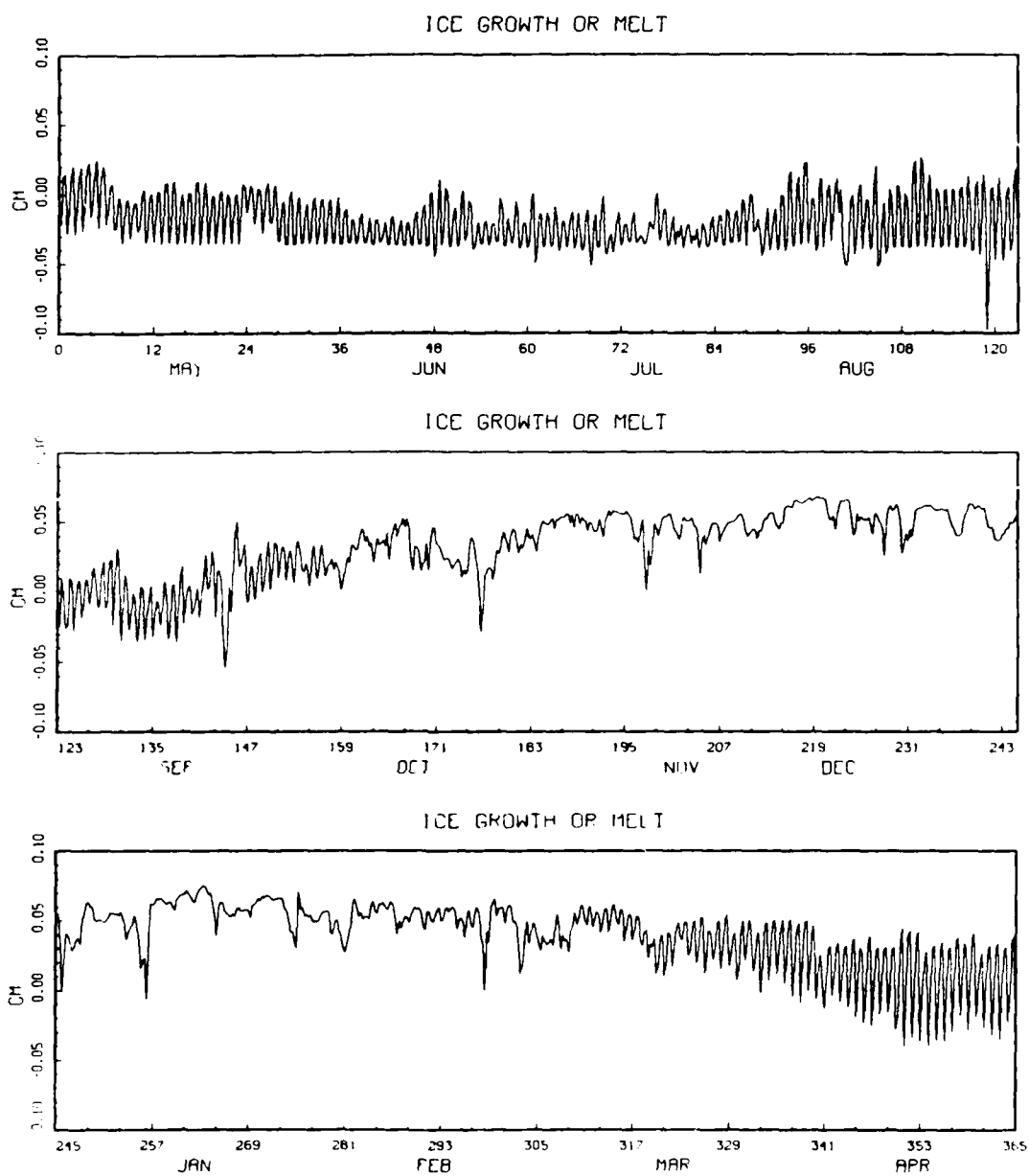


Figure 50. Ice growth or melt at the bottom of the ice when the diurnal cycle is assumed.

NO DIURNAL CYCLE

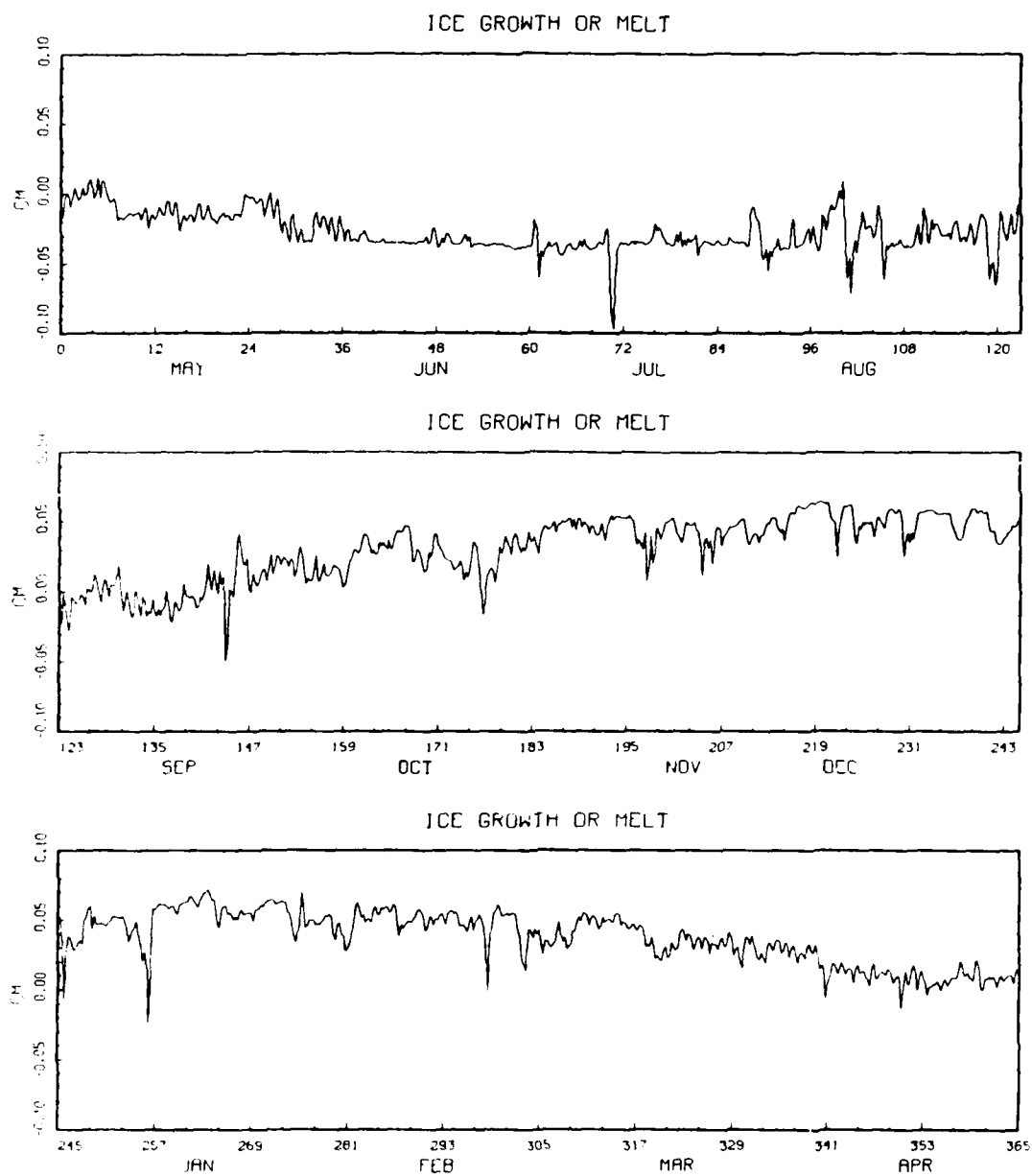


Figure 51. Ice growth or melt at the bottom of the ice when no diurnal cycle is assumed.

DIURNAL CYCLE

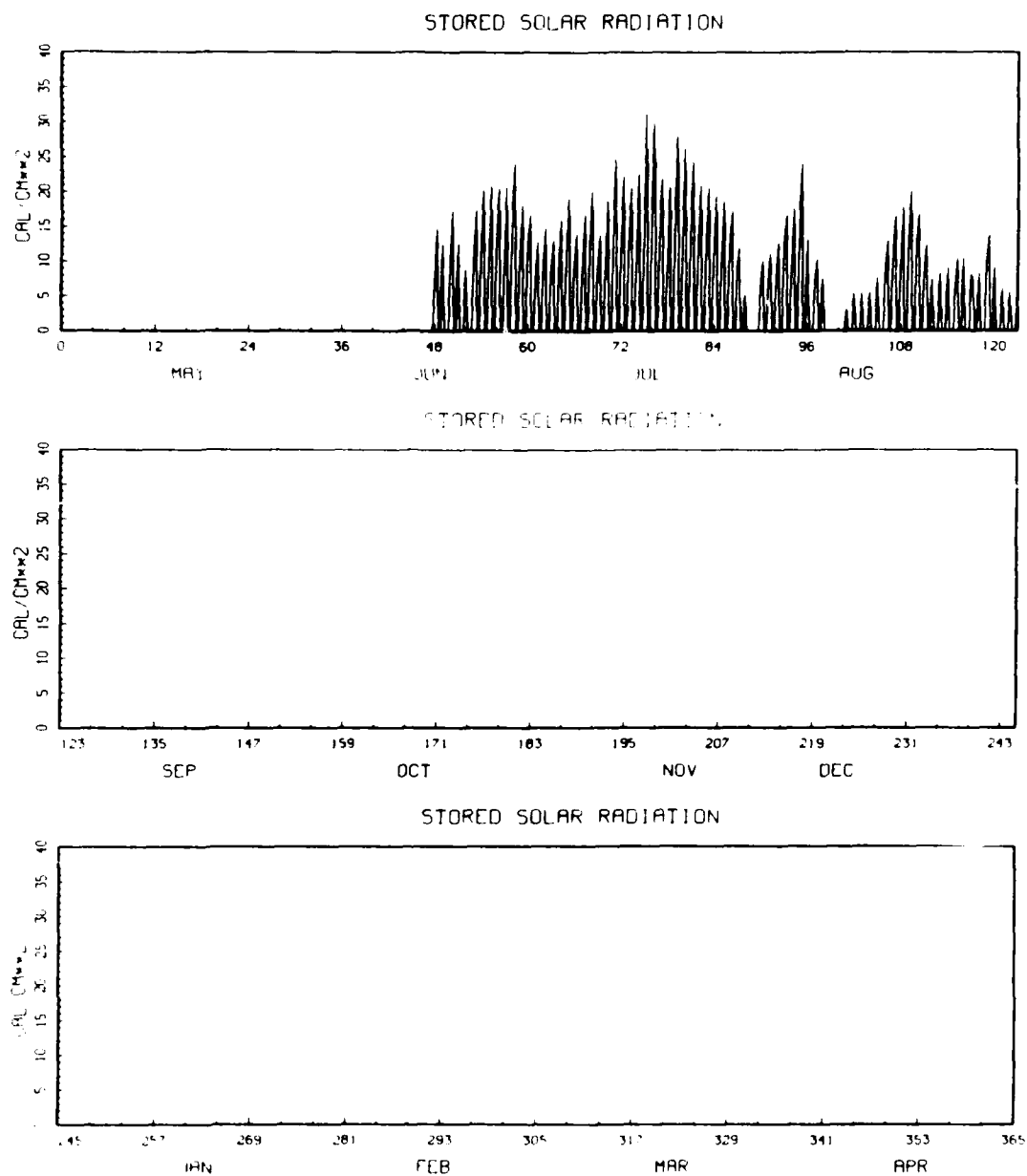


Figure 52. Heat stored in the brine pocket heat reservoir when the diurnal cycle is assumed.

NO DIURNAL CYCLE

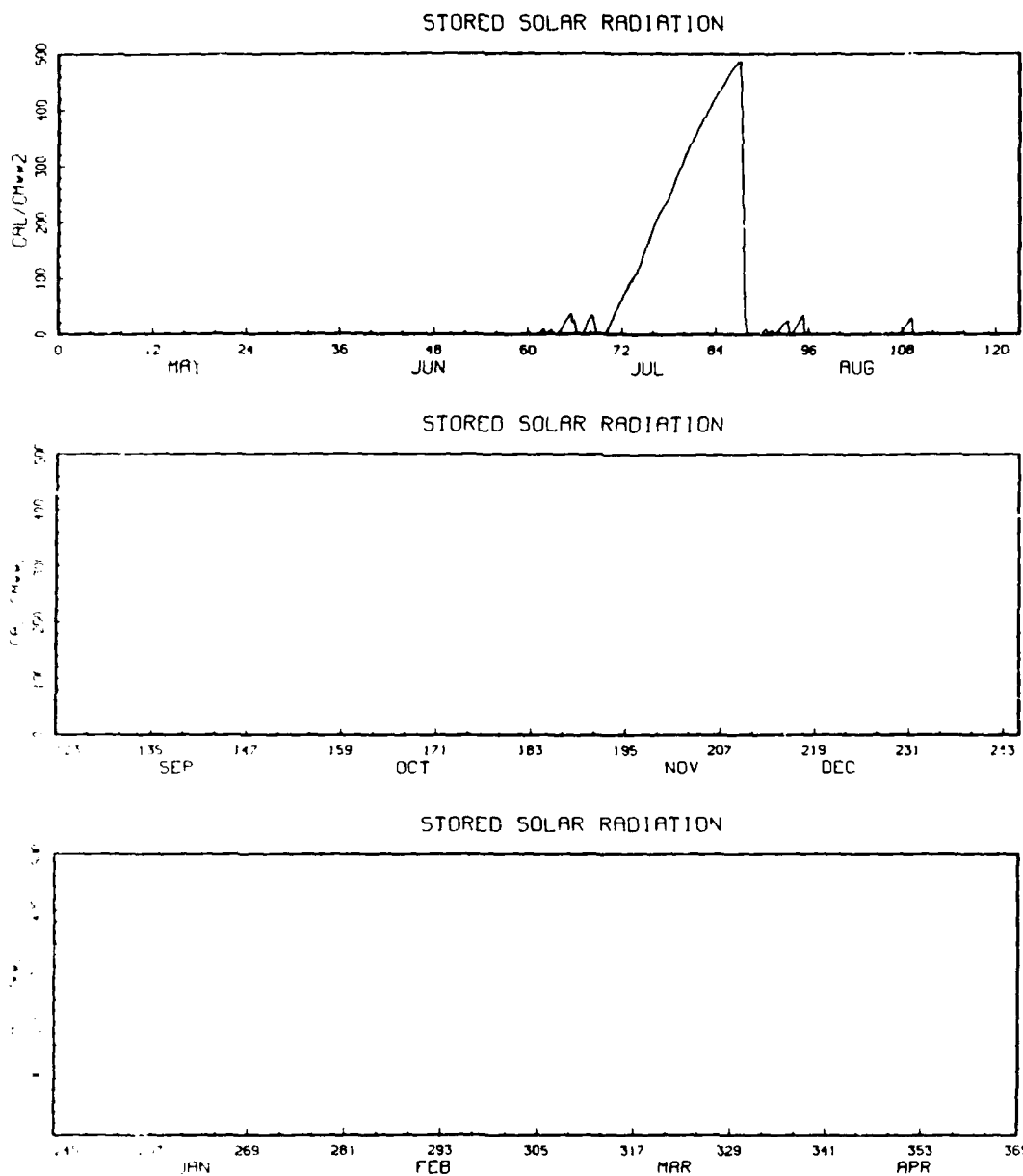
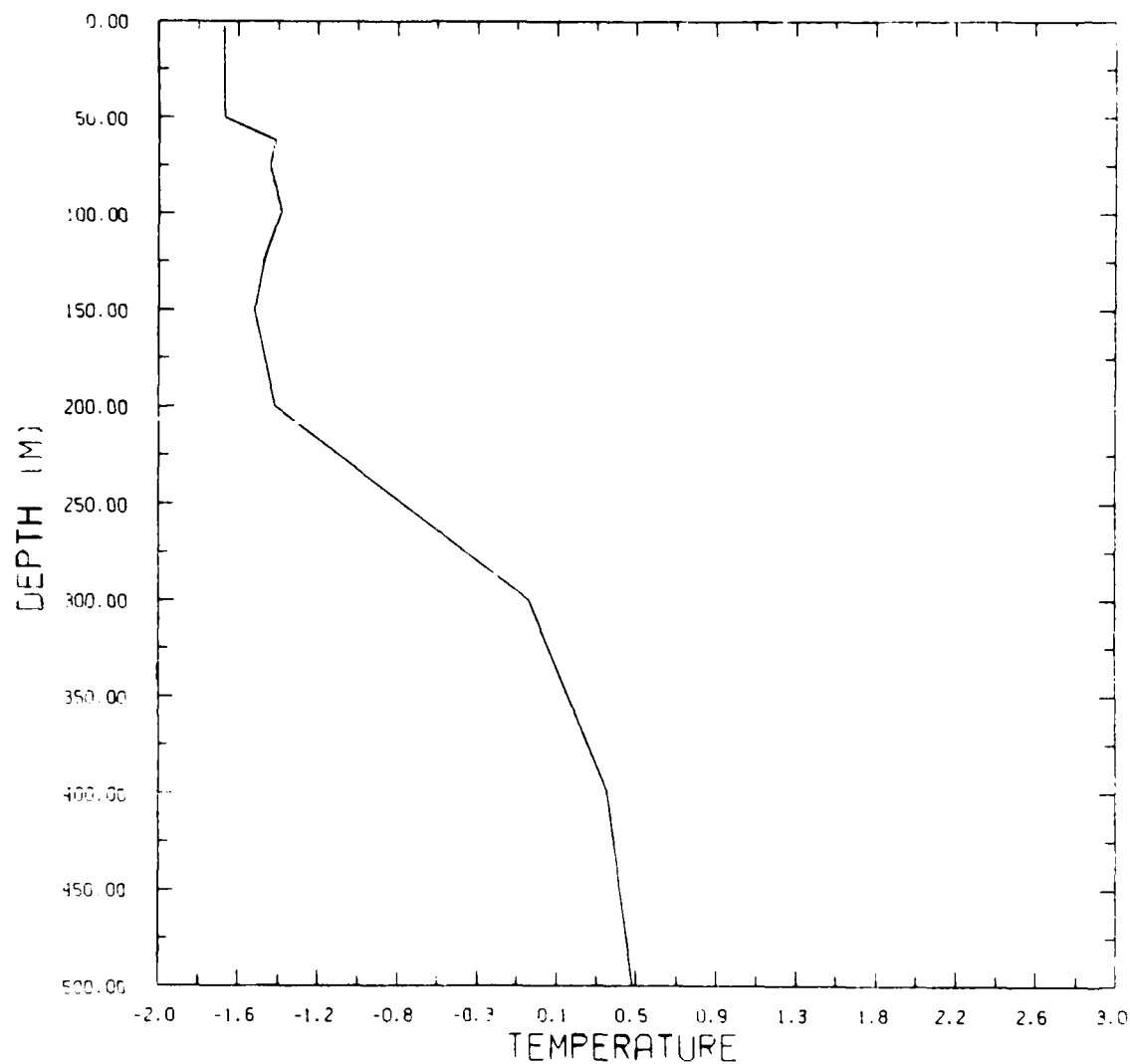


Figure 53. Heat stored in the brine pocket heat reservoir when no diurnal cycle is assumed.

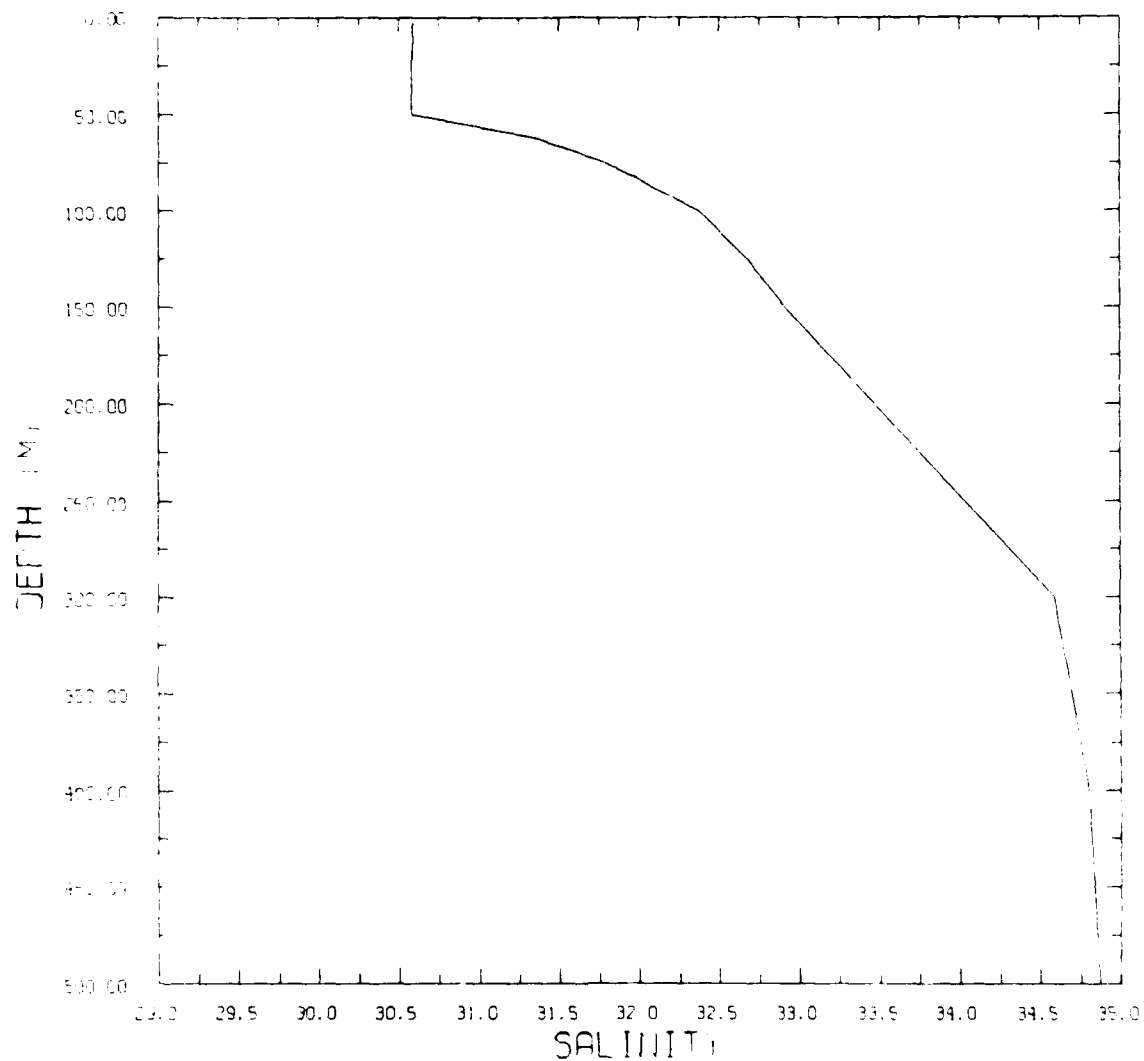
MODEL PROFILES
TEMP. STEP 1



YEAR NO. 1
VARIABLE MIXED LAYER
AIDJEX CASE 3

Figure 54. Temperature profile from May 10, 1975, camp Blue Fox. This profile is used to initialize the VML model.

MODEL PROFILES SALINITY STEP 1



YEAR NO. 1
VARIABLE MIXED LAYER
ADJEX CASE 3

Figure 55. Salinity profile from May 10, 1975, camp Blue Fox. This profile is used to initialize the VML model.

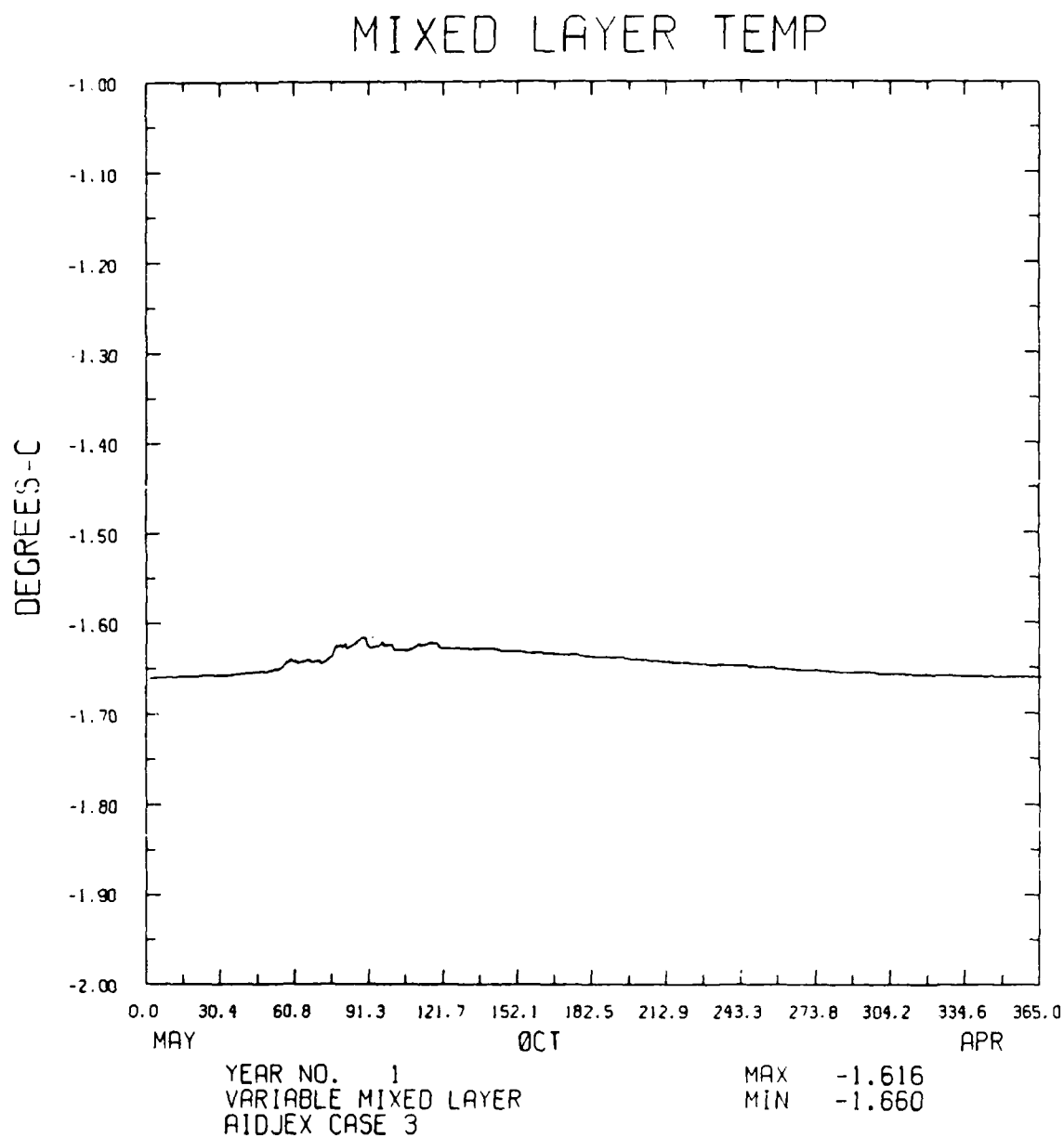


Figure 56. Mixed-layer temperature for a 1-year simulation of the VML model forced with AIDJEX forcing data. Simulation runs from May 1 to April 29.

STATION BLUEFOX TEMPERATURE

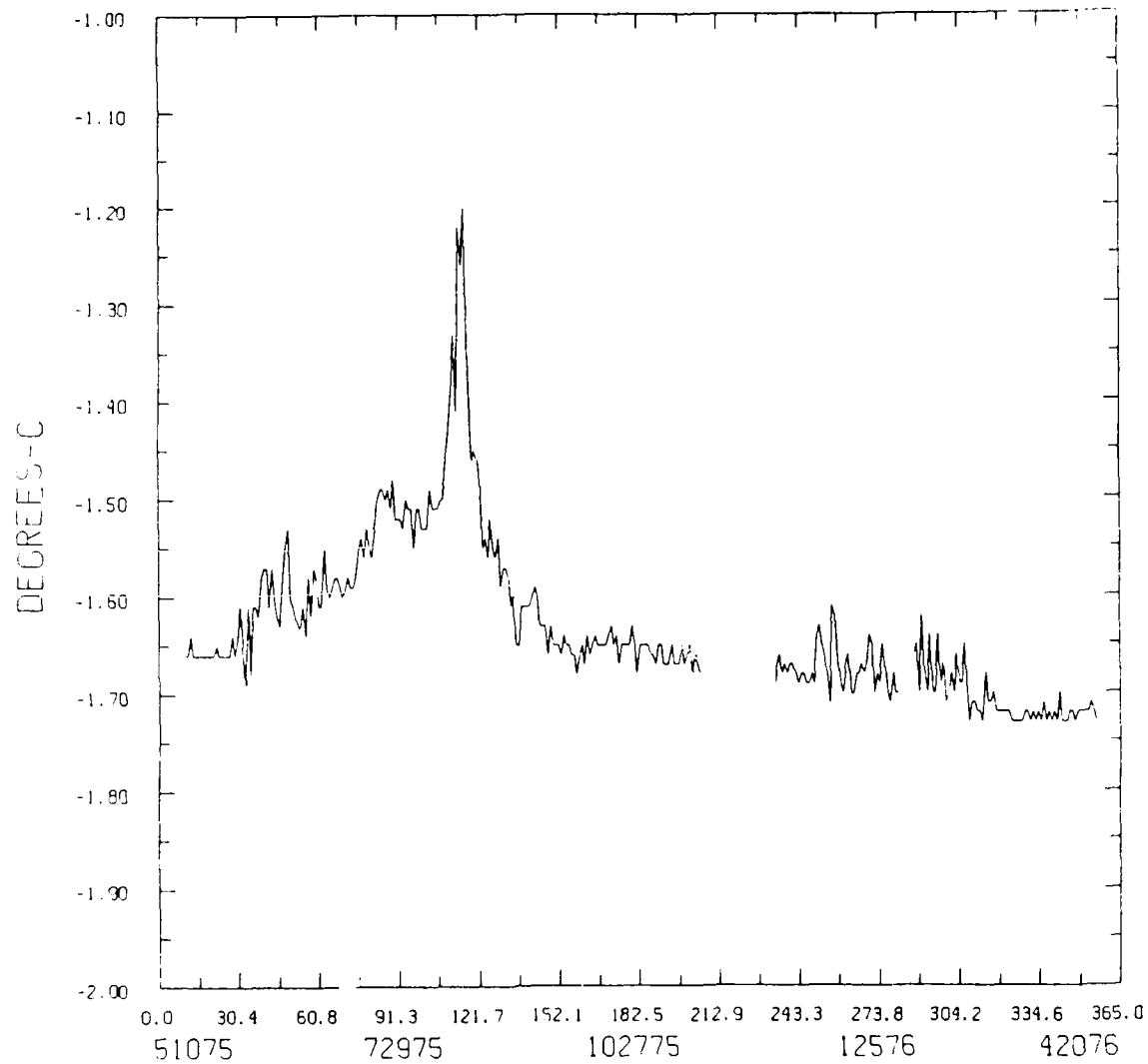


Figure 57. Mixed-layer temperature measured at camp Blue Fox from May 10, 1975, to April 20, 1976.

STATION SNOWBIRD TEMPERATURE

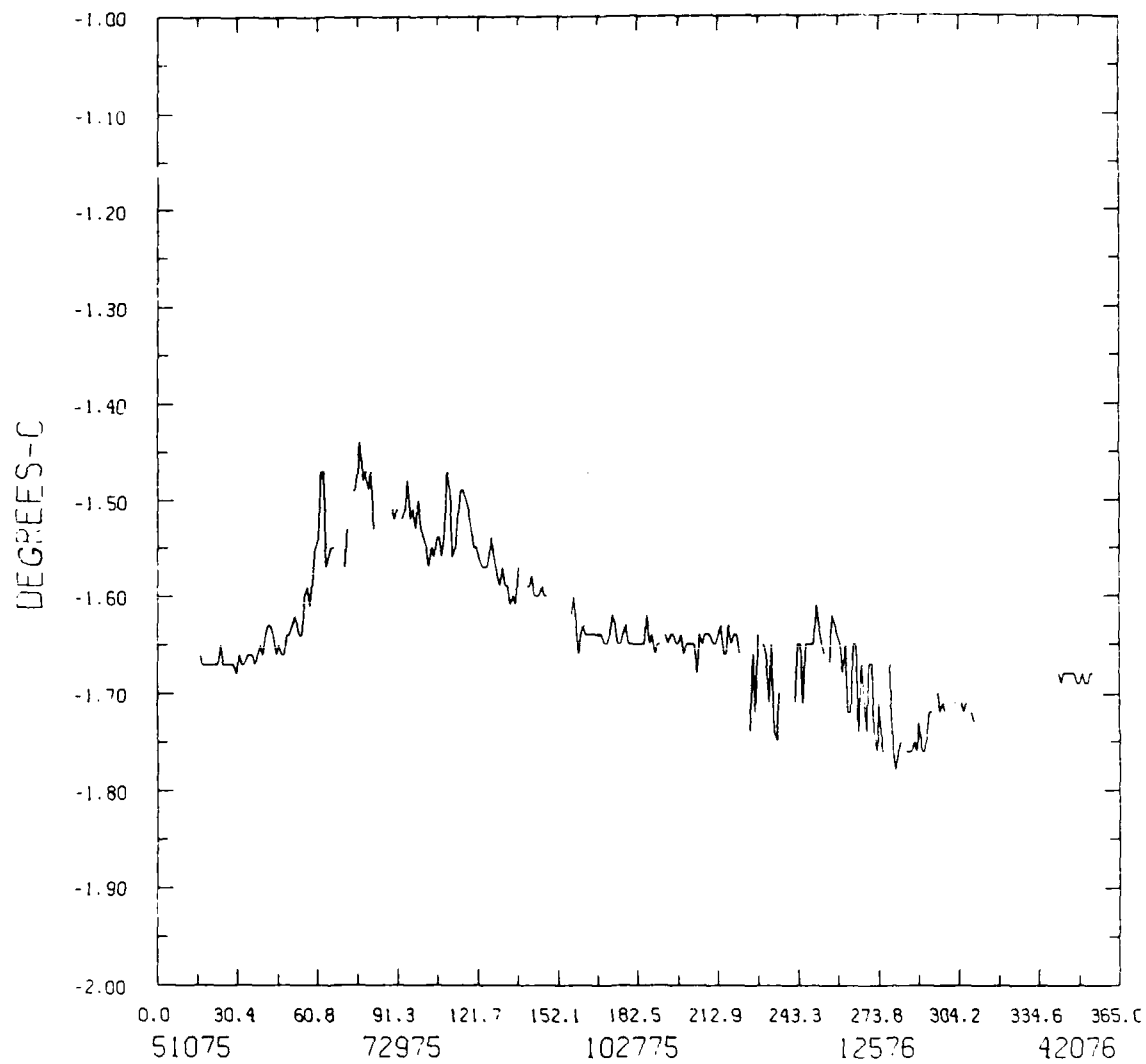


Figure 58. Mixed-layer temperature measured at camp Snowbird from May 10, 1975, to April 20, 1976.

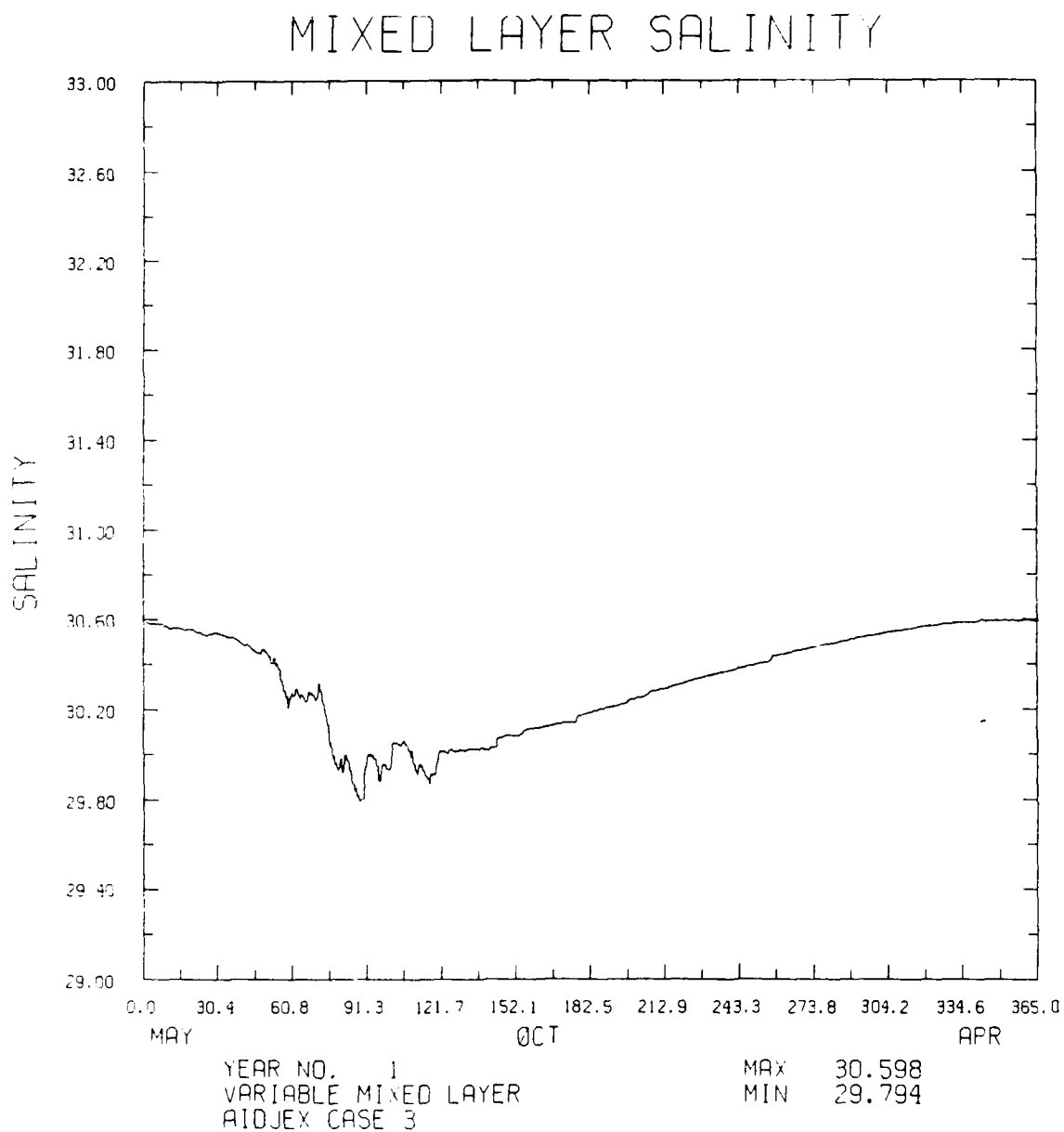


Figure 59. Mixed-layer salinity for a 1-year simulation of the VML model forced with AIDJEX forcing data. Simulation runs from May 1 to April 29.

STATION BLUEFOX SALINITY

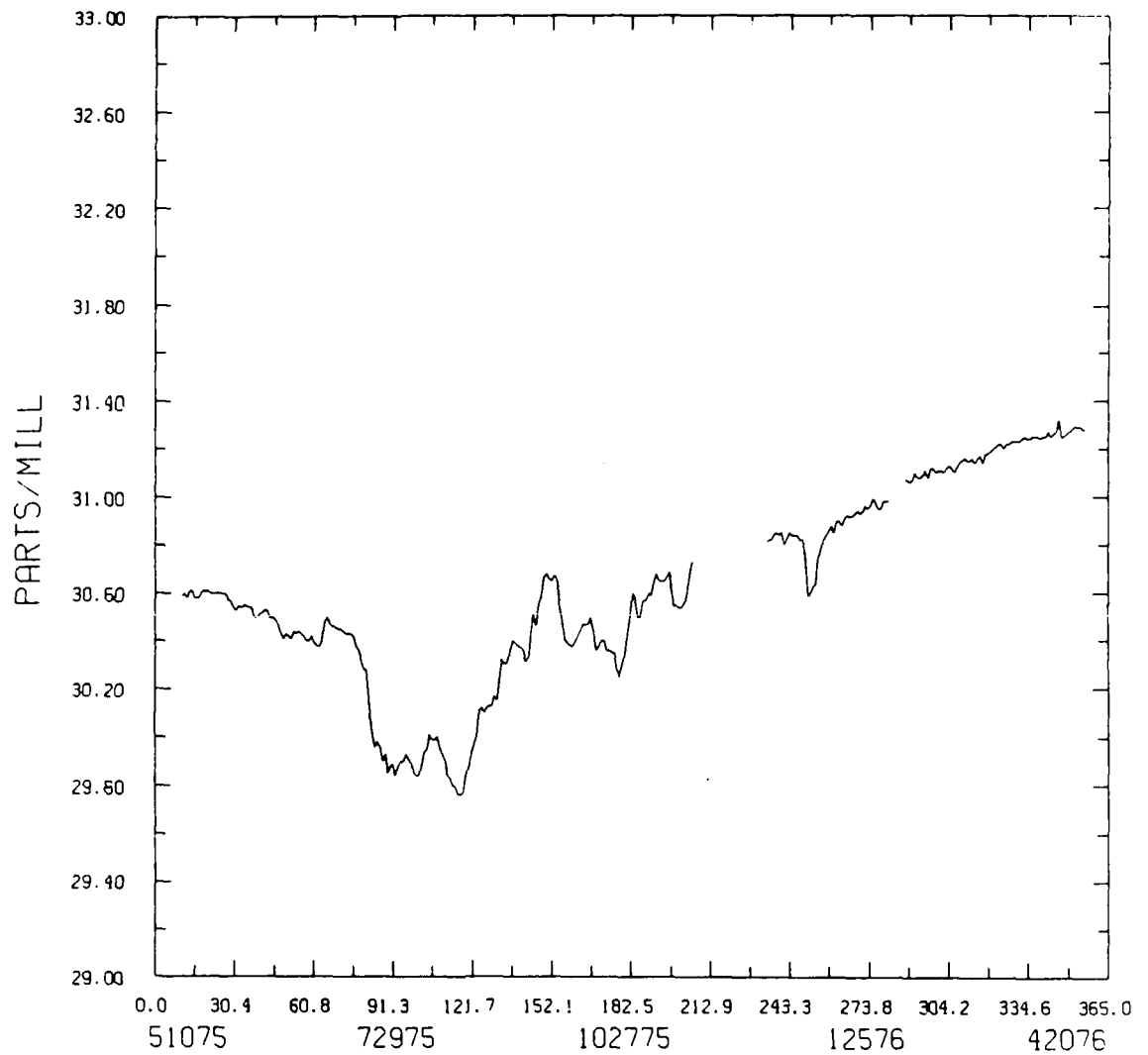


Figure 60. Mixed-layer salinity measured at camp Blue Fox from May 10, 1975, to April 20, 1976.

STATION SNOWBIRD SALINITY

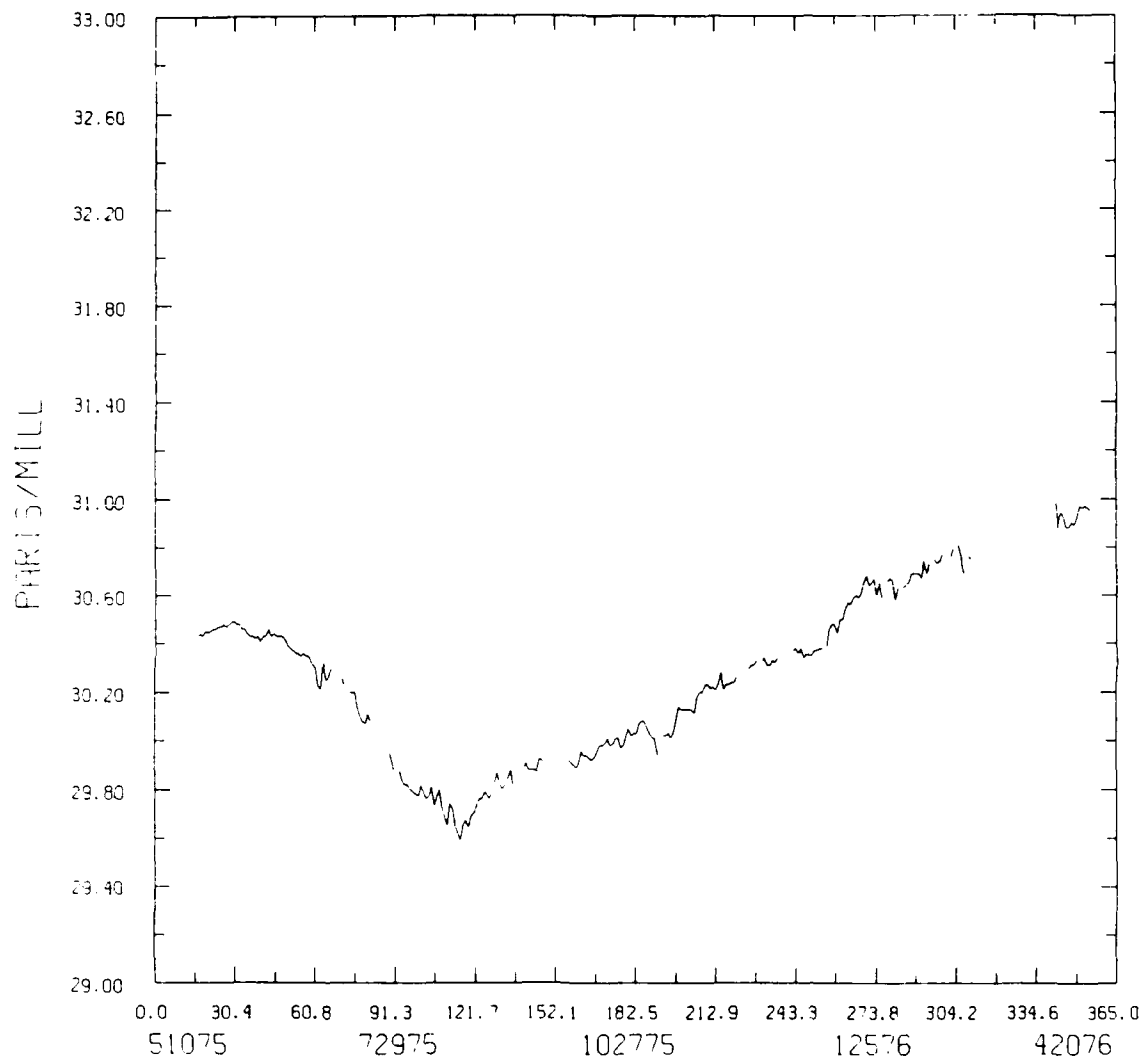


Figure 61. Mixed-layer salinity measured at camp Snowbird from May 10, 1975, to April 20, 1976.

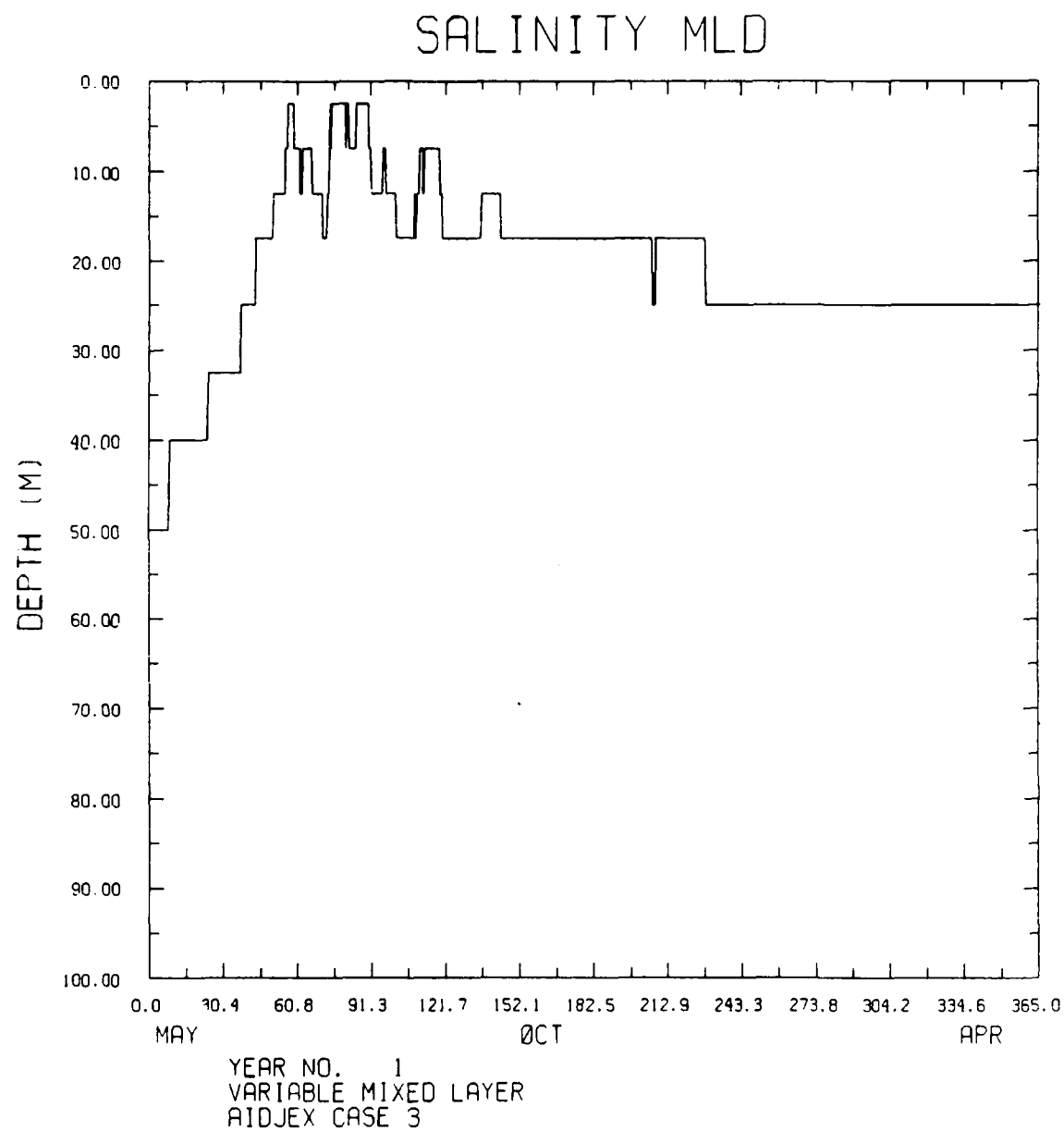


Figure 62. Mixed-layer depth computed from a 1-year simulation of the VML model forced with AIDJEX forcing data. Simulation runs from May 1 to April 29.

STATION BLUEFOX MIXED LAYER DEPTH

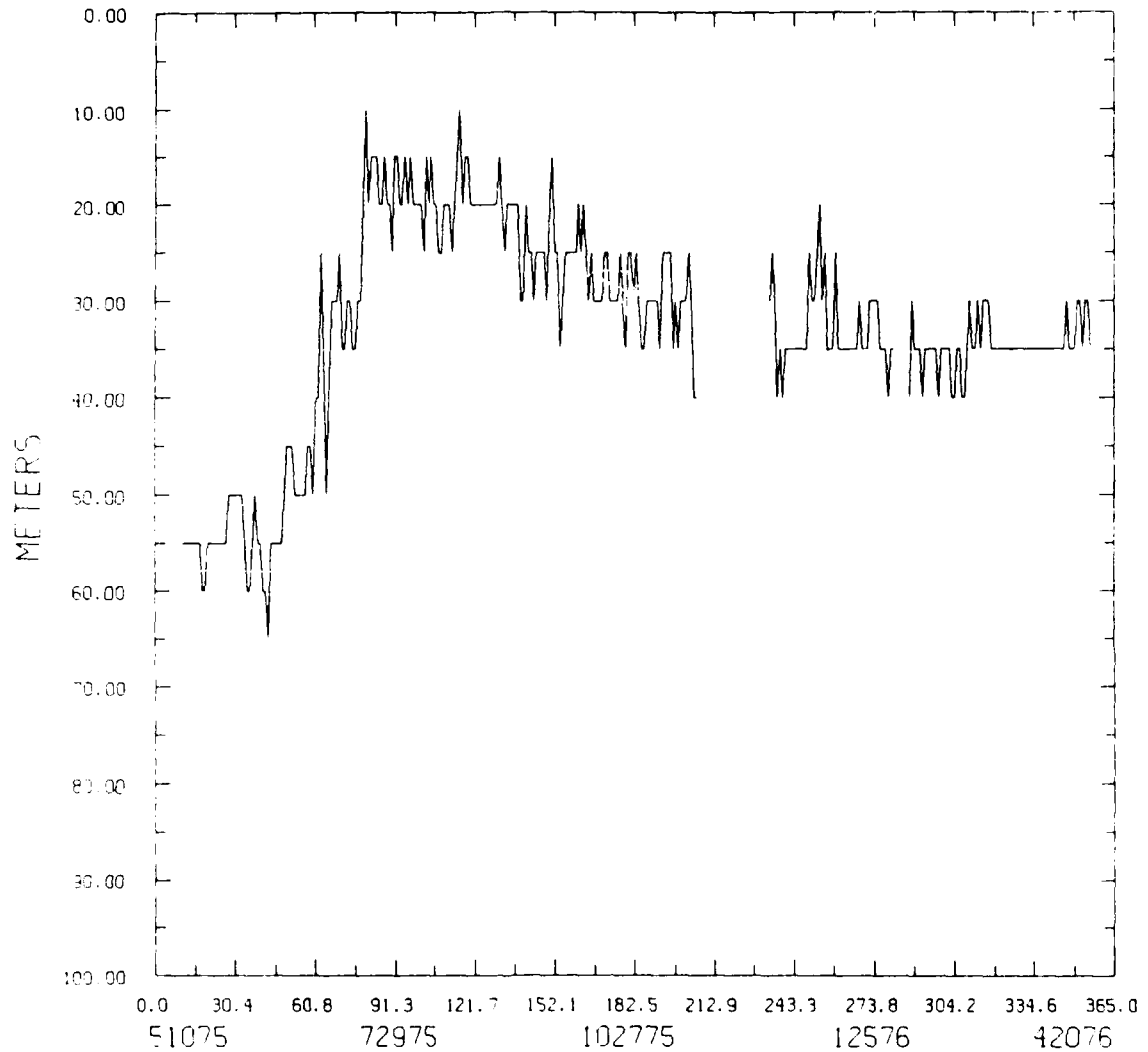


Figure 63. Mixed-layer depth measured at camp Blue Fox from May 10, 1975, to April 20, 1976.

STATION SNOWBIRD MIXED LAYER DEPTH

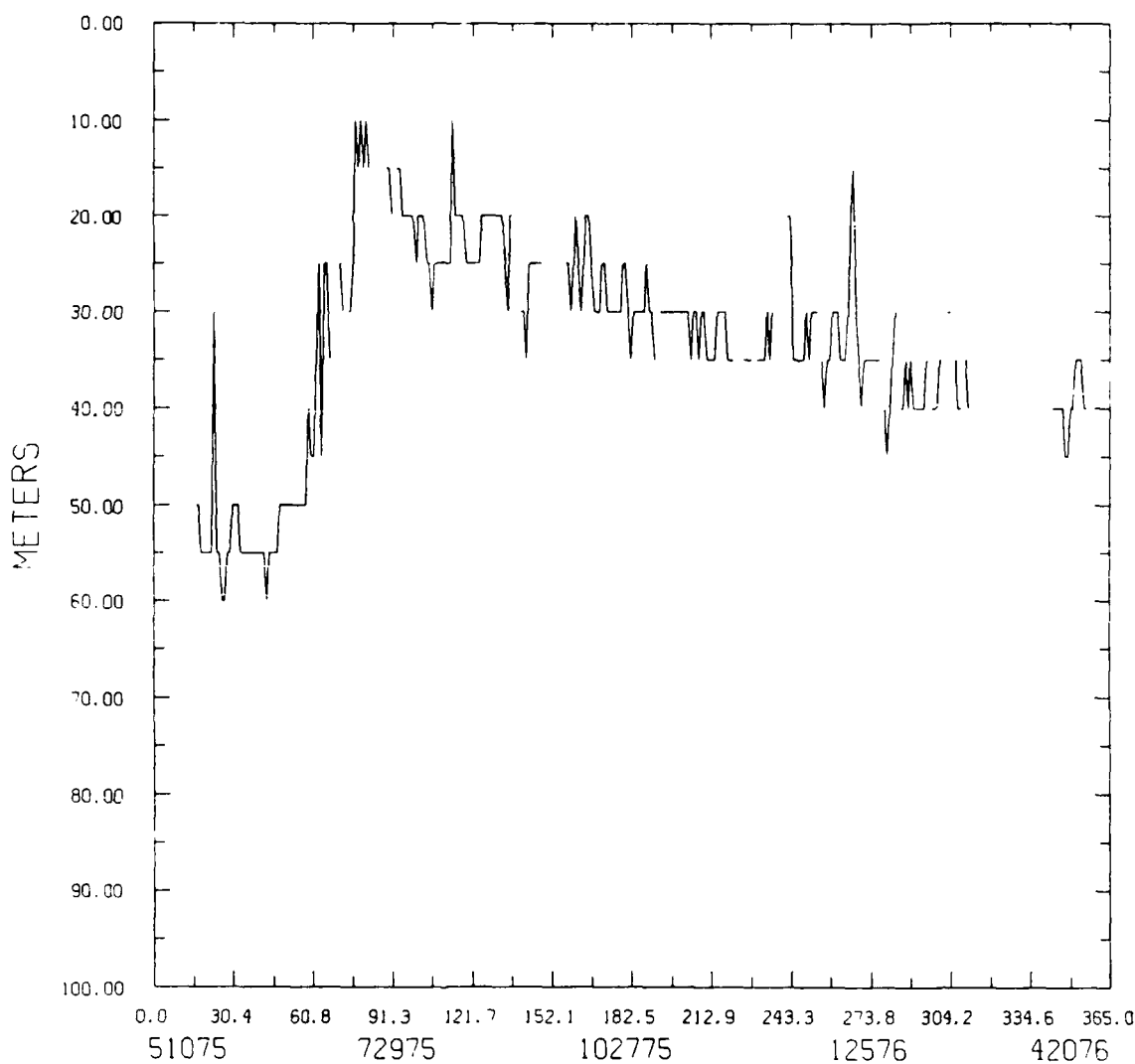


Figure 64. Mixed-layer depth measured at camp Snowbird from May 10, 1975, to April 20, 1976.

TEMPERATURE PROFILE PLOTS FOR MODEL RUN AND BLUEFOX DATA
 YEFR NO. 1

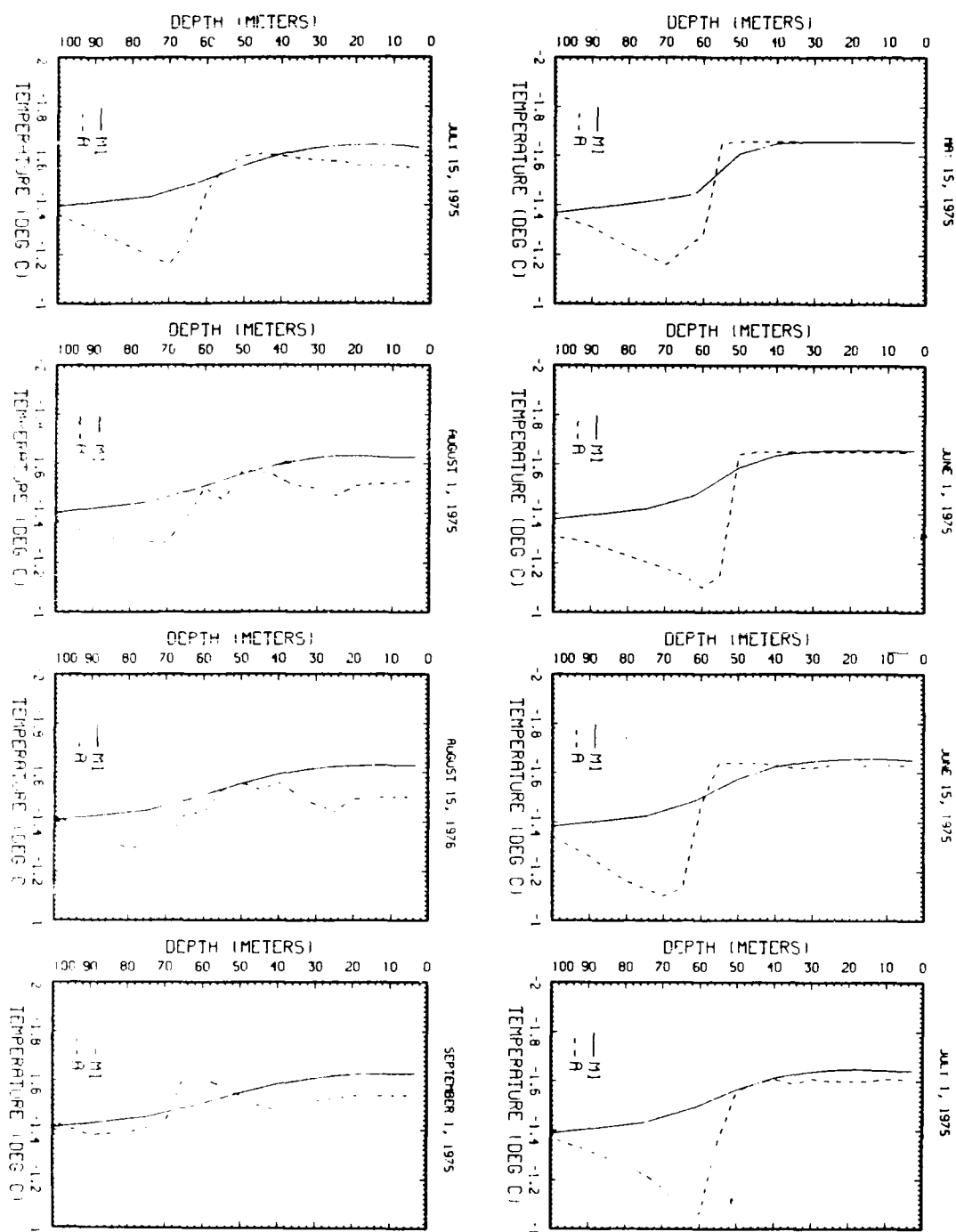


Figure 65. Comparison of temperature profiles from Case 3 and camp Blue Fox from May 15 to September 1.

TEMPERATURE PROFILE PLOTS FOR MODEL RUN AND BLUEFOX DATA
YEAR NO. 1

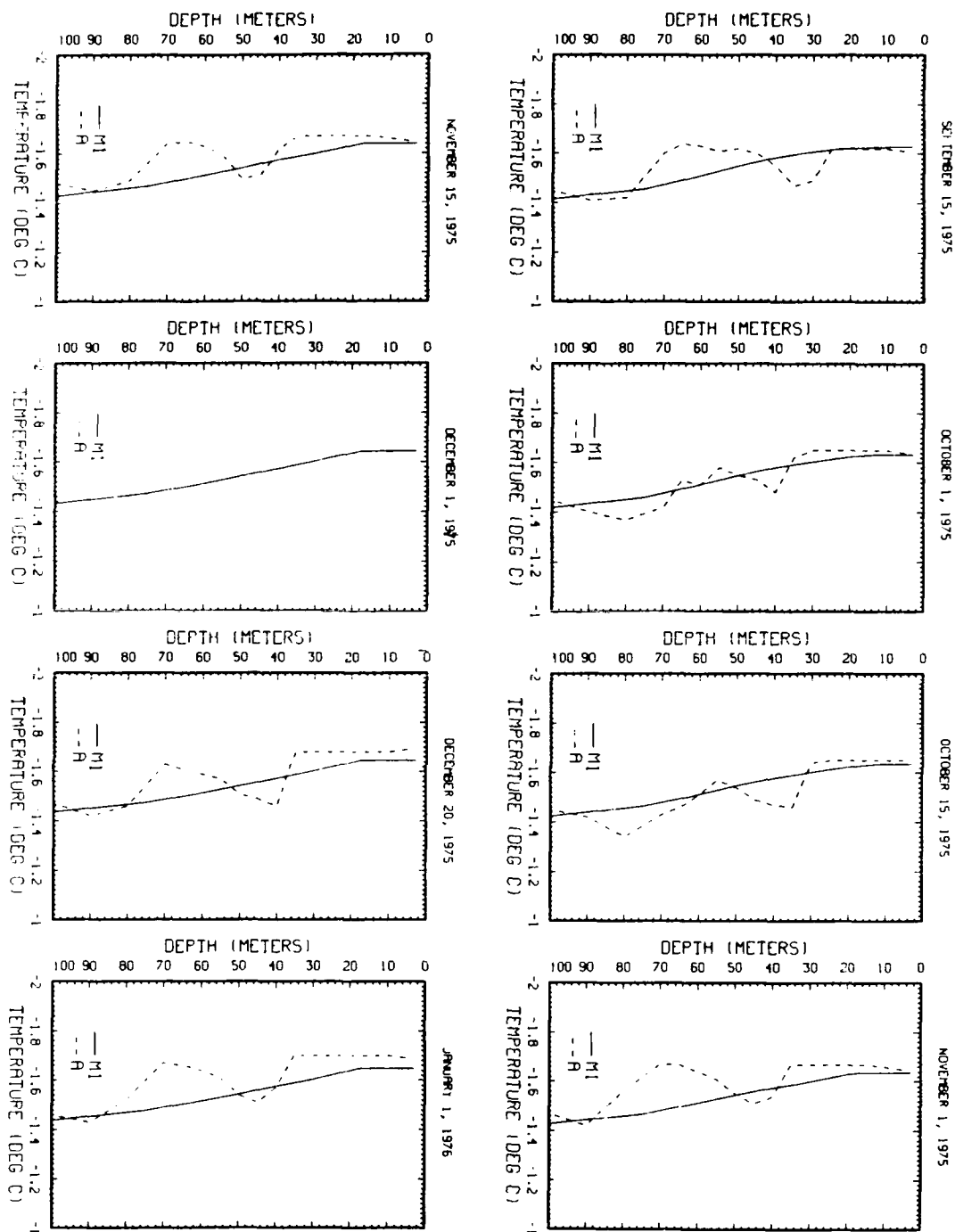


Figure 66. Comparison of temperature profiles from Case 3 and camp Blue Fox from September 15 to January 1.

TEMPERATURE PROFILE PLOTS FOR MODEL RUN AND BLUEFOX DATA
 CAR NO. 1

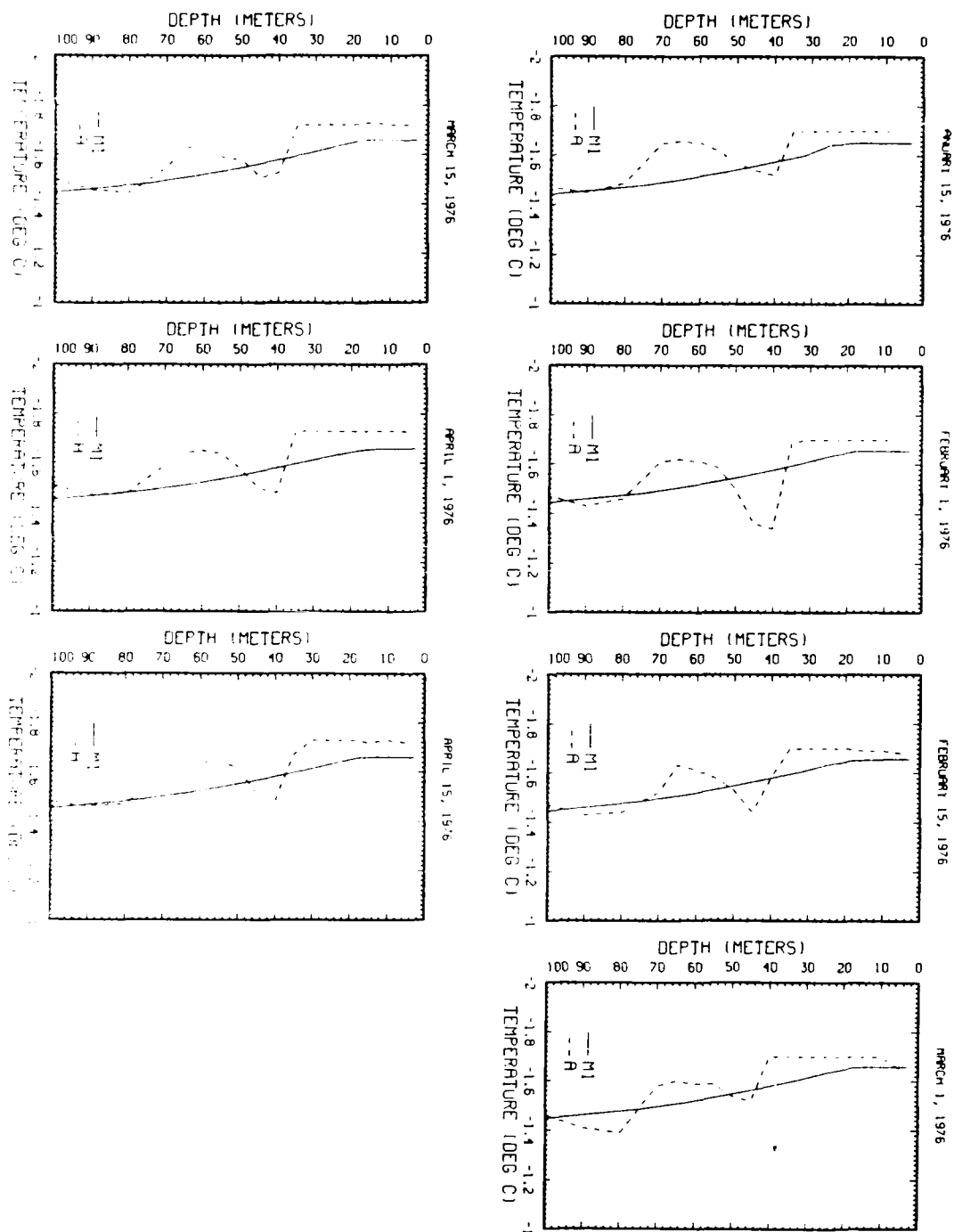


Figure 67. Comparison of temperature profiles from Case 3 and camp Blue Fox from January 15 to April 15.

SALINITY PROFILE PLOTS FOR MODEL RUN AND BLUEFOX DATA
YEAR NO. 1

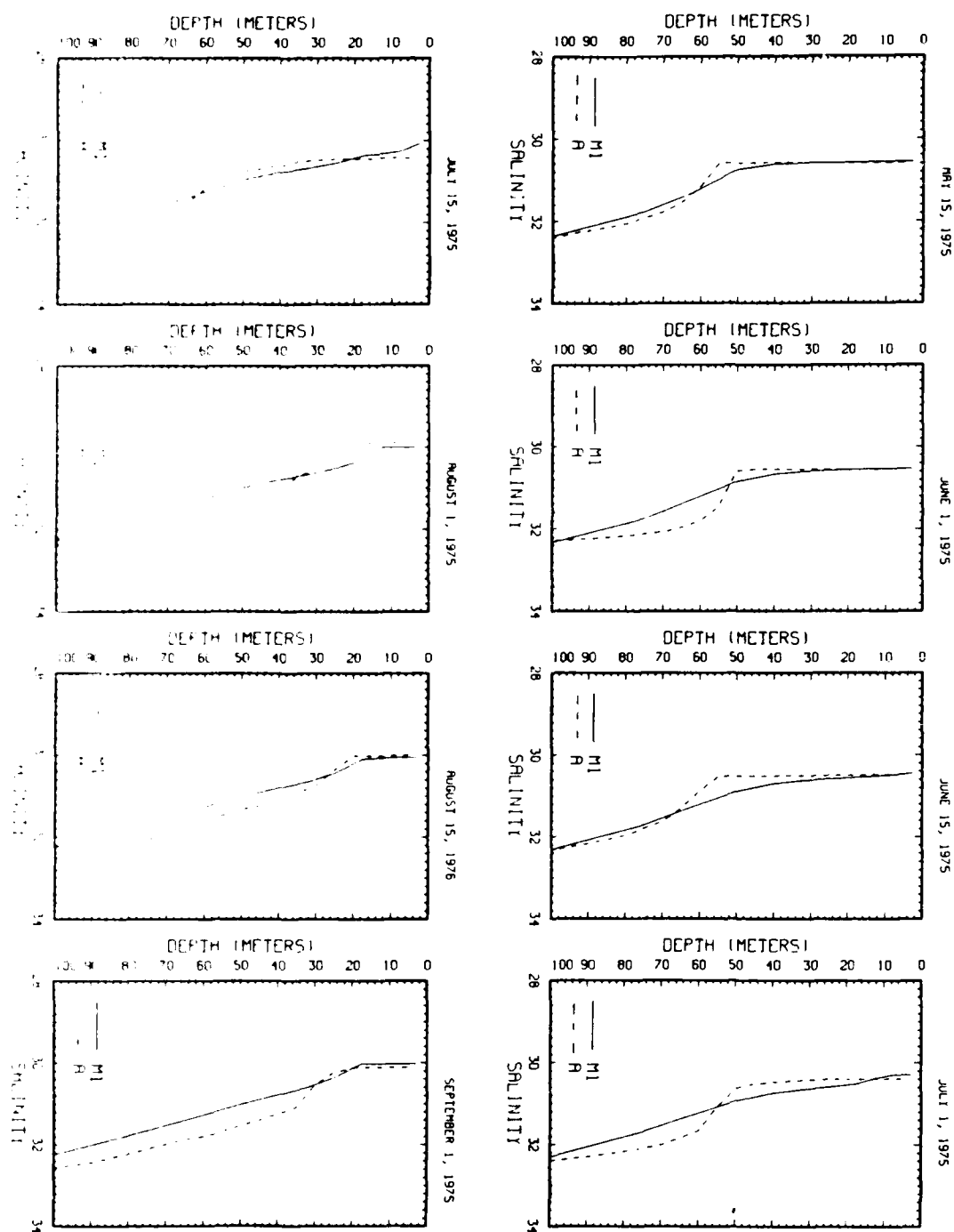


Figure 68. Comparison of salinity profiles from Case 3 and camp Blue Fox from May 15 to September 1.

SALINITY PROFILE PLOTS FOR MODEL RUN AND BLUEFOX DATA
YEAR NO. 1

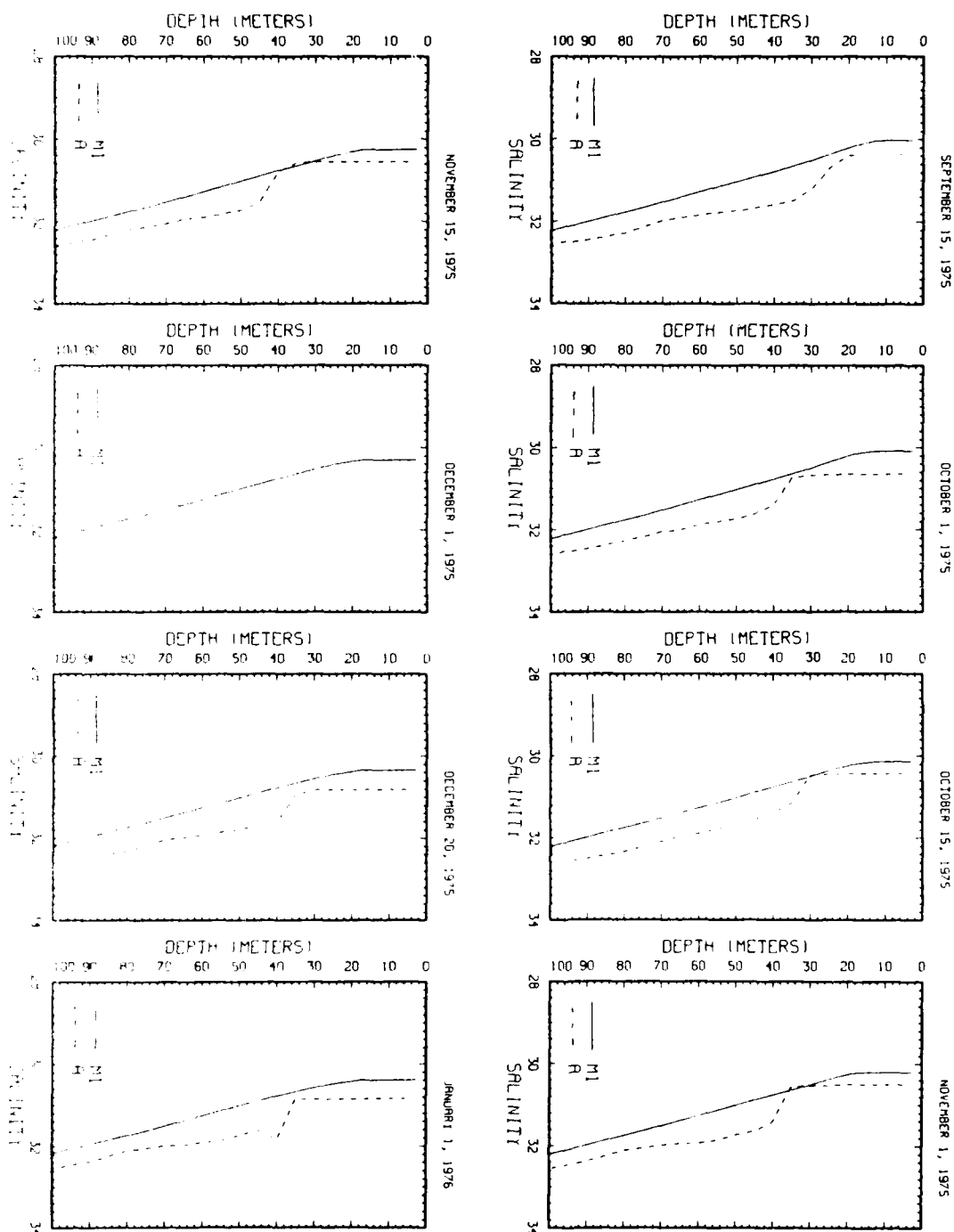


Figure 69. Comparison of salinity profiles from Case 3 and camp Blue Fox from September 15 to January 1.

SALINITY PROFILE PLOTS FOR MODEL RUN AND BLUEFOX DATA
YEAR NO. 1

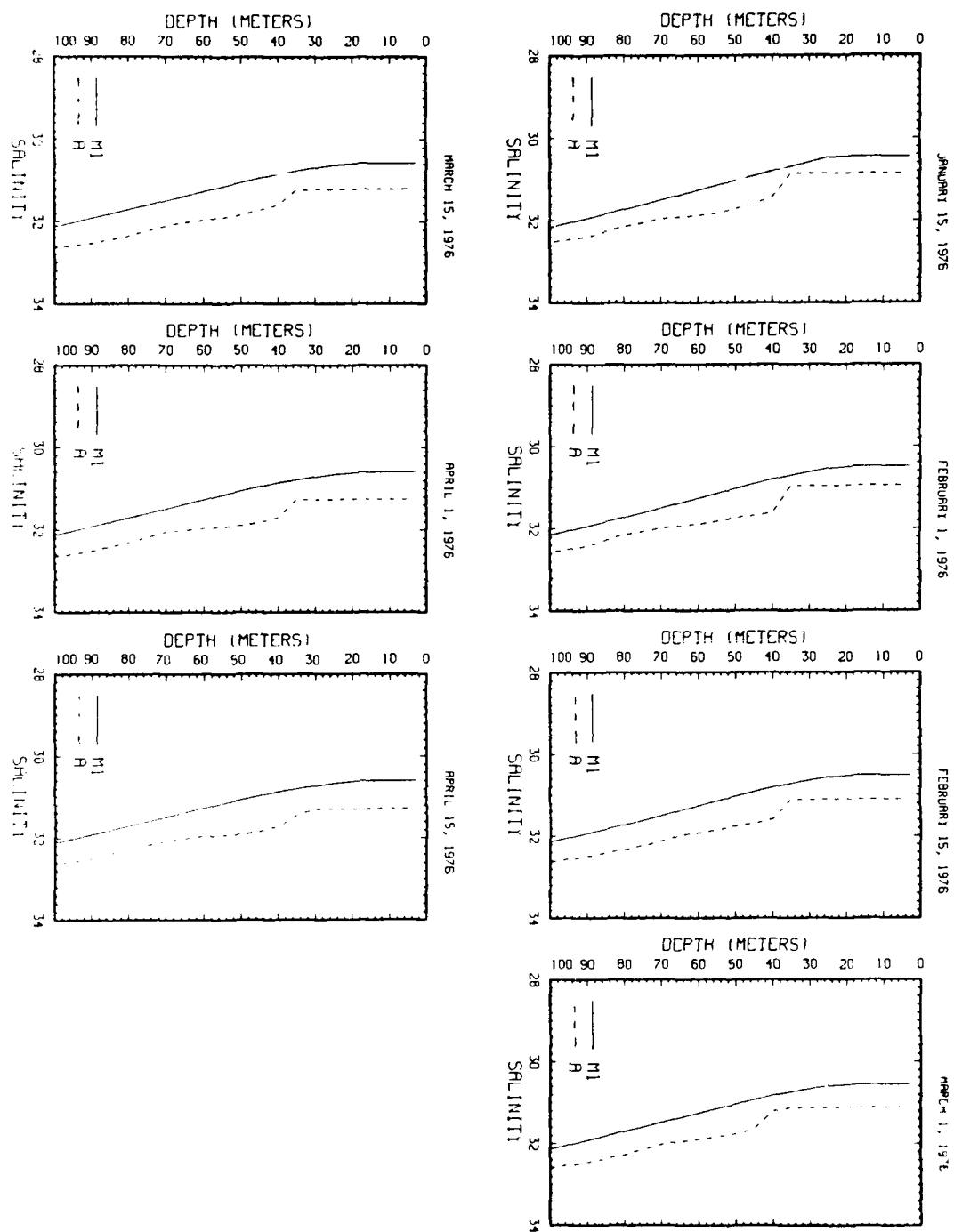


Figure 70. Comparison of salinity profiles from Case 3 and camp Blue Fox from January 1976.

AD-A189 158

PREDICTIONS AND STUDIES WITH A ONE-DIMENSIONAL
ICE/OCEAN MODEL (U) NAVAL OCEAN RESEARCH AND DEVELOPMENT
ACTIVITY NSYL STATION MS S H RIEDLINGER ET AL 888 87
NORDA-195 F7C 8/3

2/2

UNCLASSIFIED

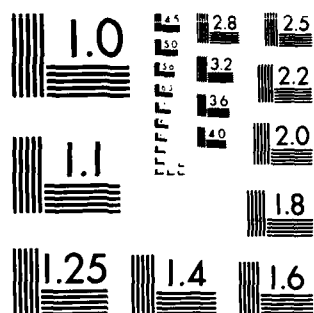
NL

END

DATE

FILED

8



MICROCOPY RESOLUTION TEST CHART
NATIONAL BUREAU OF STANDARDS-1963-A

TEMPERATURE PROFILE PLOTS FOR MODEL RUN AND SNOWBIRD DATA
YEAR NO. 1

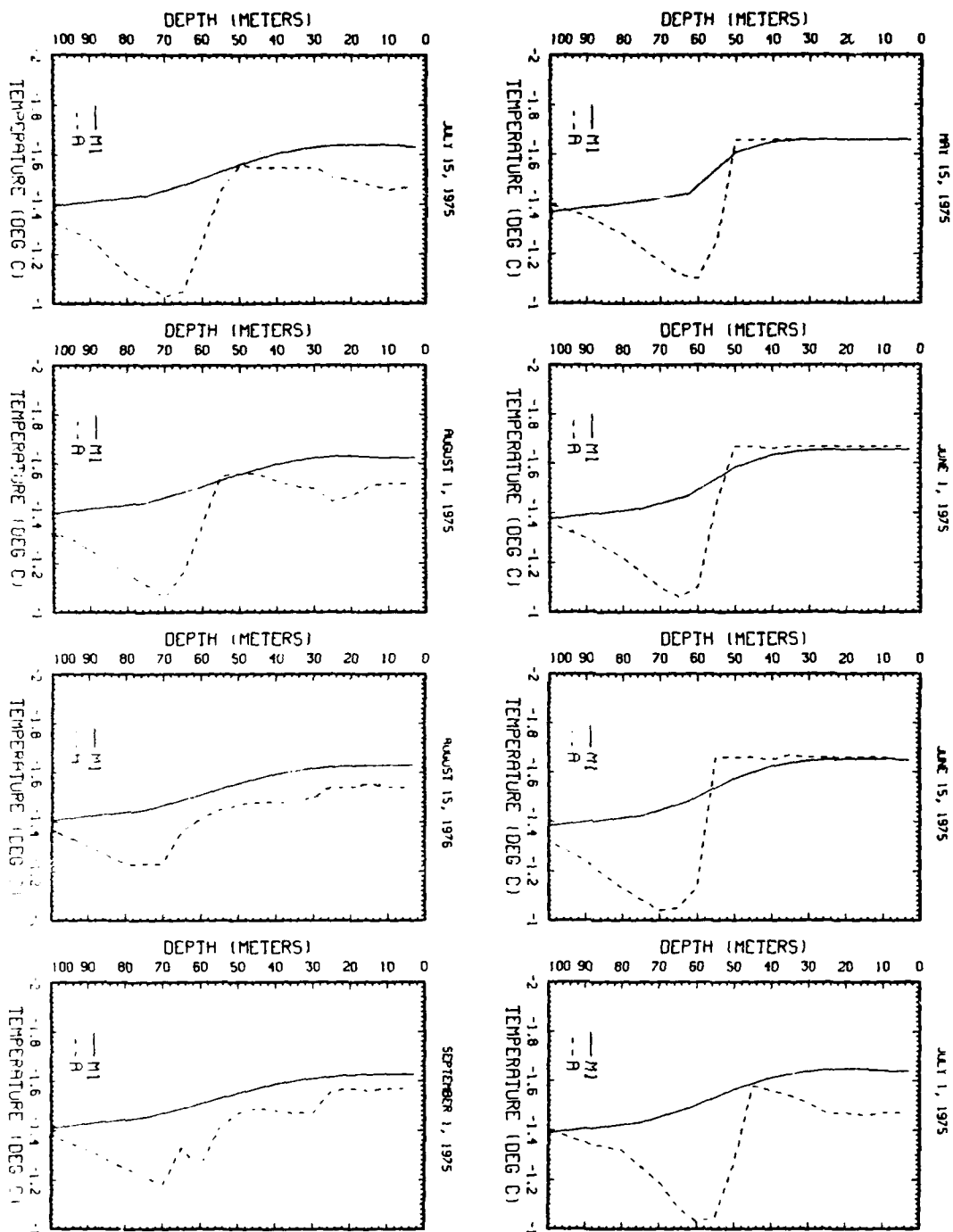


Figure 71. Comparison of temperature profiles from Case 3 and camp Snowbird from May 15 to September 1.

TEMPERATURE PROFILE PLOTS FOR MODEL RUN AND SNOWBIRD DATA
YEAR NO. 1

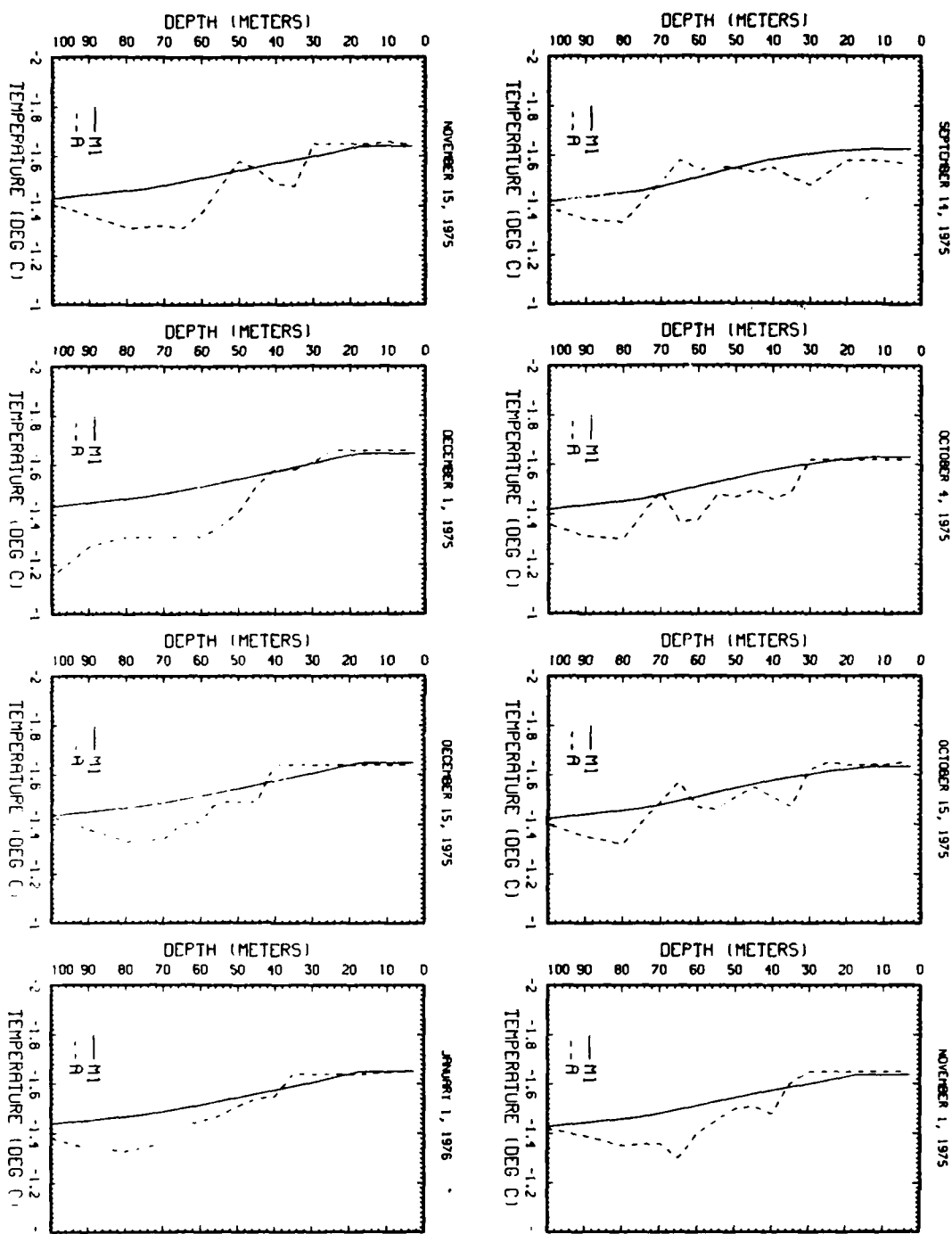


Figure 72. Comparison of temperature profiles from Case 3 and camp Snowbird from September 14 to January 1.

TEMPERATURE PROFILE PLOTS FOR MODEL RUN AND SNOWBIRD DATA
YEAR NO. 1

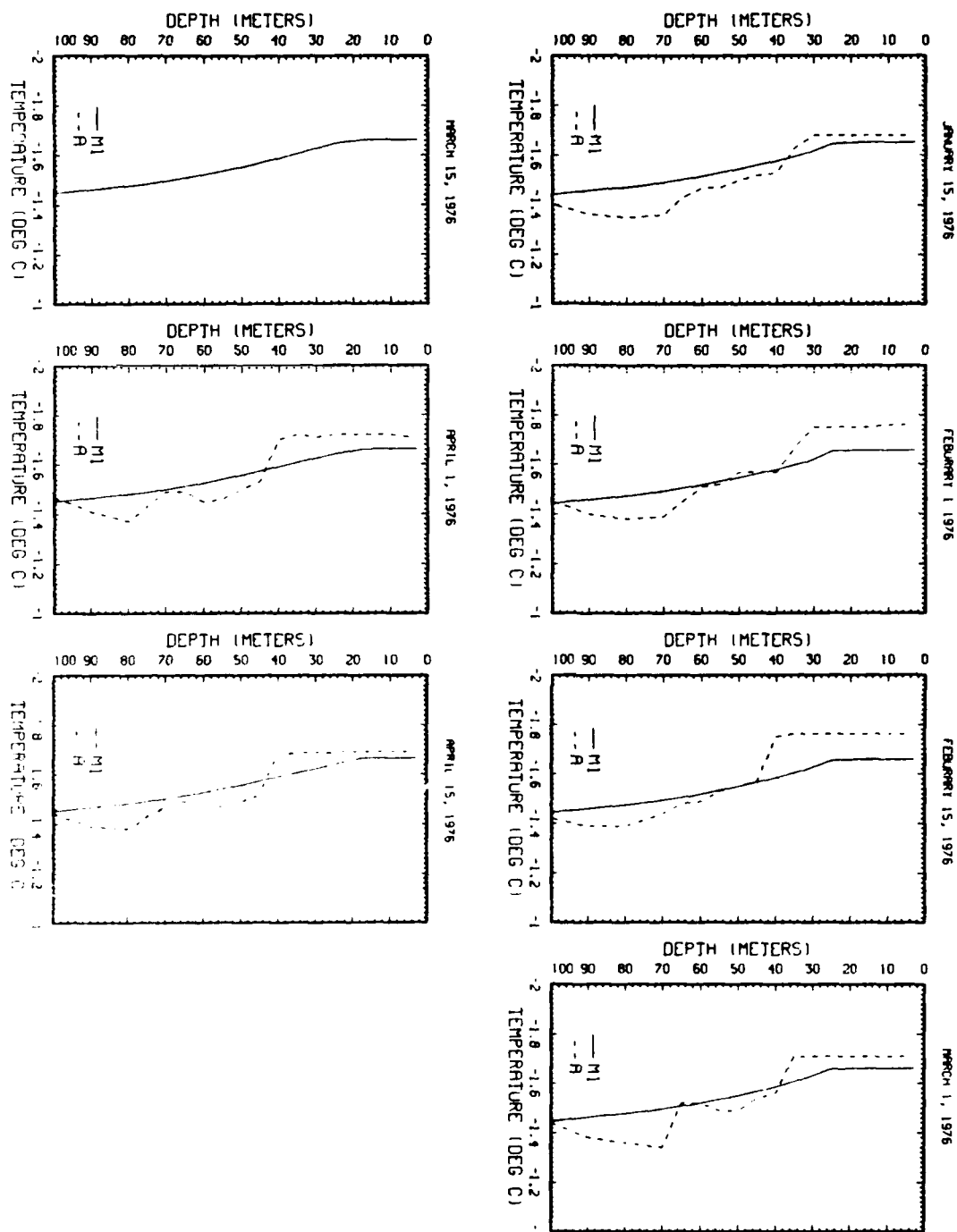


Figure 73. Comparison of temperature profiles from Case 3 and camp Snowbird from January 15 to April 15.

SALINITY PROFILE PLOTS FOR MODEL RUN AND SNOWBIRD DATA
YEAR NO. 1

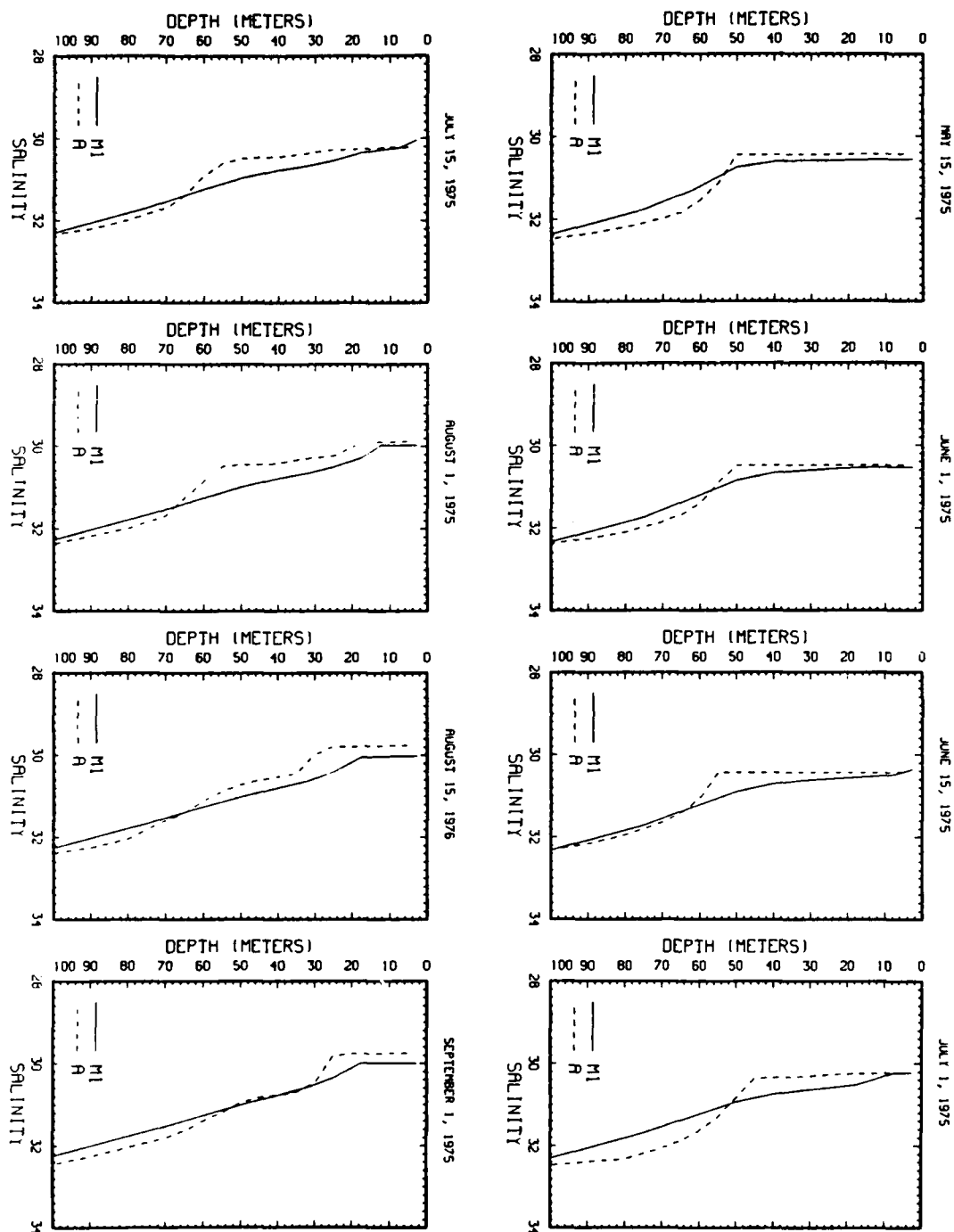


Figure 74. Comparison of salinity profiles from Case 3 and camp Snowbird from May 15 to September 1.

SALINITY PROFILE PLOTS FOR MODEL RUN AND SNOWBIRD DATA
YEAR NO. 1

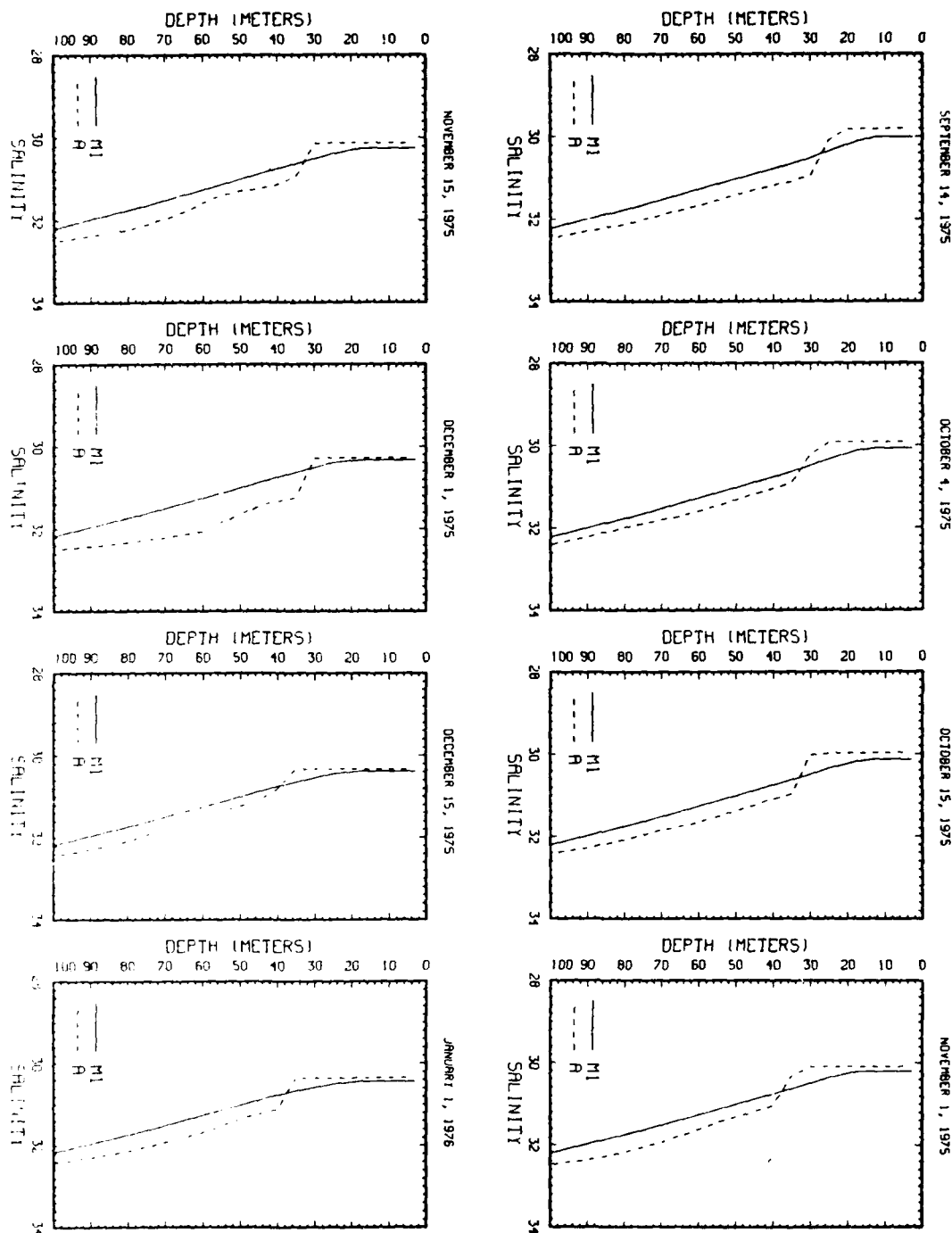


Figure 75. Comparison of salinity profiles from Case 3 and camp Snowbird from September 14 to January 1.

SALINITY PROFILE PLOTS FOR MODEL RUN AND SNOWBIRD DATA
YEAR NO. 1

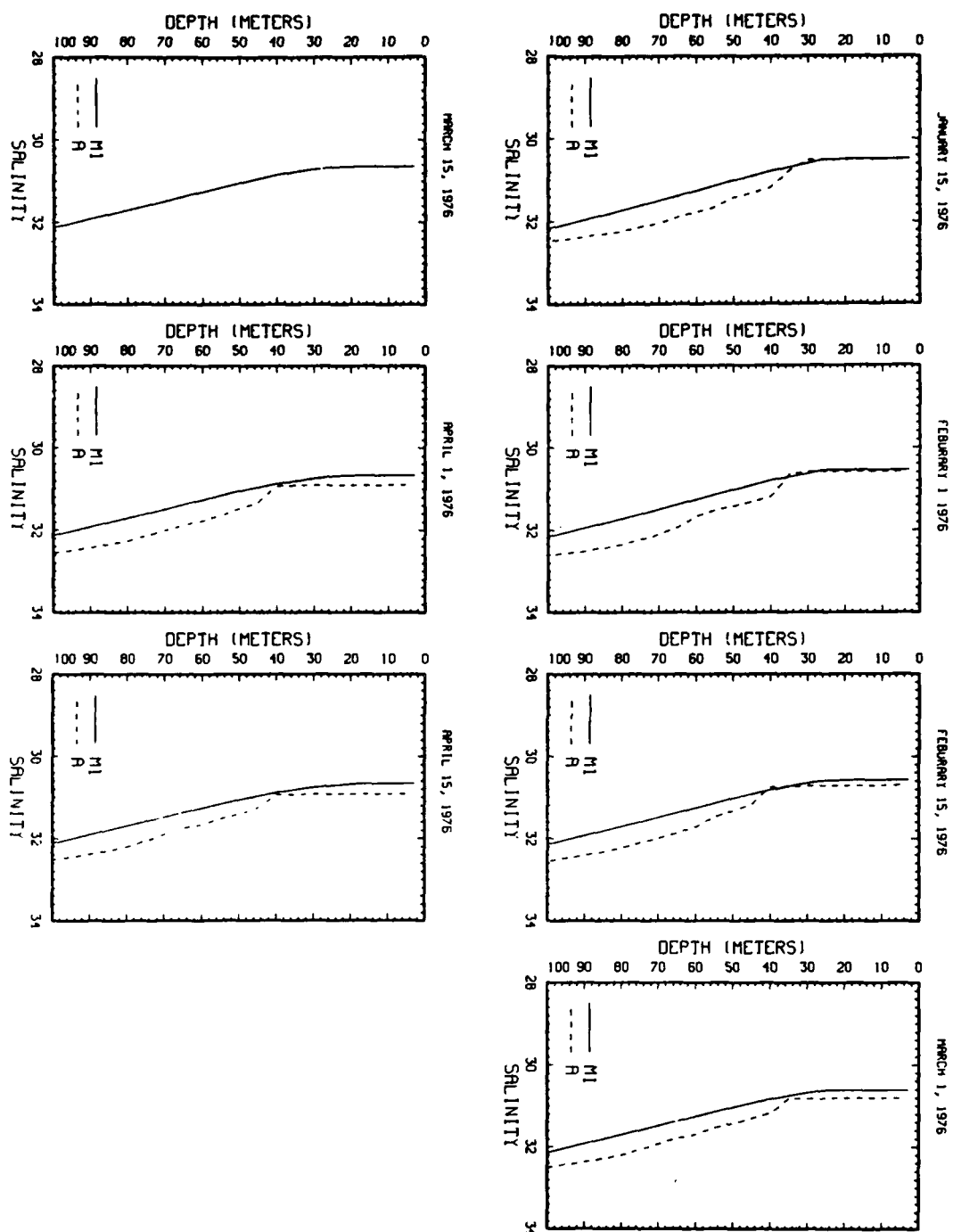


Figure 76. Comparison of salinity profiles from Case 3 and camp Snowbird from January 15 to April 15.

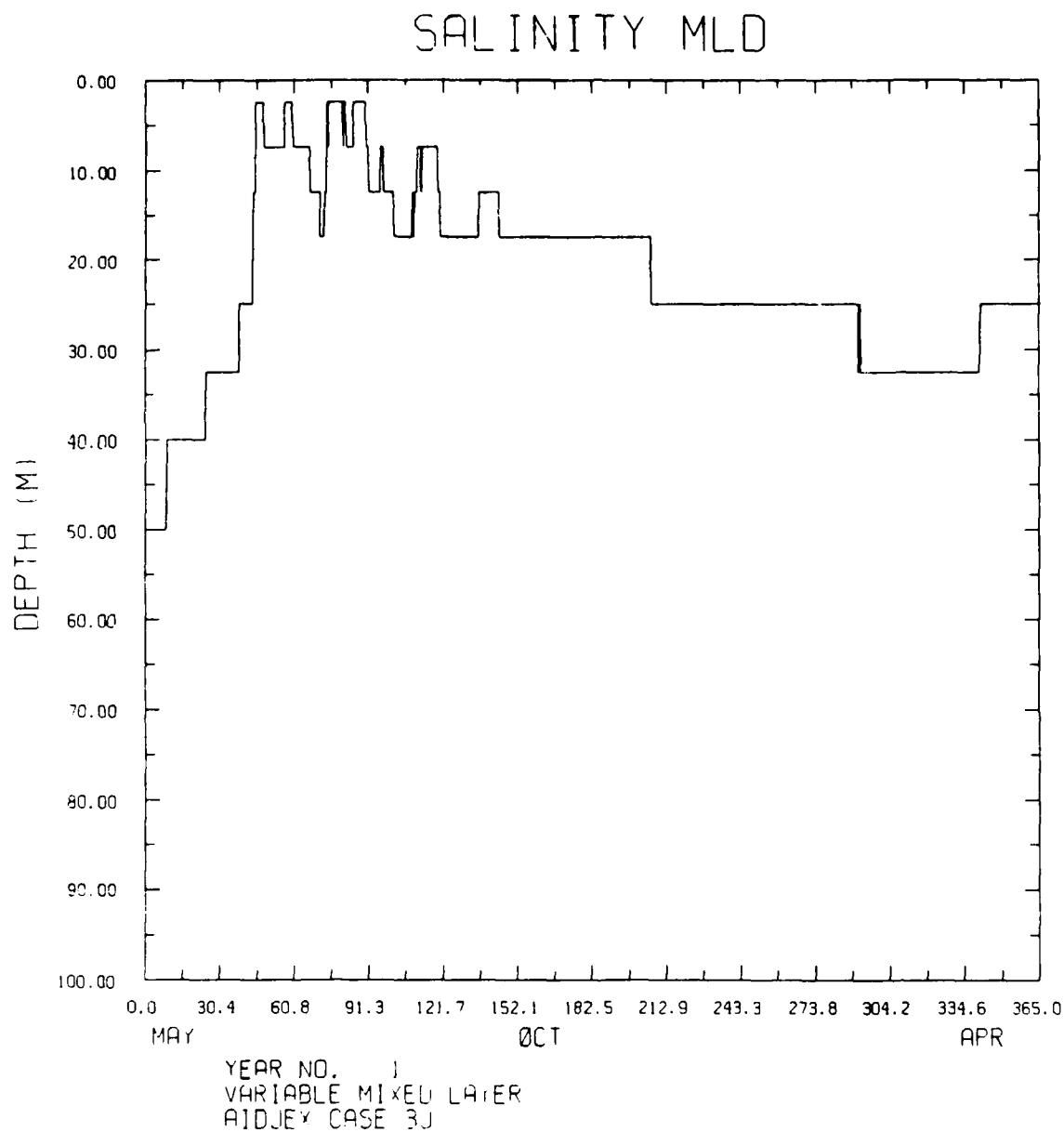


Figure 77. Mixed-layer depth for year 1 from AIDJEX Case 3J. Snowfall rate was cut in half in this simulation.

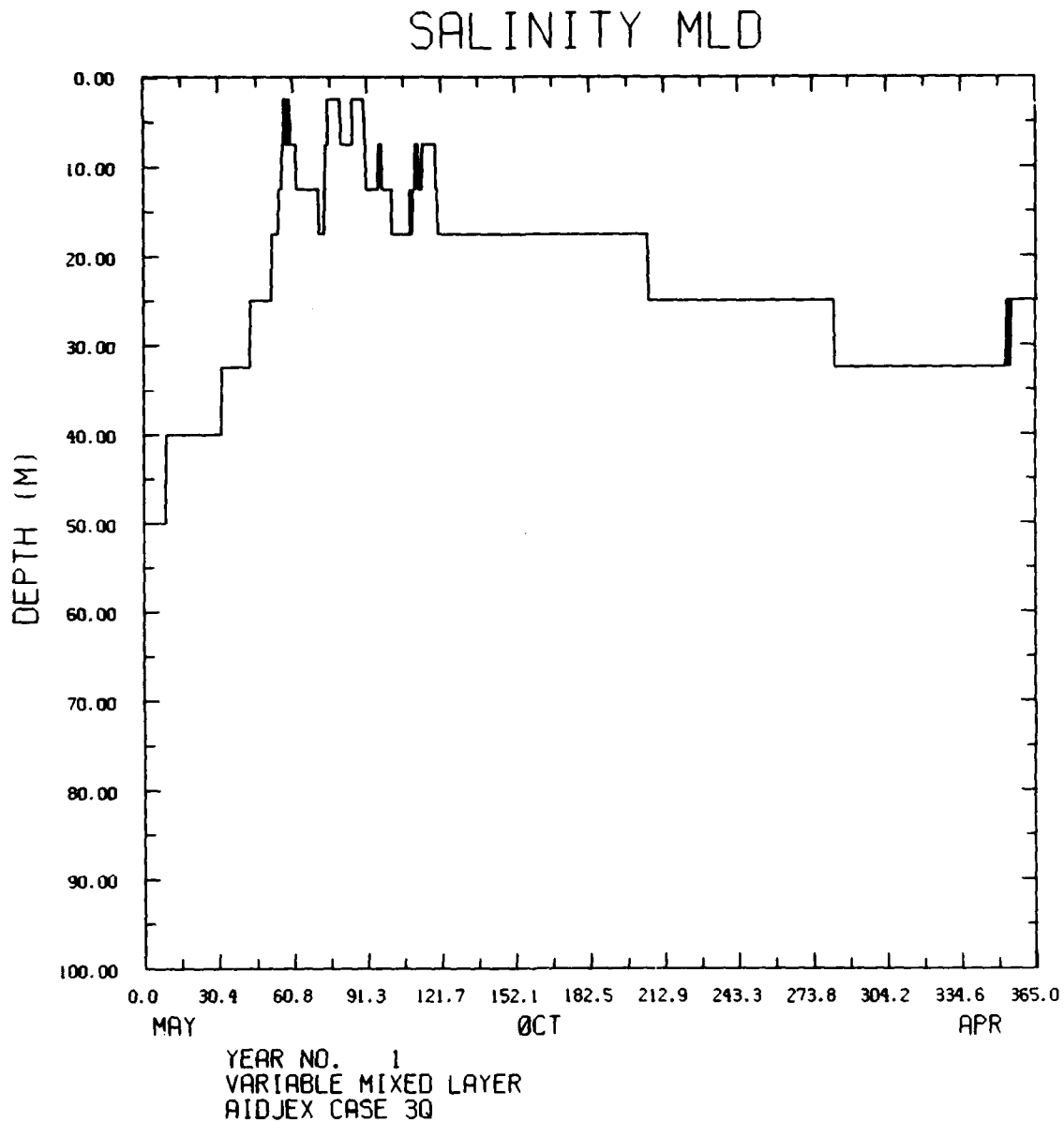


Figure 78. Mixed-layer depth for year 1 from AIDJEX Case 3Q. H_{deep} was reduced to $1.5 \text{ kcal/cm}^2/\text{year}$ in this simulation.

MIXED LAYER TEMP

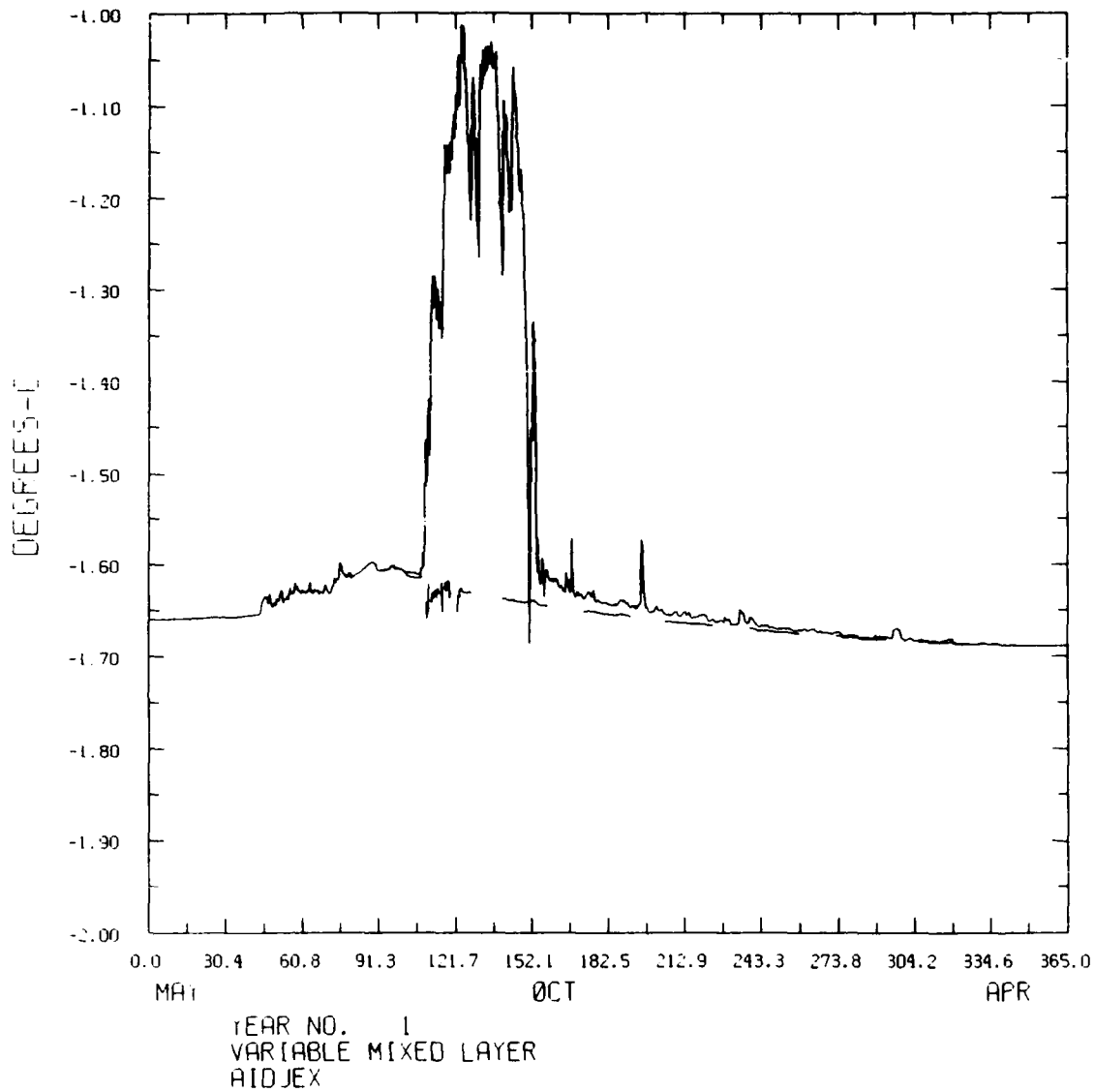


Figure 79. Comparison of mixed-layer temperature for Case 3N and Case 3O. Open water occurred in both cases. Case 3N is the dashed curve, and Case 3O is the solid curve.

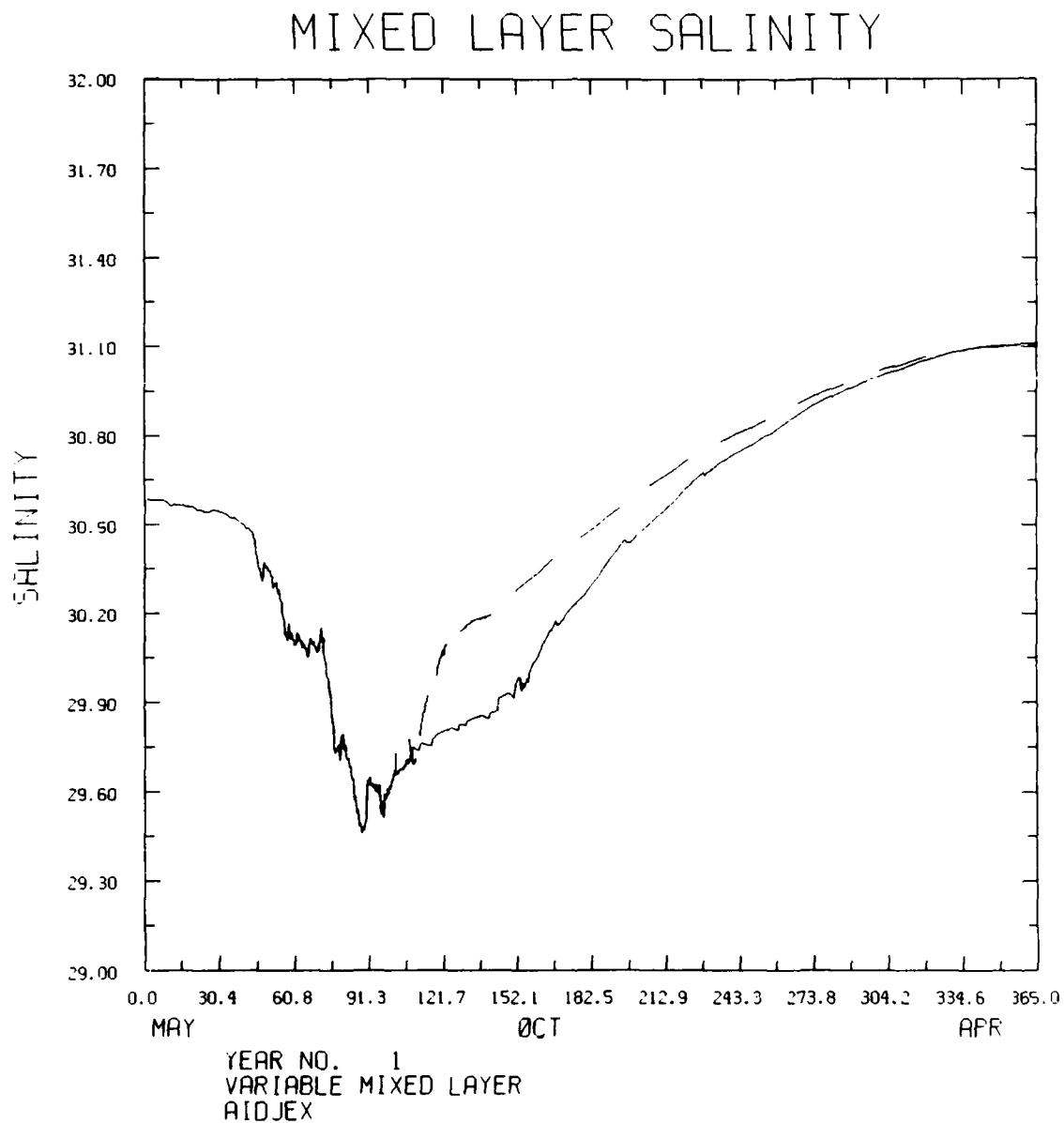


Figure 80. Comparison of mixed-layer salinity for Case 3N and Case 3O. Open water occurred in both cases. Case 3N is the dashed curve, and Case 3O is the solid curve.

ICE THICKNESS

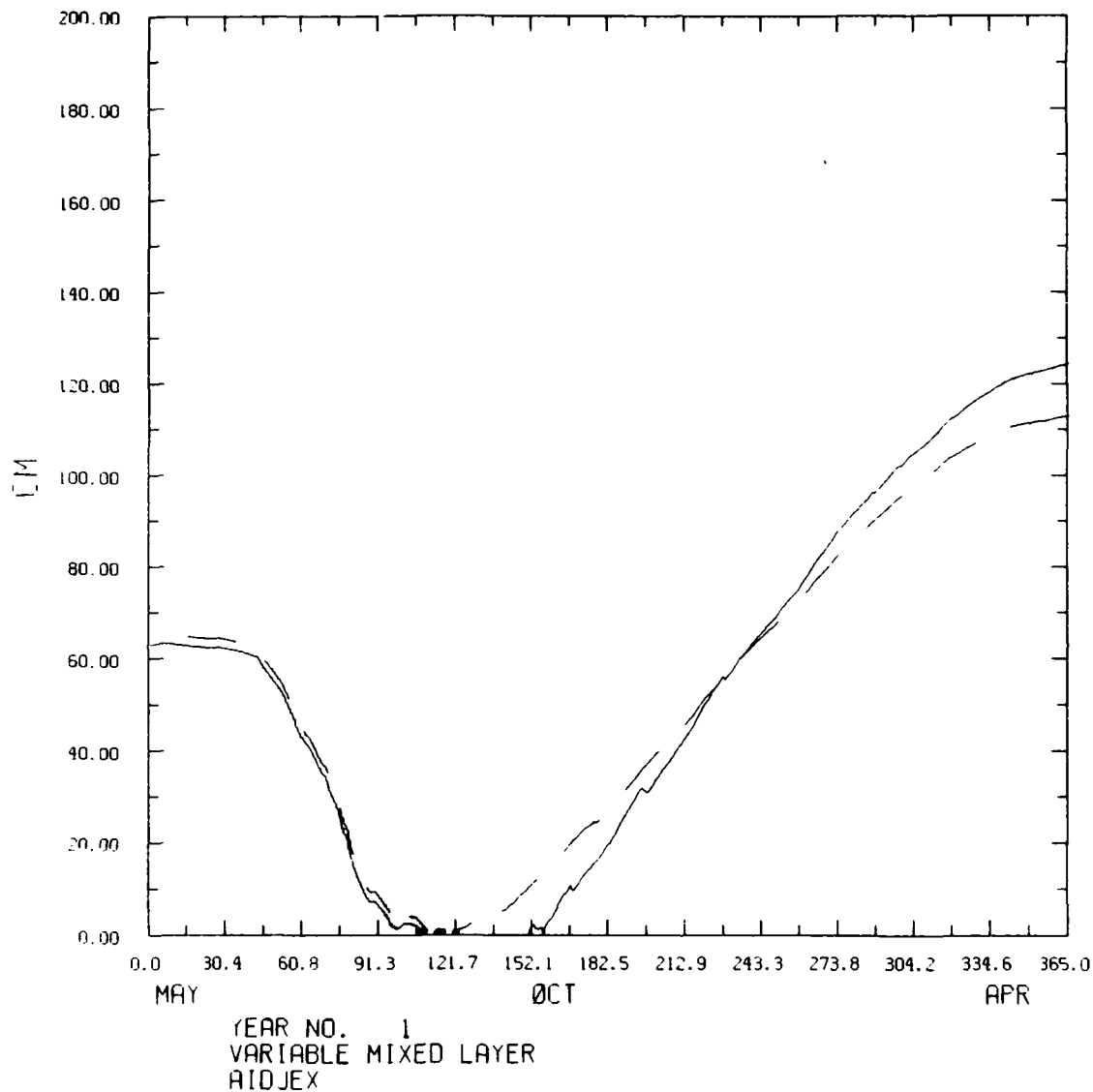


Figure 81. Comparison of ice thickness for Case 3N and Case 3O. Open water occurred in both cases. Case 3N is the dashed curve, and Case 3O is the solid curve.

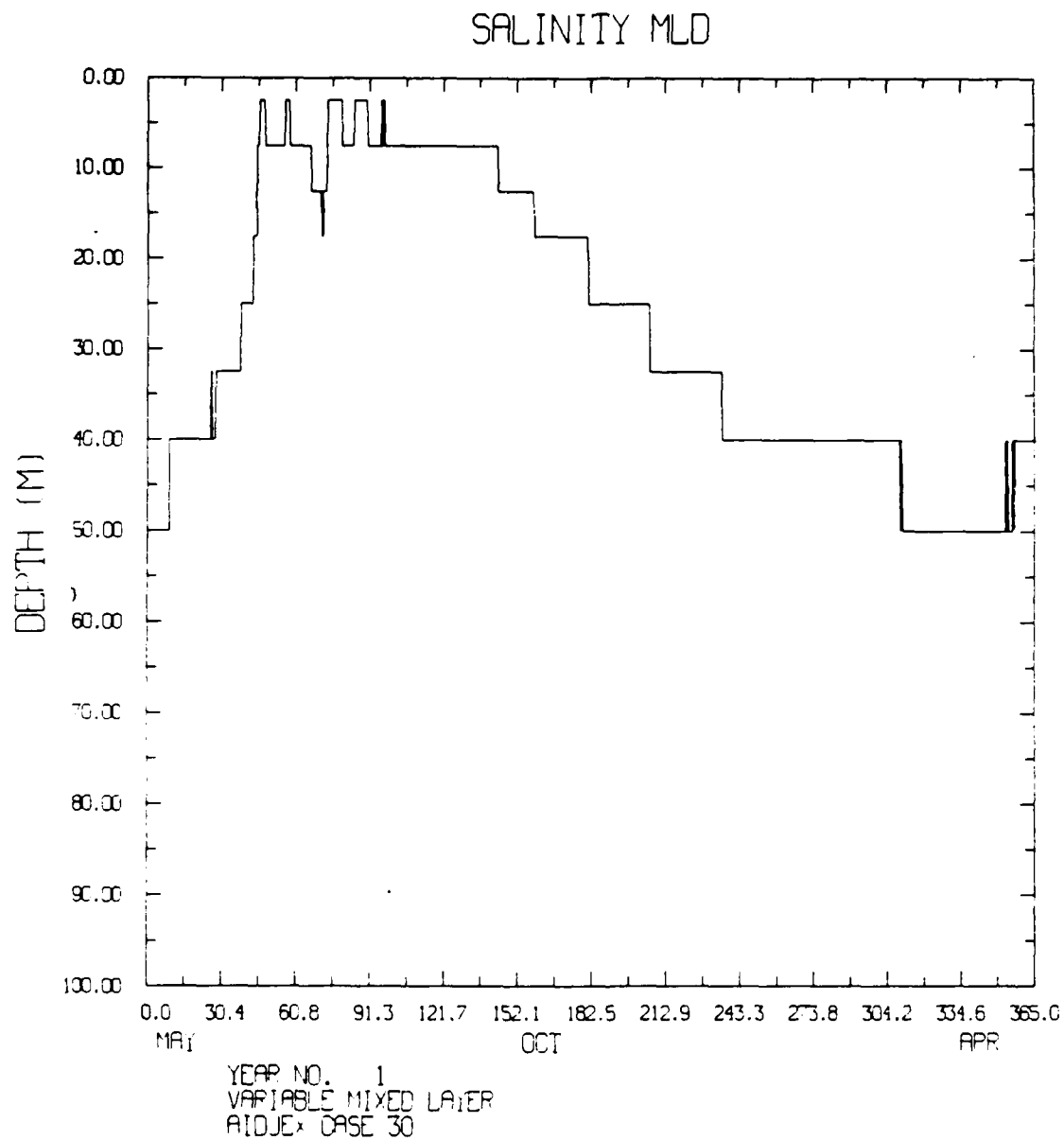


Figure 82. Mixed-layer depth for Case 30, where open water was forced by increasing H_{deep} to 6.0 kcal/cm²/year and decreasing the initial ice thickness to 63 cm.

TEMPERATURE PROFILE PLOTS FOR MODEL RUN AND BLUEFOX DATA
YEAR NO. 1

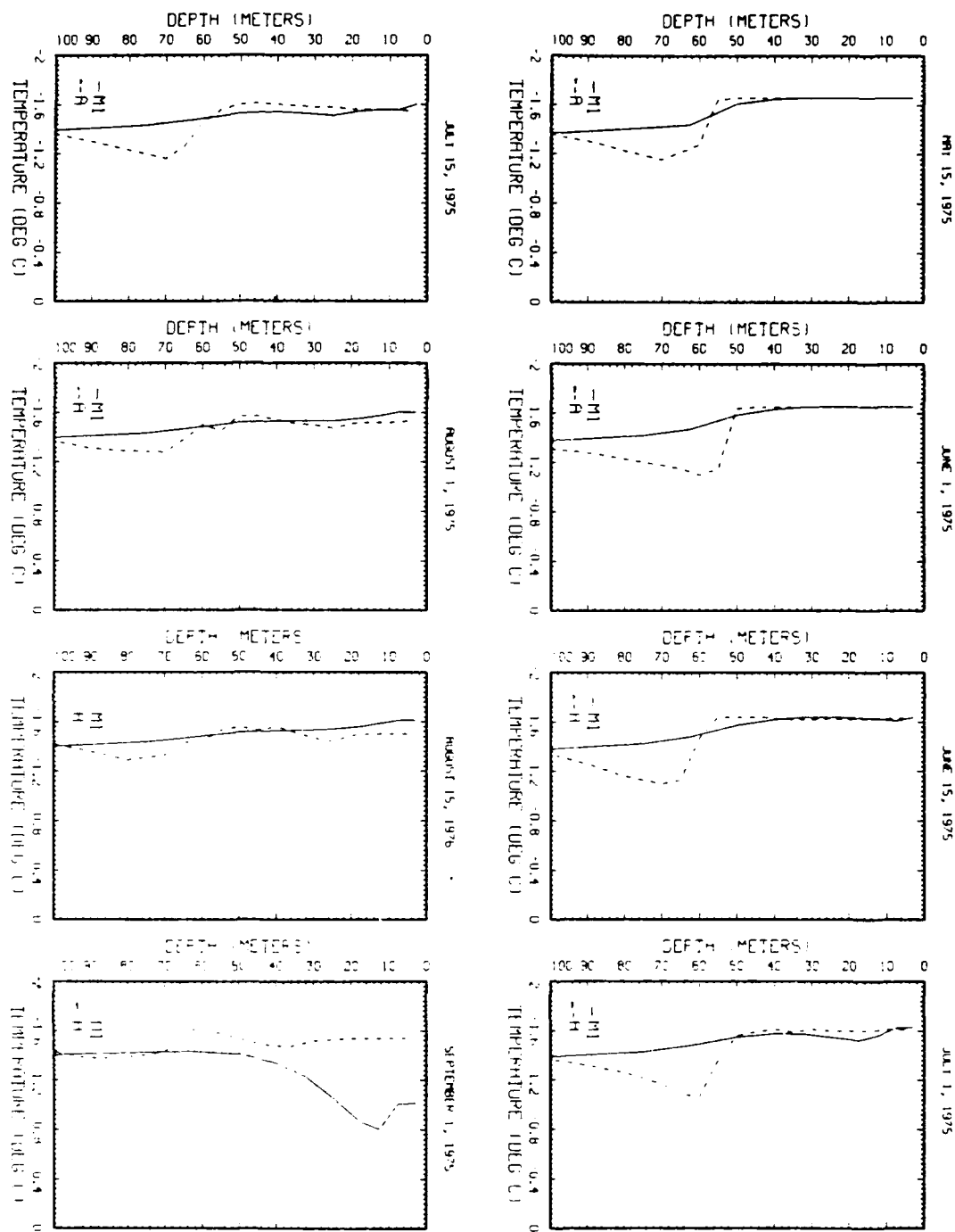


Figure 83. Comparison of temperature profiles from Case 30 and camp Blue Fox from May 15 to September 1.

TEMPERATURE PROFILE PLOTS FOR MODEL RUN AND BLUEFOX DATA
YEAR NO. 1

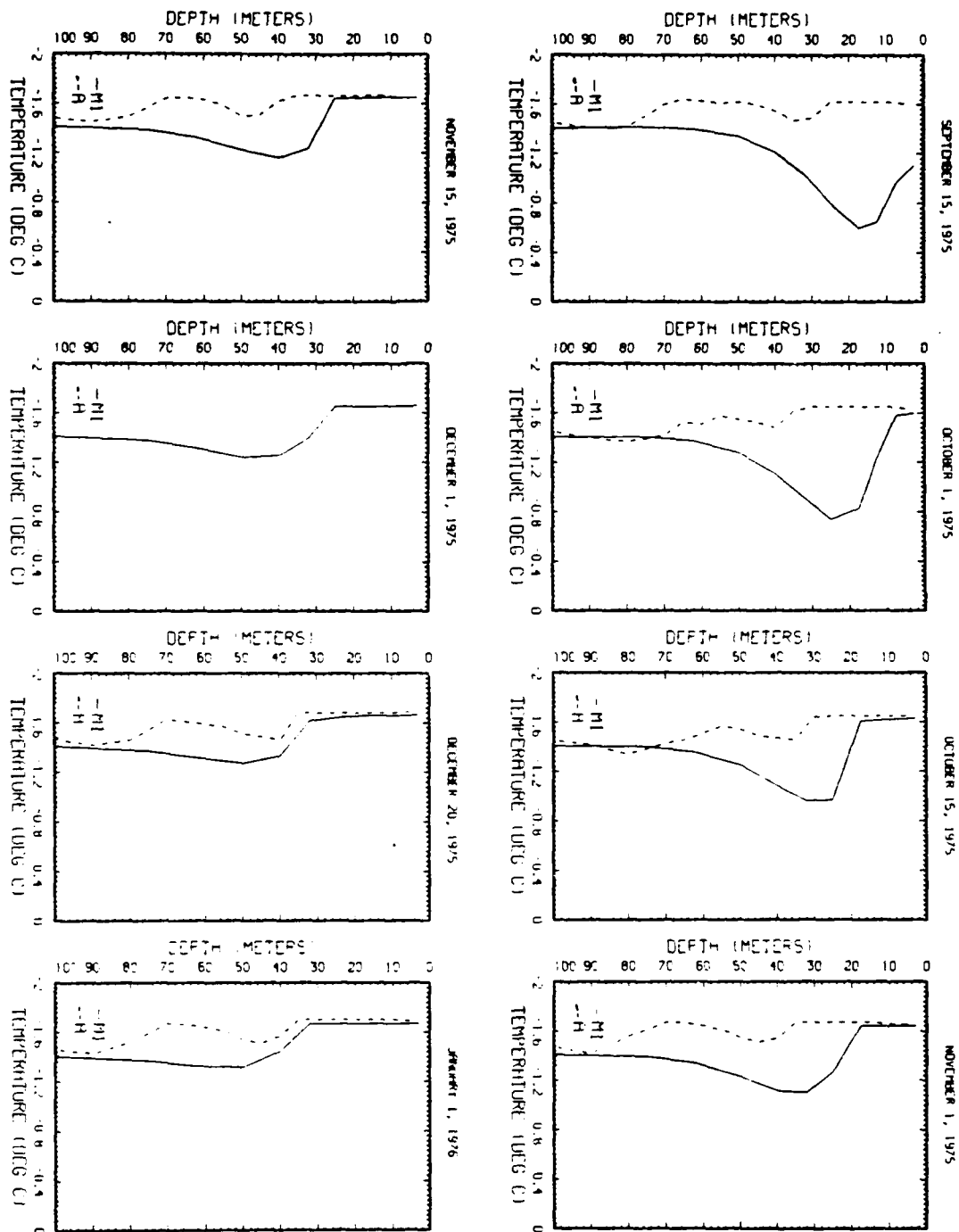


Figure 84. Comparison of temperature profiles from Case 30 and camp Blue Fox from September 15 to January 1.

TEMPERATURE PROFILE PLOTS FOR MODEL RUN AND BLUEFOX DATA
 YEAR NO. 1

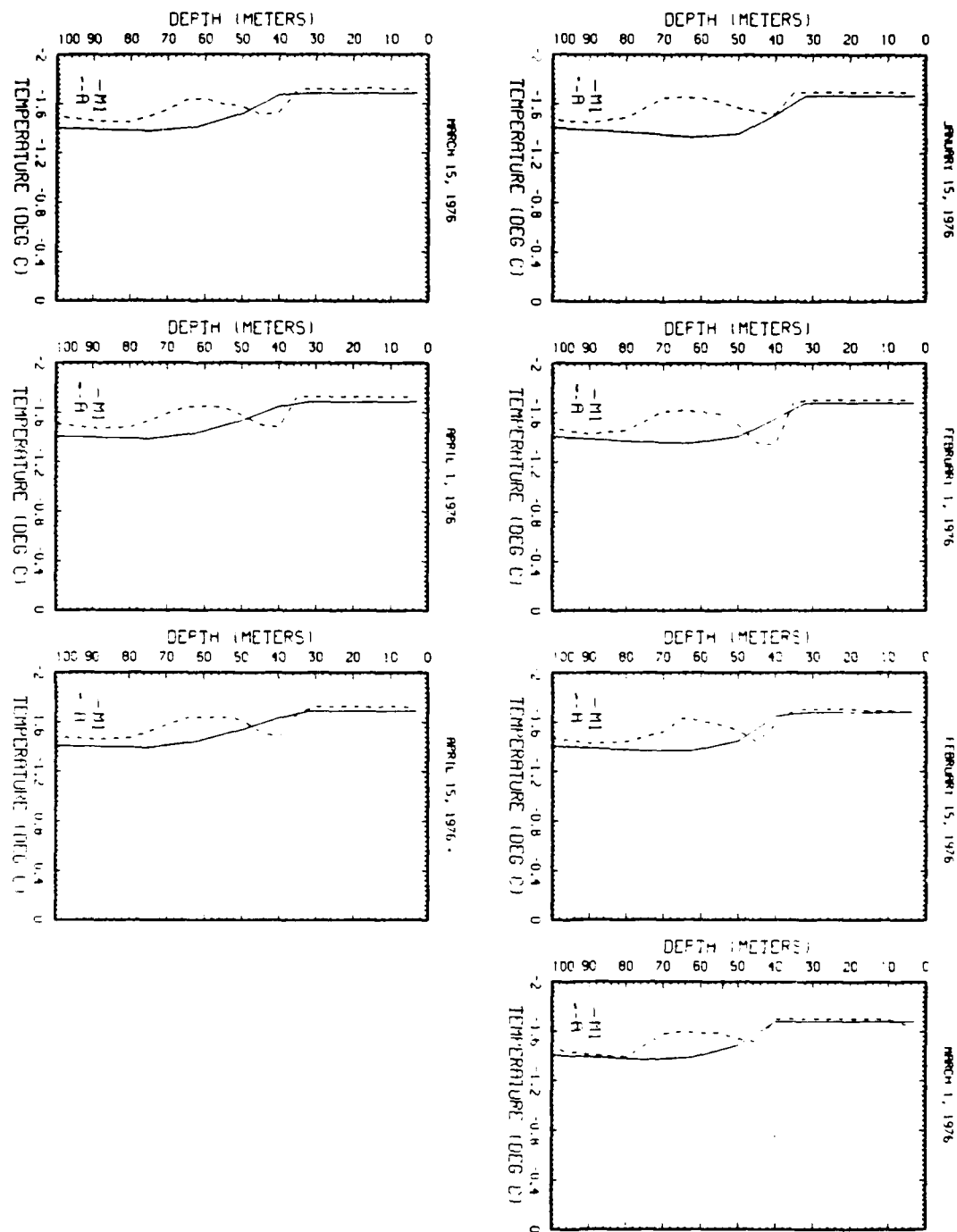


Figure 85. Comparison of temperature profiles from Case 30 and camp Blue Fox from January 15 to April 15.

SALINITY PROFILE PLOTS FOR MODEL RUN AND BLUEFOX DATA
YEAR NO. 1

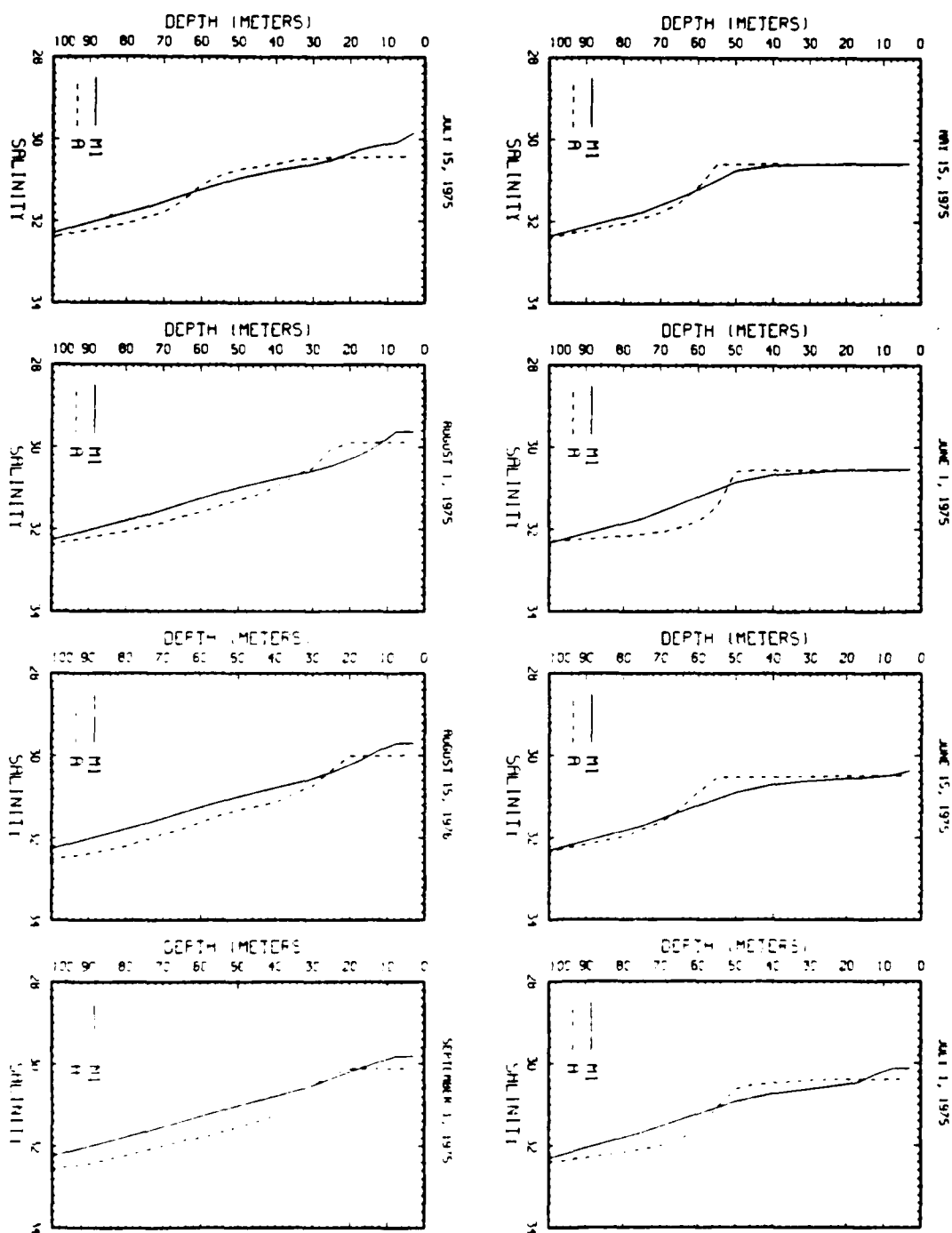


Figure 86. Comparison of salinity profiles from Case 30 and camp Blue Fox from May 15 to September 1.

SALINITY PROFILE PLOTS FOR MODEL RUN AND BLUEFOX DATA
YEAR NO. 1

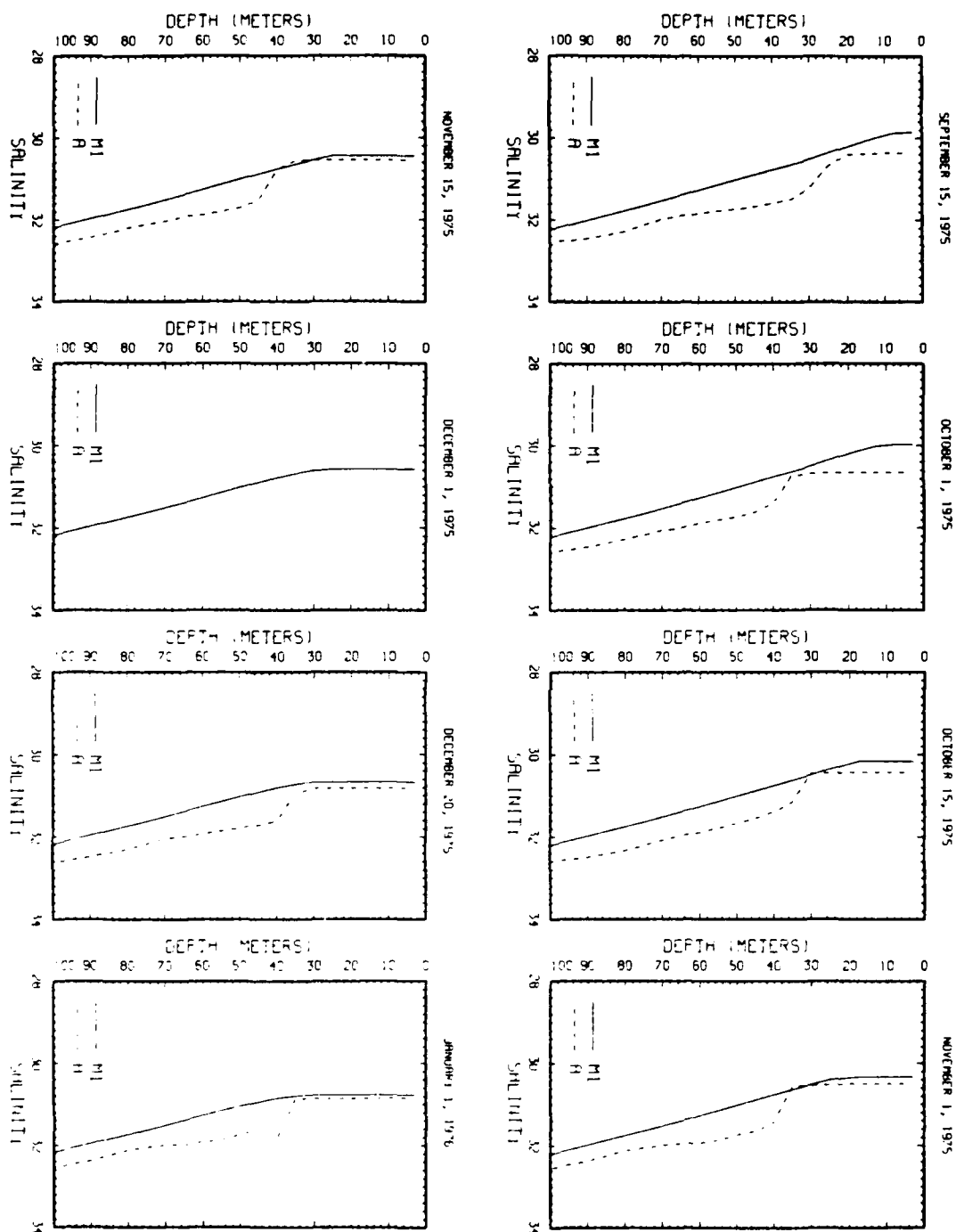


Figure 87. Comparison of salinity profiles from Case 30 and camp Blue Fox from September 15 to January 1.

SALINITY PROFILE PLOTS FOR MODEL RUN AND BLUEFOX DATA
YEAR NO. 1

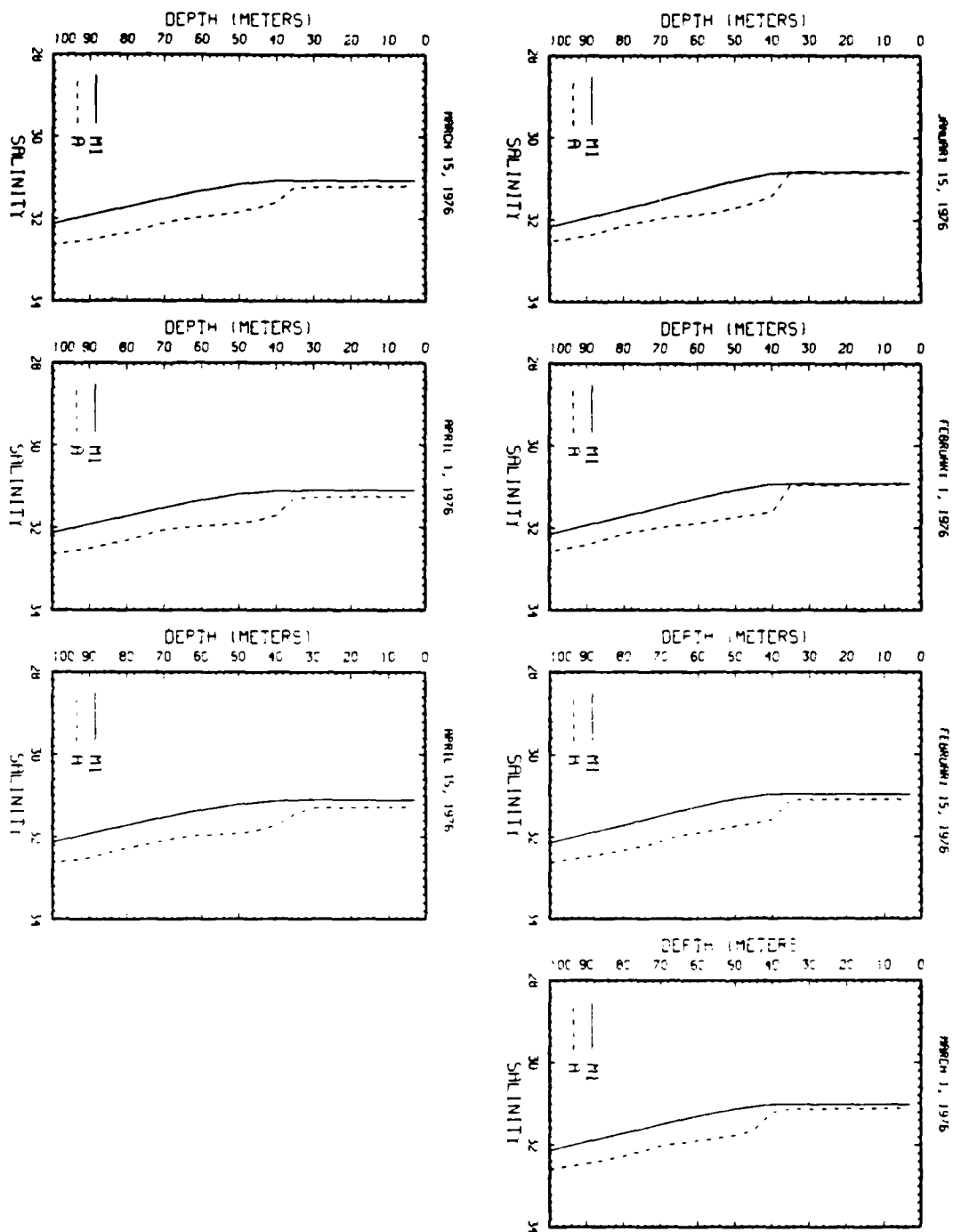


Figure 88. Comparison of salinity profiles from Case 30 and camp Blue Fox from January 15 to April 15.

Appendix A: Ocean Model Equations

a. Ice velocity equation

The ice momentum equations (Eqs. 8 and 9) can be solved by first substituting Eqs. (25) and (26) for the water stress components. The equation for the x-component of the ice velocity then becomes

$$\frac{\partial u_i}{\partial t} = f(v_i - v_g) + \frac{\tau_{ax}}{m} + 5.5E-3 \left[\frac{\rho_o}{\rho_i h_i} \right] \sqrt{[(u_g - u_i)^2 + (v_g - v_i)^2]} \\ ((u_g - u_i)\cos\theta - (v_g - v_i)\sin\theta) \quad (A1)$$

where $\theta = 25^\circ$.

The equation for the y-component becomes

$$\frac{\partial v_i}{\partial t} = -f(u_i - u_g) + \frac{\tau_{ay}}{m} + 5.5E-3 \left[\frac{\rho_o}{\rho_i h_i} \right] \sqrt{[(u_g - u_i)^2 + (v_g - v_i)^2]} \\ ((v_g - v_i)\cos\theta + (u_g - u_i)\sin\theta) \quad (A2)$$

Next let $C = 5.5E-3 \left[\frac{\rho_o}{\rho_i h_i} \right] \sqrt{[(u_g - u_i)^2 + (v_g - v_i)^2]}$ and rearrange the terms in Eq. (A1) to get

$$\frac{\partial u_i}{\partial t} = (f + C \sin\theta)v_i - (C \cos\theta)u_i - fv_g + \frac{\tau_{ax}}{m} + C u_g \cos\theta \\ - C v_g \sin\theta, \quad (A3)$$

and in Eq. (A2) to get

$$\frac{\partial v_i}{\partial t} = - (f + C \sin\theta)u_i - (C \cos\theta)v_i + fu_g + \frac{\tau_{ay}}{m} + C v_g \cos\theta \\ + C u_g \sin\theta. \quad (A4)$$

To simplify the algebraics let

$$F_x = -fv_g + \frac{\tau_{ax}}{m} + C u_g \cos\theta - C v_g \sin\theta, \quad (A5)$$

$$F_y = fu_g + \frac{\tau_{ay}}{m} + C v_g \cos\theta + C u_g \sin\theta, \quad (A6)$$

and

$$f' = f + C \sin\theta. \quad (A7)$$

Next substituting Eqs. (A5), (A6), and (A7) into Eqs. (A3) and (A4) yields

$$\frac{\partial u_i}{\partial t} = f' v_i - (C \cos \theta) u_i + F_x, \quad (\text{A8})$$

and

$$\frac{\partial v_i}{\partial t} = -f' u_i - (C \cos \theta) v_i + F_y. \quad (\text{A9})$$

The finite difference form of the above equations is as follows

$$\frac{u_i^{n+1} - u_i^n}{\Delta t} = f' v_i^{n+1} - (C \cos \theta) u_i^{n+1} + F_x^n, \quad (\text{A10})$$

and

$$\frac{v_i^{n+1} - v_i^n}{\Delta t} = -f' u_i^{n+1} - (C \cos \theta) v_i^{n+1} + F_y^n. \quad (\text{A11})$$

Next Eq. (A10) and Eq. (A11) must be solved for the future value in terms of the previous value, so first solve for u_i^{n+1} and for v_i^{n+1} . The above equations then become

$$u_i^{n+1} = \frac{u_i^n + \Delta t f' v_i^{n+1} + \Delta t F_x^n}{1 + C \Delta t \cos \theta}, \quad (\text{A12})$$

and

$$v_i^{n+1} = \frac{v_i^n - \Delta t f' u_i^{n+1} + \Delta t F_y^n}{1 + C \Delta t \cos \theta}. \quad (\text{A13})$$

Finally, substitute Eq. (A13) into Eq. (A12) and again solve for u_i^{n+1} to get

$$u_i^{n+1} = \frac{(1 + C \Delta t \cos \theta) u_i^n + (1 + C \Delta t \cos \theta) \Delta t F_x^n + \Delta t f' v_i^n + \Delta t^2 f' F_y^n}{(1 + C \Delta t \cos \theta)^2 + \Delta t f'}. \quad (\text{A14})$$

The y-component of the ice velocity can now be found by substituting the value obtained for u_i^{n+1} into Eq. (A13).

b. Water velocity

The momentum equations for the ocean (Eqs. 12 and 13) are solved using a time-splitting technique. First, since v is small, it is combined with the K_M term. Next, the x-component of the velocity is written as follows

$$\frac{u_w^{n+1} - u_w^n}{\Delta t} = f \phi v_w^{n+1} + f(1-\phi) v_w^{n+1} + \frac{\partial}{\partial z} \left[K_M \left(\frac{\partial u_w^n}{\partial z} \right) \right] - f v_g^n \quad (\text{A15})$$

where ϕ can range from 0 to 1. In most simulations, $\phi = 1$ is used.

Next solving Eq. (A15) for u_w^{n+1} yields

$$u_w^{n+1} = u_w^n + \Delta t f \phi v_w^{n+1} + \Delta t f(1-\phi) v_w^{n+1} + \Delta t \frac{\partial}{\partial z} \left[K_M \left(\frac{\partial u_w^n}{\partial z} \right) \right] - \Delta t f v_g^n. \quad (\text{A16})$$

Next, an intermediate value u_w^* is assumed such that

$$\frac{u_w^* - u_w^n}{\Delta t} = \frac{\partial}{\partial z} \left[K_M \frac{\partial u_w^*}{\partial z} \right] . \quad (A17)$$

This equation can be solved for u_w^* by using a tridiagonal solver. Using this value of u_w^* , Eq. (A16) can be rewritten as

$$\frac{u_w^{n+1} - u_w^*}{\Delta t} = f\phi v_w^{n+1} + f(1-\phi)v_w^n - f v_g^n . \quad (A18)$$

Then as

$$u_w^{n+1} = u_w^* + \Delta t f \phi v_w^{n+1} + \Delta t f (1-\phi) v_w^n - \Delta t f v_g^n . \quad (A19)$$

In a similar fashion, the y-component of the velocity can be written as

$$\frac{v_w^{n+1} - v_w^*}{\Delta t} = f\phi u_w^{n+1} - f(1-\phi)u_w^n + f u_g^n . \quad (A20)$$

then as

$$v_w^{n+1} = v_w^* - \Delta t f \phi u_w^{n+1} - \Delta t f (1-\phi) u_w^n + \Delta t f u_g^n . \quad (A21)$$

Finally, substituting Eq. (A21) into Eq. (A19) and solving for u_w^{n+1} yields

$$u_w^{n+1} = \frac{u_w^* + \Delta t f \phi v_w^* - (\Delta t f)^2 (1-\phi) \phi u_w^n + \Delta t f (1-\phi) v_w^n + (\Delta t f)^2 \phi u_g^n - \Delta t f v_g^n}{1 + (\Delta t f \phi)^2} \quad (A22)$$

The value for v_w^{n+1} can be obtained by substituting the value computed for u_w^{n+1} into Eq. (A21).

c. Parameterization of turbulent eddy fluxes

The turbulent eddy fluxes, K_M and K_H , are given by the following equations

$$K_H = l q S_H , \quad (A23)$$

and

$$K_M = l q S_M . \quad (A24)$$

where l is the turbulence length scale, q is the square root of twice the turbulent kinetic energy, and S_H and S_M are stability functions, which are a function of the gradient Richardson number Ri , where

$$Ri = \frac{-\frac{g}{\rho} \frac{\partial \bar{\rho}}{\partial z}}{\left[\left(\frac{\partial \bar{u}}{\partial z} \right)^2 + \left(\frac{\partial \bar{v}}{\partial z} \right)^2 \right]^{1/2}} . \quad (A25)$$

Here, g is the acceleration of gravity and $\bar{\rho}$ is the mean-field density.

The quantity q is calculated from a form of the turbulent kinetic energy equation that expresses a local balance of shear production, buoyancy production, and viscous dissipation of turbulent kinetic energy. The equation is

$$1qS_M \left[\left(\frac{\partial \bar{u}}{\partial z} \right)^2 + \left(\frac{\partial \bar{v}}{\partial z} \right)^2 \right] + 1qS_H \left(\frac{g}{\rho} \frac{\partial \bar{\rho}}{\partial z} \right) - \frac{q^3}{151} = 0 . \quad (A26)$$

The turbulence length scale is calculated from the ratio of the first to the zeroth moment of the turbulence field (Mellor and Durbin, 1975). Thus

$$l = \frac{0.1 \int_{-\infty}^0 |z| q \, dz}{\int_{-\infty}^0 q \, dz} . \quad (A27)$$

These equations, along with Eqs. (12) through (15), close the turbulence parameterization.

Appendix B: List of Symbols

Symbols	Definition
c	Specific heat of seawater
f	Coriolis parameter
F_A	Sum of the atmospheric heat fluxes
F_B	Heat flux from the ocean to the ice or atmosphere
F_{BR}	Heat stored in the brine pocket reservoir
F_l	Latent heat flux
F_L	Incoming longwave radiation
F_R	Incoming shortwave radiation
F_{RH}	Heat from solar radiation penetrating through the ice into the water column
F_S	Conductive heat flux through the snow/ice system
F_{SR}	Downward flux of solar radiation
F_s	Sensible heat flux
H_{deep}	Heat flux from the deep ocean
h_i	Ice thickness
h_{min}	Minimum ice thickness for which the brine pocket simulation is calculated
H_{max}	Maximum heat allowed to accumulate in the brine pockets heat reservoir
h_s	Snow thickness
I_o	Percentage of solar radiation that penetrates into the ice
K_H	Eddy diffusion coefficient for heat
k_i	Heat conductivity of ice
K_M	Eddy diffusion coefficient for momentum
k_s	Heat conductivity of snow
m	Mass of ice
q_b	Volumetric heat of fusion for ice at the bottom of the ice
q_i	Volumetric heat of fusion for ice at the top of the ice
q_s	Volumetric heat of fusion for snow
S	Ocean salinity
S_o	Reference salinity for the ocean
t	Time
T	Ocean temperature
T_B	Temperature at the bottom of the ice

T_S	Temperature at the surface of the snow/ice system or the ocean if open water occurs
u_a	x-component of the wind velocity
u_g	x-component of the geostrophic ocean current
u_i	x-component of the ice velocity
u_w	x-component of the ocean current
v_a	y-component of the wind velocity
v_g	y-component of the geostrophic ocean current
v_i	y-component of the ice velocity
v_w	y-component of the ocean current
w	z-component of the ocean current
z	Vertical coordinate, positive downward from sea surface
$(\bar{})$	Ensemble mean for equations (10)–(17)
(\prime)	Departure from above-defined averages
α_i	Albedo of ice
α_s	Albedo of snow
α_w	Albedo of open water
Δh_b	Predicted change in the ice thickness at the bottom of the ice-growth or decay
Δh_i	Predicted change in the ice thickness at the surface of the ice-melt only
Δh_s	Predicted change in the snow thickness
ΔS	Salinity change
Δt	Time step
ΔT_S	Predicted change in the surface temperature
ν	Background vertical eddy diffusion coefficient
ρ_a	Density of air
ρ_i	Density of ice
ρ_o	Reference density for the ocean
ρ_s	Density of snow
σ	Stefan-Boltzman constant
τ_{ax}	x-component of wind stress
τ_{ay}	y-component of wind stress
τ_{wx}	x-component of stress between the ice and ocean
τ_{wy}	y-component of stress between the ice and ocean

Appendix C: Corresponding Calendar Date and Model Time Step

Dates that correspond to time steps in climatology test cases

Date	Time Step
Jan 1-10	1-30
11-20	31-60
21-30	61-90
Feb 1-10	91-120
11-20	121-150
21-30	151-180
Mar 1-10	181-210
11-20	211-240
21-30	241-270
Apr 1-10	271-300
11-20	301-330
21-30	331-360
May 1-10	361-390
11-20	391-420
21-30	421-450
Jun 1-10	451-480
11-20	481-510
21-30	511-540
Jul 1-10	541-570
11-20	571-600
21-30	601-630
Aug 1-10	631-660
11-20	661-690
21-30	691-720
Sep 1-10	721-750
11-20	751-780
21-30	781-810
Oct 1-10	811-840
11-20	841-870
21-30	871-900
Nov 1-10	901-930
11-20	931-960
21-30	961-990
Dec 1-10	991-1020
11-20	1021-1050
21-30	1051-1080

Dates that correspond to time steps in AIDJEX test cases

Date	Time Step
May 1-10	1-40
11-20	41-80
21-31	81-124
Jun 1-10	125-164
11-20	165-204
21-30	205-244
Jul 1-10	245-284
11-20	285-324
21-31	325-368
Aug 1-10	369-408
11-20	409-444
21-31	445-492
Sep 1-10	493-532
11-20	533-572
21-30	573-612
Oct 1-10	613-652
11-20	653-692
21-31	693-736
Nov 1-10	737-776
11-20	777-816
21-30	817-856
Dec 1-10	857-896
11-20	897-936
21-31	937-980
Jan 1-10	981-1020
11-20	1021-1060
21-31	1061-1104
Feb 1-10	1105-1144
11-20	1145-1184
21-29	1185-1220
Mar 1-10	1221-1260
11-20	1261-1300
21-31	1301-1344
Apr 1-10	1345-1384
11-20	1385-1424
21-29	1425-1460

UNCLASSIFIED

SECURITY CLASSIFICATION OF THIS PAGE

REPORT DOCUMENTATION PAGE				
1a REPORT SECURITY CLASSIFICATION Unclassified		1b RESTRICTIVE MARKINGS None		
2a SECURITY CLASSIFICATION AUTHORITY		3 DISTRIBUTION/AVAILABILITY OF REPORT Approved for public release; distribution is unlimited.		
2b DECLASSIFICATION/DOWNGRADING SCHEDULE				
4 PERFORMING ORGANIZATION REPORT NUMBER(S) NORDA Report 195		5 MONITORING ORGANIZATION REPORT NUMBER(S) NORDA Report 195		
6 NAME OF PERFORMING ORGANIZATION Naval Ocean Research and Development Activity		7a NAME OF MONITORING ORGANIZATION Naval Ocean Research and Development Activity		
6c ADDRESS (City, State, and ZIP Code) Ocean Science Directorate NSTL, Mississippi 39529-5004		7b ADDRESS (City, State, and ZIP Code) Ocean Science Directorate NSTL, Mississippi 39529-5004		
8a NAME OF FUNDING/SPONSORING ORGANIZATION Naval Ocean Research and Development Activity	8b OFFICE SYMBOL (If applicable)	9 PROCUREMENT INSTRUMENT IDENTIFICATION NUMBER		
8c ADDRESS (City, State, and ZIP Code) Ocean Science Directorate NSTL, Mississippi 39529-5004		10 SOURCE OF FUNDING NOS		
		PROGRAM ELEMENT NO 61153N	PROJECT NO 3105	TASK NO 330
		WORK UNIT NO 132227D		
11 TITLE (Include Security Classification) Predictions and Studies with a One-Dimensional Ice/Ocean Model				
12 PERSONAL AUTHOR(S) Shelley H. Riedlinger and Alex Warn-Varnas				
13a TYPE OF REPORT Final	13b TIME COVERED From _____ To _____	14 DATE OF REPORT (Yr., Mo., Day) April 1987		15 PAGE COUNT 120
16 SUPPLEMENTARY NOTATION				
17 COSATI CODES		18 SUBJECT TERMS (Continue on reverse if necessary and identify by block number) Arctic, climatological, thermodynamic, AIDJEX isothermal, diurnal, nondiurnal, Semtner, radiation		
FIELD	GROUP			
	SUB GR			
19 ABSTRACT (Continue on reverse if necessary and identify by block number) A coupled one-dimensional ice/ocean model is developed in differential form. The ice/snow system is represented by the simplified thermodynamic model of Semtner and a dynamic approximation that neglects the internal stresses. The ocean is represented by the Mellor-Yamada Level-2 turbulence mixed-layer model. The thermodynamic coupling considers a moving ice/ocean interface and a salinity flux generated by the freezing or melting of ice. The dynamic coupling occurs via the turbulent stress that exists in the mixed layer beneath the ice. Two test cases are used for model validation and scientific studies. One is the standard climatological test used by Semtner and others. The other test case is with the AIDJEX data. The ice/ocean model is compared to Semtner's ice model to determine the effect of a variable-depth mixed layer as opposed to an isothermal, fixed-depth mixed layer. The sensitivity of the ice/ocean model to changes in certain parameters and forcing is also examined. Finally, the ability of the model to simulate Arctic conditions is shown by comparison of model results to data obtained during AIDJEX.				
20 DISTRIBUTION/AVAILABILITY OF ABSTRACT UNCLASSIFIED/UNLIMITED <input type="checkbox"/> SAME AS RPT <input checked="" type="checkbox"/> DTIC USERS <input type="checkbox"/>		21 ABSTRACT SECURITY CLASSIFICATION Unclassified		
22a NAME OF RESPONSIBLE INDIVIDUAL Shelley H. Riedlinger		22b TELEPHONE NUMBER (Include Area Code) (601) 688-4277		22c OFFICE SYMBOL Code 322

DATE
FILMED
8